Friction
(Quarterly, Started in 2013)
Volume 5 Number 2 / June 2017

ISSN 2223-7690
CN 10-1237/TH

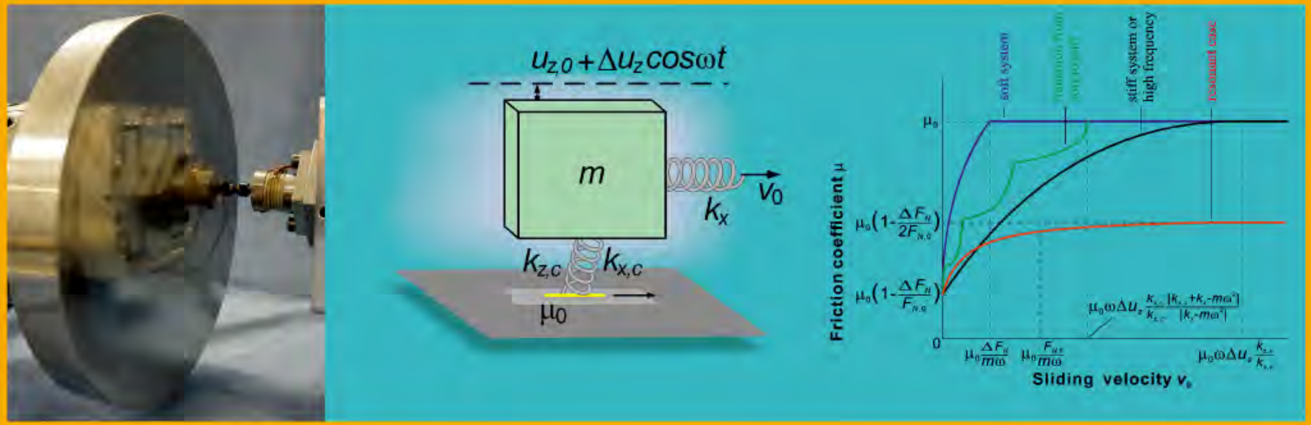

Reduction of friction by normal oscillations. II. In-plane system dynamics

摩擦（英文）　（季刊，2013年创刊）　第5卷　第2期　2017年6月出版

Editor-in-Chief	Jianbin Luo
Sponsored by	Tsinghua University
Supported by	Chinese Tribology Institute
Edited by	Friction Editorial Office
Published by	Tsinghua University Press
Address	Xueyan Building, Tsinghua University, Beijing 100084, China
Website	http://www.springer.com/40544　http://friction.tsinghuajournals.com
Online Manuscript Submission, Review and Tracking System	http://mc03.manuscriptcentral.com/friction

主管单位	教育部
主办单位	清华大学
学术支持	中国机械工程学会摩擦学分会
主　　编	雒建斌
编　　辑	《摩擦》编辑部
出版发行	清华大学出版社有限公司
印刷单位	北京天成印务有限责任公司

ISSN 2223-7690
9 772223 769170 06>

40544
Friction
Volume 5 Number 2 2017 pp 123–230

ISSN 2223-7690
CN 10-1237/TH

Friction

Volume 5 Number 2 / June 2017

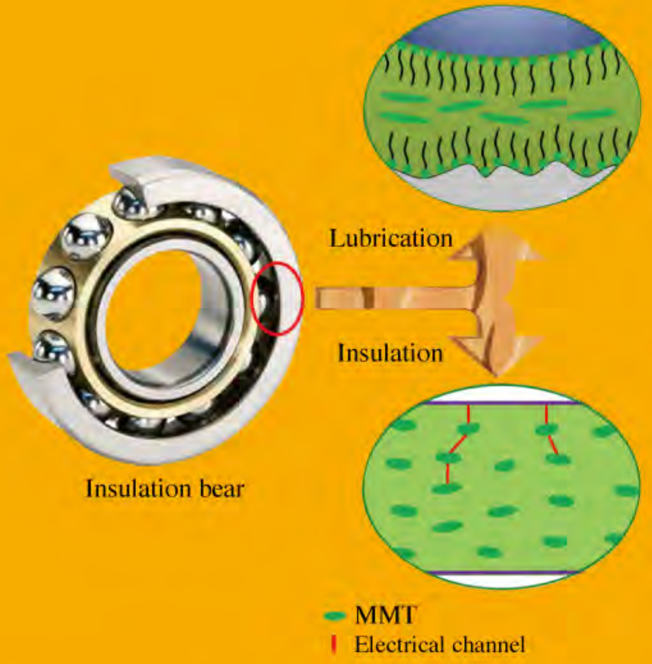

Nano-montmorillonite-doped lubricating grease exhibiting excellent insulating and tribological properties

TSINGHUA UNIVERSITY PRESS
Springer

Friction
ISSN 2223-7690
CN 10-1237/TH
Vol. 5, No. 2, June 2017

Contents

Review Article

Research Article

TSINGHUA UNIVERSITY PRESS Springer

Friction **5**(2): 123–146 (2017) ISSN 2223-7690
DOI 10.1007/s40544-017-0151-0 CN 10-1237/TH

REVIEW ARTICLE

A technical survey on tire-road friction estimation

Seyedmeysam KHALEGHIAN[1,*], **Anahita EMAMI**[2], **Saied TAHERI**[1]
[1] *Center for Tire Research (CenTiRe), Department of Mechanical Engineering, Virginia Tech, Blacksburg, VA 24061, United States*
[2] *Department of Biomedical Engineering and Mechanics, Virginia Tech, Blacksburg, VA 24061, United States*

Received: 23 September 2016 / Revised: 04 November 2016 / Accepted: 24 January 2017

Abstract: Lack of driver's knowledge about the abrupt changes in pavement's friction and poor performance of the vehicle's stability, traction, and ABS controllers on the low friction surfaces are the most important factors affecting car crashes. Due to its direct relation to vehicle stability, accurate estimation of tire-road friction is of interest to all vehicle and tire companies. Many studies have been conducted in this field and researchers have used different tools and have proposed different algorithms. This literature survey introduces different approaches, which have been widely used to estimate the friction or other related parameters, and covers the recent literature that contains these methodologies. The emphasize of this review paper is on the algorithms and studies, which are more popular and have been repeated several times. The focus has been divided into two main groups: experiment-based and model-based approaches. Each of these main groups has several sub-categories, which are explained in the next few sections. Several summary tables are provided in which the overall feature of each approach is reviewed that gives the reader the general picture of different algorithms, which are widely used in friction estimation studies.

Keywords: tire-road friction; friction estimation; model-based approach; experiment-based approach

---

1 Introduction

Approximately 120,000 people were killed on US roadways between 2010–2013 [1–3]. Even in the case of non-fatal crashes, the economic costs are undeniably high [4, 5]. Due to the large number of fatalities and the high economic costs, different studies have been conducted on the effects of different factors on car crashes [6, 7].

Twenty-four percent of all crashes are weather related, which occur on icy, snowy, or wet pavement or in the presence of rain, sleet, fog and snow [8]. Several studies have been conducted on crashes during rainfall and snowfall [9–12]. It was observed in a study on crashes before and after rain in Calgary and Edmonton that the crash rate is 70% higher on the wet pavement [13]. In a similar study, it was shown that the crash frequency on wet roads is twice the rate of the crashes on dry pavements [14]. This high rate of weather related crashes is mainly attributed to the drivers overestimating the pavement friction, and the effect of bad weather condition on the vehicle stability and safety controllers.

Tire-road friction estimation is one of the most important problems for both vehicle and tire industries that can decrease the number of weather related crashes dramatically. The effect of tire-road friction force on vehicle performance and stability and on the performance of traction and ABS controllers is undeniable [15–19].

Different studies have developed and used different algorithms to estimate the tire-road friction. Based on the approaches that they have followed, all of the related research can be divided into the following two categories:

1–Experiment-based;
2–Model-based.

In experiment-based approaches, it is attempted to

---

* Corresponding author: Seyedmeysam KHALEGHIAN, E-mail: meysam@vt.edu

find a correlation between the sensor data (acoustic sensors, temperature sensor, etc.) and tire-road friction-related parameters. The model-based approaches try to estimate the friction using simplified mathematical models, which can be divided into three sub-categories: wheel and vehicle dynamic based approaches, slip based approaches, and tire model based approaches.

In vehicle dynamic base approached, different dynamic models (single wheel model, bicycle model, planar model, etc.) are used along with an estimation algorithm (recursive least square, steady state and extended Kalman filter, sliding mode observer, etc.) to estimate the tire-road friction force and other friction-related parameters such as slip ratio, slip angle, etc. Tire model based approaches use the friction force and slip data along with one of the tire models (Magic formula, Brush model, LuGre model, etc.) to estimate the maximum tire road friction coefficient. In slip base approaches it is assumed that the value of friction in the saturated area of μ–slip curve can be estimated based on the slope of the curve in low slip region (linear region).

This study presents a technical survey of tire-road friction estimation research. For each of the above approaches, first, the method is explained briefly and then the review of the literature on the subject is presented. The rest of the paper is organized as follows: first, the tire-road friction force and aligning moment are introduced; the experiment-based friction estimation approaches are discussed in the second section. The model based friction estimation algorithms are reviewed in the third section followed by the conclusions in the last section.

Tire-road friction coefficient and self-aligning moment

In order to start with different friction estimation approaches, it is required to define the tire forces, aligning moment, and friction coefficient. Free body diagram of a single wheel is shown in Fig. 1, which F_x, F_y, F_z are longitudinal, lateral, and normal tire forces, respectively. The normalized tire traction force is defined as [20]:

$$\rho = \frac{\sqrt{F_x^{\,2} + F_y^{\,2}}}{F_z}$$

where its maximum value is called the friction coefficient (μ). The wheel aligning moment is defined as the tendency to align the wheel plane with the direction of wheel travel, which is caused by steering geometry and side deformation of a tire, which moves forward and has nonzero slip angle.

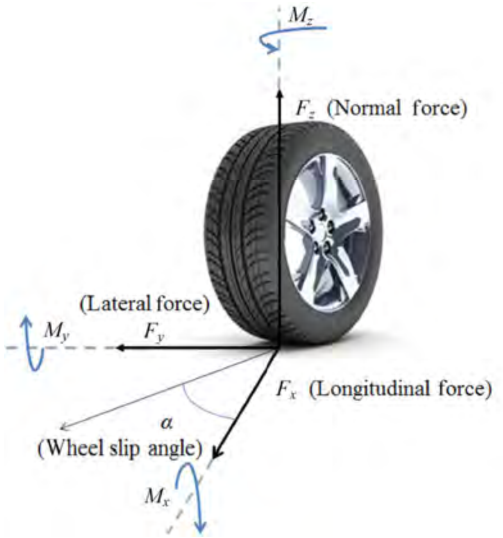

Fig. 1 Free body diagram of a single wheel.

2 Experiment-based

Figure 2 demonstrates the main philosophy behind experiment-based approaches. As it is shown in Fig. 2, most of the experiment-based methods use sensor measurements of the friction-related parameters (tire noise, tire longitudinal or lateral deformation, etc.) and try to correlate these parameters to tire-road friction [21, 22].

Based on the sensor type and the parameter which is used for this estimation, experiment-based approaches can be categorized as follows.

2.1 Optical sensors and cameras

Optical sensors and cameras are used to detect surface properties related to friction. Using optical sensors

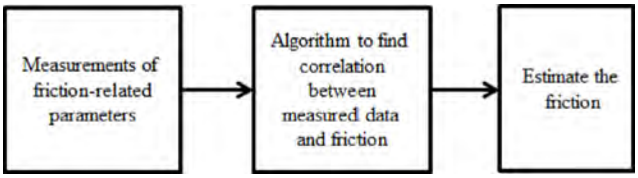

Fig. 2 Experiment-based flowchart diagram.

to measure infrared light at different wavelengths reflected from the roads, the surface type (dry, wet, icy, snowy, etc.) can be identified. The principal of road-eye sensors is shown in Fig. 3 [23]. The other use of optical sensors is to estimate the sidewall deformation and correlate it with friction [24–26].

Cameras are also used to identify the texture of different surfaces. Once the texture is evaluated, a neural network can be trained to estimate the surface friction [27]. The conventional methods of detecting road conditions are [28]:

- Detection by color difference: It uses the ratios of color signals (R, G and B) to detect road condition.
- Detection by pattern matching: This technique uses geometrical features along with pixel density to estimate the condition of the road.
- Detection by infrared rays: Infrared can be used to detect the presence of water as water has a relatively large absorption band in the infrared range.
- Detection by difference in polarized level: It uses a difference between horizontal and vertical polarization to detect road condition.

What follows is the review of the papers that have used optical sensors for friction estimation. Holzmann et al. [29] used cameras and microphones for estimating the friction coefficient. The image captured by the camera was analyzed for the luminance and neighborhood of pixels. Microphone was used as a reactive measurement to improve the accuracy of the estimation; the frequency range of 100–600 Hz was analyzed. Kuno and Sugiura [28] used a CCD camera to detect the road condition. They detected the distribution of gloss on road surface due to presence of water using the high and low levels of luminance signals. Jokela et al. [30] used two methods of measurement: polarization change and graininess analysis. The amount of vertical and horizontal polarized light reflecting from the surface was used to detect the road surface condition. Graininess analysis is done by using a low pass filter on the image making it blurry and comparing the contrast with the original image.

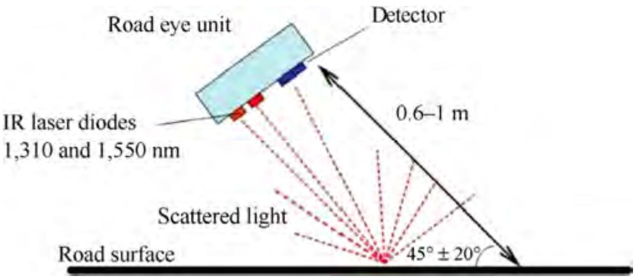

Fig. 3 The schematic of using optimal sensor to identify different surfaces [23].

2.2 Acoustic sensor

Acoustic sensors are used to classify the road surface type/condition (asphalt, concrete, wet, dry, etc.) based on the tire noise. In some of the studies, the acoustic sensors were attached to the vehicle's chassis [31]. Figure 4 demonstrates the algorithm, which uses support vector machine (SVM) to classify different surfaces based on tire noise.

Some other studies have used a microphone, installed at a fixed road location, to record the noise generated by the vehicles passing by and use the recorded data to estimate the pavement status [32–35].

2.3 Tire tread sensors

Tire tread sensors are used to monitor the interaction between tire and the road, and to estimate the

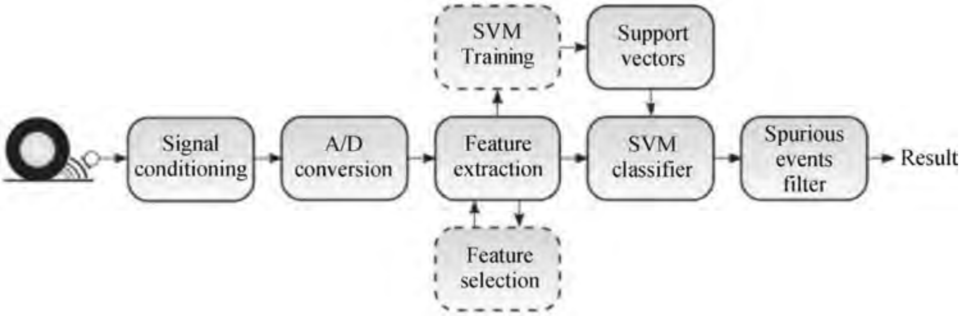

Fig. 4 Friction estimation algorithm using acoustic sensors. Reproduce with permission from Ref. [31]. Copyright Elsevier, 2014.

deflection of tread elements inside the contact patch. The sensor types are mostly accelerometer and piezo electric and magnetic sensors. Erdogan et al. used the piezoelectric sensor inside the tire (in the tread area), which estimates lateral deflection profile of the carcass and uses it to estimate the friction [36]. Magnets vulcanized into the tread of a Kevlar-belted tire are also used in some studies to measure the deflection of the tread in x, y, and z directions as a function of its position inside the contact patch [21, 22, 37–39]. Using the fact that the tread deformation is caused by the total force acting on the tire, the friction is estimated. In other studies, tri-axial accelerometers attached to the innerliner of the tire, shown in Fig. 5(b), are used to estimate the friction [40].

Matilainen and Tuononen [41, 42] used the signals from the tri-axial accelerometer inside the tire to estimate contact patch length. The algorithm detects two acceleration peaks in the longitudinal acceleration signal and uses it along with wheel angular speed to estimate contact patch. Khaleghian et al. [43, 44] and Singh et al. [40] utilized a tri-axial accelerometer attached to the innerliner of the tire; using a neural network algorithm, they estimated the tire normal load. Niskanen and Tuononen [45–47] used three tri-axial accelerometers inside the tire to find friction indicators on smooth ice and concrete surfaces. The radial acceleration signal from the accelerometer is analyzed at the leading edge of the contact patch for friction indicators. They have stated that the vibration in the leading edge due to slip on low friction surfaces can be used to determine the road surface type.

Fig. 5 Using tread sensors (tri-axial accelerometer) to estimate the friction. Reproduce with permission from Ref. [40]. Copyright Khaleghian, 2017.

In addition to the studies and approaches that were introduced in this section, several patents have been submitted, and have used different experiment based methods to estimate the friction or other related parameters; some of these patents are summarized in Table 1.

Although the tire-road friction can be estimated using some of the experiment based approaches, in most cases their accuracy is reduced when the testing condition deviates from the condition under which the algorithm was trained. In order to make the estimation algorithms more robust and take the dynamic of the vehicle into account, model-based approaches are introduced.

3 Model-based

Model-based approaches contain all the studies that use a mathematical/dynamical model to estimate the friction. No need of any expensive special sensor which is standard on today’s vehicles and accuracy and repeatability of the results in most of the cases, makes this category more popular as compared with experiment-based approaches. The model-based studies can be divided into three main groups: wheel and vehicle dynamic based, tire model based, and slip-slope based approaches.

3.1 Wheel and vehicle dynamics based

Studies, which are based on this approach, use the dynamical model of the system, in which some of the states can be measured (like angular velocity of the wheel) and some other states cannot be measured (like friction force, longitudinal speed, etc.). Based on dynamical model of the system and the measured states, the rest of the states can be estimated using different estimation algorithms such as recursive least square (RLS), Kalman filter, etc. The general flowchart of algorithm which is used in most of vehicle dynamic based studies is shown in Fig. 6.

Some of the most common dynamical models in the friction estimation studies are wheel tire model, roll

Table 1 Summary of the patents which have used experiment based methods.

Inventor name	Estimated parameters	Summary of invention
Klein [48]	Friction coefficient	He used a steering system which was controlled by a control module. They estimated the steering gain and steering load hysteresis along with a reference, they determined the friction.
Singh [49, 50]	Tire normal load, side slip-angle	Two strain sensors are attached to the inner and outer sidewalls of a tire (sidewall strain sensors) , using the average power of these signals in different tire pressures to estimate the normal load, also they developed an algorithm to estimate the side slip-angle based on properties of strain signals (then vehicle dynamic based approach was used to estimate the tire longitudinal and lateral force).
Singh et al. [50]	Tire normal load, side slip-angle	They used a set of strain sensors affixed to opposite sidewalls of the tire. Estimating the slope difference in opposite sidewalls strain signals, they estimated the side slip angle. They also estimated the tire normal load based on the average power of strain signal.
Singh et al. [51]	Tire sidewall force	They used a piezo film in one or both sidewalls of the tire. The sensor generates a signal within the contact patch area (can be used to estimate the length of the contact patch), where power of the signal indicates the sidewall deformation. The power to load map for different tire pressure is used to estimate the sidewall force.
Miyazaki [52]	Tire forces, friction coefficient	Several strain sensors are attached to the vicinity of the wheel on the axle, which provide the strain signals. The produced signals are used to estimate the tire forces and tire-road friction coefficient (from the correlation between strain signals and desired parameters).
Hattori [53]	The strain state of the tire	A series of conductors composed of plurality of conductor pieces (embedded in lines at specific interval in circumferential direction of the tire) are used to provide the strain states of the tire. A monitoring device releases signal (pulse electromagnetic wave), also receive the reflected signals from the foils. The time difference between radiation and reception in different conditions is used to evaluate the strain stress of the tire.
Hillenmayer and Kuchler [54]	Tire static load, nature of the road surface	A pressure sensor and a deformation sensor are used in the tire; using frequency-dependent analysis on the sensor signal they estimate the static loading and the nature of the road surfaces.
Miyoshi et al. [55]	Tire longitudinal force	Two magnetic sensors are used to measure the rotation angle of the wheel and wheel axle. Then they used a computing device to calculate the tire warp angle, which is derived by the difference between tire rotational angle during load and no-load condition. Then they estimated the tire longitudinal force as a function of tire warp angle.
Sistonen [56]	The friction on a surface	He developed a new device consist of a wheel, an arm which is attached to wheel axle and a spring, which is attached between measuring wheel and its axle to estimate the friction. The degree of rotation of the measuring wheel at the point, where the wheel starts to slid, is used to estimate the friction.
Bell and Bell [57]	Friction coefficient	They used tread force sensor, one end of the sensor is fixed on the tread and the other end is on the tire structure, where slipping of small discrete tread element can be detected. Compiling the sensor data of the tire deformation-induced tread gripping force, the friction coefficient is estimated.
Abe and Sawa [58]	Dynamic friction coefficient	They developed a new device to measure the dynamic friction coefficient which includes a disk with measuring rubber member, a driving disk adapted to rotate co-axially with the disk and dynamometer interconnects the disk and the driving disk. A tachometer is also used to measure the speed of the rubber. Using X-Y recorder, which records the output signals of friction measuring portion and the tachometer, the friction coefficient is estimated.

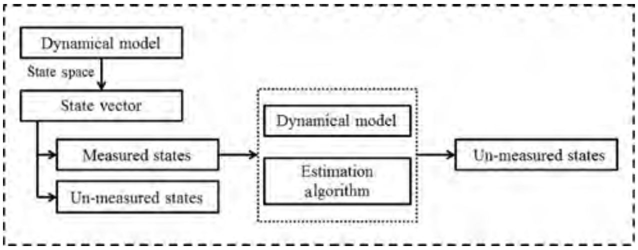

Fig. 6 The general flowchart for vehicle dynamic based approaches.

dynamic model, bicycle model, quarter-car model, and four-wheel vehicle dynamic model, which are explained in more details next.

3.1.1 *Wheel dynamic model*

Free-body diagram of a single wheel is depicted in Fig. 7 in which, F_{rr} is the rolling resistance force, and T is the transmitted wheel torque. The equations of motion for this problem are as follow:

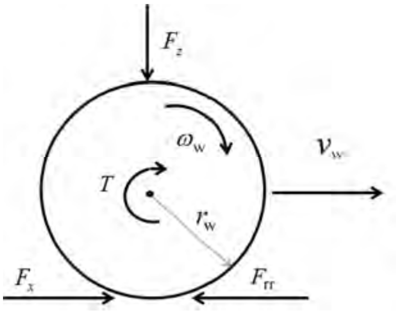

Fig. 7 Free body diagram of a single wheel.

$$m_w \dot{v}_x = F_x - F_{rr} \tag{2}$$

$$J_w \dot{\omega}_w = (T_w - T_b) - F_x r_w - F_{rr} r_w \tag{3}$$

where m_w is the total mass of the wheel, J_w is the moment of inertia of the wheel, and T_w, T_b are the drive and brake torques, respectively. The value of wheel rolling resistance force can be calculated as:

$$F_{rr} = f_r W \tag{4}$$

where W is the weight on the wheel and f_r is the rolling resistance coefficient that can be expressed as a function of tire pressure and wheel velocity. Several equations have been developed over years to estimate the rolling resistance. One suggests following equation for rolling on concrete surface [59]:

$$f_r = f_o + 3.24 f_s \left(\frac{V}{100} \right)^{2.5} \tag{5}$$

where V is the speed in mph, f_r and f_o are basic coefficient and speed effect coefficient respectively that depend on inflation pressure. Equation (3) is widely used in the literature in order to estimate the tire longitudinal friction force [18, 60, 61]. However, the accuracy of estimated longitudinal force highly depends on the accuracy of the effective rolling radius of the tire (r_w). The effective rolling radius is presented as [20]:

$$r_w = \frac{\sin\left[\arccos\left(\frac{r_{static}}{r_0} \right) \right]}{\arccos\left(\frac{r_{static}}{r_0} \right)} \tag{6}$$

$$r_{static} = r_0 - \frac{F_z}{k_t}$$

where r_0 is the initial radius of the tire and k_t is the vertical stiffness of the tire. Wheel dynamic model is mostly used with a tire model in order to estimate the longitudinal force and longitudinal friction [62, 63]. Hsiao et al. [63] substituted the measured wheel torque and wheel angular velocity into Eq. (3), obtained from moment balance equation of each wheel, to estimate the tire longitudinal force. Rajamani et al. [64] used the measured data of angular wheel speed and proposed a sliding mode observer to estimate the tire longitudinal force based on single wheel dynamic model. Cho et al. [65] used the same approach to estimate the longitudinal tire force and showed that the estimated force is accurate for the low slip vehicle maneuvers. Rabhi et al. [66, 67] used a single wheel model with cascaded first and second sliding observers to estimate the contact force. They used the measured data of longitudinal speed of the vehicle, angular position of the wheel and wheel torque along with robust differentiator and sliding mode observer to estimate the velocity and acceleration of the wheel, longitudinal and vertical tire forces and friction coefficient.

3.1.2 1DOF roll dynamic model

The most common vehicle models, which are used to estimate the roll dynamics of the vehicle, are 3DOF model, which represents lateral, yaw and roll motions of the vehicle, and 1DOF model, representing the roll dynamics.

The 1DOF roll dynamic model has practical advantages in comparison to 3DOF model, which does not need the cornering stiffness (which is not easy to be estimated), besides it is not sensitive to the nonlinear tire dynamics. For these reasons, 1DOF model is widely used in the vehicle state estimation studies. Figure 8 demonstrates the schematic of 1DOF vehicle roll model [68], where k_{roll}, c_{roll} are roll stiffness and roll damping coefficients for the combination of tire-suspension, respectively (which are assumed to be constant), and h_{roll} is the distance from the roll center to the vehicle CG. Assuming the roll axis is fixed and there is no vertical motion, the equation of motion is formulated as:

$$(I_x + m_s h^2_{roll})\ddot{\phi}_{chassis} + c_{roll}\dot{\phi}_{chassis} + k_{roll}\phi_{chassis} = -m_s h_{roll} a_{y,m} \tag{7}$$

where $I_x + m_s h^2_{roll}$ is the moment of inertia around the roll axis, I_x is the moment of inertia around x axis and

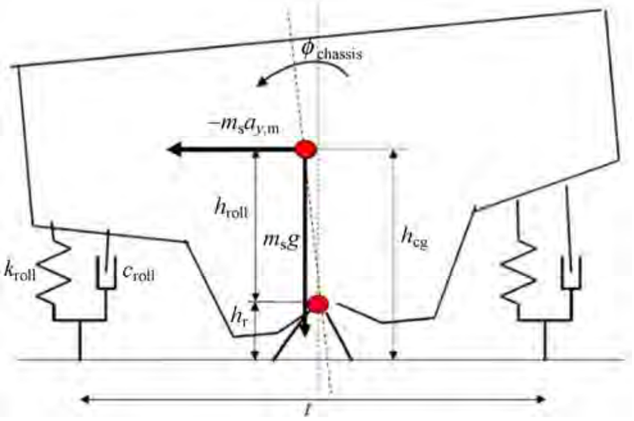

Fig. 8 The schematic of 1DOF roll vehicle model. Reproduce with permission from Ref. [68]. Copyright Singh, 2012.

m_s is the sprung mass of the vehicle. The vehicle roll dynamic model is mostly used to estimate the vehicle roll angle, which is a key factor to obtain the normal load at the wheels. Some of the studies, which have used roll dynamic model, are summarized in Table 2.

3.1.3 *Quarter car model*

The quarter car model is a 2DOF model which is mostly used to model the vertical dynamic (especially suspension) of the car. As it is shown in Fig. 9, quarter car model is represented with two lumped masses, $m_{\text{qs}}, m_{\text{qu}}$ (sprung mass and un-sprung mass), which are $\frac{1}{4}$ vehicle body mass and wheel mass respectively. The suspension system of the vehicle is presented as a set of spring damper system (k_s, c_s) while the tire is presented as a single spring (k_u) (however in some other studies, tire is considered as set of spring-damper too).

The equations of the motion for the quarter-car vehicle model shown in Fig. 8 are presented as:

$$\begin{aligned} m_s\ddot{x}_s + c_s(\dot{x}_s - \dot{x}_u) + k_s(x_s - x_u) = 0 \\ m_u\ddot{x}_u + c_s(\dot{x}_u - \dot{x}_s) + (k_u + k_s)x_u - k_s x_s = 0 \end{aligned} \tag{8}$$

Quarter car model is mainly used in friction estimation studies to obtain the tire normal force and road profile. Several studies have measured the vertical acceleration of the un-sprung mass and the suspension deflection and have used them to estimate the normal force using the following equation [75–77]:

$$F_z = c_s(\dot{x}_s - \dot{x}_u) + k_s(x_s - x_u) - m_u\ddot{x}_u \tag{9}$$

Doumiati et al. [78, 79] used the quarter car model to estimate tire normal load and the road profile. First, they used accelerometer measurements to calculate the vehicle body vertical position, and then used it as a measured state for Kalman filter to estimate the normal wheel load and road profile.

Next, the planar dynamic models of the vehicle are introduced; four-wheel vehicle model and its simplified version, bicycle model are discussed in more details which are widely used in vehicle state estimation studies.

3.1.4 *Four-wheel vehicle model*

Four-wheel vehicle model (also called two-track model) just considers the longitudinal, lateral and yaw motions of the vehicle, while roll, pitch, and vertical motion are ignored. The schematic of this model is shown in Fig. 10 [20], where t is the track length, l_f, l_r are the

Table 2 Some of the studies which have used roll dynamic model.

Authors	Measured states	Estimated states	Method
Hac et al. [69]	Lateral acceleration, yaw rate	Roll angle	Closed-loop adaptive observer was used to estimate the roll angle and roll rate with respect to the road.
Tsourapas et al. [70]	Load transfer ratio	Vehicle roll dynamic	Two rolls over indexes are introduced and analyzed; these indexes are: actual lateral transfer ratio (LTR) and predictive lateral transfer ratio and predictive lateral transfer ratio (PLTR).
Grip et al. [71]	Roll rate	Roll angle	Combination of vehicle dynamics control system and a roll over mitigation system is used to estimate the roll angle.
Chen et al. [72] Ryu et al. [73]	Lateral acceleration, yaw rate	Roll angle	They used a roll vehicle model (either 3DOF model or 1DOF model) along with Kalman filter to estimate the roll angle.
Cho et al. [74]	Longitudinal speed, yaw and roll rate, lateral acceleration	Roll angle	Vehicle state index based switching is used on the roll dynamic and kinematic model to estimate the roll angle.

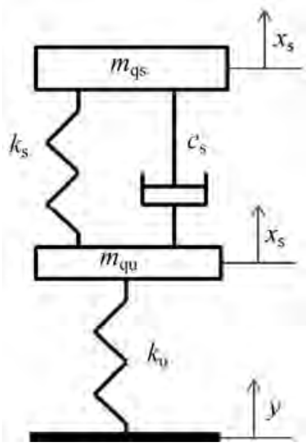

Fig. 9 Schematic of quarter car vehicle model.

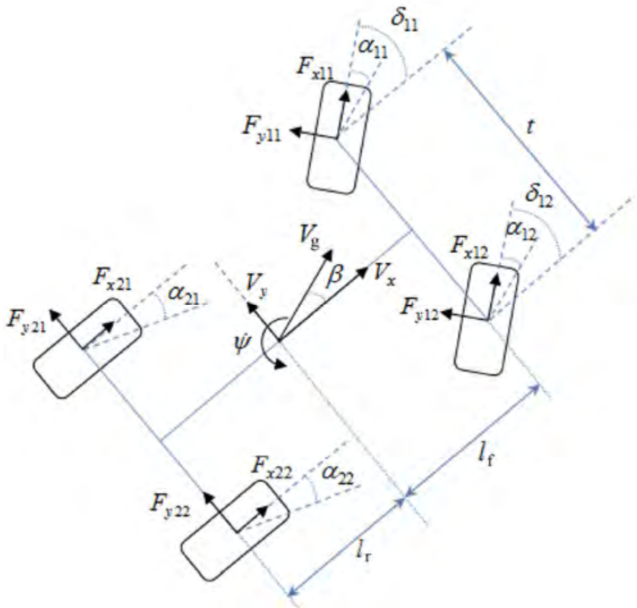

Fig. 10 The schematic of four wheel vehicle model.

distance of center of gravity of the vehicle (CG) from the front and rear axle respectively, V_g is the velocity of CG and V_x, V_y are its component in x and y direction respectively. Also $\dot{\psi}$ is the yaw rate, δ is the steering angle and it is assumed that both front wheels have the same steering angle ($\delta_{11} = \delta_{12}$). The equations of motion for this model are as follows [20]:

$$\ddot{\psi} = \frac{1}{I_z}\begin{bmatrix} l_f\left[F_{y11}\cos\delta + F_{y12}\cos\delta + F_{x11}\sin\delta + F_{x12}\sin\delta\right] \\ -l_r\left[F_{y21} + F_{y22}\right] + \frac{t}{2}[F_{y11}\sin\delta - F_{y12}\sin\delta \\ +F_{x12}\cos\delta - F_{x11}\cos\delta + F_{x22} - F_{x21}] \end{bmatrix} \tag{10}$$

$$\dot{\beta} = -\dot{\psi} + \frac{1}{m_v V_g}\begin{bmatrix} -(F_{x11} + F_{x12})\sin(\beta - \alpha) \\ +F_{y11}\cos(\beta - \alpha) + F_{y12}\cos(\beta - \alpha) \\ +F_{y11}\cos(\beta - \alpha) + (F_{y21} + F_{y22})\cos(\beta - \alpha) \\ -(F_{x21} + F_{x22})\sin\beta \end{bmatrix} \tag{11}$$

$$a_y = \frac{1}{m_v}\begin{bmatrix} F_{y11}\cos\delta + F_{y12}\cos\delta + F_{y21} + F_{y22} \\ +F_{x11}\sin\delta + F_{x12}\sin\delta \end{bmatrix} \tag{12}$$

$$a_x = \frac{1}{m_v}\begin{bmatrix} -F_{y11}\sin\delta - F_{y12}\sin\delta + F_{x21} + F_{x22} \\ +F_{x11}\cos\delta + F_{x12}\cos\delta \end{bmatrix} \tag{13}$$

$$\dot{V}_x = V_y\dot{\psi} + a_x \tag{14}$$

$$\dot{V}_y = -V_x\dot{\psi} + a_y \tag{15}$$

$$\dot{V}_g = \frac{1}{m_v}\begin{bmatrix} (F_{x11} + F_{x12})\cos(\beta - \delta) + F_{y11}\sin(\beta - \delta) \\ +F_{y12}\sin(\beta - \delta) + (F_{x21} + F_{x22})\cos\beta \\ +(F_{x21} + F_{x22})\cos\beta \\ +(F_{y21} + F_{y22})\sin\beta \end{bmatrix} \tag{16}$$

where I_z is the moment of inertia of the car around z axis, m_v is the vehicle mass and β is the vehicle side slip angle. Table 3 summarizes some of the studies which have used the four-wheel vehicle dynamic model to estimate the friction force, friction coefficient or other parameter related to friction estimation problem. The simplified version of four-wheel vehicle model is bicycle model (also called single-track model) which is introduced in the next section.

3.1.5 *Bicycle model*

The schematic of the bicycle model is shown in Fig. 11, which was introduced by Segel in 1956 [20]. The bicycle mode is widely used to describe the handling dynamics of the vehicle, in which vertical and roll motions are not taken into account.

The simplified equations of motion for the bicycle model are as follow:

$$\ddot{\psi} = \frac{1}{I_z}\left[l_f\left[F_{x1}\sin\delta + F_{y1}\cos\delta\right] - l_r F_{y2}\right] \tag{17}$$

$$\dot{\beta} = \frac{1}{m_v V_g}\begin{bmatrix} -F_{x1}\sin(\beta - \delta) + F_{y1}\sin(\beta - \delta) \\ +F_{y2}\cos\beta - F_{x2}\sin\beta \end{bmatrix} - \dot{\psi} \tag{18}$$

$$\dot{V}_g = \frac{1}{m_v}\begin{bmatrix} F_{x1}\cos(\delta - \beta) - F_{y1}\sin(\delta - \beta) \\ +F_{x2}\cos\beta + F_{y2}\sin\beta \end{bmatrix} \tag{19}$$

Table 3 Some selective studies which have used four-wheel vehicle model.

Authors	Measured states	Estimated states	Method
Samadi et al. [80]	Longitudinal acceleration, lateral acceleration for the front and rear axles, angular velocity of the wheels	Longitudinal tire force for all wheels and lateral force for front and rear axles	They used extended Kalman filter to estimate the tire forces, they used Pacejka as the tire model and nonlinear model for hydraulic braking system.
Baffet et al. [81]	Yaw rate, velocity of CG, longitudinal & lateral acceleration	Tire forces, vehicle velocity, yaw rate	They used extended Kalman filter (with random walk model for the forces) to estimate the tire forces, then they estimated the side-slip angle based on dynamic of the problem. Cornering stiffness was estimated based on the data of tire forces and side slip angle through another Kalman filter algorithm.
Shim and Margolis [82, 83]	Longitudinal & lateral acceleration, steering angle, wheel angular velocity	Tire forces	They used four-wheel dynamic model and estimate the tire forces base on the analytical tire model (relation between the measured and estimated states) which they proposed.
Doumiati et al. [84–88]	Longitudinal & lateral acceleration, steering angle, wheel angular velocity, yaw and pitch rate, suspension displacement	Tire forces, vehicle side slip angle	They used vehicle roll model to estimate the tire normal force and then used a four-wheel vehicle model dynamics of the problem; using two observer (extended and unscented Kalman filter) they estimated the tire force and vehicle side slip angle.
Ghandour et al. [89, 90]	Longitudinal & lateral acceleration, steering angle, wheel angular velocity, yaw and pitch rate, suspension displacement	Tire lateral force and side slip angle	Using the roll vehicle model, they estimated the tire normal load, then they used extended and unscented Kalman filter to estimate the lateral force and side slip angle.
Ghandour et al. [91]	Longitudinal & lateral acceleration, steering angle, wheel angular velocity, yaw and pitch rate, suspension displacement	Lateral load transfer, lateral skid indicator	They used the vehicle roll model for the normal load then they proposed a maximum friction coefficient estimation based algorithm to evaluate a lateral risk skid indicator.
Dakhlallah et al. [92] Sebsadji et al. [93]	Longitudinal & lateral acceleration, steering angle, wheel angular velocity, yaw rate	Tire forces and road grade	They used an extended Kalman filter and Luenberger observer based method on the nonlinear vehicle model to estimate the forces and road grade.
Cheng et al. [94]	Longitudinal & lateral acceleration, steering angle, wheel angular velocity, yaw rate	Vehicle side slip angle, lateral tire force and tire road friction coefficient	They used unscented Kalman filter based estimation algorithm to estimate the vehicle's desired states and tire road friction coefficient.
Ray [95, 96]	Yaw and roll rate, wheel angular velocity, longitudinal and lateral acceleration	Slip ratio, slip angle, wheel velocity, normal force at each wheel, longitudinal and lateral force	They used a nine degree of freedom model, which is a four-wheel model with vehicle roll dynamic along with extended Kalman filter to estimate the desired states.
Jin and Yin [97]	Longitudinal & lateral acceleration, steering angle, wheel angular velocity, yaw & roll rate	Tire forces for all wheels, roll angle, yaw & roll rate, velocity of CG	They proposed two extended and unscented Kalman filter based observers which used four-wheel model with the roll vehicle model to estimate the tire forces and other vehicle states
Rajamani et al. [98]	Longitudinal & lateral acceleration, steering angle, wheel angular velocity, yaw & roll rate	The tire forces, longitudinal and lateral vehicle velocities, yaw and roll angle	They used extended Kalman filter approach with 8DOF model (four-wheel model with roll vehicle dynamic model) to estimate the tire forces and other vehicle's states.

Many studies have used this vehicle model along with some estimation algorithms to estimate the lateral vehicle states, friction force and/or coefficient. Table 4 summarizes some of the research which have used bicycle model in their algorithms.

The most popular vehicle models, which are widely used in friction estimation studies, are introduced in this section; Table 5 reviews these vehicle dynamic models, their common measured states and the states which are usually estimated with these models as a

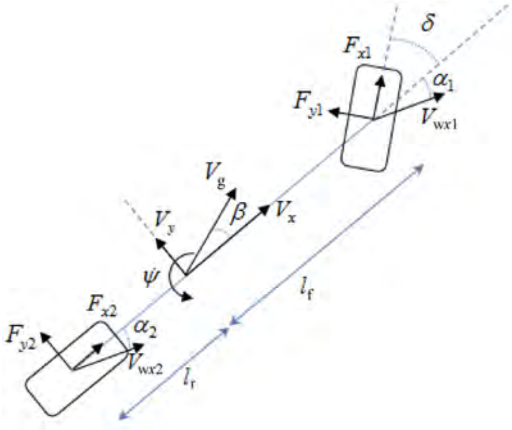

Fig. 11 The schematic of the bicycle model.

summary of dynamic wheel/vehicle based approaches. The tire model based algorithms are introduced next.

3.2 Tire model based

Tire models generally express the relationship between tire forces and moments with slip ratio/slip angle, which have been used in various studies to estimate the friction forces and friction coefficient. It is assumed that the tire forces and moment, also slip ratio and/or slip angle are available (or can be estimated) then by comparing the force/moment—slip data with different tire models, the model parameters and friction

Table 4 Some studies which have used bicycle model.

Authors	Measured states	Estimated states	Method
Baffet et al. [99, 100] Zhang et al. [101]	Yaw rate, longitudinal & lateral acceleration, steering angle	Tire forces, vehicle side slip angel	They used sliding mode observer to estimate tire road forces, then using and extended Kalman filter they estimated the cornering stiffness and side-slip angle.
Baffet et al. [81]	Yaw rate, longitudinal & lateral acceleration, vehicle velocity	Tire forces, side slip angle, cornering stiffness	First, they used extended Kalman filter to estimate the tire longitudinal and lateral forces, then another extended Kalman filter algorithm was used to estimate the side slip angle and cornering stiffness.
Baffet et al. [102]	Longitudinal & lateral acceleration, steering angle, wheel angular velocity, yaw rate	Lateral tire force, vehicle side slip angle and yaw rate and vehicle speed	They used three different extended Kalman filter based algorithm along with Burckhardt and linear tire force model to estimate the tire force, yaw rate, vehicle speed and side slip angle.
Ahn [103]	Longitudinal & lateral acceleration, steering angle, wheel angular velocity, yaw rate	Lateral force, aligning moment, side slip angle, friction coefficient	They used bicycle model with state estimator to estimate the lateral force and aligning moment; then using a sliding mode observer with brush tire model, they estimated the side slip angle and friction coefficient.
Zhang et al. [104]	Yaw rate	Side slip angle and yaw rate	They used a nonlinear observer to estimate the side slip angle, its stability conditions were obtained from analysis of energy to peak performance of the estimation error system.
Zhu and Zheng [105] Pan et al. [106]	Longitudinal & lateral acceleration, steering angle, wheel angular velocity	Wheel side slip angle and yaw rate	They used unscented Kalman filter to estimate the side slip angle and the yaw rate.
Chu et al. [107, 108]	Yaw rate, longitudinal & lateral acceleration, steering angle, wheel angular velocity	Vehicle longitudinal and lateral velocity	They used an adaptive unscented Kalman filter to estimate the vehicle longitudinal and lateral velocity.
Hsu et al. [109]	Yaw rate, longitudinal & lateral acceleration, steering angle	Tire slip angle	They used a model base estimation approach; utilizing pneumatic trail information they identified the vehicle's lateral limits.
Ray et al. [110]	Yaw rate, longitudinal & lateral acceleration, the wheel angular velocity	Vehicle's longitudinal and lateral speed, vertical displacement of front, rear and CG, pitch angle, the longitudinal and lateral force for front and rear wheels	They used a nine degree of freedom model, which is a bicycle model with a quarter-car model to simulate each of the front and rear tire and suspension. Using extended Kalman filter, they estimated the tire forces and other states.
Gao et al. [111]	Lateral acceleration, yaw rate	Side slip angle	They used a high gain observer along with a nonlinear tire model to estimate the vehicle side slip angle. They compared the results of high gain observer with the estimation results of extended Kalman filter and Leunberger observer.

Table 5 Summary of wheel/vehicle dynamic models which are used for friction estimation.

Model name	Common measured states	Common estimated states	Features
Wheel dynamic model	Longitudinal acceleration, wheel angular velocity, drive & braking torque, rolling resistance force	Longitudinal tire force, longitudinal speed,	1. Used to study the longitudinal dynamics of the vehicle. 2. The accuracy of the estimation using this model highly depends on the accuracy of the tire effective radius which is used for estimation.
1-DOF roll model	CG's lateral acceleration	Roll angle, roll rate	1. Used to estimate roll dynamics of the vehicle. 2. Roll stiffness and damping coefficient are assumed to be constant. 3. The roll axis assumed to be fixed. 4. Does not need the information of cornering stiffness. 5. It's not sensitive to nonlinear tire dynamics.
Quarter car model	Vertical acceleration of sprung mass and un-sprung mass	Tire vertical force, vertical position and velocity of sprung mass and un-sprung mass	1. Mostly used to model vertical dynamics of the vehicle and suspension modeling. 2. Pitch and roll motion are not taken into account. 3. The wheels are assumed to roll without slip and contact loss.
Four-wheel vehicle model	Longitudinal and lateral acceleration, yaw acceleration, steer angle	Tire's longitudinal and lateral force, wheel hub velocity of each wheel	1. Used to study the longitudinal and transversal vehicle dynamics. 2. Roll and pitch motion are ignored. 3. Doesn't have a suspension.
Bicycle model	Lateral acceleration, yaw acceleration, steer angle	Front and rear lateral tire force	1. Used to describe lateral dynamics of the vehicle. 2. Rear steering angle assumed to be zero. 3. Vertical and roll motion are ignored.

coefficient are estimated.

Different mathematical tire models have been developed based on model of the tire and the time behavior that can be captured (steady-state or transient) (Fig. 12) [68]; some of them which are more common for the friction estimation purpose are introduced in this article.

3.2.1 Pacejka tire model

Pacejka tire model (which is also called magic formula) is a semi-empirical tire model that was introduced for the first time by Pacejka in 1992 [112]. The model uses special functions to represent the longitudinal and lateral forces and the aligning moment. The formulation of this tire model for longitudinal and lateral force and aligning moment are as follows:

$$
\begin{aligned}
&F_x(s+S_{hx}) = \\
&\quad D_x \sin[C_x \arctan(B_x s - E_x(B_x s - \arctan(B_x s)))] + S_{vx} \\
&F_y(\alpha+S_{hy}) = \\
&\quad D_y \sin[C_y \arctan(B_y \alpha - E_y(B_y \alpha - \arctan(B_y \alpha)))] + S_{vy} \\
&M_z(\alpha+S_{hz}) = \\
&\quad D_z \sin[C_z \arctan(B_z \alpha - E_z(B_z \alpha - \arctan(B_z \alpha)))] + S_{vz}
\end{aligned}
\tag{20}
$$

where s is the slip ratio, α is the side slip angle and F_x, F_y, M_z are the longitudinal force, lateral force and aligning moment respectively. The meaning of other parameters (B, C, D, S_h, S_v) are shown in Fig. 13.

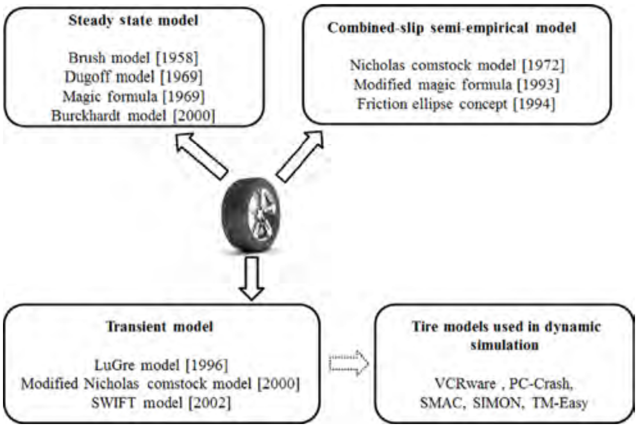

Fig. 12 Different tire models. Reproduce with permission from Ref. [68]. Copyright Singh, 2012.

In the newer version of the magic formula, the camber angle, cornering stiffness, and load variation also transient properties of the tire are also taken into account [113]. Magic formula has been widely used in literature for vehicle states and tire friction

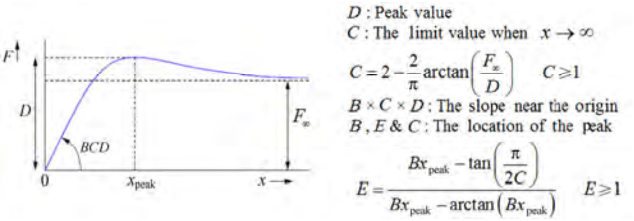

Fig. 13 Magic Formula's parameters.

estimation [112, 114, 115]. van Oosten et al. [116] clarified the determination of Magic Formula parameters from the experimental data, and discussed all the difficulties involved. Kim et al. [117] used the traditional concept of friction to formulate the friction; they assumed that the coefficients of Magic Formula are known. Using an instrumented vehicle they estimated the forces on each wheel with the help of Magic Formula. Then they estimated the longitudinal and lateral friction coefficients. Yi et al. [118] used an observer-based algorithm, in which the Magic Formula with known parameters was used for the longitudinal force, to estimate the tire road friction coefficient. First, they used a sliding mode observer (angular velocity of the wheel was measured) to estimate the vehicle states, then using a recursive least square algorithm, they estimated the tire road friction coefficient. Jayachandran et al. [119] developed a fuzzy logic based algorithm to estimate the value of longitudinal and lateral forces, also aligning moment based on slip ratio and slip angle. They used Magic Formula with known coefficients to calculate the tire forces and moment based on different slip values; then they defined a fuzzy membership function between the inputs (slip ratio, slip angle) and outputs (tire forces, aligning moment) of fuzzy-logic algorithm based on the calculated values.

3.2.2 *Dugoff tire model*

Dugoff tire model is a physical model, which was introduced by Dugoff et al. in 1969 [120]. In this model, a uniform vertical pressure distribution is assumed on the tire contact patch. In its simplest form, Dugoff model expresses the relation between longitudinal and lateral force and the slip as a function of two parameters; the tire stiffness (C_x, C_y), which explains the slope of force-slip curve in low slip region and the tire-road friction coefficient (μ) that describes its curvature and peak value. The Dugoff model is formulated as follows:

$$\begin{aligned} F_x &= C_x \frac{s}{1+s} f(\lambda) \\ F_y &= C_y \frac{\tan(\alpha)}{1+s} f(\lambda) \\ \lambda &= \frac{\mu F_z (1+s)}{2\sqrt{(C_x s)^2 + (C_y \tan\alpha)^2}} \\ f(\lambda) &= \begin{matrix} (2-\lambda)\lambda & \lambda < 1 \\ 1 & \lambda \geqslant 1 \end{matrix} \end{aligned} \tag{21}$$

where C_x, C_y are the slopes of the longitudinal force—slip ratio and lateral force—slip angel in the low slip values (linear part of the curve respectively). In the following context, some of the studies that have used the Dugoff tire model in order to estimate the friction or related parameters are introduced. Ghandour et al. [89] developed an algorithm, using Dugoff to simulate the lateral force, to estimate the lateral friction coefficient. First, they developed an estimation algorithm to obtain the lateral force and slip angle. Then, they estimated the friction coefficient utilizing nonlinear method of optimization to minimize the error between estimated lateral force and lateral force provided by Dugoff model. In another study, a new algebraic filtering technique was used by Villagra et al. [121] to estimate the longitudinal and lateral force and slip ratio, then they used a weighted Dugoff model to estimate the friction coefficient, for instance for the longitudinal direction simplifying the Dugoff equation gives:

$$\mu_{x-\max}^2 F_z^2 - 2\mu_{x-\max} \left|C_x \tau\right| F_z + \left|C_x \tau\right| F_z = 0 \tag{22}$$

where in this equation $\tau = \frac{s}{1+s}$. The solution for this equation is expressed as:

$$\mu_{x-\max} = \frac{\left(\left|C_x \tau\right| \pm \sqrt{C_x \tau (C_x \tau - F_x)}\right)}{F_z} \tag{23}$$

Comparing the behavior of Dugoff model with Pacejka's model, the maximum friction coefficient is obtained as follows:

$$\begin{aligned} &\mu_{x-\max}^D(t_k) = \frac{\alpha_1}{F_z(t)}\left(\left|C_x \tau(t_k)\right| - \sqrt{C_x \tau(t_k)(C_x \tau(t_k) - F_x(t_k))}\right) \\ &\quad \lambda(t_k) < 1 \\ &\mu_{x-\max}^D(t_k) = \mu_{x-\max}^D(t_k - 1) \quad \lambda(t_k) \geqslant 1 \end{aligned} \tag{24}$$

where α_1 is a weighting factor. Nilanjan et al. [122] proposed a sliding mode observer along with modified Dugoff model to estimate the longitudinal velocity and friction coefficient; the only measured state was wheel angular velocity. Doumiati et al. [86] proposed a real time algorithm to estimate the tire-road lateral forces and side slip angle using two estimation algorithms of extended and unscented Kalman filter, in which the lateral force was modeled using Dugoff model. Four-wheel vehicle model was used as the dynamical model of the system, and the measured states were longitudinal and lateral acceleration, yaw and roll rate, left and right suspension deflection and the angular velocity of each wheel.

3.2.3 Brush tire model

In this model, it is assumed that the surface area which is in contact with the road can be modeled as infinitesimal bristles. As it is shown in Fig. 14, the contact patch area is partitioned into two regions [123]: adhesion and sliding. In the first region, the bristles transfer the force by mechanical adhesion and in the second region the slide of the bristles on the road results in friction force; the vertical pressure distribution is assumed to be parabolic.

The brush tire model can be divided into 3 cases: pure side-slip, pure longitudinal slip, and combined slip problem.

3.2.3.1 Pure side-slip

Figure 15 demonstrates the schematic of the contact patch in small and large side slip conditions. For the pure side slip problem, the formulation of brush tire model for low slip angle values is as follows [124]:

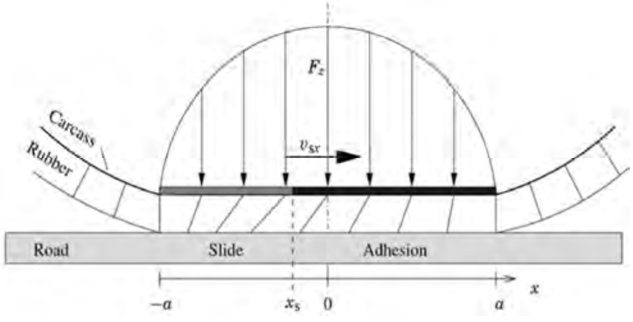

Fig. 14 The schematic of adhesion and sliding regions in the contact patch [123].

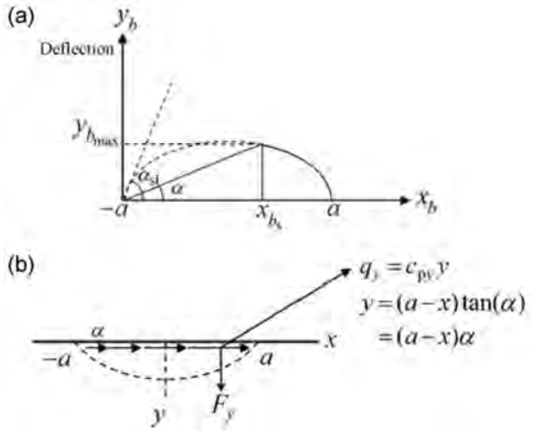

Fig. 15 Schematic of the contact patch: (a) load distribution and (b) deflection.

$$\begin{aligned} F_y &= C_{F\alpha}\alpha \\ M_z &= \frac{a}{3}F_y \end{aligned} \tag{25}$$

where a is the contact patch length and $C_{F\alpha}$ is the cornering stiffness. For large side slip values the equations are expressed as [125]:

$$\begin{aligned} F_y &= 3\mu F_z \frac{\tan(\alpha)}{\tan(\alpha_{sl})}\left(1-\left|\frac{\tan(\alpha)}{\tan(\alpha_{sl})}\right|+\frac{1}{3}\frac{\tan^2(\alpha)}{\tan^2(\alpha_{sl})}\right) \\ M_z &= -\mu F_z a\frac{\tan(\alpha)}{\tan(\alpha_{sl})}\left\{1-3\left|\frac{\tan(\alpha)}{\tan(\alpha_{sl})}\right|+3\frac{\tan^2(\alpha)}{\tan^2(\alpha_{sl})}\right. \\ &\quad \left.-\left|\frac{\tan(\alpha)}{\tan(\alpha_{sl})}\right|^3\right\} \\ \mu &= \frac{2c_{py}a^2}{3F_z}\tan(\alpha_{sl}) \end{aligned} \tag{26}$$

where c_{py} is the lateral stiffness of the tread element per unit length of the contact area, α is the side-slip angle and α_{sl} is shown in Fig. 15(b).

3.2.3.2 Pure longitudinal slip

With the assumption of pure longitudinal slip, parabolic vertical load distribution, and constant friction level, the longitudinal force is expressed as follows [126]:

$$F_x = \begin{cases} -C_x s + \dfrac{C_x^2 s|s|}{3\mu F_z} - \dfrac{C_x^3 s^3}{27\mu^2 F_z^2} & s < s^{\mathrm{o}} \\ \mu F_z \operatorname{sgn}(s) & \text{otherwise} \end{cases} \tag{27}$$

where $s^{\mathrm{o}} = 3\dfrac{\mu F_z}{C_x}$ and s is the slip ratio.

3.2.3.3 Combined slip

For the case that both longitudinal and lateral slip are available, to simplify the problem it is assumed that the normal force distribution is parabolic, and the longitudinal and lateral stiffness of the tread elements, and the longitudinal and lateral friction coefficients are equal [124].

$$\begin{aligned} c_{\mathrm{p}} &= c_{\mathrm{p}x} = c_{\mathrm{p}y} \\ \mu &= \mu_x = \mu_y \end{aligned} \tag{28}$$

The theoretical slips are defined as follow:

$$\begin{aligned} \sigma_x &= \frac{s}{1+s} \\ \sigma_y &= \frac{\tan\alpha}{1+s} \\ \sigma &= \sqrt{{\sigma_x}^2 + {\sigma_y}^2} \end{aligned} \tag{29}$$

The magnitude of total force is expressed as follows:

$$\begin{aligned} F &= \begin{matrix} \mu F_z\{3\theta\sigma - 3(\theta\sigma)^2 + (\theta\sigma)^3\} & \sigma \leqslant \sigma_{\mathrm{sl}} \\ \mu F_z & \sigma \geqslant \sigma_{\mathrm{sl}} \end{matrix} \\ \theta &= \frac{2}{3}\frac{c_p a^2}{\mu F_z} \end{aligned} \tag{30}$$

where $\sigma_{\mathrm{sl}} = \dfrac{1}{\theta}$ and a is half of the contact patch length as it is shown in Fig. 14. Several studies have used different forms of brush model in their friction estimation algorithms, some of these studies are summarized in Table 6.

3.2.4 LuGre tire model

LuGre tire model is a physics based dynamic tire model, which was first introduced by de Wit et al. in 1995. The surfaces are assumed to be in contact through elastic bristles. This is shown in Fig. 16 [130].

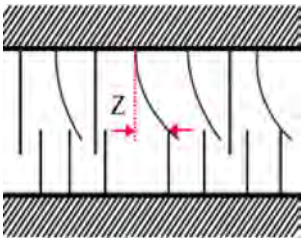

Fig. 16 LuGre model-contact surfaces.

The average deflection of the bristles in the lumped LuGre model (which is presented by z) is expressed as [130]

$$\begin{aligned} \frac{\mathrm{d}z}{\mathrm{d}t} &= v - \frac{|v|}{g(v)}z \\ F &= \sigma_0 z + \sigma_1 \frac{\mathrm{d}z}{\mathrm{d}t} + \sigma_2 v \\ \sigma_0 g(v) &= F_{\mathrm{c}} + (F_{\mathrm{s}} - F_{\mathrm{c}})\mathrm{e}^{-\left(\frac{v}{v_s}\right)^2} \end{aligned} \tag{31}$$

where v is the relative velocity between the two surfaces, v_{s} is Stribeck velocity, F_{c} is the Coulomb friction level, F_{s} is the level of stiction force, σ_0 is rubber stiffness, σ_1 is rubber damping coefficient, and σ_2 is the viscous relative damping. In the distributed LuGre Model, an area of contact is assumed between the tire and the road, which formulates the friction force as follows [131]:

$$\begin{aligned} F(s) &= \mathrm{sgn}(v_{\mathrm{r}})F_{\mathrm{n}}g(s)\left(1 + \gamma\frac{g(s)}{\sigma_0 L|s|}(e^{-\frac{\sigma_0 L|s|}{g(s)}} - 1)\right) + F_{\mathrm{n}}\sigma_2 r\omega s \\ \gamma &= 1 - \sigma_1|v_{\mathrm{r}}|/g(s) \\ g(s) &= \mu_{\mathrm{c}} + (\mu_{\mathrm{s}} + \mu_{\mathrm{c}})\mathrm{e}^{-|r\omega s/v_s|^{\frac{1}{2}}} \end{aligned} \tag{32}$$

where F_{n} is the normal load, L is the contact patch length and $v_{\mathrm{r}} = (r\omega - v)$ is the relative velocity. Several studies have used LuGre model to estimate the friction force or friction coefficient. de-Wit et al. [62] used a single wheel dynamic model with lumped LuGre friction model and introduced a new parameter which represented the road change. Using the measured data of angular velocity of the wheel, they designed an online observer for the vehicle longitudinal velocity and the road condition parameters [62, 60]. Alvarez et al. [132] also used the same approach to design a tire friction model for emergency braking control. They also used a single wheel dynamic model along with lumped LuGre formulation for the force. Utilizing the measured data of wheel angular speed, the internal state of the LuGre model (z), the longitudinal and relative velocity (v_{r}) are estimated. Chen et al. used a bicycle model and propose the following observer in order to estimate the internal states of LuGre tire

Table 6 Sample studies in which brush model have been used.

Author's name	Method which was used
Svendenius [120]	Developed a brush based tire model to derive the tire forces and moment at combined slip, from scaling the forces given by empirical pure slip (σ_x,σ_y,γ), at certain pure slips: ($\sigma_{0x}(\sigma_x,\sigma_y,\gamma),\sigma_{0y}(\sigma_x,\sigma_y,\gamma)$) $F_x(\sigma_x,\sigma_y,\gamma)=G_{\mathrm{ax}}F_{0x}(\sigma_{0x\mathrm{a}})+G_{\mathrm{s}x}F_{0x}(\sigma_{0x\mathrm{s}})$ $F_y(\sigma_x,\sigma_y,\gamma)=G_{\mathrm{a}y}F_{0y}(\sigma_{0y\mathrm{a}})+G_{\mathrm{s}y}F_{0y}(\sigma_{0y\mathrm{s}})+G_{\mathrm{cam}y}F_{0\mathrm{cam}}(\gamma)$ $M_z(\sigma_x,\sigma_y,\gamma)=G_{\mathrm{a}y}F_{0y}(\sigma_{0y\mathrm{a}})+G_{\mathrm{mz}}M_{0z}(\sigma_{0z})+G_{\mathrm{camz}}F_{0\mathrm{cam}}(\gamma)$ where F_{0x},F_{0y} are from the empirical pure slip model, $F_{0\mathrm{cam}}$ is the empirical pure cambering model, the normal load assumed to be parabolic distributed and the scale factors G_{ij} are derived from the analytical expressions of brush model.
Andersson et al. [127]	They used an extended brush model in combined with slip mode to estimate the lateral friction. They used self-aligning torque as the estimation basis, instead of lateral force (because it shows more nonlinear behavior at low slip angle) to broaden the operation area of lateral estimator.
Nishihara et al. [128]	They used brush model to describe the essential relation between the tire forces and aligning moment and the grip margin, which is defined as the residual tire forces normalized by the radius of friction circle: $\varepsilon=1-\dfrac{\sqrt{F_x^2+F_y^2}}{\mu F_z}$ It is assumed that the lateral force, aligning moment and the contact patch length are available, the friction coefficient is determined as: $\mu=\dfrac{\sqrt{F_x^2+F_y^2}}{(1-\varepsilon)F_z}$ $\varepsilon=\dfrac{1}{729}\left[\dfrac{2^{1/3}(9\xi+\xi^2)}{W(\xi)}+\xi+\dfrac{W(\xi)}{2^{1/3}}\right]^3 \quad \xi=\dfrac{6M_z}{F_y a}$ $W(\xi)=(2\xi^3+27\xi^2+243\xi+27\xi\sqrt{\xi^2+14\xi+81})^{\frac{1}{3}}$
Matilainen and Tuoronen [41]	They estimate the friction potential during the lateral driving maneuver without any knowledge of tire stiffness based on brush tire model. Having the tire forces (estimated using bicycle model) the friction potential is calculated as follows: $\mu_{\mathrm{potential}}(F_y/F_z,\lambda)=-\dfrac{F_y/F_z}{(\lambda^3-1)}$ where λ is defined as $\dfrac{M_z}{aF_y}=-\dfrac{\lambda^3}{\lambda^2+\lambda+1}$
Yamazaki et al. [129]	They used brush tire model (with the assumption of parabolic distributed normal load) to estimate the longitudinal friction coefficient for two cases of partially sliding and pure sliding. For the case of partially sliding μ can be determined from: $9\mu_x^2F_z^2(F_x-C_xs)+3\mu_xF_zC_x^2s^2-C_x^3s^3/3=0$ And for pure sliding mode: $\mu_x=\dfrac{F_x}{F_z}$

model [126].

$$\dot{\hat{z}}=v_{\mathrm{r}}-\bar{\theta}\sigma_0 f(v_{\mathrm{r}})\hat{z}+K(\mu_i-\hat{\mu}) \tag{33}$$

With $\hat{\mu}=\sigma_0\hat{z}-\bar{\theta}\sigma_0\sigma_1 f(v_{\mathrm{r}})\hat{z}+(\sigma_1+\sigma_2)v_{\mathrm{r}}$ and $\bar{\theta}$ is a constant, ensure that $\lim_{t\to\infty}\hat{z}=z$ for each tire, $K=1/\sigma_1$ and $\mu_i=\dfrac{F_{xi}}{F_{\mathrm{n}i}}$ which is calculated form dynamical equation of the motion for each wheel. Knowing the parameters of the LuGre tire model, the friction coefficient is estimated using a recursive least square algorithm. In another study, Alvarez et al. [132]

developed an adaptive friction estimation algorithm based on LuGre tire model. They used a quarter car model in which the forces were modeled using LuGre formulation and estimated the vehicle velocity and internal parameters of LuGre model using sliding mode observer. The measured states were the wheel angular velocity and the longitudinal acceleration. Matusko et al. [133] have used lumped LuGre model to explain the dynamics of friction force. They used a single wheel dynamic model along with LuGre tire model to estimate the friction force. A Neural Network (NN) algorithm is also used to compensate the uncertainties in the tire friction model. They used Lyapanov Direct Method to adapt the parameters of the NN algorithm. In some studies, LuGre tire model has been used as the basis to develop new dynamic models. Cleays et al. [61] have developed a LuGre based tire model, which describes the longitudinal and lateral forces and the aligning moment with a set of first order differential equations suitable for use in traction and ABS braking controllers.

In this section, four tire models which have been used more than other tire models were discussed; the overall specifications of these models are summarized in Table 7.

The slip-slop based algorithm which is another member of the model based approaches are discussed in following section.

3.3 The slip-slope method

This method is based on the hypothesis that the low slip—low μ part of the slip curve (during normal driving condition) can be used to estimate the maximum tire-road friction. This has been claimed in several studies [22, 63, 66, 134–136]. Slip is defined as the relative velocity between the tire and the road [77].

$$\begin{aligned} s &= \frac{\omega_{\mathrm{w}} r_{\mathrm{w}} - v_{\mathrm{w}}}{v_{\mathrm{w}}} \quad \text{during braking} \\ s &= \frac{\omega_{\mathrm{w}} r_{\mathrm{w}} - v_{\mathrm{w}}}{\omega_{\mathrm{w}} r_{\mathrm{w}}} \quad \text{during accelerating} \end{aligned} \tag{34}$$

where r_{w} is the effective rolling radius of the wheel, $\omega_{\mathrm{w}}, v_{\mathrm{w}}$ are the angular and circumferential velocity of the wheel respectively. It is assumed that the values of slip ratio and normalized traction force $\left(\frac{F_x}{F_{\mathrm{N}}}\right)$ are available (through ABS sensor or other methods). Using different regression models on the linear region of μ–slippage curve, the maximum value of friction coefficient is estimated. In other studies a linear model has been used to fit the data. Gustafsson [77] suggested the following regression model to be used for μ–slippage curve:

$$\begin{aligned} &\mu = ks - k\delta \\ &\delta = s\,|_{\mu\approx 0}\ ,\ k = \left.\frac{\mathrm{d}\mu}{\mathrm{d}x}\right|_{\mu\approx 0} \end{aligned} \tag{35}$$

Table 7 Specifications of discussed tire models.

Year	Name	properties	Feature
1958	Brush model	Physical based	1. It's a general model which is physically derived from variants of brush model. 2. Describe the forces in: pure accelerating/braking, pure cornering and combined mode. 3. The friction assumed to be constant. 4. Partition the contact patch to two parts: adhesion and sliding regions. 5. The effect of carcass deformation is neglected. 6. The elements are assumed to be linearly elastic.
1969	Dugoff model	Physical based	1. It's a velocity independent tire model. 2. Use two constants: longitudinal and lateral stiffness (C_x, C_y) to describe the tire behavior. 3. Describe the forces in: pure accelerating/braking, pure cornering and combined mode. 4. Consider a coupled relationship between longitudinal and lateral tire force.
1987	Magic formula	Semi-Empirical	1. Can accurately fit to measured data. 2. Describe the steady state tire behavior. 3. Has lots of revised version. 4. It's physically meaningful. 5. Easy to use.
1995	LuGre model	Physical based	1. It's a velocity dependent tire model. 2. Can capture the Stribeck* effect. 3. Can describe the hysteresis loop, pre-sliding displacement, … 4. Has two versions of lumped mass and distributed mass.

Then a Kalman filter supported by change detection algorithm is used to accurately estimate the so-called slip slope. Germann et al. [137] used a second order polynomial to express the μ–slip relation as follows:

$$\mu = a_0 + a_1 s + a_2 s^2 \tag{36}$$

where the coefficients of this polynomial are calculated from μ–slip curve, they showed that this model works well for the slip range of less than 0.3 (30%). Müller et al. [138] used the μ–slip data collected from a braking maneuver and proposed the following regression model:

$$\mu = \mu' \frac{s}{c_1 s^2 + c_2 s + 1} \tag{37}$$

where μ' is the slope of μ–slip curve and c_1, c_2 are calculated using a least square algorithm. Several other studies have used similar algorithms to obtain the maximum friction coefficient from the slip-slope curve [135, 139]. Lee et al. [140] used a wheel dynamic model to estimate the longitudinal force and wheel slip; then using recursive least square, they calculated the slope of μ–slip curve.

3.4 Other friction models

Although the main focus of this study is to introduce the most popular approaches, which are widely used in tire-road friction estimation, there are many valuable studies that have tried to develop a new friction model. Some of these approaches are discussed in this section.

The first model which is discussed is Persson's friction model. Persson [141, 142] proposed a physics-based multiscale friction model based on the nature of the substrate surface roughness and viscoelastic behavior of the rubber at different length scale from micro to macro scale. He assumed that the friction force is directly related to internal friction of the rubber which occurs due to oscillating forces on the rubber surface at different magnifications. He obtained the hysteresis friction as a function of sliding velocity v_{s} and wave vector q at different length scales as:

$$\mu_{\mathrm{H}}(v_s) = \frac{1}{2}\int_{q_0}^{q_1} \mathrm{d}q q^3 C(q) P(q) \int_0^{2\pi} \mathrm{d}\phi \cos\phi Im \frac{E(\omega, T_q)}{(1-\vartheta^2)\sigma_0} \tag{38}$$

where ϑ and σ_0 are Poisson ratio and the nominal pressure of the tire, respectively. The Young modulus E is a function of loading frequency $(\omega = q v_{\mathrm{s}} \cos\phi)$ applied by multiscale asperities of the road surface and flash temperature T_q at different length scale. $C(q)$ is the roughness power spectrum of the surface and $P(q)$ is the ratio of the tire–substrate apparent contact area to the nominal contact area, both as a function of spatial frequency. The lower limit of the integral is a reference wave vector at the lowest magnification q_0 and the upper limit is the large wave vector cut-off q_1 which is related to material properties of tire when there is no contamination on the substrate surface, otherwise it is related to the size of contamination particles.

Later, Lorenz et al. [143] added a semi-empirical adhesion model of friction coefficient to Persson's hysteresis model to find the total friction at low velocities.

$$\mu_{\mathrm{Ad}}(v_{\mathrm{s}}) = \frac{\tau_{\mathrm{f0}}}{\sigma_0 P(q_1)} \exp\left(-c\left[\log\left(\frac{v_{\mathrm{s}}}{v_0}\right)\right]^2\right) \tag{39}$$

where c, v_0, and τ_{f0} are empirical constants.

Klüppel and his colleagues [144, 145] proposed a friction theory similar to Persson's. Their approach also relates the rubber friction on rough surfaces to the dissipated energy of the rubber during sliding stochastic excitations on a broad frequency scale. Instead of wave vector (spatial frequency), they worked in temporal frequency domain $\omega = q v_s$ and separated the effect of macro and micro texture using following model:

$$\begin{aligned}\mu_{\mathrm{H}}(v_s) = \frac{1}{2}\frac{\langle\delta\rangle}{\sigma_0 v_s}\Big\{&\int_{\omega_{\min}}^{\omega_2} \mathrm{d}\omega\, \omega \mathrm{Im}(E(\omega)) S_1(\omega) \\ &+\int_{\omega_2}^{\omega_{\max}} \mathrm{d}\omega\, \omega \mathrm{Im}(E(\omega)) S_2(\omega)\Big\}\end{aligned} \tag{40}$$

where $\langle\delta\rangle$ *is* the excited layer thickness which is proportional to the mean penetration depth of rubber. $S_1(\omega)$ and $S_2(\omega)$ are the power spectrum densities in frequency space for the macrotexture and the microtexture, respectively. In contrast to Persson's model, which is fully 3D, Klüppel model takes into account the 3D profile of surface roughness in some average way and gives different numerical results.

Later, Motamedi et al. [146] combined the two-scaling regimes approach (macro and micro) of Klüppel [144] with theoretical model of Persson [141] to compare the physics-based theory with indoor experimental results. He found fair agreements between theory and experiments. He also discussed the possible factors involved in experiments, which is not considered in the theatrical model such effect of rubber wear and wear particles on rubber friction.

Since all these physic-based theories developed based on mechanisms of a sliding rubber block, they cannot solely provide a complete description of tire friction. Ignatiev and Wies [147] demonstrated a hierarchy of approaches on vehicle, tire, and rubber-road contact scales should be used to obtain a good estimation of tire-road friction. They also reviewed modeling, simulation and experimental approaches for investigations of tire-road interactions in their article.

Henry et al. [148, 149] developed a friction model (also known as Pennsylvania State friction model) that uses an exponential form to express the relation between the friction and slip in steady state condition. A modified version of Pennsylvania State friction model is Permanent International Association of Road Congresses or the World Road Association (PIARC) friction model [149], which is as follows:

$$\mathrm{SN}_2 = \mathrm{SN}_1 \mathrm{e}^{\frac{-(\mathrm{sv})_2-(\mathrm{sv})_1}{S_\mathrm{p}}} \tag{41}$$

where $\mathrm{SN}_1, \mathrm{SN}_2$ are the skid numbers measured at the slip speed of $(\mathrm{sv})_1$ and $(\mathrm{sv})_2$ respectively and S_p is the speed constant related to the macrotexture of the pavement that is determined using following equation [148]:

$$S_\mathrm{p} = 14.2 + 89.7\mathrm{MPD} \tag{42}$$

where MPD stands for the mean profile depth of the pavement. The most important advantage of both of these friction models (Penn State model and PIARC model) is that they included the pavement macrotexture properties along with the slip speed in the friction model.

4 Conclusions

Sudden change in the pavement friction, caused by change in weather condition (rain, snow, etc.) plays one of the most important roles in car crashes. Unawareness of the driver about the pavement friction change and malfunction of vehicle's stability controllers lead to fatal car accidents; therefore, friction estimation is of interest to vehicle and tire industries. Several research studies have been conducted to estimate the friction force, friction coefficient and other parameters related to tire-road friction problem.

These studies can be divided into two main categories: experiment-based and model based. In the experiment-based approaches, it is attempted to correlate the measured data to friction related parameters. While in model based approaches, a mathematical model of the problem is developed first, then based on the developed model and measured states, the friction force or other friction related parameters are estimated. The properties of each of these methods are summarized in Table 8. Two factors of accuracy and repeatability are used in this table. Different methods are ranked as low, medium and high, which demonstrates how accurate a method is to estimate the desired parameters or how a study is repeatable.

The most important shortcoming of experiment-based approaches is observed to be the repeatability. When the testing conditions have some deviations from which these algorithms were trained, their accuracy decreased dramatically. Also, for the slip slope based approach, although it is claimed in several studies that there is a direct relation between the slip slope and the maximum friction coefficient, it is observed that changing the testing conditions (tire pressure, tire temperature, etc.) will change the slope of μ–slip curve in the linear region which affects the accuracy and repeatability of this method.

This literature survey introduces the development of the most popular algorithms which are widely used to estimate tire-road friction and other friction-related parameters.

Table 8 Summary of friction estimation approaches.

Major category	Sub- category	Short description	Accuracy	Repeatability
Experiment-based	Optical sensors and camera	Using optical sensors and cameras to detect friction related surface properties.	Medium	Medium
	Acoustic sensors	The tire noise is used to classify the surface type or surface condition and correlate it to the tire-road friction.	Medium	Low
	Tire tread sensors	Using different sensor inside the tire to monitor the interaction between tire and the road.	High	Medium
Model-based	Vehicle dynamic based method	Using a dynamical model of the problem and the data of measured states and try to estimate the unmeasured states.	High	High
	Tire model based method	Using a tire model, which expresses the relation between slip/slip ratio and tire forces and moments to estimate the friction.	High	Medium
	Slip-slope based method	Try to estimate value of friction coefficient in the saturated part of $\mu-\text{slip}$ curve based of the slope of the curve in linear region	Medium	Low

References

[1] Fatality analysis reporting system. National Highway Traffic Safety Administration, 2012.

[2] Fatality analysis reporting system. National Highway Traffic Safety Administration, 2011.

[3] Fatality analysis reporting system. National Highway Traffic Safety Administration, 2010.

[4] Connelly L B, Supangan R. The economic costs of road traffic crashes: Australia, states and territories. *Accident Analysis & Prevention* **38**(6): 1087–1093 (2006)

[5] Andreassen D. Preliminary costs for accident-types. (1992)

[6] Najafi S, Flintsch G W, Khaleghian S. Fuzzy logic inference-based Pavement Friction Management and real-time slippery warning systems: A proof of concept study. *Accident Analysis & Prevention* **90**: 41–49 (2016)

[7] Najafi S, Flintsch G W, Khaleghian S. Pavement friction management–artificial neural network approach. *International Journal of Pavement Engineering*: 1–11 (2016)

[8] Pisano P A, Goodwin L C, Rossetti M A. US highway crashes in adverse road weather conditions. In *24th Conference on International Interactive Information and Processing Systems for Meteorology, Oceanography and Hydrology*, New Orleans, LA, 2008.

[9] Andrey J. Long-term trends in weather-related crash risks. *Journal of Transport Geography* **18**(2): 247–258 (2010)

[10] Lamm R, Choueiri E M, Mailaender T. Comparison of operating speeds on dry and wet pavements of two-lane rural highways. *Transportation Research Record* **1280**(8): 199–207 (1990)

[11] Zhang L, Prevedouros P. Motorist perceptions on the impact of rainy conditions on driver behavior and accident risk. In *Proceedings of the 84th Annual Meeting of the Transportation Research Board*, Washington, DC, 2005.

[12] Satterthwaite S. An assessment of seasonal and weather effects on the frequency of road accidents in California. *Accident Analysis & Prevention* **8**(2): 87–96 (1976)

[13] Andrey J, Yagar S. A temporal analysis of rain-related crash risk. *Accident Analysis & Prevention* **25**(4): 465–472 (1993)

[14] Brodsky H, Hakkert A S. Risk of a road accident in rainy weather. *Accident Analysis & Prevention* **20**(3): 161–176 (1988)

[15] Alvarez L, Yi J. Adaptive emergency braking control in automated highway systems. In *Proceedings of the 38th IEEE Conference on Decision and Control*, IEEE, 1999: 3740–3745.

[16] Schinkel M, Hunt K. Anti-lock braking control using a sliding mode like approach. In *American Control Conference*, IEEE, 2002: 2386–2391.

[17] Wellstead P, Pettit N. Analysis and redesign of an antilock brake system controller. *IEEE Proceedings-Control Theory and Applications* **144**(5): 413–426 (1997)

[18] Tsiotras P, De Wit C C. On the optimal braking of wheeled vehicles. In *American Control Conference*, IEEE, 2000: 569–573.

[19] Zhang D, Zheng H, Sun J, Wang Q, Wen Q, Yin A,Yang Z. Simulation study for anti-lock braking system of a light bus. In *Vehicle Electronics Conference, 1999, (IVEC'99) Proceedings of the IEEE International*, IEEE, 1999: 70–77.

[20] Doumiati M, Charara A, Victorino A, Lechner D. *Vehicle Dynamics Estimation using Kalman Filtering: Experimental Validation*. John Wiley & Sons, 2012.

[21] Eichhorn U, Roth J. Prediction and monitoring of tyre/road friction. In *XXIV FISITA CONGRESS*, LONDON, 1992.

[22] Breuer B, Eichhorn U, Roth J. Measurement of tyre/road-friction ahead of the car and inside the tyre. In *International Symposium on Advanced Vehicle Control*, Yokohama, Japan, 1992.

[23] Andersson M, Bruzelius F, Casselgren J, Gäfvert M, Hjort M, Hultén J, Håbring F, Klomp M, Olsson G, Sjödahl M. Road friction estimation. *Saab Automobile AB, Trollhättan, Sweden* (2007)

[24] Tuononen A J. Optical position detection to measure tyre carcass deflections. *Vehicle System Dynamics* **46**(6): 471–481 (2008)

[25] Tuononen A, Hartikainen L. Optical position detection sensor to measure tyre carcass deflections in aquaplaning. *International Journal of Vehicle Systems Modelling and Testing* **3**(3): 189–197 (2008)

[26] Tuononen A. Optical position detection to measure tyre carcass deflections and implementation for vehicle state estimation. Ph.D Thesis. Espoo (Finland): Helsinki University of Technology, 2009.

[27] Howard A, Seraji H. Vision-based terrain characterization and traversability assessment. *Journal of Field Robotics* **18**(10): 577–587 (2001)

[28] Kuno T, Sugiura H. Detection of road conditions with CCD cameras mounted on a vehicle. *Systems and computers in Japan* **30**(14): 88–99 (1999)

[29] Holzmann F, Bellino M, Siegwart R,Bubb H. Predictive estimation of the road-tire friction coefficient. In *Computer Aided Control System Design, 2006 IEEE International Conference on Control Applications, 2006 IEEE International Symposium on Intelligent Control, IEEE*, 2006: 885–890.

[30] Jokela M, Kutila M, Le L. Road condition monitoring system based on a stereo camera. In *Intelligent Computer Communication and Processing, IEEE 5th International Conference on*, IEEE, 2009: 423–428.

[31] Alonso J, López J, Pavón I, Recuero M, Asensio C, Arcas G, Bravo A. On-board wet road surface identification using tyre/road noise and Support Vector Machines. *Applied Acoustics* **76**: 407–415 (2014)

[32] Kongrattanaprasert W, Nomura H, Kamakura T, Ueda K. Automatic detection of road surface conditions using tire noise from vehicles. *The lnstuute of Elecironics, Information and Communication Engineers* **108**: 55–60 (2009)

[33] Kongrattanaprasert W, Nomura H, Kamakura T, Ueda K. Detection of road surface conditions using tire noise from vehicles. *IEEJ Transactions on Industry Applications* **129**: 761–767 (2009)

[34] Kongrattanaprasert W, Nomura H, Kamakura T,Ueda K. Detection of road surface states from tire noise using neural network analysis. *IEEJ Transactions on Industry Applications* **130**: 920–925 (2010)

[35] Kongrattanaprasert W, Nomura H, Koji Ueda T K. Automatic detection of road surface states from tire noise using neural network analysis. In *Proceedings of 20th International Congress on Acoustics (ICA)*, Sydney, Australia, 2010: 1–4.

[36] Erdogan G, Alexander L, Rajamani R. Estimation of tire-road friction coefficient using a novel wireless piezoelectric tire sensor. *IEEE Sensors Journal* **11**(2): 267–279 (2011)

[37] Breuer B, Barz M, Bill K, Gruber S, Semsch M, Strothjohann T, Xie C. The mechatronic vehicle corner of Darmstadt University of Technology—Interaction and cooperation of a sensor tire, new low-energy disc brake and smart wheel suspension. *International Journal of Automotive Technology* **3**(2): 63–70 (2002)

[38] Bachmann T. *The Importance of The Integration of Road, Tyre And Vehicle Technologies*. PIARC, 1995.

[39] Hollingum J. Autonomous radio sensor points to new applications. *Sensor Review* **21**(2): 104–107 (2001)

[40] Khaleghian S. The application of intelligent tires and model based estimation algorithms in tire-road contact characterization. Ph.D Thesis. Virginia (USA): Virginia Polytechnic Institute and State University, 2017.

[41] Matilainen M J, Tuononen A J. Tire friction potential estimation from measured tie rod forces. In *Intelligent Vehicles Symposium (IV)*, IEEE, 2011: 320–325.

[42] Matilainen M J, Tuononen A J. Intelligent tire to measure contact length in dry asphalt and wet concrete conditions. In *Proceedings of the 11th International Symposium on Advanced Vehicle Control*, Seoul, Korea, 2012: 9–12.

[43] Khaleghian S, Ghasemalizadeh O, Taheri S. Estimation of the tire contact patch length and normal load using intelligent tires and its application in small ground robot to estimate the tire-road friction. *Tire Science and Technology* **44**(4): 248–261 (2016)

[44] Khaleghian S, Taheri S. Terrain classification using intelligent tire. *Journal of Terramechanics* **71**: 15–24 (2017)

[45] Niskanen A J, Tuononen A J. Three 3-axis accelerometers fixed inside the tyre for studying contact patch deformations in wet conditions. *Vehicle System Dynamics* **52**(sup1): 287–298 (2014)

[46] Niskanen A J, Tuononen A J. Three 3-axis accelerometers on the inner liner of a tyre for finding the tyre-road contact friction indicators. In *Proc. of AVEC International Symposium on Advanced Vehicle Control*, Tokyo, Japan, 2014.

[47] Niskanen A J, Tuononen A J. Accelerometer tyre to estimate the aquaplaning state of the tyre-road contact. In *Intelligent Vehicles Symposium (IV)*, IEEE, 2015: 343–348.

[48] Klein S D. Friction estimation and detection for an electric power steering system. Google Patents, 2015.

[49] Singh K B. Intelligent tire-based road friction estimation system and method. Google Patents, 2016.

[50] Singh K B, Parsons A W, Engel M. Tire slip angle estimation system and method. Google Patents, 2015.

[51] Singh K B, Parsons A W, Engel M, Suh P J M. Tire load estimation system using road profile adaptive filtering. Google Patents, 2014.

[52] Miyazaki N. Road surface friction sensor and road surface friction coefficient detector, and vehicle antilock braking device. Google Patents, 2001.

[53] Hattori Y. Method for detecting strain state of tire, device for detecting the strain state, sensor unit for the method and device, and tire provided with the sensor unit. Google Patents, 2003.

[54] Hillenmayer F, Kuchler G. System for monitoring a vehicle with pneumatic tires, signal analysis method, and vehicle tire. Google Patents, 2006.

[55] Miyoshi A, Tsurita T, Kunii M. System and method for determining tire force. Google Patents, 2007.

[56] Sistonen M. Device for measuring the friction on a surface. Google Patents, 1990.

[57] Bell L D, Bell C D. Method and apparatus for monitoring the coefficient of friction between a tire and rolling surface, particularly to provide the vehicle operator with coefficient of friction, tire tread wear out and skid warning indications. Google Patents, 1999.

[58] Abe Y, Sawa T. Dynamic friction coefficient measuring apparatus. Google Patents, 1986.

[59] Gillespie T D. *Fundamentals of Vehicle Dynamics*. Society of Automotive Engineers, Warrendale, PA, 1992.

[60] De Wit C C, Horowitz R, Tsiotras P. Model-based observers for tire/road contact friction prediction. In *New Directions in Nonlinear Observer Design*. Springer, 1999: 23–42.

[61] Claeys X, Yi J, Alvarez L, Horowitz R, de Wit C C. A dynamic tire/road friction model for 3D vehicle control and simulation. In *Intelligent Transportation Systems, 2001. Proceedings. 2001 IEEE*, IEEE, 2001: 483–488.

[62] de-Wit C, Petersen M L, Shiriaev A. A new nonlinear observer for tire/road distributed contact friction. In *Decision and Control, 2003. Proceedings. 42nd IEEE Conference on*, IEEE, 2003: 2246–2251.

[63] Hsiao T, Liu N-C, Chen S-Y. Robust estimation of the friction forces generated by each tire of a vehicle. In *American Control Conference (ACC)*, IEEE, 2011: 5261–5266.

[64] Rajamani R, Phanomchoeng G, Piyabongkarn D, Lew J Y. Algorithms for real-time estimation of individual wheel tire-road friction coefficients. *IEEE/ASME Transactions on Mechatronics* **17**(6): 1183–1195 (2012)

[65] Cho W, Yoon J, Yim S, Koo B, Yi K. Estimation of tire forces for application to vehicle stability control. *IEEE Transactions on Vehicular Technology* **59**(2): 638–649 (2010)

[66] Rabhi A, M'sirdi N, Elhajjaji A. Estimation of contact forces and tire road friction. In *Control & Automation, 2007. MED'07. Mediterranean Conference on*, IEEE, 2007: 1–6.

[67] M'sirdi N, Rabhi A, Ouladsine M, Fridman L. First and high-order sliding mode observers to estimate the contact forces. In *Variable Structure Systems, VSS'06, International Workshop on*, IEEE, 2006: 274–279.

[68] Singh K B. Development of an intelligent tire based tire-vehicle state estimator for application to global chassis control. Virginia Polytechnic Institute and State University, 2012.

[69] Hac A, Brown T, Martens J. Detection of vehicle rollover. SAE Technical Paper, 2004.

[70] Tsourapas V, Piyabongkarn D, Williams A C, Rajamani R. New method of identifying real-time predictive lateral load transfer ratio for rollover prevention systems. In *American Control Conference, 2009. ACC'09.*, IEEE, 2009: 439–444.

[71] Grip H F, Imsland L, Johansen T A, Kalkkuhl J C, Suissa A. Estimation of road inclination and bank angle in automotive vehicles. In *American Control Conference, 2009. ACC'09.*, IEEE, 2009: 426–432.

[72] Chen S-K, Moshchuk N, Nardi F, Ryu J. Vehicle rollover avoidance. *IEEE Control Systems* **30**(4): 70–85 (2010)

[73] Ryu J, Moshchuk N K, Chen S-K. Vehicle state estimation for roll control system. In *American Control Conference, 2007. ACC'07*, IEEE, 2007: 1618–1623.

[74] Cho K, Son H, Choi S B, Kang S. Lateral acceleration compensation of a vehicle based on roll angle estimation. In *Control Applications (CCA), 2010 IEEE International Conference on*, IEEE, 2010: 1363–1368.

[75] Wang J, Alexander L, Rajamani R. GPS based real-time tire-road friction coefficient identification. In *Technical Report of Minnesota Department of Transportation.* Minnesota, U.S. 2004.

[76] Hahn J-O, Rajamani R,Alexander L. GPS-based real-time identification of tire-road friction coefficient. *IEEE Transactions on Control Systems Technology* **10**(3): 331–343 (2002)

[77] Gustafsson F. Slip-based tire-road friction estimation. *Automatica* **33**(6): 1087–1099 (1997)

[78] Doumiati M, Victorino A, Charara A, Lechner D. Estimation of road profile for vehicle dynamics motion: experimental validation. In *American Control Conference (ACC)*, IEEE, 2011: 5237–5242.

[79] Doumiati M, Charara A, Victorino A, Lechner D. Road safety: embedded observers for estimation of vehicle's vertical tyre forces. *International Journal of Vehicle Autonomous Systems* **10**(1–2): 117–143 (2012)

[80] Samadi B, Kazemi R, Nikravesh K Y, Kabganian M. Real-time estimation of vehicle state and tire-road friction forces. In *American Control Conference, 2001. Proceedings of the 2001*, IEEE, 2001: 3318–3323.

[81] Baffet G, Charara A, Lechner D, Thomas D. Experimental evaluation of observers for tire–road forces, sideslip angle and wheel cornering stiffness. *Vehicle System Dynamics* **46**(6): 501–520 (2008)

[82] Shim T, Margolis D. Model-based road friction estimation. *Vehicle System Dynamics* **41**(4): 249–276 (2004)

[83] Shim T, Margolis D. An analytical tyre model for vehicle simulation in normal driving conditions. *International Journal of Vehicle Design* **35**(3): 224–240 (2004)

[84] Doumiati M, Victorino A, Charara A, Lechner D. Unscented Kalman filter for real-time vehicle lateral tire forces and sideslip angle estimation. In *Intelligent Vehicles Symposium*, IEEE, 2009: 901–906.

[85] Doumiati M, Victorino A, Charara A, Lechner D. A method to estimate the lateral tire force and the sideslip angle of a vehicle: Experimental validation. In *American Control Conference (ACC)*, IEEE, 2010: 6936–6942.

[86] Doumiati M, Victorino A C, Charara A, Lechner D. Onboard real-time estimation of vehicle lateral tire–road forces and sideslip angle. *IEEE/ASME Transactions on Mechatronics* **16**(4): 601–614 (2011)

[87] Doumiati M, Victorino A, Charara A, Lechner D. Estimation of vehicle lateral tire-road forces: a comparison between extended and unscented Kalman filtering. In *Control Conference (ECC), 2009 European, IEEE*, 2009: 4804–4809.

[88] Doumiati M, Victorino A, Lechner D, Baffet G, Charara A. Observers for vehicle tyre/road forces estimation: experimental validation. *Vehicle System Dynamics* **48**(11): 1345–1378 (2010)

[89] Ghandour R, Victorino A, Doumiati M, Charara A. Tire/road friction coefficient estimation applied to road safety. In *Control & Automation (MED), 2010 18th Mediterranean Conference on*, IEEE, 2010: 1485–1490.

[90] Ghandour R, Victorino A, Charara A, Lechner D. A vehicle skid indicator based on maximum friction estimation. *IFAC Proceedings Volumes* **44**(1): 2272–2277 (2011)

[91] Ghandour R, da Cunha F H, Victorino A, Charara A, Lechner D. Risk indicators prediction based on the estimation of tire/road forces and the maximum friction coefficient: Experimental validation. In *Control & Automation (MED), 2011 19th Mediterranean Conference on*, IEEE, 2011: 700–705.

[92] Dakhlallah J, Glaser S, Mammar S, Sebsadji Y. Tire-road forces estimation using extended Kalman filter and sideslip angle evaluation. In *American Control Conference*, IEEE, 2008: 4597–4602.

[93] Sebsadji Y, Glaser S, Mammar S, Dakhlallah J. Road slope and vehicle dynamics estimation. In *American Control Conference*, IEEE, 2008: 4603–4608.

[94] Cheng Q, Correa-Victorino A, Charara A. A new nonlinear observer using unscented Kalman filter to estimate sideslip angle, lateral tire road forces and tire road friction coefficient. In *Intelligent Vehicles Symposium (IV)*, IEEE, 2011: 709–714.

[95] Ray L R. Nonlinear tire force estimation and road friction identification: Simulation and experiments. *Automatica* **33**(10): 1819–1833 (1997)

[96] Ray L R. Experimental determination of tire forces and road friction. In *American Control Conference, 1998. Proceedings of the 1998*, IEEE, 1998: 1843–1847.

[97] Jin X, Yin G. Estimation of lateral tire–road forces and sideslip angle for electric vehicles using interacting multiple model filter approach. *Journal of the Franklin Institute* **352**(2): 686–707 (2015)

[98] Rajamani R, Piyabongkarn N, Lew J, Yi K, Phanomchoeng G. Tire-road friction-coefficient estimation. *IEEE Control Systems* **30**(4): 54–69 (2010)

[99] Baffet G, Charara A, Lechner D. *Estimation of Tire-Road Forces and Vehicle Sideslip Angle*. INTECH Open Access Publisher, 2008.

[100] Baffet G, Charara A, Lechner D. Estimation of vehicle sideslip, tire force and wheel cornering stiffness. *Control Engineering Practice* **17**(11): 1255–1264 (2009)

[101] Zhang W, Ding N, Yu G, Zhou W. Virtual sensors design in vehicle sideslip angle and velocity of the centre of gravity estimation. In *Electronic Measurement & Instruments, 2009. ICEMI'09. 9th International Conference on*, IEEE, 2009: 3-652-653-656.

[102] Baffet G, Charara A, Dherbomez G. An observer of tire–road forces and friction for active security vehicle systems. *IEEE/ASME Transactions on Mechatronics* **12**(6): 651–661 (2007)

[103] Ahn C S. Robust estimation of road friction coefficient for vehicle active safety systems. The University of Michigan, 2011.

[104] Zhang H, Huang X, Wang J, Karimi H R. Robust energy-to-peak sideslip angle estimation with applications to ground vehicles. *Mechatronics* **30**: 338–347 (2015)

[105] Zhu T, Zheng H. Application of unscented Kalman filter to vehicle state estimation. In *Computing, Communication, Control, and Management, 2008. CCCM'08. ISECS International Colloquium on*, IEEE, 2008: 135–139.

[106] Pan Z, Zong C, Zhang J, Xie X, Dong Y. UKF and EKF estimator design based on a nonlinear vehicle model containing UniTire model. In *Mechatronics and Automation, 2009. ICMA 2009. International Conference on*, IEEE, 2009: 4780–4784.

[107] Chu L, Shi Y, Zhang Y, Liu H, Xu M. Vehicle lateral and longitudinal velocity estimation based on Adaptive Kalman Filter. In *Advanced Computer Theory and Engineering (ICACTE), 2010 3rd International Conference on*, IEEE, 2010: V3-325-V323-329.

[108] Chu L, Zhang Y, Shi Y, Xu M, Liu M. Vehicle lateral and longitudinal velocity estimation based on Unscented Kalman Filter. In *Education Technology and Computer (ICETC), 2010 2nd International Conference on*, IEEE, 2010: V3-427-V423-432.

[109] Hsu Y-H J, Laws S M, Gerdes J C. Estimation of tire slip angle and friction limits using steering torque. *IEEE Transactions on Control Systems Technology* **18**(4): 896–907 (2010)

[110] Ray L R. Nonlinear state and tire force estimation for advanced vehicle control. *IEEE Transactions on Control Systems Technology* **3**(1): 117–124 (1995)

[111] Gao X, Yu Z, Neubeck J, Wiedemann J. Sideslip angle estimation based on input–output linearisation with tire–road friction adaptation. *Vehicle System Dynamics* **48**(2): 217–234 (2010)

[112] Pacejka H B, Bakker E. The magic formula tyre model. *Vehicle System Dynamics* **21**(S1): 1–18 (1992)

[113] Pacejka H, Besselink I. Magic formula tyre model with transient properties. *Vehicle System Dynamics* **27**(S1): 234–249 (1997)

[114] Bakker E, Nyborg L, Pacejka H B. Tyre modelling for use in vehicle dynamics studies. SAE Technical Paper, 1987.

[115] Pacejka H B, Sharp R S. Shear force development by pneumatic tyres in steady state conditions: a review of modelling aspects. *Vehicle System Dynamics* **20**(3–4): 121–175 (1991)

[116] van Oosten J J, Bakker E. Determination of magic tyre model parameters. *Vehicle System Dynamics* **21**(S1): 19–29 (1992)

[117] Kim C-S, Hong K-S, Yoo W-S, Park Y-W. Tire-road friction estimation for enhancing the autonomy of wheel-driven vehicles. In *Control, Automation and Systems, 2007. ICCAS'07. International Conference on*, IEEE, 2007: 273–277.

[118] Yi K, Hedrick K, Lee S-C. Estimation of tire-road friction using observer based identifiers. *Vehicle System Dynamics* **31**(4): 233–261 (1999)

[119] Jayachandran R, Ashok S D, Narayanan S. Fuzzy Logic based Modelling and Simulation Approach for the estimation of Tire Forces. *Procedia Engineering* **64**: 1109–1118 (2013)

[120] Svendenius J. Tire modeling and friction estimation. PhD Theses, 2007.

[121] Villagra J, d'Andréa-Novel B, Fliess M, Mounier H. A diagnosis-based approach for tire–road forces and maximum friction estimation. *Control Engineering Practice* **19**(2): 174–184 (2011)

[122] Patra N, Datta K. Observer based road-tire friction estimation for slip control of braking system. *Procedia Engineering* **38**: 1566–1574 (2012)

[123] Svendenius J, Gäfvert M, Bruzelius F, Hultén J. Experimental validation of the brush tire model 5. *Tire Science and Technology* **37**(2): 122–137 (2009)

[124] Pacejka H. *Tire and Vehicle Dynamics*. Elsevier, 2005.

[125] Erdogan G. Lateral and longitudinal tire forces. In *Tire Modeling lecture*, 2009.

[126] Chen Y, Wang J. Adaptive vehicle speed control with input injections for longitudinal motion independent road frictional condition estimation. *IEEE Transactions on Vehicular Technology* **60**(3): 839–848 (2011)

[127] Andersson M, Bruzelius F, Casselgren J, Hjort M, Löfving S, Olsson G, Rönnberg J, Sjödahl M, Solyom S, Svendenius J. Road friction estimation Part II. Technical Report, IVSS project 2004: 17750, 2010, available at www. ivss. com, 2010.

[128] Nishihara O, Masahiko K. Estimation of road friction coefficient based on the brush model. *Journal of Dynamic Systems, Measurement, and Control* **133**(4): 041006 (2011)

[129] Yamazaki S, Furukawa O, Suzuki T. Study on real time estimation of tire to road friction. *Vehicle System Dynamics* **27**(S1): 225–233 (1997)

[130] De Wit C C, Olsson H, Astrom K J, Lischinsky P. A new model for control of systems with friction. *IEEE Transactions on Automatic Control* **40**(3): 419–425 (1995)

[131] De Wit C C, Tsiotras P. Dynamic tire friction models for vehicle traction control. In *Decision and Control, 1999. Proceedings of the 38th IEEE Conference on*, IEEE, 1999:

3746–3751.

[132] Alvarez L, Yi J, Horowitz R, Olmos L. Dynamic friction model-based tire-road friction estimation and emergency braking control. *Journal of Dynamic Systems, Measurement, and Control* **127**(1): 22–32 (2005)

[133] Matuško J, Petrović I, Perić N. Neural network based tire/road friction force estimation. *Engineering Applications of Artificial Intelligence* **21**(3): 442–456 (2008)

[134] Dieckmann T. Assessment of road grip by way of measured wheel variables. In *XXIV FISITA CONGRESS*, LONDON, 1992.

[135] Hwang W, Song B-s. Road condition monitoring system using tire-road friction estimation. In *Proceedings of AVEC, 2000*: 437–442.

[136] Fischlein H, Gnadler R, Unrau H-J. The influence of the track surface structure on the frictional force behaviour of passenger car tyres in dry and wet track surface conditions. *ATZ Worldwide* **103**(10): 20–24 (2001)

[137] Germann S, Wurtenberger M, Daiß A. Monitoring of the friction coefficient between tyre and road surface. In Proceedings of the third IEEE Conference on Control Applications, 1994: 613–618.

[138] Müller S, Uchanski M, Hedrick K. Estimation of the maximum tire-road friction coefficient. *Journal of Dynamic Systems, Measurement, and Control* **125**(4): 607–617 (2003)

[139] Wang J, Alexander L, Rajamani R. Friction Estimation on highway vehicles using longitudinal measurements. *Journal of Dynamic Systems, Measurement, and Control* **126**(2): 265–275 (2004)

[140] Lee C, Hedrick K, Yi K. Real-time slip-based estimation of maximum tire-road friction coefficient. *IEEE/ASME Transactions on Mechatronics* **9**(2): 454–458 (2004)

[141] Persson B N. Theory of rubber friction and contact mechanics. *The Journal of Chemical Physics* **115**(8): 3840–3861 (2001)

[142] Persson B N. Rubber friction: role of the flash temperature. *Journal of Physics: Condensed Matter* **18**(32): 7789 (2006)

[143] Lorenz B, Oh Y, Nam S, Jeon S, Persson B. Rubber friction on road surfaces: Experiment and theory for low sliding speeds. *The Journal of Chemical Physics* **142**(19): 194701 (2015)

[144] Klüppel M, Heinrich G. Rubber friction on self-affine road tracks. *Rubber chemistry and technology* **73**(4): 578–606 (2000)

[145] Le Gal A, Klüppel M. Investigation and modelling of rubber stationary friction on rough surfaces. *Journal of Physics: Condensed Matter* **20**(1): 015007 (2007)

[146] Motamedi M, Taheri S, Sandu C. Rubber–road contact: Comparison of physics-based theory and indoor experiments. *Tire Science and Technology* **44**(3): 150–173 (2016)

[147] Ignatiev P, Wies B. Tire road interaction: Improved modeling, simulation and experimental validation of tire road-interaction. *Tire Technology International* **8**(3): 14–18 (2016)

[148] Henry J J. The relationship between texture and pavement friction. *Tire Science and Technology* **6**(4): 215–232 (1978)

[149] ASTM E. *Standard Practice for Calculating International Friction Index of a Pavement Surface*. ASTM International, 2003.

Seyedmeysam KHALEGHIAN. He received his B.S. degree in mechanical engineering from Sharif University of Technology, Tehran, Iran, in 2008, his M.S. degree in mechanical engineering from University of Tehran, Tehran, Iran, in 2011, and his Ph.D. degree in engineering mechanics from Department of Biomedical Engineering and Mechanics at Virginia Polytechnic Institute and State University. He is currently a postdoctoral fellow at the Center for Tire Research (CenTire) Virginia Tech working on intelligent tire based and vehicle dynamic based friction estimation algorithms. His research interests are vehicle dynamics, state estimation, contact mechanics, tire mechanics, and experimental and numerical stress analysis.

Friction **5**(2): 147–154 (2017)
DOI 10.1007/s40544-016-0126-6
ISSN 2223-7690
CN 10-1237/TH
RESEARCH ARTICLE

Effect of carbon nanotubes on friction and wear of a piston ring and cylinder liner system under dry and lubricated conditions

Zhinan ZHANG[1,2,*], **Jun LIU**[2], **Tonghai WU**[3], **Youbai XIE**[1,2]

[1] *State Key Laboratory of Mechanical System and Vibration, Shanghai Jiaotong University, Shanghai 200240, China*
[2] *School of Mechanical Engineering, Shanghai Jiaotong University, Shanghai 200240, China*
[3] *Key Laboratory of Education Ministry for Modern Design and Rotor-Bearing System, Xi'an Jiaotong University, Xi'an 710049, China*

Received: 03 August 2016 / Revised: 24 August 2016 / Accepted: 11 September 2016

Abstract: This study involves the application of carbon nanotubes (CNTs) to a piston ring and cylinder liner system in order to investigate their effect on friction and wear under dry and lubricated conditions. Carbon nanotubes were used as a solid lubricant and lubricant additive in dry and lubricated conditions, respectively. Simulation and measurement of friction and wear were conducted using a reciprocating tribometer. Surface analysis was performed using a scanning electron microscope and an energy dispersive spectrometer. The results indicate that carbon nanotubes can considerably improve the tribological performance of a piston ring and cylinder liner system under dry sliding conditions, whereas improvement under lubricated conditions is not obvious. Under dry friction, the effective time of the CNTs is limited and the friction coefficient decreases with an increase in CNT content. Furthermore, the dominant wear mechanism during dry friction is adhesive.

Keywords: carbon nanotubes; piston ring; tribological behavior; friction; wear

---

1 Introduction

The piston ring and cylinder liner (PRCL) is a key tribosystem in an automotive engine. The friction and wear properties of the PRCL directly relate to automotive engine performance. Meanwhile, the never-ending evolution of energy conservation and emission reduction regulations for automobiles has driven the auto industry to continuously attempt to reduce friction loss in engine components in order to meet such regulations and maintain a competitive edge in the market [1]. The tribological problems regarding the PRCL system remain; however, they must be overcome in order to keep adapting with the development of auto engines [2].

Researchers have developed or improved various motion models to understand the detailed interactions between the piston ring and cylinder liner [3–6]. Numerous methods have been proposed for reducing the friction and wear of the PRCL tribosystem, e.g., surface modification [4, 5], lubrication improvement [6], and mechanical design [7]. Currently, lubricating oil additives have gained considerable research interest [3]. Carbon nanotubes (CNTs) [8, 9] have attracted much attention for industrial applications [10–13] owing to their outstanding mechanical properties, e.g., high elastic modulus, high tensile strength, and good thermal conductivity. Although CNTs provide excellent performance, whether they are a viable lubricating oil additive for the PRCL system is still in question.

Some investigations show that CNTs can be used as a reinforcing material in polymer-based composites. For example, Yan et al. [14] investigated the friction and wear properties of pure epoxy resin and aligned carbon nanotube-reinforced epoxy resin composites under water lubricated conditions and found that the latter showed a lower friction coefficient and higher wear rates than pure epoxy resin. Düzcükoğlu et al. [15]

---

* Corresponding author: Zhinan ZHANG, E-mail: zhinanz@sjtu.edu.cn

and Cui et al. [16] investigated the tribological behavior of multiwall carbon nanotube (MWCNT)-modified epoxy resin under dry sliding conditions and concluded that nanoparticle modification resulted in enhanced wear resistance and reduced friction coefficient and working temperature under dry conditions. LaBarre et al. [17] evaluated the influence of MWCNTs on the impact performance and contributing constituent properties of Kevlar. The results suggested that MWCNT treatment has the potential to improve the ballistic limit of fabrics through increased inter-filament and inter-yarn friction without compromising fiber strength or adding significant mass. Gandhi et al. [18] presented the effect of the addition of CNTs to polypropylene on wear performance under dry sliding conditions. They found that an increase in CNT content improved the wear properties of the studied material and an increase in CNT percentage increased the wear resistance. Lee et al. [19] studied the effect of CNT length on the wear of polyamide 6,6 nanocomposites and observed that wear resistance improved with long CNTs and this improvement was more obvious at elevated temperatures.

CNTs can also be used as a reinforcing phase in a metal matrix, because their high strength and toughness help to decrease friction and wear. Al-Qutub et al. [20] studied the friction and wear behavior of an Al6061 monolithic alloy and a 1 wt% CNT-reinforced Al6061 composite prepared via ball milling and spark plasma sintering. They observed that under mild wear conditions, the composite displayed a lower wear rate and friction coefficient compared with the monolithic alloy. However, under severe wear conditions, the composite displayed a higher wear rate and friction coefficient compared with the monolithic alloy. Bastwros et al. [21] studied the effects of CNT content on the wear behavior of aluminum–carbon nanotube composites. They found that hardness and wear resistance significantly increased with CNT content. The CNTs were either partially or fully crushed, forming a carbon film that covered the surface and acted as a solid lubricant, significantly enhancing the wear behavior. Abdullahi et al. [22] developed a wear map that served as a tool for identifying and displaying regimes of different types of wear for a CNT-Al nanocomposite material, e.g., mild adhesive wear, mixed wear and severe adhesive wear. Khuu et al. [23] investigated the effects of MWCNT content on the adhesive strength, wear, and corrosion resistance of epoxy composite coatings prepared on aluminum alloy 2024-T3 substrates and found that the adhesive strength improved with increasing MWCNT content. In addition, increased MWCNT content decreased the friction coefficient and increased the wear and coating pore resistances.

Furthermore, CNTs can be added to oil to form a stable and homogeneous CNT grease that provides better lubrication performance and wear resistance than oil [24]. To reduce the friction loss in an internal combustion engine, Kałużny et al. [25] conducted engine tests using pistons with carbon nanotubes covering the skirt and demonstrated the resulting advantages. They found that a nanotube layer on the piston skirt contributes to a considerable reduction in friction losses under a wide range of engine operational conditions. In fact, in an internal combustion engine, about 20%–30% of the mechanical power loss is caused by friction loss in the PRCL tribosystem [2]. Therefore, the application of CNTs to a PRCL tribosystem may be beneficial. To the best of our knowledge, limited research has been conducted on this topic.

This study applied CNTs to a PRCL tribosystem and analyzed the tribological performance of the system under different working conditions. In the dry sliding tests, the CNTs acted as a solid lubricant by decreasing friction and wear. In the lubricated tests, the CNTs were used as a lubricant additive to improve lubrication performance. The tests were conducted using a friction abrasion testing machine, and the wear surfaces were observed with a scanning electron microscope (SEM) and energy dispersive spectrometer (EDS).

2 Experimental method

2.1 Samples

The test ring samples were prepared by cutting commercial piston rings (top piston ring with a barrel profile) into small specimens. The piston ring was made of low-carbon steel P617 with a 0.01-mm-thick multi-layered Cr coating on the outer circle. The height of the piston ring and barrel profile were 1.2 mm and 2.0×10^{-3} mm, respectively. The cylinder liner sample was made of 70-mm long, 35-mm wide, and 3-mm deep steel 45. Figure 1 shows the structure of PRCL samples, and their material properties are presented in Table 1.

The lubricant was a high-performance semi-synthetic oil, i.e., SL10W-30. The key performance factors of this kind of oil include a density of 0.8627 g/cm^3, flash point of 218 °C in an open environment, and a viscosity of 11.12 mm^2/s at 100 °C.

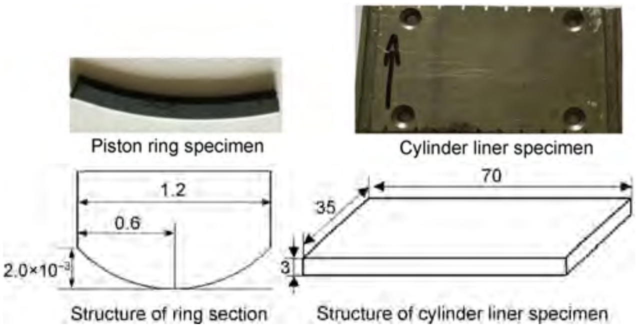

Fig. 1 Samples and structure of piston ring and cylinder liner.

The carbon nanotubes (model L-MWNT-2040) were supplied by the Shenzhen Nanotech Port Co. Ltd. These carbon nanotubes are synthesized by the catalytic chemical vapor deposition (CVD) process and possess excellent mechanical performance, superior electrical conductivity, and good thermal conductivity. The outer diameter of the CNTs was 20–40 nm, the length was 5–15 μm, and the purity was over 97%. The specific surface area was 90–120 m^2/g, the ash content was below 3 wt%, and the tap density was 0.15–0.28 g/cm^3. These properties are summarized in Table 2.

2.2 Experimental technique

The experimental work was performed in the Key Laboratory of the Education Ministry for Modern Design and Rotor-Bearing Systems at Xi'an Jiaotong University. The tribological testing of the PRCL system was conducted using a multifunctional tribometer (e.g., pin-on-disc and reciprocating tribology tests), which was designed and developed by the third and first authors, as shown in Fig. 2(a). The friction coefficients were continuously recorded by the

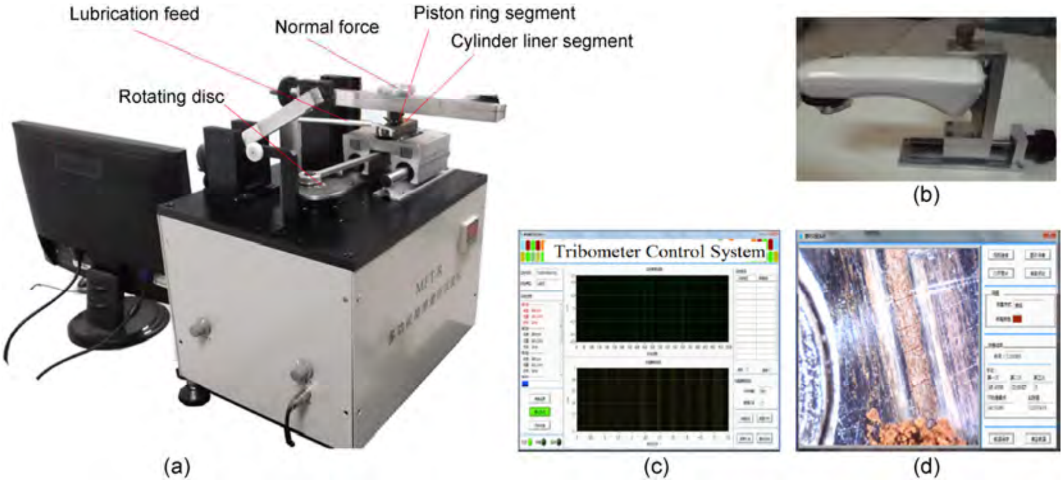

Fig. 2 Multi-functional tribometer. (a) Reciprocating tribometer test rig; (b) in-situ wear scar measurement and visualization system; (c) test control system; (d) online in-situ wear scar analysis.

Table 1 Material properties of piston ring and cylinder liner.

Samples	Material	Elasticity modulus	Hardness	Bending strength
Piston ring	P617	≈186 Gpa	⩾HV400	⩾1470 MPa
Cylinder liner	Steel 45 (C45)	≈206 Gpa	⩾HRC55	⩾355 MPa

Table 2 Properties of carbon nanotubes.

Outer diameter	Length	Purity	SSA	ASH	Tap density
20–40 nm	5–15 μm	>97%	90–120 m^2/g	<3 wt%	0.15–0.28 g/cm^3

reciprocating tribometer, as shown in Fig. 2(c). The wear scars on the PRCL samples were measured and visualized using an in situ wear scar measurement system and visualization software, as shown in Figs. 2(b) and 2(d). The environmental conditions for the experiment were approximately 70% relative humidity and about 20 °C room temperature. Experimental parameters for the tribological testing are presented in Table 3.

Four types of tribological testing were conducted in this study: (1) dry friction without CNTs, (2) dry friction with CNTs, (3) lubricated conditions without CNTs, and (4) lubricated conditions with CNTs. All tests were performed at a speed of 100 rpm under a constant load of 2 N. Each test was performed for 45 min or more and repeated at least twice. Before and after testing, the samples were cleaned in acetone for 15 min and then dried in a drying chamber for 30 min.

2.3 Surface analysis

Surface analysis of the worn area was conducted in order to study the wear mechanism. First, a moving digital microscope on a micro displacement table was used, and the focal length and amplification factor were set in advance with the help of a surveyor's rod. During the friction test, a camera was pointed at the wear scar via the micro displacement table, and the focus was adjusted. After taking a photograph, the image of the wear scar was imported into the analysis system. The computer software analyzed and calculated the width of the wear scar in real time. Accordingly, the wear data was stored and displayed. Second, an SEM (MERLIN COMPACT) and an EDS (OCTANE PLAS) were used to analyze the micrograph of the worn surfaces and the chemical element configuration, respectively.

Table 3 Tribological testing parameters.

Test specification	Value
Load (N)	2
Speed (r/min)	100
Frequency (Hz)	10
Stroke (mm)	40
Room temperature (℃)	20
Oil temperature (℃)	100

3 Results and discussion

3.1 Friction

Figure 3 shows the friction coefficients, with and without CNTs, under dry sliding conditions. It is clear that the friction coefficient value without CNTs is about 1 during the stable period, whereas that with CNTs is 0.1–0.2. Comparison of the tribological testing results shows that the friction coefficient with CNTs is far less than that without CNTs. We conclude that during dry sliding tests, adding CNTs as a solid lubricant to the PRCL system can greatly decrease friction [26] because CNTs cover the contact surfaces and have sp2 bonding that generates a lower shear force and helps to reduce friction [15, 27]. Moreover, a decrease in the friction coefficient can reduce the heat generated during sliding. Owing to the outstanding thermal conductivity of CNTs, the thermal conductivity of the PRCL system is enhanced, and this helps to liberate the heat generated during the sliding process.

Figure 4 presents the friction coefficient with CNTs over a longer period of time. Before the test, we added some CNTs to the contact region. During the first 100 min, the friction coefficient was low. From 100 to 127 min, the friction coefficient greatly increased because of a reduction of CNTs in the motion trail. At the 127th minute, we added more CNTs to the motion trail. The friction coefficient then decreased over 127–145 min. It can be concluded that the effective

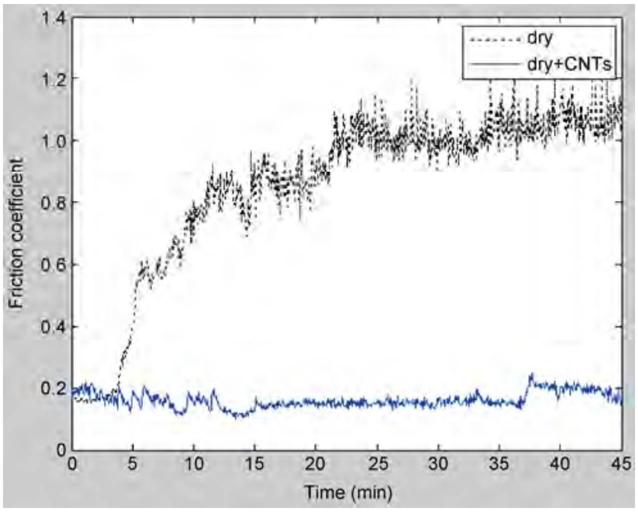

Fig. 3 Friction coefficients with or without CNTs under dry sliding condition.

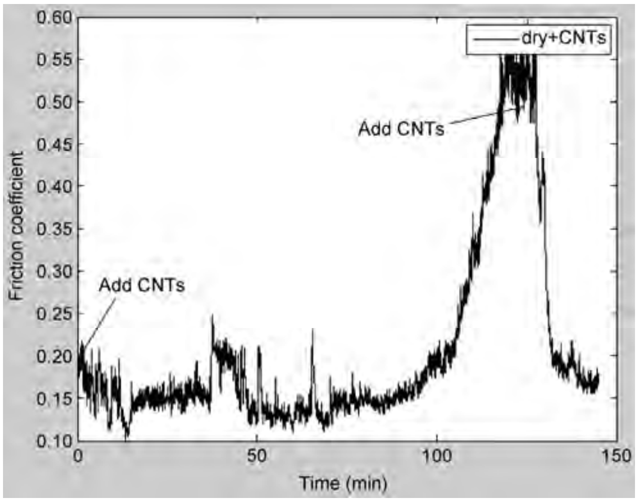

Fig. 4 Friction coefficient with CNTs in a long time.

time of CNTs is limited and the magnitude of the friction coefficient decreases with an increase in CNT content [28, 29].

Figure 5 presents the friction coefficients with and without CNTs under lubrication. It can be seen that the friction efficient increased slightly when CNTs were added to the lubricant. This may be because the CNTs act as grains in the lubricant, increasing abrasive wear and friction. Therefore, CNTs are not considered suitable as lubricant additives based on current investigation. However, further study is required to investigate whether CNTs can be used as lubricant additives in engines using bench test approach.

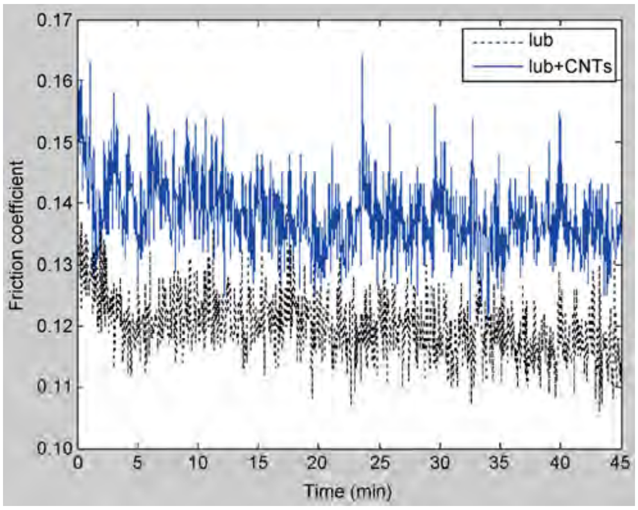

Fig. 5 Friction coefficient with or without CNTs under lubricated condition.

3.2 Wear

Figure 6 depicts the wear traces on the contact surfaces under dry sliding conditions. Figure 6(a) shows a wear trace, about 1 mm wide, on the cylinder liner without CNTs. Figure 6(b) shows a wear scar on the piston ring without CNTs, which is elliptic and dictated by the profile of the piston ring. The wear scar is not in the middle of the ring surface because the holder position was offset. Figure 6(c) shows a wear trace, about 0.6 mm wide, on the cylinder liner with CNTs. Figure 6(d) shows a wear scar on the piston ring with CNTs, which is obviously smaller than the one in Fig. 6(b).

It is evident that the width of the wear trace with CNTs under dry sliding conditions is smaller than that without CNTs. Hence, it can be concluded that adding CNTs to the PRCL system can result in wear reduction.

Under lubricated conditions, the wear trace is not obvious and cannot be measured directly. It is known from Fig. 5 that adding CNTs to the PRCL system under lubricated conditions slightly increases the friction coefficient. Also, it can be estimated that the difference between the wear traces under lubricated conditions with and without CNTs is small.

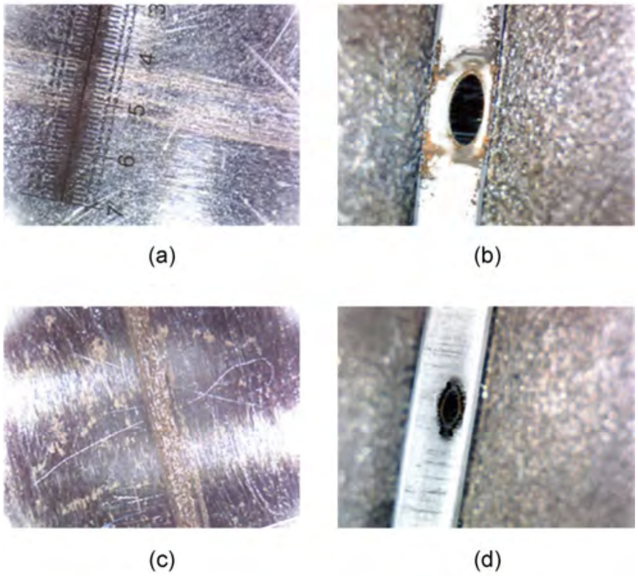

Fig. 6 Wear scar under dry sliding conditions. (a) Cylinder liner without CNTs; (b) piston ring without CNTs; (c) cylinder liner with CNTs; (d) piston ring with CNTs.

3.3 Surface analysis

Surface analysis was conducted to investigate the wear mechanism under dry sliding condition with CNTs, and the contact surfaces were observed with an SEM and EDS. Figure 7 shows the SEM images of the piston ring with CNTs under dry sliding conditions. Figures 7(a) and 7(b) show the ring surface before and after testing, respectively. Before the test, the ring surface was homogenous, while after the test, a large wear scar was observed on the contact surface. It can be seen that a carbon film formed on the surface. The elements in the contact region after the test are shown in Fig. 8. The elements were C, O, Fe, and Cr, where: Fe is the substrate of the piston ring; Cr is the coating on the ring surface; O comes from the oxide layer; and C comes from the CNTs. It can be deduced that the CNTs covered the contact surface and protected it from friction and wear. The special tubular structure, high strength, and high toughness of CNTs can significantly improve the anti-friction and wear resistance of the metal matrix [24].

Figure 9 presents the wear trace of the cylinder liner with CNTs under dry sliding conditions. Figure 9(a) is the SEM image and Fig. 9(b) is the EDS spectrum. It is clear from Fig. 9(a) that the dominant wear mechanism is adhesive wear [20]. As can be seen in Fig. 9(b), the elements in the contact region are C, O, and Fe; Fe is the substrate, O comes from the oxide layer, and C comes from the CNTs. It is confirmed that the CNTs adhered to the contact surface of the cylinder liner and formed a protective layer. Because of the low shear characteristics of CNTs, the friction coefficient is smaller than without CNTs.

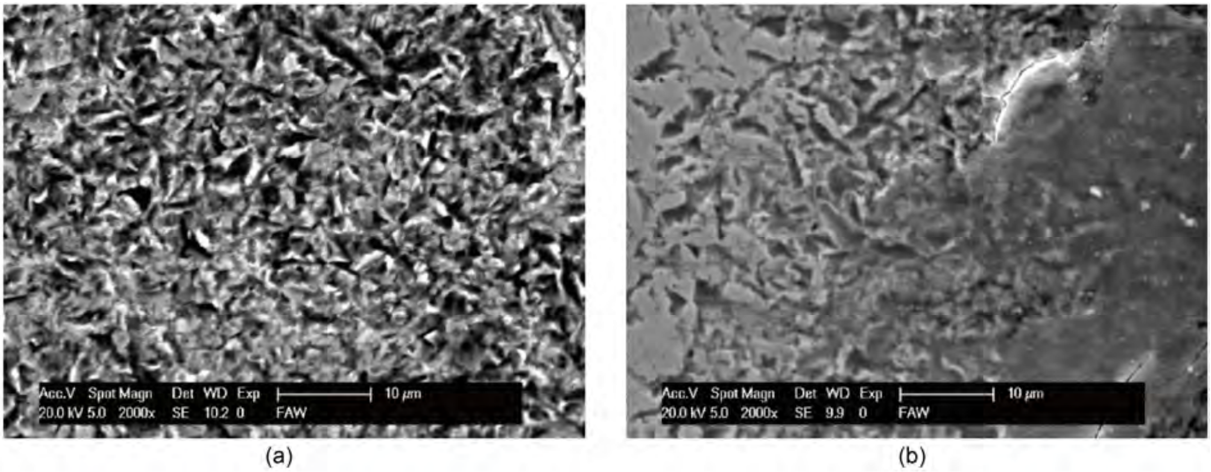

Fig. 7 SEM images of the piston ring under dry sliding conditions with CNTs: (a) before the tribological testing, and (b) after the tribological testing.

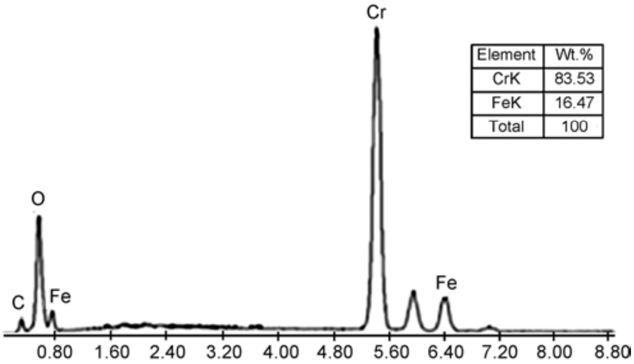

Fig. 8 EDS spectrum of the ring surface after the test.

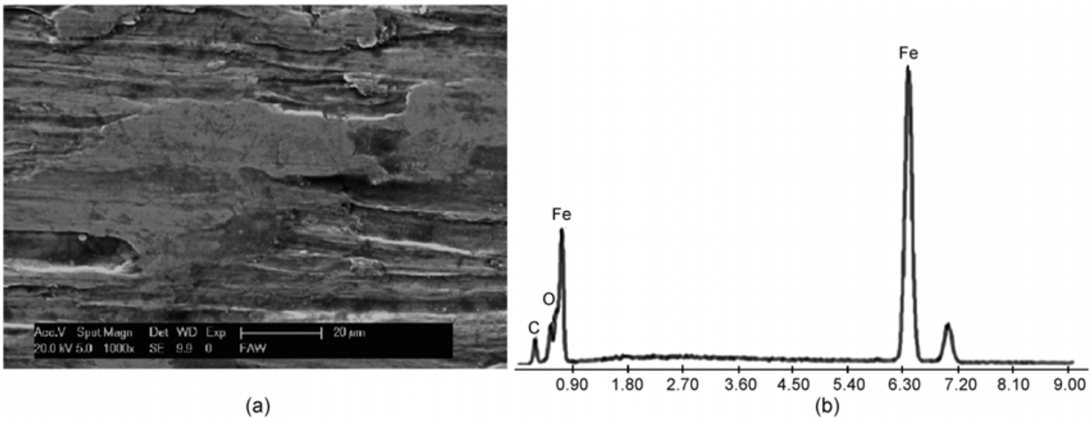

Fig. 9 Wear trace of the cylinder liner under dry sliding conditions with CNTs. (a) SEM image, and (b) EDS spectrum.

4 Conclusions

This study investigated the effects of carbon nanotubes on the tribological performance of a PRCL system under dry and lubricated conditions. Under dry friction, the CNTs act as a solid lubricant, and under lubricated conditions, it can be regarded as a kind of additive to the lubricant. Under dry sliding conditions, adding CNTs to a PRCL system can result in a large reduction in friction and wear. Based on SEM and EDS analysis, it was found that CNTs formed a carbon film covering the contact surfaces. Because of the low shear property of CNTs, the friction coefficient decreased compared to those samples without CNTs. Under dry friction, the effective time of CNTs is limited, and the friction coefficient decreases with an increase in CNT content. The wear mechanism under dry friction is mainly adhesive wear. Under lubricated conditions, adding CNTs to the lubricant slightly increases the friction coefficient.

Acknowledgments

The research presented in this paper was partially funded by the National Natural Science Foundation of China (Nos. 51575340 and 51575342) and Research Project of State Key Laboratory of Mechanical System and Vibration (No. MSVZD201104).

Reference

[1] Holmberg K, Andersson P, Erdemir A. Global energy consumption due to friction in passenger cars. *Tribol Int* **47**: 221–234 (2012)

[2] Tung S, McMillan M L. Automotive tribology overview of current advances and challenges for the future. *Tribol Int* **37**(7): 517–536 (2004)

[3] Wong V W, Tung S. Overview of automotive engine friction and reduction trends–Effects of surface, material and lubricant-additive technologies. *Friction* **4**(1): 1–28 (2016)

[4] Etsion I, Sher, E. Improving fuel efficiency with laser surface textured piston rings. *Tribol Int* **42**(4): 542–547 (2009)

[5] Skopp A, Kelling N, Woydt M, Berger L M. Thermally sprayed titanium suboxide coatings for piston ring/cylinder liners under mixed lubrication and dry-running conditions. *Wear* **262**(9–10): 1061–1070 (2007)

[6] Meng F M, Wang J X, Xiao K. A study of the influences of particles in the gas flow passage of a piston ring pack on the tribological performances of the piston ring. *Proc IMechE, Part C: J Mech Eng Sci* **224**(1): 201–215 (2010)

[7] Smith E H. Optimising the design of a piston-ring pack using DoE methods. *Tribol Int* **44**: 29–41 (2011)

[8] Iijima S. Helical microtubules of graphitic carbon. *Nature* **354**(6348): 56–58 (1991)

[9] Ajayan P M. Nanotubes from carbon. *Chem Rev* **99**(99): 1787–1800 (1999)

[10] Suhr J, Koratkar N, Keblinski P, Ajayan P. Viscoelasticity in carbon nanotube composites. *Nat Mater* 4(2): 134–137 (2005)

[11] Tu J P, Yang Y Z, Wang L Y, Ma X C, Zhang X B. Tribological properties of carbon-nanotube-reinforced copper composites. *Tribol Lett* **10**(4): 225–228 (2001)

[12] Ulus H, Üstün T, Eskizeybek V, Ömer Sinan Şahin Avcı A, Ekrem M. Boron nitride-mwcnt/epoxy hybrid nanocomposites: Preparation and mechanical properties. *Appl Surf Sci* **318**: 37–42 (2014)

[13] Treacy M M J, Ebbesen T W, Gibson J M. Exceptionally high young's modulus observed for individual carbon nanotubes. *Nature* **381**(6584): 678–680 (1996)

[14] Yan L, Wang H, Wang C, Sun L, Liu D, Zhu Y. Friction and wear properties of aligned carbon nanotubes reinforced epoxy composites under water lubricated condition. *Wear* **308**(308): 105–112 (2013)

[15] Düzcükoğlu H, Ekinci Ş, Şahin Ö S, Avci A, Ekrem M, Ünaldi M. Enhancement of wear and friction characteristics of epoxy resin by multiwalled carbon nanotube and boron nitride nanoparticles. *Tribol Trans* **58**(4): 635–642 (2015)

[16] Cui L J, Geng H Z, Wang W Y, Chen L T, Gao J. Functionalization of multi-wall carbon nanotubes to reduce the coefficient of the friction and improve the wear resistance of multi-wall carbon nanotube/epoxy composites. *Carbon* **54**(4): 277–282 (2013)

[17] LaBarre E D, Calderon-Colon X, Morris M, Tiffany J, Wetzel E, Merkle A, TrexLer M. Effect of a carbon nanotube coating on friction and impact performance of kevlar. *J Mater Sci* **50**(16): 5431–5442 (2015)

[18] Gandhi R A, Palanikumar K, Ragunath B K, Davim J P. Role of carbon nanotubes (cnts) in improving wear properties of polypropylene (pp) in dry sliding condition. *Mater Design* **48**(2): 52–57 (2012)

[19] Lee S M, Shin M W, Jang H. Effect of carbon-nanotube length on friction and wear of polyamide 6,6 nanocomposites. *Wear* **320**(s1–2): 103–110 (2014)

[20] Al-Qutub A M, Khalil A, Saheb N, Hakeem A S. Wear and friction behavior of Al6061 alloy reinforced with carbon nanotubes.*Wear* **297**(s1–2): 752–761 (2013)

[21] Bastwros M M H, Esawi A M K, Wifi A. Friction and wear behavior of Al–CNT composites. *Wear* **307**(1–2): 164–173 (2013)

[22] Abdullahi U, Maleque M A, Nirmal U. Wear mechanisms map of CNT-Al nano-composite. *Procedia Eng* **68**(12): 736–742 (2013)

[23] Khun N W, Troconis B C R, Frankel G S. Effects of carbon nanotube content on adhesion strength and wear and corrosion resistance of epoxy composite coatings on aa2024-t3. *Prog Organic Coat* 77(1): 72–80 (2014)

[24] Liu H, Ji H, Hong H, Younes H. Tribological properties of carbon nanotube grease. *Ind Lubr Tribol* **6**(5): 2–2 (2014)

[25] Kałużny J, Iskra A, Babiak M, Krzymień P, Giersig M, Kempa K. Selected applications of carbon nanotubes in construction of internal combustion engine. *J Peripheral Nervous System* **18**(2): 192–194 (2014)

[26] Jacobs O, Xu W, Schädel B, Wu W. Wear behaviour of carbon nanotube reinforced epoxy resin composites. *Tribol Lett* **23**(23): 65–75 (2006)

[27] Bastwros M M H, Esawi A M K, Wifi A. Friction and wear behavior of Al–CNT composites. *Wear* **307**(1–2): 164–173 (2013)

[28] Zoo Y S, An J W, Lim D P, Lim D S. Effect of carbon nanotube addition on tribological behavior of uhmwpe. *Tribol Lett* 252(5–6): 512–517 (2002)

[29] Choi H J, Lee S M, Bae D H. Wear characteristic of aluminum-based composites containing multi-walled carbon nanotubes. *Wear* **270**(1): 12–18 (2010)

Zhinan ZHANG. He received his Ph.D. degree in 2011 from Shanghai Jiaotong University, Shanghai, China. After that he was a post doctor in Shanghai Jiaotong University. He is now working as an assistant researcher in the School of Mechanical Engineering, Shanghai Jiaotong University. His research interests include computational design and analysis of tribosystems, and theory and methods of design engineering and innovation.

Friction **5**(2): 155–170 (2017)
DOI 10.1007/s40544-017-0141-2

ISSN 2223-7690
CN 10-1237/TH

RESEARCH ARTICLE

Surface roughness measurements in NFMQL assisted turning of titanium alloys: An optimization approach

Munish K. GUPTA[*], **P. K. SOOD**

MED, NIT, Hamirpur (H.P.) 177005, India

Received: 19 September 2016 / Revised: 26 October 2016 / Accepted: 11 December 2016

Abstract: The prediction and optimization of surface roughness values remain a critical concern in nano-fluids based minimum quantity lubrication (NFMQL) turning of titanium (grade-2) alloys. Here, we discuss an application of response surface methodology with Box–Cox transformation to determine the optimal cutting parameters for three surface roughness values, i.e., R_a, R_q, and R_z, in turning of titanium alloy under the NFMQL condition. The surface roughness prediction model has been established based on the selected input parameters such as cutting speed, feed rate, approach angle, and different nano-fluids used. Then the multiple regression technique is used to find the relationship between the given responses and input parameter. Further, the experimental data were optimized through the desirability function approach. The findings from the current investigation showed that feed rate is the most effective parameter followed by cutting speed, different nano-fluids, and approach angle on R_a and R_q values, whereas cutting speed is more effective in the case of R_z under NFMQL conditions. Moreover, the predicted results are comparatively near to the experimental values and hence, the established models of RSM using Box-Cox transformation can be used for prediction satisfactorily.

Keywords: nano-fluids; optimization; surface roughness; turning; titanium alloy

1 Introduction

Nowadays, surface finishing is considered as a critical performance parameter in various manufacturing industries that appreciably affects the mechanical properties of parts namely creep life, resistant to corrosion and fatigue behavior. It additionally influences other useful qualities of machined parts like wear, friction, lubrication, heat transmission and electrical conductivity [1]. Thus, accomplishing good surface quality is of immense significance for the usefulness of the machine parts [2]. The various factors such as cutting speed, feed rate, depth of cut, and tool material directly affect the surface quality of the machined parts [3]. Among these factors, the uses of cutting fluids are still considered as one of the major factors [4]. Cutting fluids not only improve the surface finishing by reducing the cutting temperature, but also provide the proper lubrication effect between the tool-chip interfaces. The various sorts of environmentally friendly strategies such as dry machining, minimum quantity lubricant (MQL) and nano-fluids with MQL, have been presently developed to increment the overall efficacy of the machining process [5].

Dry machining is not feasible during machining of difficult to cut and sticky materials like titanium base alloy, because these materials when machined dry tend to stick to the tool face leading to tool failure and result in a poor surface finish on the machined surface [6]. Therefore, the use of the MQL technique can be regarded as an attractive alternative solution, in which a very small amount of cutting fluid along

---

* Corresponding author: Munish K. GUPTA, E-mail: munishguptanit@gmail.com

NOMENCLATURE

a_p, Depth of cut (mm)	f, Feed rate (mm/rev)
V_c, Cutting speed (m/min)	ϕ, Side cutting edge angle or approach angle (degree °)
ANOVA, Analysis of variance	Al_2O_3, Aluminium oxide
CBN, Cubic boron nitride	C.F., Cutting fluid
MoS_2, Molybdenum disulfide	NFMQL, Nano-fluids based minimum quantity lubrication
R_a, Average roughness (μm)	R_q, Root mean square (μm)
R_z, Maximum peak to valley (μm)	RSM, Response surface methodology
SEM, Scanning electron microscopy	

with compressed air is directly applied to the machining area through the set of nozzles by drop-by-drop and mist [7, 8]. The MQL technique with nano-particles (nano-fluids) also contributes to greener or cleaner manufacturing, as the harmful effects of other MWFs are completely eliminated from the machining process [5].

A perusal of current literatures provides numerous studies which primarily focus on nano-fluids with the MQL technique in various machining operations. For the first research group, the grinding experiments were performed by Shen et al., on cast iron to evaluate the tribological behavior and performance of novel MoS_2 nano-particles. The outcome seems that the cutting fluid with novel MoS_2 nano-particles drastically reduce the friction and grinding force [9]. Several other researchers, namely Ramesh et al. [10–12], Sridharan and Malkin [13], Kwon and Drzal [14], Nam et al. [15], Samuel et al. [16], Park et al. [17], Vasu and Reddy [18], Ramesh et al. [19], Khanderkar et al. [20], Kalita et al. [21], Nguyen et al. [22], Amrita et al. [23], Paul and Varadarajan [24], Srikiran et al. [25], Amrita et al. [26], Sharma et al. [27], Su et al. [28] and Gupta et al. [5] have applied different nano fluids in various sorts of machining operations. Table 1 clearly describes that, the use of nano-particles with MQL in machining has proved to be an effective method to minimize the given responses. Moreover, some former researchers such as Barzani et al. [29, 30] and Unune et al. [31] presented the various prediction model used for estimating the surface roughness values (as described in Table 1). From the published works in the scientific database, it has been revealed that, the majority of work done under NFMQL has been carried out on various other materials, such as EN 24 alloy steel, Inconel-600 alloy, Ti-6Al-4V alloy, AISI 4340 steel, AISI 1040 steel, AISI 316L steel etc., and the general machining characteristics in terms of cutting forces, tool wear, cutting temperature and arithmetic average surface roughness (R_a) have been investigated. But, to the best of our knowledge, till now there has not been any systematic study conducted on turning of titanium (grade-2) alloy under NFMQL conditions while considering three surface roughness values, i.e., average roughness (R_a), root mean square (R_q), and maximum peak to valley (R_z). However, this does not exclude its importance, as there are also highly used alloys in orthopedic applications, such as implants and prosthesis, airframe and aircraft engine parts, marine chemical parts, condenser tubing and heat exchangers. Apart from this, it is totally resistant to corrosion. Thus, it would be interesting as well as enlightening to study the machining characteristics of this particular grade such as titanium (grade-2) alloy considering NFMQL conditions. Therefore, this study represents the first attempt to investigate the effect of process parameters while turning titanium (grade-2) alloy under NFMQL conditions by using response surface methodology (RSM) with Box–Cox transformation. For this purpose, the series of experiments on the CNC turning center have been performed. After that, the input (machining parameters) and output (surface roughness values) data have been collected (1) to develop the prediction model by using RSM with Box–Cox transformation, (2) to study the effect of machining parameters on surface roughness values, and (3) to optimize the machining parameters by using the desirability function approach.

Table 1 Literature survey/ work done using the NFMQL technique.

References	Author and year	W/P material	Type of nano-particles used	Machining operation	Investigations/findings
[10]	Ramesh et al., 2008	Ti-6Al-4V alloy	—	Turning	Surface roughness (R_a)
[11]	Ramesh et al., 2008	Ti-6Al-4V alloy	—	Turning	Cutting force, surface Roughness (R_a), tool flank wear
[12]	Ramesh et al., 2009	Ti-6Al-4V alloy	—	Turning	Cutting force, surface Roughness (R_a), tool flank wear
[13]	Sridharan & Malkin, 2009	—	CNT & MoS_2	Grinding	G-ratio, surface roughness, specific energy
[14]	Kwon & Drzal, 2010	—	Graphite	—	—
[15]	Nam et al., 2011	Al-6061 alloy	Diamond	Micro-drilling	Drilling torque, thrust force & quality of hole
[16]	Samuel et al., 2011	—	Graphene	—	Fluid properties
[17]	Park et al., 2011	AISI 1045 steel	Graphene	Ball milling	Tribological behavior & tool wear
[18]	Vasu & Reddy, 2011	Inconel-600 alloy	Al_2O_3	Turning	Tool wear, surface roughness (R_a), cutting temperature
[19]	Ramesh et al., 2012	Ti-6Al-4V alloy	—	Turning	Surface roughness (R_a)
[20]	Khanderkar et al., 2012	AISI 4340	Al_2O_3	Turning	Wettability, cutting force, tool wear, surface roughness (R_a), chip morphology & chip thickness
[21]	Kalita et al., 2012	EN 24 alloy steel	MoS_2	Grinding	Specific energy, friction coefficient, Grinding (G)-ratio
[22]	Nguyen et al., 2012	AISI 1045 steel	xGnP & hBN nano-platelets	Ball milling	Tribological behavior & tool wear
[23]	Amrita et al., 2013	AISI 1040 steel	Graphite	Turning	Cutting force, cutting temperature, tool wear
[24]	Paul & Varadarajan, 2013	AISI 4340 steel	Semi-Solid Lubricants	Turning	Cutting force, cutting temperature, tool wear & surface roughness (R_a), tool vibrations
[25]	Srikiran et al., 2014	AISI 1040 steel	Nano-crystalline graphite powder	Turning	Cutting forces, tool temperature & surface roughness (R_a)
[26]	Amrita et al., 2014	AISI1040 steel	Graphite	Turning	Cutting force, cutting temperature, tool wear, surface roughness (R_a), chip morphology
[27]	Sharma et al., 2015	AISI D2 steel	CNT	Turning	Cutting temperature, surface roughness (R_a)
[28]	Su et al., 2015	AISI 1045 steel	Graphite	Turning	Dynamic viscosity, surface tension, wettability, thermal conductivity, cutting forces, cutting temperature
[5]	Gupta et al., 2016	Titanium alloy	Graphite, MoS_2 & Al_2O_3	Turning	Cutting force, cutting temperature, tool wear & surface roughness (R_a)
[29]	Barzani et al., 2015	Al–Si–Cu cast alloy	Dry	Turning	Surface roughness and cutting force
[30]	Barzani et al., 2015	Al–Si–Cu–Fe die casting alloy	Dry	Turning	Prediction of average surface roughness using Fuzzy logic
[31]	Unune et al., 2016	Nimonic 80A	Dry	Abrasive-mixed electro-discharge diamond surface grinding	Prediction of material removal rate and average surface roughness using Fuzzy logic

*hBN = hexagonal Boron Nitride, xGnP = Graphene, CNT = Carbon nano-tubes, MoS_2 = Molybdenum disulfide, Al_2O_3 = Aluminum oxide

2.1 Materials and methods

2.2 Preparation of nano-fluids

In this study, the nano-fluids were prepared using a two-step method. The three different types of nano-particles, i.e., aluminum oxide (Al_2O_3), molybdenum disulfide (MoS_2) and graphite, each having an average diameter of 40 nm were used. Vegetable oil was chosen as the base oil due to its good biodegradability and low environmental impact. The concentrations of nano-particles in the vegetable based oils were 3 wt%. The concentration was then ultra-sonicated in a sonicator (40 kHz, 100W) (for 1 h) and magnetic stirrer (30 min), respectively. The process was repeated several times until all the nano-particles dispersed consistently within the vegetable based oil. The results indicated that the nano-fluid prepared was steady and no settlement of particles was found throughout the entire machining operation. The properties of the nano-fluids were measured and shown in Table 2.

2.2 Work material and cutting tool

For the experiments, titanium (grade-2) alloy having 50 mm diameter and 150 mm length was used. The chemical composition of the selected material is shown in Table 3. The cubic boron nitride inserts (CCGW 09T304-2, Positive 7°, Clearance 80°, rhombic, nose radius 0.4 mm) were used for performing the experiments.

2.3 Turning tests

A high precision CNC turning center (Sprint 16 TC equipped with a Siemens control system) having three simultaneously controlled axes (*X*, *Y*, and *Z* axis), was used for machining the given alloy. The NFMQL set up used in the current investigation was imported from Israel (NOGA made, mini cool system). The flow rate of 30 ml/h, air flow rate and pressure of 60 L/min and 5 bar, respectively were fixed throughout the turning experiments.

2.4 Surface roughness measurements

Surface roughness is defined as the finer irregularities of the surface texture that usually result from the inherent action of the machining process. The portable roughness tester (SJ301-MITUTOYO make) was used for measuring the three surface roughness values, i.e., average roughness (R_a), root mean square (R_q) and maximum peak to valley (R_z). The roughness tester has three measuring driving units namely the standard drive unit, the transverse tracing drive unit and the retractable drive unit. In the present study, the measurements have been taken with the standard drive unit according to the ISO 97 R standard, which includes the measuring force of 4 mN, stylus tip radius of 5 μm and tip material diamond and conical-taper angle of 90°. Moreover, one height stand is used (to hold and adjust the surface roughness tester), one surface plate and one V-block are required for the workpiece placement. The complete procedure for measuring the surface roughness is discussed here. Firstly, a stylus with the help of a moving height stand is adjusted on the machine surface of the workpiece, which is placed on the V-Block. Then, the center line of the stylus tip and workpiece has been matched. When the stylus is moved on the center "cut" lines made by the point cutting tool, the readings are displayed on the screen. After that, the workpiece is rotated three times at an angle of 120° and measures the surface roughness values. Finally, the mean of all three surface roughness values are considered. Figure 1 explains the measurement procedure of the surface roughness. In the end, the machined surface of titanium (grade-2) was characterized by scanning electron microscopy (SEM, Bruker make).

Table 2 Properties of nano-fluids.

Properties	Vegetable based oil	Al_2O_3 nano-fluid	MoS_2 nano-fluid	Graphite nano-fluid
Appearance	Bright and clear	White	Black	Grayish black
Viscosity (CP) (at 20 °C)	68.16	120.23	100.56	83.12
Thermal conductivity (W/(m·K))	0.1432	0.2085	0.2362	0.2663

Table 3 Chemical composition of Titanium (grade-2).

C	Fe	H	O	N	Ti
0.1% max	0.3%	0.015%	0.25%	0.03%	99.2%

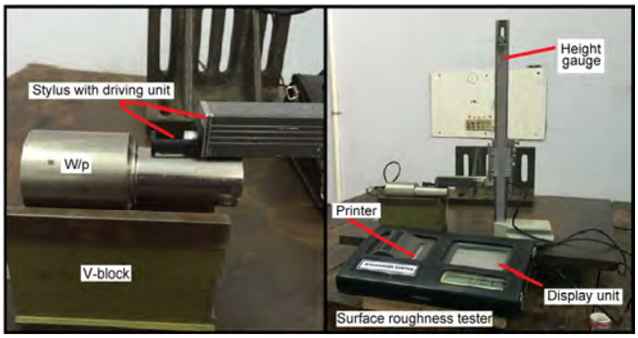

Fig. 1 Equipments used to measure the surface roughness values.

2.5 Cutting parameters and their levels

The turning tests were performed at different levels of cutting speed, feed rate, approach angle and different nano-fluids. A poor surface finish due to premature tool failure was observed at higher level of cutting speed (>300 m/min). However, no such phenomenon occurred when turning at lower cutting speed (>200 m/min). Therefore, the cutting speed range of 200–300 m/min was selected for turning of titanium (grade-2) alloy under NFMQL conditions, whereas feed rate and approach angle ranges were decided based on literature reviews and tool manufacturer's recommendations. A constant depth of cut of 1 mm was used for the experiments. The complete experimental procedure is displayed in Fig. 2.

2.6 Design of experiment

The purposed methodology is divided into the following stages. Firstly, the experiments were designed and planned using the Box-Behnkens RSM technique. It is a group of numerical and measurable strategies

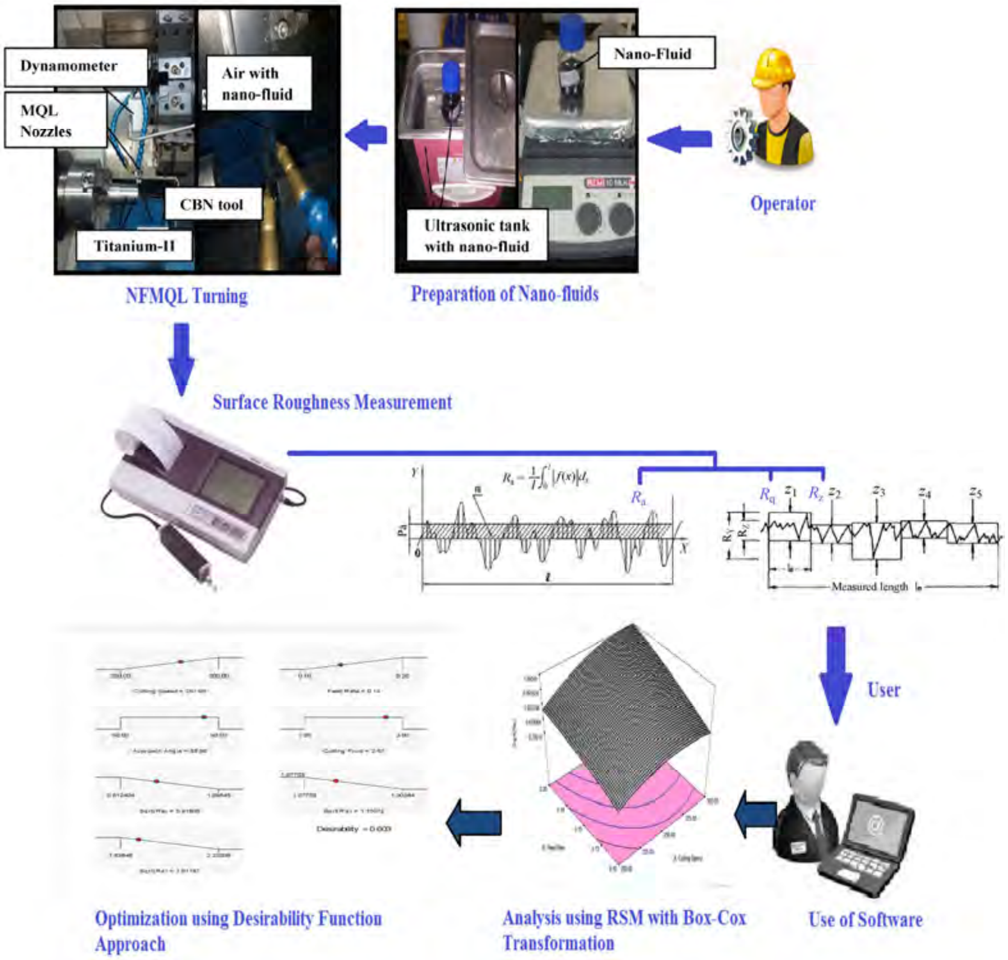

Fig. 2 Experimental procedure used to determine surface roughness values.

that are helpful for displaying and examining issues in which a reaction of interest is impacted by a few variables and the goal is to improve this output [32–34]. The experimental conditions and results of the given responses are tabulated in Table 4. In the second stage, the predictive models are established with the help of regression equations and the Box-Cox transformation. Generally, the Box–Cox transformation gives a group of changes to standardize the information, which is not typically conveyed by distinguishing a fitting example (lambda, λ). The lambda demonstrates the ability to which all information ought to be raised. The Box-Cox transformation initially imagined this change as a panacea for and at the same time revising typicality, linearity and homogeneity. In the third stage, the multi-response optimization is performed by using the desirability function approach. The flowchart of the RSM technique is shown in Fig. 3.

Table 4 Machining parameters with the experimental design and their results.

Sr. No.	V_c (m/min)	f (mm/rev)	ϕ (°)	Nano-fluids*	R_a (μm)	R_q (μm)	R_z (μm)
1	300	0.15	75	3	0.90	1.48	4.15
2	250	0.15	75	2	0.92	1.42	3.51
3	250	0.15	75	2	0.91	1.41	3.50
4	250	0.1	90	2	0.74	1.18	3.46
5	250	0.1	75	3	0.68	1.24	3.63
6	250	0.2	60	2	1.10	1.62	4.73
7	250	0.15	75	2	0.92	1.42	352
8	250	0.15	90	1	0.88	1.38	4.03
9	300	0.15	90	2	0.98	1.40	4.02
10	200	0.15	90	2	0.72	1.22	3.74
11	250	0.15	90	3	0.80	1.30	3.98
12	250	0.2	75	1	1.12	1.54	4.38
13	250	0.15	75	2	0.92	1.42	3.51
14	200	0.15	75	1	0.79	1.27	3.42
15	250	0.2	90	2	1.04	1.60	4.83
16	300	0.15	75	1	1.08	1.46	4.59
17	300	0.2	75	2	1.02	1.70	4.93
18	200	0.15	75	3	0.71	1.21	3.38
19	250	0.15	60	1	1.08	1.58	4.38
20	250	0.15	75	2	0.91	1.41	3.52
21	300	0.15	60	2	0.96	1.58	4.48
22	250	0.2	75	3	1.2	1.52	4.68
23	200	0.15	60	2	0.77	1.27	3.86
24	250	0.1	60	2	0.82	1.32	4.12
25	300	0.1	75	2	0.70	1.28	4.08
26	200	0.2	75	2	0.78	1.28	3.67
27	200	0.1	75	2	0.66	1.16	3.40
28	250	0.1	75	1	0.78	1.20	4.73
29	250	0.15	60	3	1.02	1.52	3.81

*Cutting fluid: 1—Signifies Al_2O_3 based nano-fluid, 2—signifies MoS_2 based nano-fluid, and 3—signifies graphite based nano-fluid.

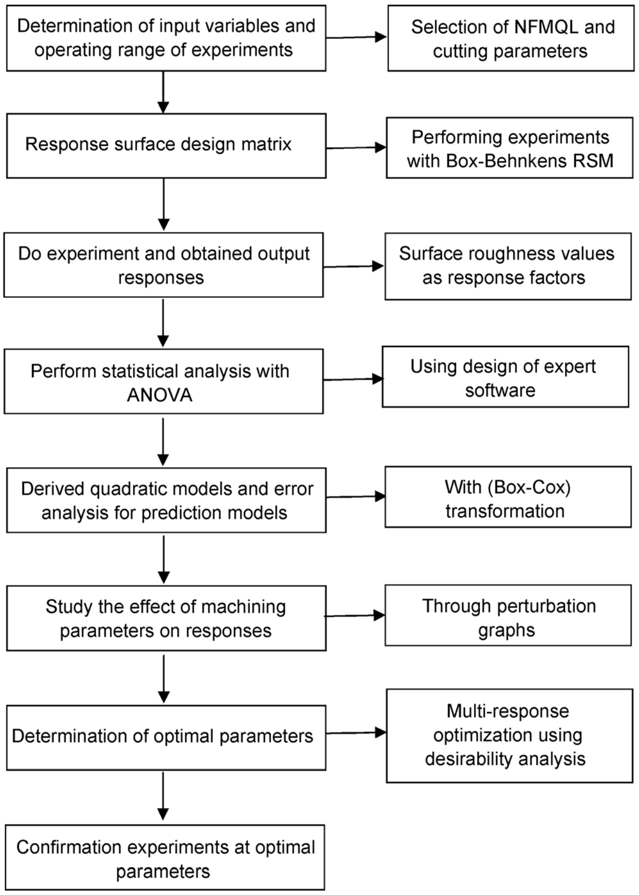

Fig. 3 Flow chart of the response surface methodology (RSM) technique.

3 Results and discussion

The experimental results obtained from Table 4 were used to establish the prediction models for R_a, R_q and R_z through RSM with the Box-Cox transformation. The adequacy of the established models was affirmed with the help of ANOVA. Then, the square root change on the reaction is required to make the residuals regularly disseminated. Finally, the error analysis of the predictive models and effect of the machining parameters on surface roughness were investigated and discussed.

3.1 Development of the prediction model with transformation for R_a, R_q and R_z

The best-fit equations to relate the responses (R_a, R_q and R_z) to the cutting parameters (V_c, f, φ and C.F.) are achieved by adapting general measurable techniques of regression analysis with the benefit of design expert software. In the case of the R_a and R_q (Table 5 and Table 6, respectively) a linear model is selected, and the cutting speed (V_c), the feed rate (f) as well as the nano-fluid (C.F.) are the significant model terms. Whereas, for R_z (Table 7) the quadratic model is suggested and the main effect of cutting speed, feed rate and nano-fluid, second-order effect of feed rate, approach angle (φ) and nano-fluid, interaction effect of feed rate and nano-fluid are the noteworthy terms. The Prob > *F*" from ANOVA for all demonstrations are less than 0.0500; hereafter, the models are thought to be adequate. The correlation coefficient (R^2 close to unity) was persistent to depict the adequacy of a fitted regression models and it was found that for all models R^2 was close to solidarity. Moreover, there is reasonable agreement between the "Pred R-Squared" and "Adj R-Squared" values, which confirms the adequacy of the model. The adequate precision ratio of all established models (ratio>4 is desirable) provides a satisfactory indication to utilize the proposed model. The final regressions Eqs. (1)–(3) with the square root transformation for R_a, R_q and R_z are represented as:

$$\sqrt{R_a} = 0.59012 + 1.08538\text{E-}003 \times V_c + 1.65475 \times f - 1.72109\text{E-}003 \times \varphi - 0.019258 \times \text{C.F.} \tag{1}$$

$$\sqrt{R_q} = 0.86963 + 1.05573\text{E-}003 \times V_c + 1.32362 \times f - 1.89800\text{E-}003 \times \varphi - 5.61066\text{E-}003 \times \text{C.F.} \tag{2}$$

$$\sqrt{R_z} = 5.07360 + 1.99235\text{E-}003 \times V_c - 15.11368 \times f - 0.053138 \times \varphi - 0.56240 \times \text{C.F.} + 44.21514 \times f^2 + 3.41977\text{E-}004 \times \varphi^2 + 0.067071 \times \text{C.F.}^2 + 1.70043 \times f \times \text{C.F.} \tag{3}$$

Furthermore, in order to confirm the adequacy or efficacy of the develped model, diagnostic plots were used. They guarantee that the measurable theory fits the systematic information accodingly. Figure 4 uncovers that, in the case of R_a the residuals for all demonstrations fall on a straight line, which signifies that the errors were normally distributed. The simillar trend is observed for the remaining responses, i.e., for R_q and R_z, which confirms the adequacy of the developed models. Similarly, Fig. 5 shows a Box–Cox plot for power transformation with respect to R_a. For all the models, the blue line indicates the current value of lambda for residuals as 0.5, which lie outside

Table 5 ANOVA for R_a with transformation.

Source	Sum of squares	DF	Mean square	*F* value	Prob > *F*	Remarks
Model	0.129937	4	0.032484	18.48896	< 0.0001	Significant
V_c	0.035342	1	0.035342	20.11545	0.0002	
f	0.082146	1	0.082146	46.75517	< 0.0001	
φ	0.004451	1	0.004451	2.533099	0.1246	
C.F.	0.007998	1	0.007998	4.552105	0.0433	
Residual	0.042167	24	0.001757			
Lack of fit	0.042134	20	0.002107	257.0153	< 0.0001	Significant
Pure error	3.28E-05	4	8.2E-06			
Cor total	0.172103	28				
Std. Dev.	0.041916		R-Squared	0.754992		
Mean	0.942079		Adj R-Squared	0.714157		
C.V.	4.449302		Pred R-Squared	0.619395		
PRESS	0.065503		Adeq Precision	15.74371		

Table 6 ANOVA for R_q with transformation.

Source	Sum of squares	DF	Mean square	*F* value	Prob > *F*	Remarks
Model	0.096101	4	0.024025	38.94489	< 0.0001	Significant
V_c	0.033437	1	0.033437	54.20177	< 0.0001	
f	0.052559	1	0.052559	85.19868	< 0.0001	
φ	0.000378	1	0.000378	0.612342	0.4416	
C.F.	0.009727	1	0.009727	15.76676	0.0006	
Residual	0.014806	24	0.000617			
Lack of fit	0.014784	20	0.000739	139.466	0.0001	Significant
Pure error	2.12E-05	4	5.3E-06			
Cor total	0.110906	28				
Std. Dev.	0.024837		R-Squared	0.866503		
Mean	1.178531		Adj R-Squared	0.844254		
C.V.	2.107497		Pred R-Squared	0.793814		
PRESS	0.022867		Adeq Precision	23.07093		

the 95% confidence limit. But the best recommended value of lambda is approximately −0.42 for R_a, −0.61 for R_q and −1.06 for R_z as shown by the green line. The optimum Box-Cox transformation was calculated by finding the value of lambda that maximizes the negative log likelihood. Moreover, from ANOVA it was found that the feed rate is the most effective parameter followed by cutting speed, different nano-fluids and approach angle on R_a and R_q values under NFMQL conditions; whereas cutting speed is more effective in the case of R_z.

3.2 Error analysis for prediction models

In order to verify the predictiveness of the established models using the Box-Cox transormation, an error analyis based on statistical methods of percentage mean absolute error (%MAE) and percentage mean square error (%MSE) was performed. These values

Table 7 ANOVA for reduced quadratic model for R_z with transformation.

Source	Sum of squares	DF	Mean square	*F* value	Prob > *F*	Remarks
Model	0.366231	8	0.045779	15.54117	< 0.0001	Significant
V_c	0.119083	1	0.119083	40.42686	< 0.0001	
f	0.072236	1	0.072236	24.52277	< 0.0001	
φ	0.009156	1	0.009156	3.108434	0.0932	
C.F.	0.018303	1	0.018303	6.213477	0.0216	
f^2	0.082198	1	0.082198	27.90486	< 0.0001	
φ^2	0.039829	1	0.039829	13.52122	0.0015	
C.F.^{2}	0.030263	1	0.030263	10.27386	0.0044	
f*C.F.	0.028915	1	0.028915	9.816054	0.0052	
Residual	0.058913	20	0.002946			
Lack of fit	0.058893	16	0.003681	738.4153	< 0.0001	Significant
Pure error	1.99E-05	4	4.98E-06			
Cor total	0.425144	28				
Std. Dev.	0.054274		R-Squared	0.861428		
Mean	1.996677		Adj R-Squared	0.805999		
C.V.	2.718209		Pred R-Squared	0.6685		
PRESS	0.140935		Adeq Precision	12.32878		

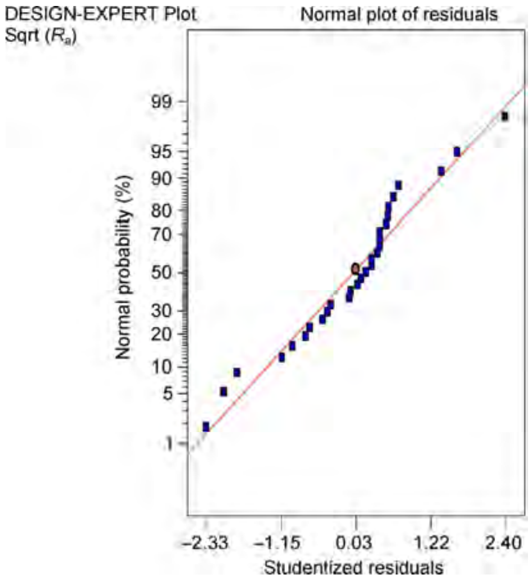

Fig. 4 Normal probability plot for R_a.

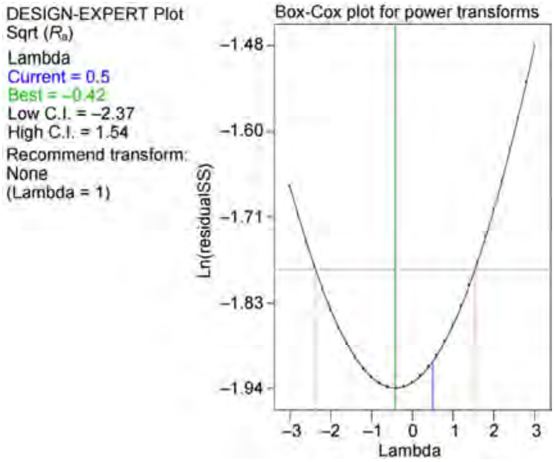

Fig. 5 Box-Cox power transformation plots for R_a.

were determined using Eqs. (4)–(5), respectively:

$$\%\,\mathrm{MAE} = \left(\frac{1}{n}\sum_i \left|\frac{e_i - p_i}{e_i}\right|\right)\times 100 \tag{4}$$

$$\%\,\mathrm{MSE} = \left(\frac{1}{n}\sum_i \left|e_i - p_i\right|^2\right)\times 100 \tag{5}$$

where e is the experimental value, p is the predicted value and n is the number of iterations for experimentation. From the error analysis, it was found that the value of maximum percentage absolute error reduces from 48.56 to 8.79 for R_a, 36.78 to 111.42 for R_q, and 56.63 to 9.69 for R_z using a Box–Cox transformation. Furthermore, the maximum percentage square error reduces from 8.23 to 0.421 for R_a, 7.96 to 0.134 for R_q, and 16.33 to 1.914 for R_z. This indicates the better prediction ability of the developed models using the Box–Cox transformation.

In the end, the adequacy of the developed model is validated and checked by comparing the predicted and experimental surface roughness values. Figure 6 represents the comparative assesment of the predicted and experimental values for R_a. As shown in Fig. 6, it was found that the predicted values for R_a are very closer to the experimental values and the errors are also found to be much less, which confirms good efficacy of the developed model. The same trend is found for the remaining responses and good agreement is observed between these values. Hence, an application of RSM with the Box-Cox transformation was found to be an effective method for identification and development of models within the seletced ranges of cutting parameters.

3.3 Effect of machining parameters on surface roughness values

The influence of all cuttting parameters after the Box-Cox transformation on average surface roughness was performed with the help of perturbation analysis, as shown in Figs. 7(a)–7(c).

Effect of cutting speed on R_a, R_q and R_z: Cutting speed greatly influenced all surface roughness values, i.e., R_a, R_q, and R_z. So the three values of cutting speed (200, 250, 300 m/min) have been considered for the current investigation. The characterization of machined samples is performed at the preferred machining parameters. It was found that, in the case of NFMQL turning during sticky material like titanium (grade-2), the values of surface roughness moderately increase with the change in cutting speed from 200 m/min to 300 m/mn. This might occur because, at higher values of cutting speeds, the major portion of the chips will move from the tool cutting edge and generate high friction, which results in higher values of surface roughness. Also, the high cutting speed creates the built up edge at the tool, thus lowering the surface finish.

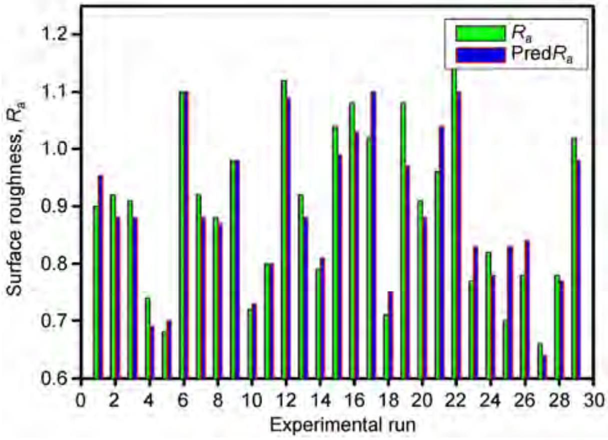

Fig. 6 Surface roughness as a function of experimental run using predicted and experimental R_a.

Effect of feed rate on R_a, R_q, and R_z: Due to the high ductility of titanium and its alloys, the built up edge are formed on the tool rake face. At the point when the impact of the built-up edge is viewed as unimportant, the cutting tool profile, i.e., curved or pointed gets embossed on the workpiece and the surface roughness starting here relies on upon the feed rate. Furthermore, it is well known fundamental of metal cutting that, the pitch of the surface to be machined is greatly affected by the feed rate ($R_a = \frac{f^2}{32r}$). This explains why the surface roughness is sharply incremented with the increase in feed rate from 0.10 mm/rev to 0.20 mm/rev. Also, it has been found that the tool moves very qucikly at higher cutting speed and feed rates, resulting in deteriorated surface quality, machine chattering and vibrations. Hence, the leads to higher surface roughness values. Gupta et al. also discovered the similar results [35].

Effect of approach angle on R_a, R_q and R_z: The main cutting edge moves towards the workpiece with an approaching angle. For large approach angles, the contact surface is distributed over a shorter section of the cutting edge whereas with small approach angles, it is spread over a greater length. The thickness of the cutting chip also depends on the approach angle. The approach angle plays an important role in the tool's life, therefore it is imperative to evaluate the effect of approach angle on other parameters such as surface roughness by keeping the speed and feed constant. It is for this reason that with the increased approach angles, the contact length of the cutting tool tip with respect to the work material is less, which further decreases the friction between the tool and work piece, which leads to low vibration in the machining and increases the surface finishing.

Effect of different nano-fluids on R_a, R_q and R_z: The change in nano-fluid also shows surprising results on the surface roughness values. It has been found that, the values of surface roughness decrease with the change in nano-fluid from aluminum-oxide based nano-fluid to graphite based nano-fluid. Because the

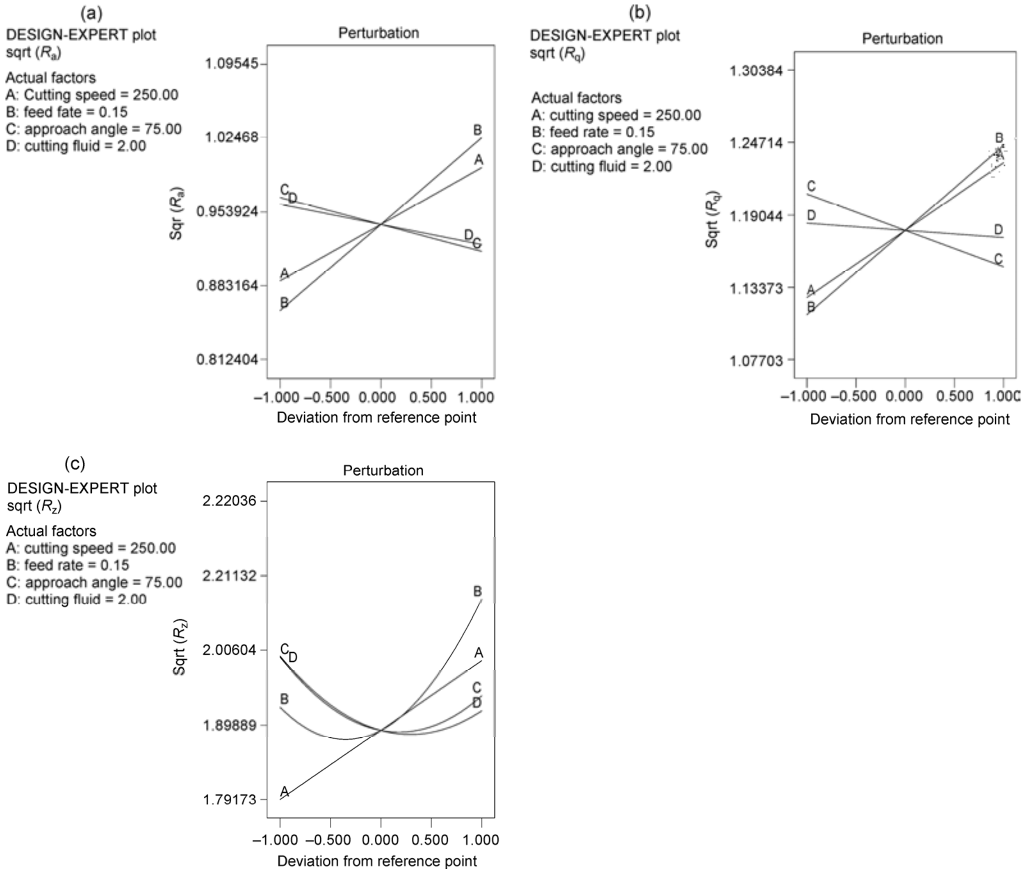

Fig. 7 Perturbation graphs for: (a) R_a, (b) R_q, and (c) R_z.

viscosity of graphite is lower compared to the other two fluids, which results in the proper settlement of the nano-fluids between the workpiece and the tool, hence, this provides the cushioning effect which may induce low machine chattering and vibrations and increase the surface finishing of the titanium (grade-2) alloy. Moreover, the decrease in surface roughness values with graphite based nano-fluid is also associated with its thermal conductivity. The higher thermal conductivity of graphite based nano-fluids helps to dissipate the heat from the primary cutting zone, which leads to less tool wear. Less tool wear helps in accomplishing better surface quality by diminishing the redeposition of materials on the machined surface. The same trend was examined by Sharma et al. [27]. Figure 8 uncovers the reduced redeposition on the machined surface while utilizing graphite-based nano-fluids. Figure 9 depicts that feed marks are clealry

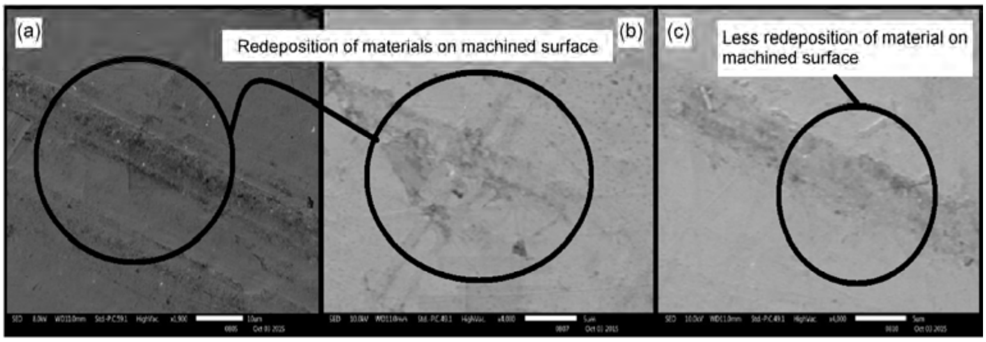

Fig. 8 Machined surface at cutting speed = 250 m/min, feed rate = 0.2 mm/rev and approach angle = 75°: (a) Al_2O_3 based nano-fluid, (b) MoS_2 based nano-fluid, and (c) graphite based nano-fluid.

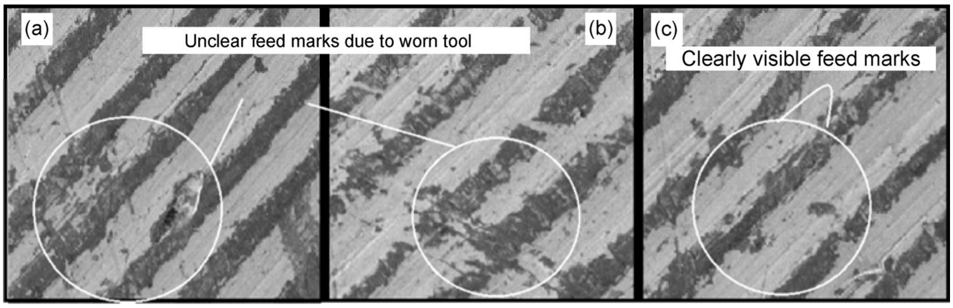

Fig. 9 Machined surface at cutting speed = 250 m/min, feed rate = 0.2 mm/rev and approach angle = 75°: (a) Al_2O_3 based nano-fluid, (b) MoS_2 based nano-fluid, and (c) graphite based nano-fluid.

visible and clean surface are obtained without any plastic deformation under graphite based nano-fluids as compared to others.

4 Desirability based multi response optimization

The desirability based multi response optimization is performed to obtain minimal surface roughness values. In this study, the ranges of input parameters viz. cutting speed and feed rate are selected to be maximum, whereas the approach angle and nano-fluids are selected within ranges shown in Table 8. An arrangement of three ideal solutions are determined for the particular design space constraints for surface roughness values by using the design expert statistical software. The arrangement of conditions having the most desirability value is chosen as ideal conditions for the given outputs. Once the ideal level of the procedure parameters is chosen, the last stride is to predict and confirm the enhancement of the performance characteristics utilizing the ideal level of the machining parameters [35]. The ramp function graph for the desired objectives was selected as shown in Fig. 10. The point on every ramp shows the parameter setting or output prediction for that output characteristic. The height of every point demonstrates the level of desirability. Furthermore, the contour plots for overall desirability has been plotted to show the sensitivity of the results as shown in Fig. 11. The near optimal area was positioned close to the the left hand base area of the plot, which had a general desirability value more prominent than 0.6 that slowly decreased as we moved right and upwards. Sensitivities are acquired utilizing the shape of the contour lines in Fig. 11. The optimal values are tabulated in Table 9.

Table 8 Range of input parameters and responses for desirability optimization.

Parameter	Goal	Lower limit	Upper limit	Lower weight	Upper weight	Importance
Cutting speed	maximize	200	300	1	1	3
Feed rate	maximize	0.1	0.2	1	1	3
Approach angle	is in range	60	90	1	1	3
Nano-fluid	is in range	1	3	1	1	3
Sqrt (R_a)	minimize	0.812404	1.095445	1	1	3
Sqrt (R_q)	minimize	1.077033	1.30384	1	1	3
Sqrt (R_z)	minimize	1.83848	2.22036	1	1	3

Table 9 Optimization results.

Sr. No.	Cutting speed	Feed rate	Approach angle	Nano-fluid	Sqrt (R_a)	Sqrt (R_q)	Sqrt (R_z)	Desirability	
1	253.55	0.14	87.04	3	0.899	1.146	1.913	0.615721	Selected
2	245.17	0.13	87.28	2	0.883	1.124	1.895	0.502346	
3	273.89	0.14	72.25	2	0.961	1.200	1.937	0.501354	

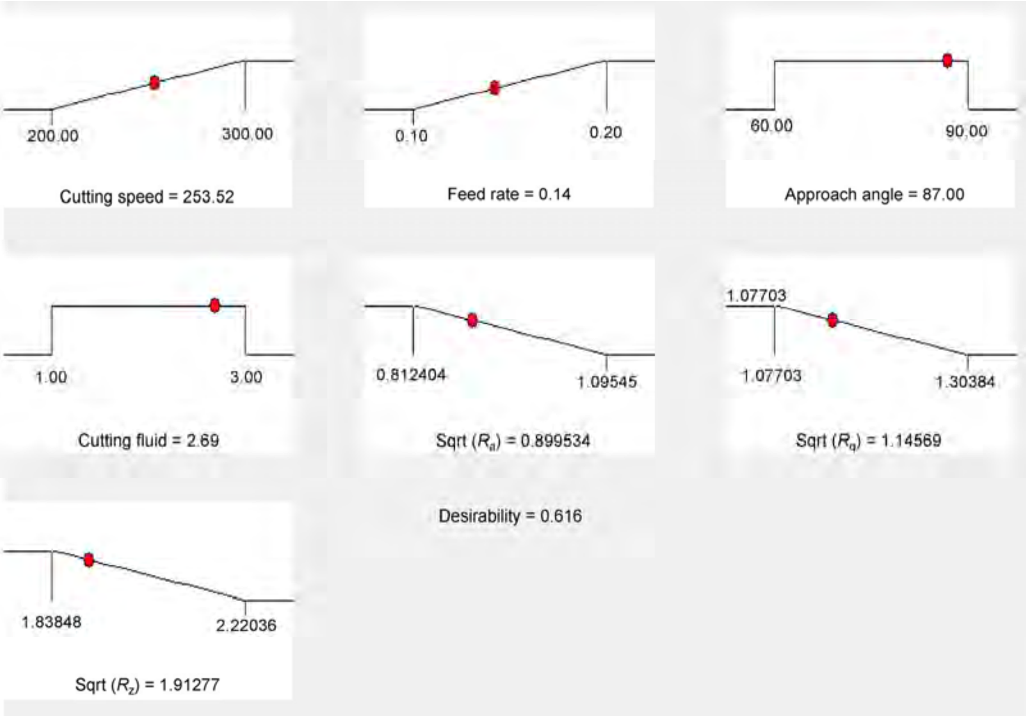

Fig. 10 Ramp function graphs of desirability optimizations.

Then, the confirmation experiments have been performed to validate the established model as presented in Table 10. The predicted and experimental values are near to each other, which demonstrates the importance of the established models.

Table 10 Confirmation test for the optimization value.

Parameters	Initial result at optimum value	Experimental result at optimum value
Cutting speed	253.55	253.55
Feed rate	0.14	0.14
Approach angle	87	87
Nano-fluid	3	3
Sqrt (R_a)	0.899	0.874
Sqrt (R_q)	1.146	1.1123
Sqrt (R_z)	1.913	1.803

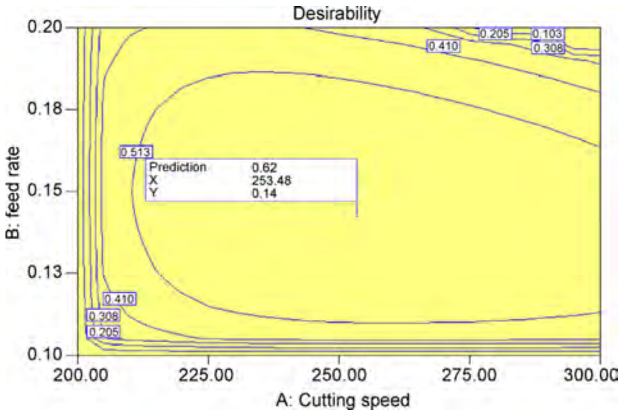

Fig. 11 Contour plots for result of overall desirability function (cutting speed vs. feed rate).

5 Conclusion

In the present work, nano-fluid based MQL environments are developed to meet the the demands for environmentally friendly machining processes. The effect of the machining variables (cutting speed, feed rate and approach angle) and different nano-fluids on three surface roughness values in turning of titanium-II under NFMQL conditions has been investigated. Then, the surface roughness prediction model using RSM with the Box-Cox transformation has been established. The following conclusions are drawn from the analysis of the results within the selected range of parameters:

1. The outcomes demonstrate that, feed rate is the most effective parameter followed by cutting speed, different nano-fluids and approach angle on R_a and

R_q under NFMQL conditions, whereas cutting speed is more effective in the case of R_z.

2. It has been observed that as in the case of NFMQL turning during sticky materials like titanium (grade-2), the values of surface roughness moderately increase due to the rise in cutting speed, whereas it sharply increases due to the rise in feed rate. This might occur because, at higher values of cutting speeds, the major portion of the chips will move from the tool's cutting edge and generates high friction, which results in higher values of surface roughness.

3. However, with increasing in approach angles the contact length of the cutting tool tip with respect to the work material is less, which further decreases the friction between the tool and the work piece, which leads to low vibration in the machining and an increase in the surface finishing.

4. The change in nano-fluid also shows surprising results on the surface roughness values. It has been found that, the values of surface roughness decrease with the change in nano-fluid from aluminum-oxide based nano-fluid to graphite based nano-fluid. Because the viscosity of graphite is lower compared to the other two fluids, this results in proper settlement of the nano-fluids between the workpiece and the tool, hence, which provides the cushioning effect which may induce low machine chattering and vibrations and increase the surface finishing of the titanium (grade-2) alloy.

5. The RSM with the Box-Cox transformation was found to be an effective method for identification and development of significant relationships between the cutting parameters and the given responses.

6. The contour effect plots for overall desirability function revealed the desirability range when responses are given equal weighting. It shows that the cutting speed of 253 m/min, the feed rate of 0.14 mm/rev, the approach angle of 87° and the graphite based nano-fluids are desirable for obtaining the optimal conditions.

The results clearly showed that this optimisation method was effective and incredibly diminished the machining cost. This model can be efficiently applied to find the suitable cutting conditions, in order to achieve the preferred surface roughness value. The future empirical work will look into the effect of different parameters such nose radius, tool materials, work materials, etc. on the surface roughness values under NFMQL conditions.

Acknowledgement

The authors are extremely grateful to Dr. Vishal S. Sharma, NIT Jalandhar for providing the research facilities. Authors also acknowledge the MHRD, Govt. of India and Central Workshop NIT Hamirpur (H.P.) for the financial support.

References

[1] Routara B C, Bandyopadhyay A, Sahoo P. Roughness modeling and optimization in CNC end milling using response surface method: effect of work piece material variation. *Int J Adv Manuf Technol* **40**: 1166–1180 (2008)

[2] Davim J P, Gaitonde V N, Karnik S R. Investigations into the effect of cutting conditions on surface roughness in turning of free machining steel by ANN models. *J Mater Process Technol* **205**: 16–23 (2007)

[3] Bhardwaj B, Kumar R, Singh P K. Surface roughness (Ra) prediction model for turning of AISI 1019 steel using response surface methodology and Box-Cox transformation. *Proc IMechE, Part B: J Eng Manuf* **228(2)**: 223–232 (2013)

[4] Sharma V S, Dogra M, Suri N M. Cooling techniques for improved productivity in turning. *Int J Mach Tool Manu* **49(6)**: 435–453 (2009)

[5] Gupta M K, Sood P K, Sharma V S. Optimization of machining parameters and cutting fluids during nano-fluid based minimum quantity lubrication turning of titanium alloy by using evolutionary techniques. *J Cleaner Production* **135:** 1276–1288 (2016)

[6] Dureja JS, Singh R, Singh T, Singh P, Dogra M, Bhatti M S.. Performance evaluation of coated carbide tool in machining of stainless steel (AISI 202) under minimum quantity

lubrication (MQL). *Int J Precis Eng Manuf* **2**: 123–129 (2015)

[7] Gupta M K, Sood P K, Sharma V S. Machining parameters optimization of titanium alloy using response surface methodology and particle swarm optimization under minimum quantity lubrication environment. *Mater Manuf Process* **31:** 1671–1682 (2016)

[8] Sharma VS, Singh G, Sorby K. A review on minimum quantity lubrication for machining processes. *Mater Manuf Process* **30**(8): 935–953 (2015)

[9] Shen B, Malshe A P, Kalita P, Shih A J. Performance of novel MOS_2 nano-particles based grinding fluids in minimum quantity lubrication grinding. *Trans NAMRI/SME* **36**: 357–364 (2008)

[10] Ramesh S, Karunamoorthy L, Palanikumar K. Surface roughness analysis in machining of titanium alloy. *Mater Manuf Process* **23**(2): 174–181 (2008)

[11] Ramesh S, Karunamoorthy L, Palanikumar K. Fuzzy Modeling and analysis of machining parameters in machining titanium alloy. *Mater Manuf Process* **23**(4): 439–447 (2008)

[12] Ramesh S, Karunamoorthy L, Senthilkumar V S, Palanikumar K. Experimental study on machining of titanium alloy (Ti64) by CVD and PVD coated carbide inserts. *Int J Manuf Technol Manag* **17**(4): 373–385 (2009)

[13] Sridharan U, Malkin S. Effect of minimum quantity lubrication (MQL) with nano-fluid on grinding behavior and thermal distortion. *Trans NAMRI/SME* **37:** 629–636 (2009)

[14] Kwon P, Drzal L T. Nanoparticle graphite-based minimum quantity lubrication method and composition. U.S. Patent **649**: 12–655, 2010.

[15] Nam J S, Lee P H, Lee S W. Experimental characterization of micro-drilling process using nano-fluid minimum quantity lubrication. *Int J Mach Tool Manuf* **51**(7–8): 649–652 (2011)

[16] Samuel J, Rafiee J, Dhiman P, Yu Z Z, Koratkar N. Graphene colloidal suspensions as high performance semi-synthetic metal-working fluids. *J Phys Chem C* **115**(8): 3410–3415 (2011)

[17] Park K H, Ewald B, Kwon P Y. Effect of nano-enhanced lubricant in minimum quantity lubrication balling milling. *J Tribol* **133**: 031803 (2011)

[18] Vasu V, Reddy P K G. Effect of minimum quantity lubrication with Al_2O_3 nanoparticles on surface roughness, tool wear and temperature dissipation in machining Inconel 600 alloy. *Proc Inst Mech Eng Part N J Nanoeng and Nanosyst* **225**: 3–16 (2011)

[19] Ramesh S, Karunamoorthy L, Palanikumar K. Measurement and analysis of surface roughness in turning of aerospace titanium alloy (gr5). *Measurement* **45:** 1266-1276 (2012)

[20] Khandekar S, Sankar M R, Agnihotri V, Ramkumar J. Nano-cutting fluid for enhancement of metal cutting performance. *Mater Manuf Process* **27**(9): 963–967 (2012)

[21] Kalita P, Malshe A P, Arun Kumar S, Yoganath V G, Gurumurthy T. Study of specific energy and friction coefficient in minimum quantity lubrication grinding using oil-based nanolubricants. *J Mater Process Technol* **14**: 160–166 (2012)

[22] Nguyen T K, Do I, Kwon P. A tribological study of vegetable oil enhanced by nano-platelets and implication in MQL machining. *Int J Prec Eng Manuf* **13(7)**: 1077–1083 (2012)

[23] Amrita M, Srikant R, Sitaramaraju A, Prasad M, Krishna P V. Experimental investigations on influence of mist cooling using nanofluids on machining parameters in turning AISI 1040 steel. *Proc Inst Mech Eng Part J J Eng Tribol* **227:** 1334–1346 (2013)

[24] Paul P S, Varadarajan A S. Performance evaluation of hard turning of AISI 4340 steel with minimal fluid application in the presence of semi-solid lubricants. *Proc Inst Mech Eng Part J J Eng Tribol* **227**: 738–748 (2013)

[25] Srikiran S, Ramji K, Satyanarayana B, Ramana S. Investigation on turning of AISI 1040 steel with the application of nano-crystalline graphite powder as lubricant. *Proc Inst Mech Eng Part C J Mech Eng Sci* **228**: 1570–1580 (2014)

[26] Amrita M, Srikant R R, Sitaramaraju A V. Performance evaluation of nanographite-based cutting fluid in machining process. *Mater Manuf Process* **29**: 600–605 (2014)

[27] Sharma P, Sidhu B S, Sharma J. Investigation of effects of nanofluids on turning of AISI D2 steel using minimum quantity lubrication. *J Cleaner Production* **108**: 72–79 (2015)

[28] Su Y, Gong L, Li B, Liu Z, Chen D. Performance evaluation of nanofluid MQL with vegetable-based oil and ester oil as base fluids in turning. *Int J Adv Manuf Technol* **83**(9): 2083–2089 (2015)

[29] Barzani M M, Sarhan A A D, Farahany S, Ramesh S, Maher I. Investigating the machinability of Al–Si–Cu cast alloy containing bismuth and antimony using coated carbide insert. *Measurement* **62**: 170–178 (2015)

[30] Barzani M M, Zalnezhad E, Sarhan A A D, Farahany S, Ramesh S. Fuzzy logic based model for predicting surface roughness of machined Al–Si–Cu–Fe die casting alloy using different additives-turning. *Measurement* **61**: 150–161 (2015)

[31] Unune DR, Barzani MM, Mohite SS, Mali HS. Fuzzy logic-based model for predicting material removal rate and average surface roughness of machined Nimonic 80A using abrasive-mixed electro-discharge diamond surface grinding. *Neural Computing and Applications,* in press, DOI 10.1007/s00521-016-2581-4 (2016)

[32] Oudjene M, Ben-Ayed L, Delamézière A, Batoz J L. Shape optimization of clinching tools using the response surface methodology with Moving Least-Square approximation. *J Mater Process Technol* **209**: 289–296 (2009)

[33] Hewidy M S, El-Taweel T A, El-Safty M F. Modelling the machining parameters of wire electrical discharge machining of Inconel 601 using RSM. *J Mater Process Technol* **169**: 328–336 (2005)

[34] Montgomery D C. *Design and Analysis of Experiments*. New York: Wiley, 2001.

[35] Gupta M K, Sood P K, Sharma V S. Investigations on surface roughness measurement in minimum quantity lubrication turning of titanium alloys using response surface methodology and Box–Cox transformation. *J Manuf Sci Product* **16:** 75–88 (2016)

Munish Kumar GUPTA. He received his bachelor degree in mechanical engineering in 2008 from I. K. Guzral PTU, Jalandhar. After then, he was M. Tech. student at the same university. He is recently a Ph.D. research scholar in Department of Mechanical Engineering at NIT, Hamirpur. His areas of interest include machining, casting and rapid prototyping.

Friction **5**(2): 171–182 (2017) ISSN 2223-7690
DOI 10.1007/s40544-017-0144-z CN 10-1237/TH

RESEARCH ARTICLE

Tribological response of an epoxy matrix filled with graphite and/or carbon nanotubes

M. M. SAKKA[1,*], **Z. ANTAR**[1], **K. ELLEUCH**[1], **J. F. FELLER**[2]

[1] *Laboratoire de Génie des Matériaux et Environnement, ENIS, Université de Sfax, Sfax BP. 1173-3038, Tunisia*

[2] *Smart Plastics Group, European University of Brittany (UEB), LIMATB-UBS, Lorient 56321, France*

Received: 29 July 2016 / Revised: 19 October 2016 / Accepted: 21 December 2016

Abstract: Reinforced polymer–matrix composites are widely used under sliding contact conditions in various boating and automotive applications. In this paper, the friction and wear of bulk epoxy and carbon filler reinforced epoxy composites have been investigated using a pin-on-disc tribometer. The effect of different fillers on the tribological behavior of an epoxy has been studied using treated and untreated carbon nanotubes, graphite, and a mixture of graphite and carbon nanotubes. Filler addition greatly enhances the tribological properties of the epoxy resin, by reducing the friction coefficient and the wear rate. In addition, it was found that the treated carbon nanotubes/epoxy composites have the best tribological behavior. Moreover, a correlation between contact temperature and friction coefficient is reported. Finally, the wear mechanisms were determined by scanning electronic microscopy.

Keywords: epoxy composites; carbon nanotubes; wear; friction temperature

---

1 Introduction

Polymers play a very important part in mechanical and materials engineering, not just because they are easy to manufacture and their per unit cost is low, but also for their excellent tribological performance in engineered forms [1]. In the bulk or pristine form, only a few polymers would satisfy most of the tribological requirements; however, in their hybrid and composite forms, polymers often have the advantage of low weight and corrosion resistant over other materials such as metals and ceramics [1]. Tribological applications of polymers include gears [2], a range of bearings [3], artificial human joint bearing surfaces [4], bearing materials for space applications [5], tires, shoe soles, automobile brake pads, non-stick frying pans, floorings, and various types of surfaces for optimum tactile properties, such as fibers [6]. Similar to the bulk mechanical responses, tribological characteristics of polymers are greatly influenced by temperature, relative speed of the interacting surfaces [7], the normal load [8], and the environment [9]. Therefore, to deal with these effects and for better control of the responses, polymers are modified by adding appropriate fillers to suit the particular application. Thus, they are invariably used as a composite or in a blended form for optimum friction and wear performance [10].

Over the last decade, epoxy composites have seen increased use as structural materials in boating, automotive, and various other industries due to their lower weight compared to traditional materials like metals and ceramics [11]. Among these applications, many are related to the tribological components, where the self-lubrication properties of epoxy-based composites are very important [12]. The characteristic that makes epoxy composites promising in many applications is the possibility to control their properties by adding special fillers with different volume fractions, shapes, and sizes [13, 14]. The integration of well-dispersed carbon particles into an epoxy

---

[*] Corresponding author: M. M. SAKKA, E-mail: sakkamedmahdi@yahoo.fr

matrix has been demonstrated to be quite effective at improving the performance of epoxy composites, including their tribological properties [15]. It has been found that nano- and micro-sized carbon particles can be used to modify the tribological properties of polymeric materials [16]. Friedrich and Schlarb have demonstrated that these fillers could considerably improve the wear and friction properties of both coatings and bulk materials by strengthening the matrix (high load-carrying capacity), improving the sub-surface crack arresting ability (better toughness), and improving the lubricating effect at the interface by decreasing shear stress [6]. Among all fillers, graphite is widely used as an efficient solid lubricant to enhance the tribological properties of polymer composites due to the weak Van der Waals bonds between the graphite layer structures. In fact, under sliding conditions, the shear force can easily break the graphite structure. Graphite flakes are symmetrically distributed on the sliding surface, which reduces the direct contact between the composites and steel counterparts [17]. Zhang et al. [18] confirmed that the wear rate and the friction coefficient of polyphtalazinone ether sulfone ketone (PPESK) composites decreased with the increase of the graphite volume fraction. Chang et al. [19] found that the specific wear rate of polyetherimide (PEI) filled with graphite was 800 times lower than that of a neat matrix under standard testing conditions.

Shalwan et al. studied the influence of date palm fiber and graphite filler on mechanical and wear characteristics of epoxy composites. They concluded that the addition of graphite allows the enhancement of wear resistance over the natural fiber/polymer composites. However, the authors also found that a high graphite ratio deteriorates the mechanical properties [20].

Apart from graphite, other fillers can be used to enhance the tribological properties, especially nanoscale fillers. It has been found that particle size has great influence on the tribological performance of polymer composites [21]. When the particle size is reduced down to the nanoscale, the friction and wear behavior of filled polymers is greatly affected at very low nanoparticle content as compared to the effect of low micro-filler content on friction and wear behavior of the filled polymers [22]. But the influence on friction and wear behavior of nanoparticles in polymer matrices depends on many factors such as the type of polymer, type of nanoparticle, filler content, size, shape, and operating conditions [6].

Multiwalled carbon nanotubes (MWCNTs) are a class of nanomaterials that have a diameter of a few dozens of nm and a length of some mm. Thanks to this high-aspect ratio, carbon nanotubes (CNTs) can provide special mechanical properties, which are experimentally demonstrated by different researchers [23–26]. Several research efforts on the effect of CNTs on the tribological properties of polymers have been published. Gong et al. compared the tribological properties of carbon fiber composites with CNT composites. They proved that composites with CNTs as reinforcing elements exhibit more stable frictional coefficients and lower wear rates, especially at high temperatures due to their perfect graphite layered structure [27]. Chen et al. report that CNTs can clearly decrease the friction coefficient and the wear rate of copper and polytetrafluoroethylene (PTFE) based composites [28, 29]. Lim et al. [30] studied carbon/carbon composites coated with CNT reinforced carbon, and they found that the wear rate decreased with increasing CNT volume fraction. In the case of PTFE based composites, the friction coefficient decreased continuously with increasing CNT content up to 30 vol%. Zoo et al. studied the effect of MWCNT addition on the tribological behavior of ultra high molecular weight polyethylene (UHMWPE) [31]. In contrast to the previous findings for PTFE, they found that the friction coefficient increases continuously when CNTs are added up to 0.5 wt%. These results were explained by the poor dispersion of MWCNTs in the composite, which has a direct impact on the composite tribological and mechanical properties.

To solve this dispersion problem, many solutions [32–34] have been suggested, like the addition of dispersing agents [35], shear mixing [36], and functionalization [37]. The last solution is one of the most efficient methods, which improves compatibility between CNTs and the polymer matrix. For example, by adding 0.1 to 1 wt% MWCNTs grafted with epoxy, Jia et al. [38] observed a 45% increase in tensile strength and 90% improvement in tensile modulus. Sun et al. [39] successfully grafted PAMAM-0 on thesurfaces of the single walled carbon nanotubes(SWCNTs), which induced an enhanced dispersion and adhesion state of CNTs in epoxy resin.

Cha et al. have tried to improve the dispersion of carbon nanotubes (CNTs) in epoxy matrix composites by attaching polystyrene sulfonate (PSS) and poly(4-aminostyrene) (PAS) on the surface of CNTs by noncovalent functionalization; they found that this incorporation of noncovalently functionalized CNTs into the modified bisphenol-A type epoxy matrix yielded a Young's modulus of 3.89 GPa and a tensile strength of 82.59 MPa, with the addition of 1 wt.% PAS-CNTs. These results were explained by the better dispersion of CNTs in the matrix and the chemical bonding generated between the amino groups and the epoxide groups in the epoxy matrix [40].

The fundamental and detailed understanding of the influence of nanoparticles on tribological properties of filled polymers remains an open field for further research. Several studies have been conducted on the tribological properties of carbon/epoxy composites, but few have focused on the correlation between the friction coefficient and generated heat. Unfortunately, few authors have given much attention to the synergetic effect of two incorporated fillers on epoxy matrix. In the present study, graphite and/or CNTs were incorporated into an epoxy matrix. The purpose of our work is to investigate the synergistic effect of the two fillers on the tribological behavior of epoxy-carbon filler composites. Scanning electron microscopy (SEM) observations were used to determine the wear mechanisms of the implemented composite. Finally, special importance is attributed to thermal phenomena related to the coefficient of friction.

2 Experimental details

2.1 Materials

The epoxy resin used in this study, Epolam 2020, was purchased from Axon Technologies. It was designed for the production of composite structures by the usual wet lay-up methods, vacuum infusion, low-pressure injection, or filament winding. Carbon nanotubes master batches, 3150 and 3152, were provided by NANOCYL (Belgium). The main difference between the two grades is the use of functionalized CNTs for the 3152 grade, where NH_2 groups are grafted to CNTs via a NANOCYL patented process. CNTs are produced via the catalytic carbon vapor deposition (CCVD) process. The average diameter of the CNTs was 9.5 nm, and the average length was about 1 μm. Graphite TIMREX BNB 90 was provided by TIMCAL (Switzerland). Expanded graphite foil size varied between 10 μm and 85 μm.

2.2 Sample preparation

Five different types of samples were prepared as mentioned in Table 1. In each of the non-neat samples, a 1.5% weight fraction of either CNTs, NH_2-CNTs (TCNTs), graphite or CNTs/graphite were introduced. The ratio used for the mixture of CNT and graphite was 1/3 to 2/3, respectively. A reference sample was prepared from neat epoxy. Samples were prepared by mixing the epoxy resin with 34 wt%. of hardener. Subsequently, the mixture was flowed into a mold of 2 mm thickness.

The reticulation process was conducted by drying the mixture for 24 hours at room temperature. The post curing cycle (Fig. 1), uses a temperature ramp of 20 °C/h. The epoxy was held at 40 °C for 3 hours,

Table 1 Designation and composition of the different prepared samples.

Specimens	Composition
Ep	Neat epoxy
Ep-Gr	Epoxy + 1.5 wt% graphite
Ep-CNTs	Epoxy + 1.5 wt% CNTs
Ep-TCNTs	Epoxy + 1.5 wt% TCNTs
Ep-HYB	Epoxy + 1.5 wt% (1/3 CNTs + 2/3 graphite)

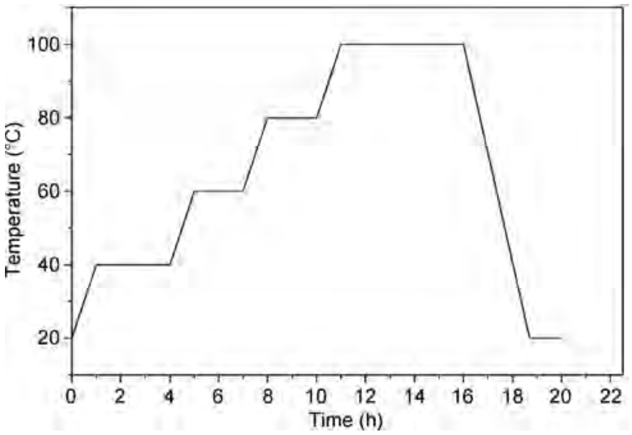

Fig. 1 Postcuring cycle of epoxy samples.

at 60 °C for 2 hours, at 80 °C for 2 hours, and then at 100 °C for 5 hours. The cooling rate was 30 °C/hour. The obtained plates were cut by milling to get square samples of 20 mm on a side. All samples were polished using abrasive papers (from 400 to 1000 grades) and diamond paste.

2.3 Friction and wear test

Friction and wear tests were conducted using a rotating pin-on-disc tribometer under dry sliding conditions. This tribometer is shown in Fig. 2. The friction test was performed using a 6 mm diameter 100Cr6 ball bearing, and the radius of the wear track is 5 mm. The different values of normal load and velocity are illustrated in the legend of Fig. 3. The steel ball was kept stationary and a continuous rotating motion was applied to the composite specimen. The maximum contact pressure, calculated with Hertz theory, was 130 MPa. Tests were performed at 25 °C and a relative humidity of 60%. The sliding test duration was about 64 min. At least three tests were performed for each set of conditions. The average contact temperature was measured during the test using a thermocouple connected to the steel ball that was 2 mm from the contact point and located at the edge of the ball. Weight loss values were determined by using a balance of 10^{-4} g of precision.

The wear rate was calculated by measuring weight loss of each sample Δm after wear testing, divided by the applied load F_n and the sliding distance S. The corresponding density was given by ρ. The cumulative wear rate W_r can be determined by the following equation:

$$W_r = \frac{\Delta m}{F_n \cdot \rho \cdot S}$$

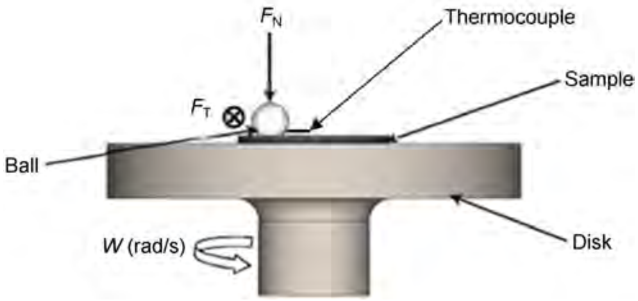

Fig. 2 Pin-on-disc tribometer.

The main variables that affect wear are sliding velocity and normal load. In addition, the materials' structure, properties, and the environmental conditions affect the wear rate.

2.4 Scanning electron microscopy

After the wear test, wear tracks were observed (after metal coating) with a JEOLJSM-6031F scanning electronic microscope, using a conventional tungsten cathode at 12 kV accelerating voltage in secondary electron image mode.

3 Results and discussion

3.1 Friction coefficient

The friction coefficients of the prepared samples are presented as a function of time in Fig. 3. We notice that, at first, the friction coefficients can be significantly less when fillers are incorporated into the epoxy matrix. The highest friction coefficient value of 0.65, and the lowest, of 0.1, were obtained with neat epoxy and treated carbon nanotube filled composites, respectively.

Moreover, we could easily distinguish the existence of two different types of response curves; it is clear that Ep and Ep-TCNT samples behave differently from other samples. In the case of the Ep-TCNT composite, treated carbon nanotubes are well dispersed on the epoxy due to the presence of NH_2 groups. As a result, generated debris, which are probably rich in NH_2-CNT, will change the friction contact properties by the creation of a low-friction tribo-layer. The transfer film, obtained during sliding, could act as a lubricant, which would lead to a significant decrease of the friction coefficient [41].

In the case of the Ep samples brought into contact with the 100Cr6 steel ball, we assume that a transfer film was formed on the ball and stuck to it, via tribo-chemical interactions with the counter body material [42]. When this layer is present on both contacting surfaces, the composition of the sample and the sliding counter body becomes similar and then the coefficient of friction becomes stable [43].

For the second type of curves (Ep-CNT, Ep-Gr, and Ep-HYB in Fig. 3), three stages can be observed. The first stage, which corresponds to a run-in-period, is characterized by a stable friction coefficient of 0.1, 0.1,

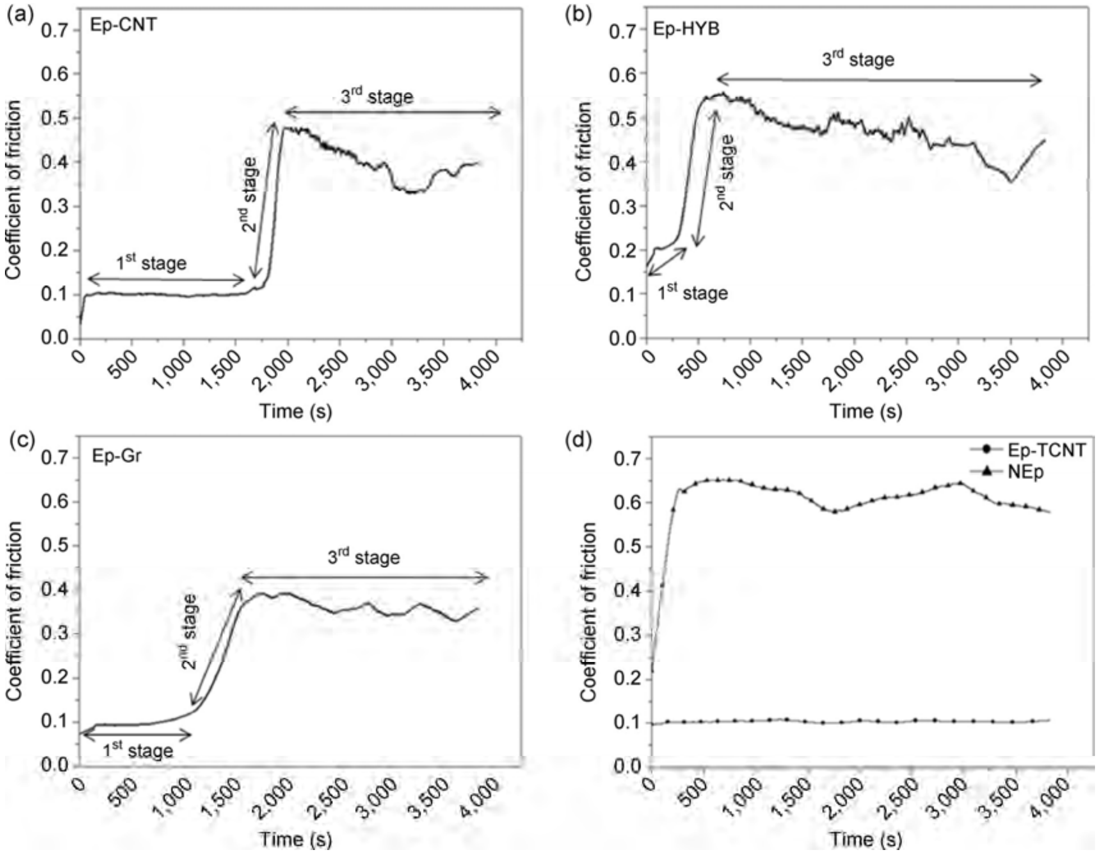

Fig. 3 Coefficient of friction evolution for the different types of samples at 400 rpm and F_n = 4 N.

and 0.2 for the Ep-CNT, Ep-Gr, and Ep-HYB, respectively. The duration of this stage is about 1,750 s, 1,200 s, and 250 s for each of those. Consequently, it can be concluded that CNTs have the best adhesion to the epoxy matrix, since it takes more time for them to be extracted. In fact, CNTs have higher specific surfaces than graphite, which explains their better adhesion to epoxy. The second stage was characterized by a significant increase of friction coefficient from 0.1 to 0.47, 0.1 to 0.4, and 0.2 to 0.55 for Ep-CNT, Ep-GR, and Ep-HYB, respectively. The increase of friction coefficients could be explained as follows. Firstly, debris was created, which then accumulated on the sliding track, and finally adhered to the steel ball. At this moment, the contact was no longer between 100Cr6 and the sample but, instead, switched to sample-sample contact. In the third stage, the sliding rotating motion intermittently ejects a fraction of the created debris out of the wear track circumference, which explains the fluctuations of the friction coefficient curves.

3.2 Correlation between friction coefficients and temperature

A strong correlation between friction coefficient and temperature is observed in the samples (Fig. 4). Specifically, the temperature considerably increases when debris are initially created (stage II) at the interface. The wear track roughness increases and local heating begins. In fact, on the microscopic scale, the flash temperature occurs at the contact asperities over a very short duration, lower than a millisecond. These local, but microscopic, flash temperature fluctuations are, actually, hundreds of times higher than the average contact temperature [44]. The accumulation of these flash temperature events could be responsible for the rise of the average temperature measured by the thermocouple. It is also observed that a higher velocity of rotation leads to a higher temperature (Fig. 5). This result is explained by the increase of sliding distance, which creates more heat.

Figure 5 shows the presence of brown zones, which

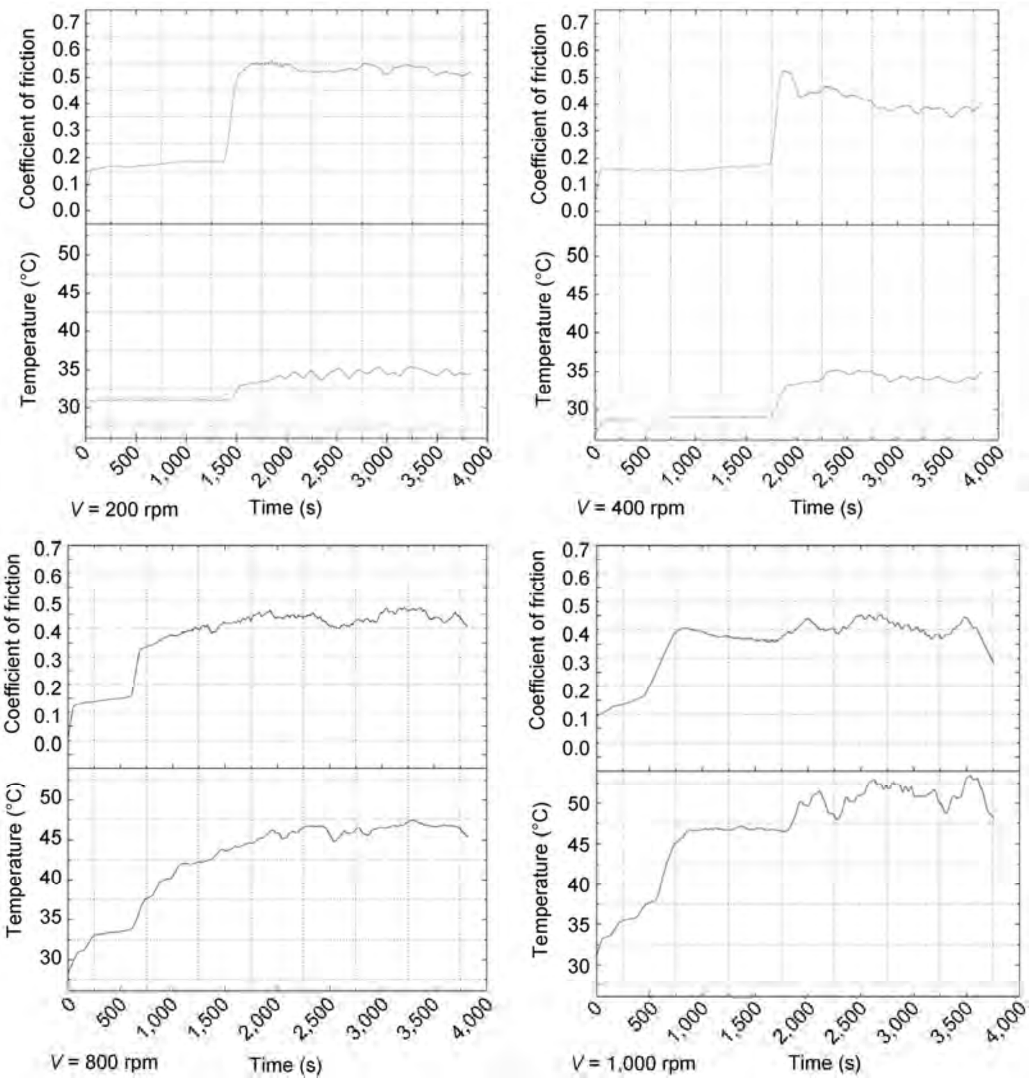

Fig. 4 Correlation between the coefficient of friction and temperature for the Ep-CNT samples at F_n = 8 N and different velocities.

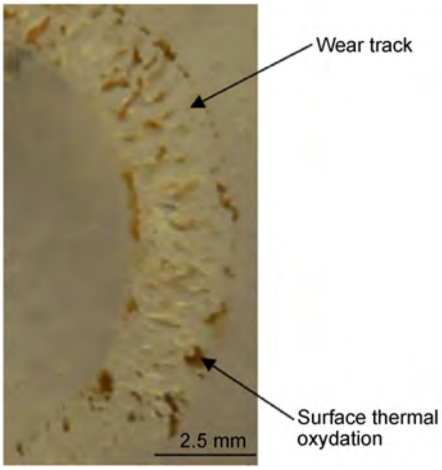

Fig. 5 Surface color modification after dry sliding test of Ep sample at F_n = 8 N and V = 1,000 rpm.

are a thermal modification of the wear track surface. In fact, the color of the tested surface shifts from yellowish to brown after the sliding test. Similar results were also reported by Hancox [45] and Greer et al [46], and they explain the color change by a chemical modification of the resin surface. More precisely, it was thought that color change is essentially the result of thermal oxidation caused by the flash temperature [47].

3.3 Wear loss and wear mechanism

Figure 6 shows the effect of the incorporation of TCNTs, CNTs, GR, and HYB fillers on the wear rate of the epoxy resin. It is clearly shown that filler

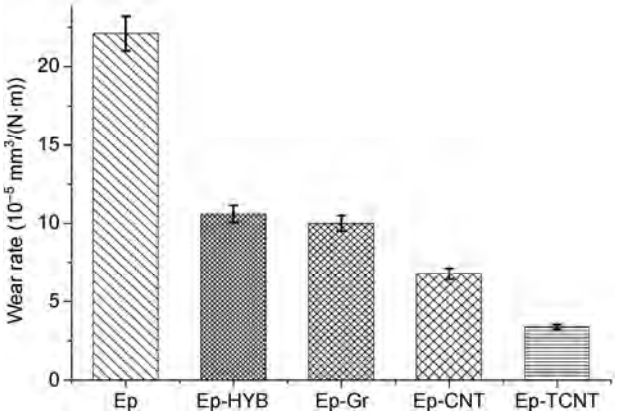

Fig. 6 Wear rate of different types of samples.

addition, to the neat epoxy, can decrease significantly the wear rate. It was found that the least wear rate was obtained when 1.5 wt% TCNTs was added to the epoxy matrix; in fact, the wear rate of Ep decreases from 22.1×10^{-5} mm^3·N^{-1}·m^{-1} to 3.37×10^{-5} mm^3·N^{-1}·m^{-1}. Moreover, similar behavior was observed for the other composites. Samples could be classified according to their wear rate, from the highest to the lowest, as follow: Ep, Ep-HYB, Ep-GR, Ep-CNTs, and Ep-TCNTs. These results may be explained by the difference of adhesion quality between fillers and the epoxy matrix [48, 49]. CNTs have a better adhesion due to their high aspect ratio. However, graphite pieces are easily extracted as they have a layered planar structure [50, 51]. The functionalization of CNTs with amine groups enhances the interaction between CNTs and the epoxy matrix [52], which improves the mechanical properties and the wear resistance of the obtained composite.

The SEM images of the worn surfaces, presented in Fig. 7, give some information about the wear mechanism. The lack of grooves on the wear track indicates that an abrasive mechanism does not contribute to the wear for all composites. The worn surfaces (Figs. 7(a)–7(d)) are rough and present delamination marks suggesting an adhesive wear mechanism. This result is due to the poor wear resistance of the Ep [53] and the poor adhesion of fillers to the epoxy matrix. Moreover, it seems that wear debris are crushed and spread on the wear track surface.

Figure 8 shows a thin film adherent to the steel ball after testing. Thus, wear progress of the composite can be described by three different stages [54]. First, adhesive processes cause the resin transfer to the ball surface and a progressive rise of the real contact surface. At the same time, in the sub-surface of the epoxy resin, progressive damage is taking place that is caused by the propagation of sub-surface cracks. When these cracks emerge on the surface, the final phase occurs, which is characterized by mechanical and thermal fatigue wear [54].

However, Ep-TCNTs composites have a different behavior, as they were characterized by a smooth worn surface and the absence of delamination marks (Fig. 7(e)). It can be concluded that the adhesion on the worn surface of Ep-TCNT composites is reduced. Thus, it seems that the improved adhesion of CNTs can considerably decrease the adhesion mechanism. As a result, the Ep-TCNTs composites show better wear resistance than the neat epoxy.

According to Chen et al. [54–56] and Cai et al. [57], wear of Ep-TCNT nano-composites, in dry sliding against a carbon steel ball, may be controlled by two factors. The incorporation of CNTs in Ep helps to ameliorate the mechanical properties of the nano-composites (Table 2), which leads to an enhancement of the wear resistance [50].

Moreover, the well dispersed TCNTs (Fig. 9) are removed from the nano-composites and transferred to the interface between the nano-composites and the steel ball. Hence, CNTs may play the role of spacers preventing close contact between the steel ball and the nano-composites. In fact, CNTs will be shortened first and then flatten to form a graphene-like lamella, which decreases the wear loss and causes the decrease of the friction coefficient [51] (Fig. 10).

4 Conclusions

The study of the effects of carbon fillers on the tribological behavior of an Epolam 2020 epoxy resin sliding against a 100Cr6 steel ball revealed some interesting points in relation to the wear and friction of this material.

- Two tribological behaviors are observed: the first is characterized by a constant friction coefficient (Ep and Ep-TCNTs) and the second by the detection of three friction stages.

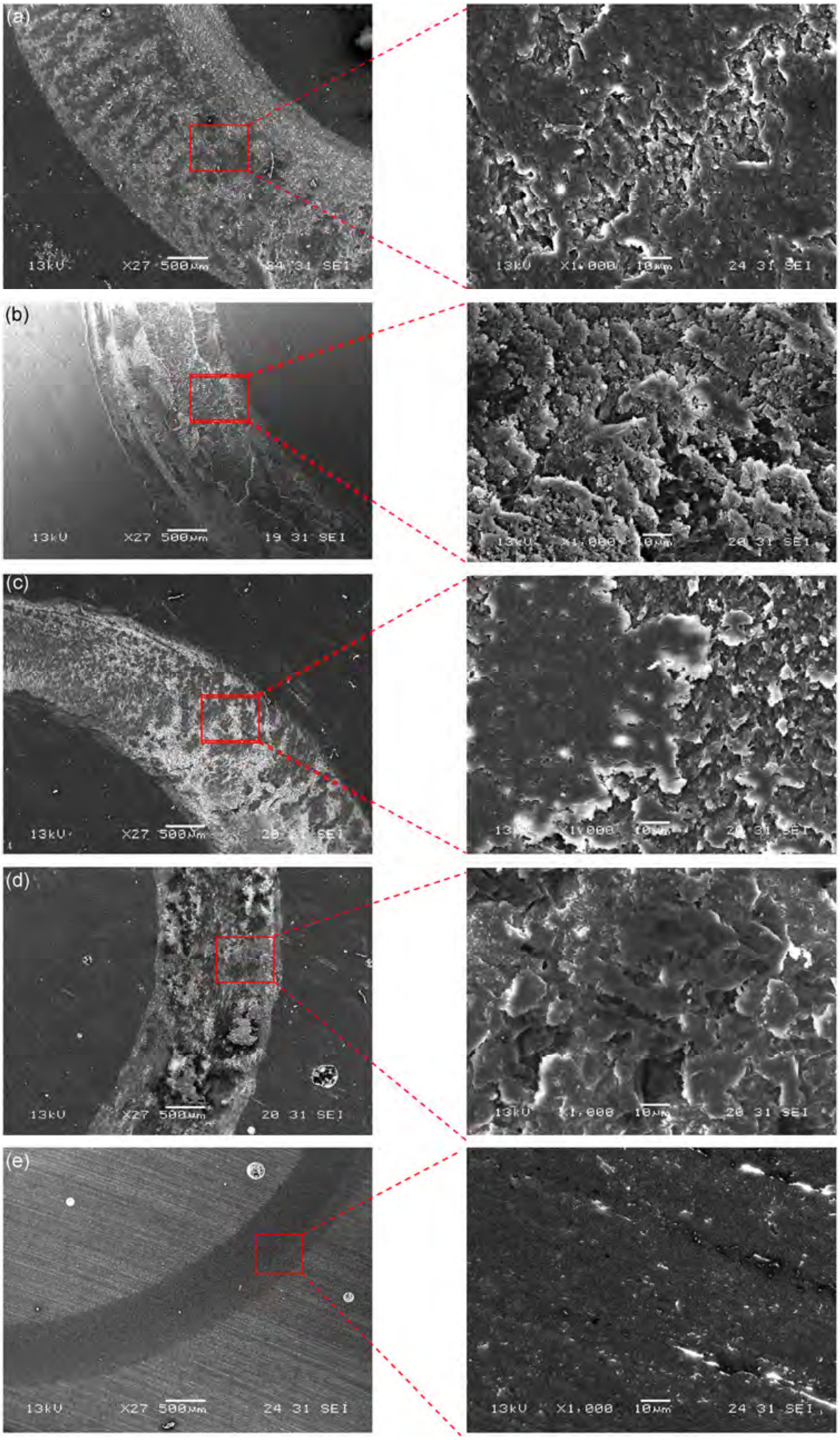

Fig. 7 SEM observation of worn surfaces for the different types of samples: (a) Ep, (b) Ep-Gr, (c) Ep-CNT, (d) Ep-HYB, and (e) Ep-TCNT.

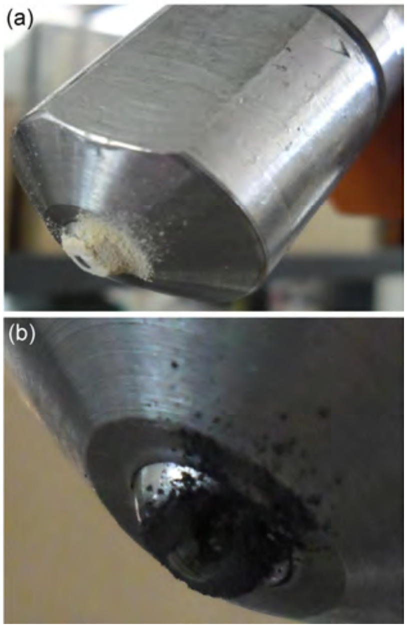

Fig. 8 Transfer film adherent to the steel ball: (a) Ep and (b) Ep-Gr.

Table 2 Young's modulus of the different tested specimens.

Specimens	Young modulus (GPa)
Ep	2.6
Ep-Gr	2.9
Ep-CNTs	3.3
Ep-TCNTs	3.8
Ep-HYB	2.7

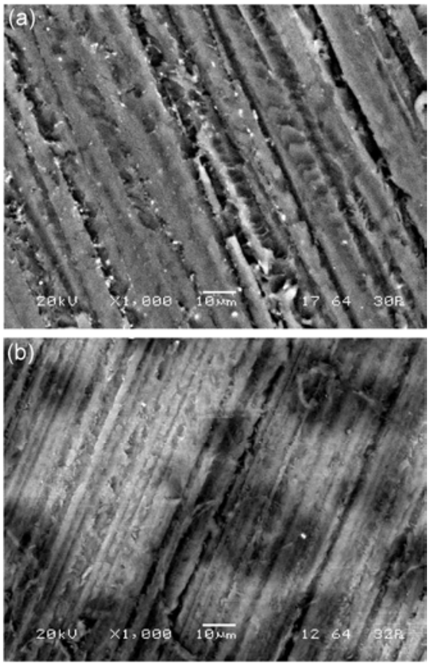

Fig. 9 SEM images showing the dispersion of (a) TCNT and (b) CNT in an epoxy matrix.

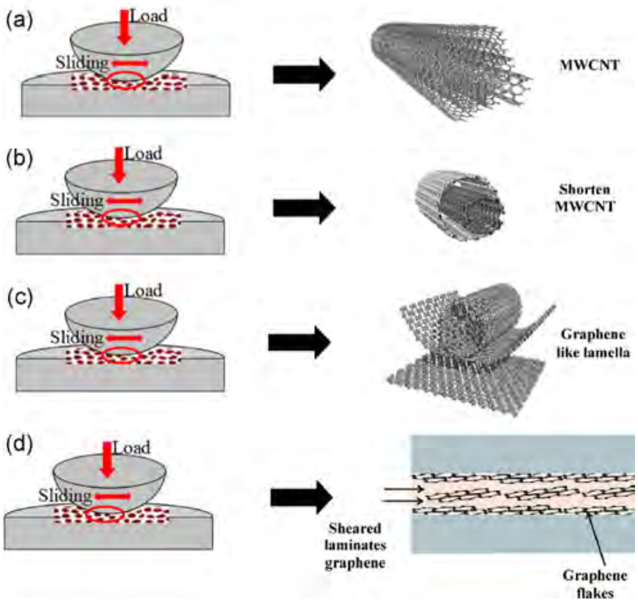

Fig. 10 Schematic diagram showing the effect of carbon additives on the wear resistance of epoxy matrix: (a) stage 1, (b) stage 2, (c) stage 3, and (d) stage 4.

- Wear resistance is enhanced by the incorporation of carbon fillers in the epoxy matrix. The best result is obtained with TCNTs, which are well dispersed in the epoxy matrix due to the presence of the NH_2 groups.
- A correlation between friction coefficient and the measured average contact temperature is found. The rise of this temperature could be explained by the accumulation of flash temperature events, which are higher than the average contact temperature.
- The predominant wear mechanism is adhesive wear, which leads to both crack emergence on the surface and delamination. This mechanism is encountered in all composites, except Ep-TCNT composites.
- Despite the enhanced wear resistance of both Ep-CNTs and Ep-Gr, Ep-HYB has the inferior tribological properties of the three. Consequently, there is no synergetic effect between graphite and CNTs.

Acknowledgements

This work was supported by the national school of engineers of Sfax, Tunisia represented by the Laboratory of material engineering and environment (LGME) and the University of South Brittany, Lorient, France, and represented by the laboratory of material engineering of Brittany (LimatB), smart plastic group.

References

[1] Briscoe B J, Sinha S K. Tribology of polymeric solids and their composites. In *Wear—Materials, Mechanism and Practice*, **2005**: 223–267.

[2] Yousef S. Polymer nanocomposite components: A case study on gears. In *Light Weight Composite Structures in Transport Design, Manufacturing, Analysis and Performance*. 2016: 385–420.

[3] Koike H, Kida K, Santos E C, Rozwadowska J, Kashima Y, Kanemasu K. Self-lubrication of PEEK polymer bearings in rolling contact fatigue under radial loads. *Tribol Int* **49**: 30–38 (2012)

[4] Juvonen T, Selenius M. Joint bearing surfaces and replacement joint design. In *Joint Replacement Technology (Second Edition)*. Finland, 2014: 167–185.

[5] Joshi M, Chatterjee U. Polymer nano-composite: An advanced material for aerospace applications. In *Advanced Composite Materials for Aerospace Engineering, Processing, Properties and Applications*. New Delhi, 2016: 241–264.

[6] Friedrich K, Schlarb A. Tribology of polymeric nano-composites. In *Tribology and Interface Engineering Series, No. 55*. Series Editor. Briscoe B J, 2008.

[7] Cho D-H, Bhushan B. Friction and wear of various polymer pairs used for label and wiper in labeling machine. *Tribol Int* **98**: 10–19 (2016)

[8] Larsen J, Hinge M. Temperature- and time dependency on high friction poly(styrene-co-butyl methacrylate) coated paper Christoffer Bjerremand. *Tribol Int* **103**: 261–265 (2016)

[9] Laux K A, Jean-Fulcrand A, Sue H J, Bremner T, Wong J S S. The influence of surface properties on sliding contact temperature and friction for polyetheretherketone (PEEK). *Polymeric Materials and Characterization Methods for Water Purification* **103**: 397–404 (2016)

[10] Friedrich K, Pei X Q. Friction and wear of polymer composites. *Reference Module in Materials Science and Materials Engineering* (2016)

[11] Jin F-L, Li X. Synthesis and application of epoxy resins: A review. *J Ind Eng Chem* **29**(25): 1–11 (2015)

[12] Kumar V, Sinha S K, Agarwal A K. Tribological studies of epoxy composites with solid and liquid fillers. *Tribol Int* **105**: 27–36 (2017)

[13] Katiyar J K, Sinha S K, Kumar A. Friction and wear durability study of epoxy-based polymer (SU-8) composite coatings with talc and graphite as fillers. *Wear* **362–363**: 199–208 (2016)

[14] Zhang L, Zhang G, Chang L, Wetzel B, Jim B, Wang Q. Distinct tribological mechanisms of silica nano-particles in epoxy composites reinforced with carbon nanotubes, *Tribol Int* **104**: 225–236 (2016)

[15] Zhang G, Sebastian R, Burkhart T, Friedrich K. Role of monodispersed nanoparticles on the tribological behavior of conventional epoxy composites filled with carbon fibers and graphite lubricants. *Wear* **292–293**: 176–187 (2012)

[16] Zhang M Q, Rong M Z, Yu S L, Wetzel B, Friedrich K. Effect of particle surface treatment on the tribological performance of epoxy based nano-composites. *Wear* **253**: 1086–1093 (2002)

[17] Suresha B, Chandramohan G, Renukappa M N, Siddaramaiah. Mechanical and tribological properties of glass–epoxy composites with and without graphite. *J Appl Polym Sci* **103**: 2472–2480 (2007)

[18] Zhang X, Liao G, Jin Q, Feng X, Jian X. On dry sliding friction and wear behavior of PPESK filled with PTFE and graphite. *Tribol Int* **41**: 195–201 (2008)

[19] Chang L, Zhang Z, Zhang H, Friedrich K. Effect of nanoparticles on the tribological behavior of short carbon fibre reinforced poly(etherimide) composites. *Tribol Int* **38**: 966–973 (2005)

[20] Shalwan A, Yousif B F. Influence of date palm fibre and graphite filler on mechanical and wear characteristics of epoxy composites. *Materials and Design* **59**: 264–273 (2014)

[21] Lin J-C. Compression and wear behavior of composites filled with various nano-particles. *Composites. Part B—Engineering* **38**: 79–85 (2007)

[22] Chauhan S R, Thakur S. Effects of particle size, particle loading and sliding distance on the friction and wear properties of chemosphere particulate filled vinyl ester composites. *Materials & Design* **51**: 398–408 (2013)

[23] Meyyappan M. *Carbon Nanotubes: Science and Applications.* Taylor & francis Group, CRC Press, 2005.

[24] Ruoff R S, Lorents D C. Mechanical and thermal properties of carbon nanotubes. *Carbon* **33**: 925–930 (1995)

[25] Gojny F H, Schulte K. Functionalisation effect on the thermo-maechanical behiviour of multi-wall carbon nanotube/epoxy

composite. *Composite Science Technology* **64**: 2303–2308 (2004)

[26] Allaoui A, Bai S, Cheng H M, Cheng J B. Mechanical and electrical properties of a MWNT/epoxy composite. *Composite Science Technology* **62**: 1993–1998 (2002)

[27] Gong Q, Li D, Li Z, Yi X, Liang J. Chapter 10 – Tribological properties of carbon nanotube-reinforced composites. In *Tribology of Polymeric Nanocomposites (Second Edition), Friction and Wear of Bulk Materials and Coatings*, **2013**: 353–386.

[28] Chen W X, Li F, Han G, Xia J B, Wang L Y, Tu J P, Xu Z D. Tribological behavior of carbon-nanotube-filled PTFE composites. *Tribol Lett* **15**: 275–278 (2003)

[29] Chen W X, Tu J P, Wang L Y, Gan H Y, Xu Z D, Zhang X B. Tribological application of carbon nanotubes in a metal-based composite coating and composites. *Carbon* **41**: 215–222 (2003)

[30] Lim D-S, An J-W, Lee H J. Effect of carbon nanotube addition on the tribological behavior of carbon/carbon composites. *Wear* **252**: 512–517 (2002)

[31] Zoo Y-S, An J-W, Lim D-P, Lim D-S. Effect of carbon nanotube addition on tribological behavior of UHMWPE. *Tribol Lett* **16**: 305–309 (2004)

[32] Khare B N, Wilhite P, Quinn R C, Chen B, Schingler R H, Tran B, Imanaka H, So C R, Bauschlicher W, Meyyappan M. Functionalization of carbon nanotubes by ammonia glow-discharge: Experiments and modeling. *J Phys Chem* **108**: 8166–8172 (2004)

[33] Felten A, Bittencourt C, Pireaux J J, Lier G V, Charlier J C. Radio-frequency plasma functionalization of carbon nanotubes surface O_2, NH_3, and CF_4 treatments. *J Appl Phys* **98**: 074308 (2005)

[34] Rodríguez M A, Gil L, Camero S, Fréty N, Santana Y, Caro J. Effects of the dispersion time on the microstructure and wear resistance of WC/Co-CNTs HVOF sprayed coatings. *Surface Coat Technol* **258**: 38–48 (2014)

[35] Kim M T, Rhee K Y, Lee J H, Hui D, Lau A K T. Property enhancement of a carbon fiber/epoxy composite by using carbon nanotubes. *Composites: Part B* **42**: 1257–1261 (2011)

[36] Jacobs O, Xu W, Schadel B, Wu W. Wear behaviour of carbon nanotube reinforced epoxy resin composites. *Tribol Lett* **23**: 65–75 (2006)

[37] Yang K, Gu M, Guo Y, Pan X, Mu G. Effects of carbon nanotube functionalization on the mechanical and thermal properties of epoxy composites. *Carbon* **47**: 1723–1737 (2009)

[38] Jia J, Chen J, Zhou H, Hu L, Chen L. Comparative investigation on the wear and transfer behaviors of carbon fiber reinforced polymer composites under dry sliding and water lubrication. *Compos Sci Technol* **65**: 1139–1147 (2005)

[39] Sun L, Warren G L, O'Reilly J Y, Everett W N, Lee S M, Davis D, Lagoudas D, Sue H-J. Mechanical properties of surface-functionalized SWCNT/epoxy composites. *Carbon* **46**: 320–328 (2008)

[40] Cha J, Jin S, Shim J H, Park C S, Ryu H J. Functionalization of carbon nanotubes for fabrication of CNT/epoxy nano-composites. *Materials & Design* **95**: 1–8 (2016)

[41] Lu X, Wong K C, Wong P C, Mitchell K A R, Cotter J, Eadie D T. Surface characterization of polytetrafluoroethylene (PTFE) transfer films during rolling-sliding tribology tests using X-ray photoelectron spectroscopy. *Wear* **261**(10): 1155–1162 (2006)

[42] Suresha B, Siddaramaiah, Kishore, Seetharamu S, Kumaran PS. Investigations on the influence of graphite filler on dry sliding wear and abrasive wear behavior of carbon fabric reinforced epoxy composites. *Wear* **14**: 1405–1414 (2009)

[43] Davim J P, Cardoso R. Effect of the reinforcement (carbon or glass fibers) on friction and wear behaviour of the PEEK against steel surface at long dry sliding. *Wear* **266**: 795–799 (2009)

[44] Zaidi H, Frene J. Tempertaure de l'interface des contacts glissant à sec. In *19ème congrès français de mécanique*, Marseille, france, 2009.

[45] Hancox N L. Thermal effects on polymer matrix composites: Part 2. Thermal degradation. *Materials & Design* **19**: 93–97 (1998)

[46] Rose N, le Bras M, Bourbigot S, Delobel R. Thermal oxidative degradation of epoxy resins: evaluation of their heat resistance using invariant kinetic parameters. *Polymer Degradation and Stability* **45**: 387–397 (1994)

[47] Buch X, Shanahan M E R. Thermal and thermo-oxidative ageing of an epoxy adhesive. *Polymer Degradation and Stability* **68**: 403–411 (2000)

[48] Suresha B, Ramesh B N, Subbaya K M, Ravi Kumar B N, Chand Ramohan G. Influence of graphite filler on two-body abrasive wear behaviour of carbon fabric reinforced epoxy composites. *Materials and Design* **31**: 1833–1841 (2010)

[49] Gantayat S, Prusty G, Rout D R, Swain S K. Expanded graphite as a filler for epoxy matrix composites to improve their thermal. *Mechanical and Electrical Properties* **30**: 432–437 (2015)

[50] Dong B, Yang Z, Huang Y, Li H-L. Study on tribological properties of multi-walled carbon nanotubes/epoxy resin nano-composites. *Tribol Lett* **20**(3–4): 251–254 (2005)

[51] Jacobs O, Xu W, Scha del B, Wu W. Wear behaviour of carbon nanotube reinforced epoxy resin composites. *Tribol Lett* **23**: 65–75 (2006)

[52] Luo Y, Zhao Y, Cai J, Duan Y, Du S. Effect of amino-functionalization on the interfacial adhesion of multi-walled carbon nanotubes/epoxy nano-composites. *Materials & Design* **33**: 405–412 (2012)

[53] Dong B, Yang Z, Huang Y, Li H-L. Study on tribological properties of multi-walled carbon nanotubes/epoxy resin nano composites. *Tribol Lett* **20**: 251–254 (2005)

[54] Chen W X, Tu J P, Wang L Y, Gan H Y, Xu Z D, Zhang X B. Tribological application of carbon nanotubes in a metal-based composite coating and composites. *Carbon* **41**: 215–222 (2003)

[55] Chen W X, Li F, Han G, Xia J B, Wang L Y, Tu J P, Xu Z D. Tribological behavior of carbon nanotube-filled PTFE composites. *Tribol Lett* **15**: 275–278 (2003)

[56] Chen W X, Tu J P, Xu Z D, Chen W L, Zhang X B, Cheng D H. Tribological properties of Ni–P-multi-walled carbon nanotubes electroless composite coating. *Mater Lett* **57**: 1256–1260 (2003)

[57] Cai H, Yuan F Y, Xue Q J. Investigation of tribological properties of polyimide/carbon nanotube nano-composites**.** *Mater Sci Eng* **364**: 94–100 (2004)

M. M. SAKKA. He received his engineer degree in materials engineering in 2010 from école nationale d’ingénieurs de Sfax, ENIS, Sfax University, Tunisia. In 2012, he had his master degree in materials and surfaces conducted in both University of Sfax, Tunisia and University of South Brittany, UBS, France.

His current position is a Ph.D student in the laboratory of material engineering and environment, LGME in ENIS, Sfax, Tunisia. He had been a PhD visitor student between 2013 and 2016, in the frame work of the Marie-Curie research staff exchange scheme in Departement Materiaalkunde, MTM, KU Leuven, Belgium.

His research interests include polymers composite coating, thermal aspect of the contact, wear and friction of polymers.

Friction **5**(2): 183–193 (2017)
DOI 10.1007/s40544-017-0145-y

ISSN 2223-7690
CN 10-1237/TH

RESEARCH ARTICLE

Experimental investigation and prediction of wear behavior of cotton fiber polyester composites

Hiral H. PARIKH[1,*], **Piyush P. GOHIL**[2]

[1] *Department of Mechanical Engineering, School of Science and Engineering, Navrachana University, Vadodara 391410, India*

[2] *Department of Mechanical Engineering, Faculty of Technology & Engineering, the MS University of Baroda, Kalabhavan, Vadodara 390001, India*

Received: 20 June 2016 / Revised: 27 October 2016 / Accepted: 11 January 2017

Abstract: The cotton fiber reinforced polyester composites were fabricated with varying amount of graphite fillers (0, 3, 5 wt.%) with a hand lay-up technique. Wear tests were planned by using a response surface (Box Behnken method) design of experiments and conducted on a pin-on-disc machine (POD) test setup. The effect of the weight percentage of graphite content on the dry sliding wear behavior of cotton fiber polyester composite (CFPC) was examined by considering the effect of operating parameters like load, speed, and sliding distance. The wear test results showed the inclusion of 5 wt.% of graphite as fillers in CFPC increase wear resistance compared to 3 wt.% of graphite fillers. The graphite fillers were recommended for CFPC to increase the wear resistance of the material. A scanning electron microscope (SEM) was used to study the wear mechanism. To predict the wear behavior of the composite material, comparisons were made between the general regression technique and an artificial neural network (ANN). The conformation test results revealed the predicted wear with the ANN was acceptable when compared with the actual experimental results and the regression mathematical models.

Keywords: wear; composites; cotton fiber reinforced polyester composites; artificial neural network; pin-on-disc

---

1 Introduction

Within the last few decades natural fiber reinforced polymer matrix composites (NFRPCs) were in boom due to their low cost, low weight, easy availability, and biodegradability. The natural fibers were in demand in automobile and structural sectors [1]. In the present work focus was placed on the cotton fiber due to its high strength, durability, biodegradability, and ease of blending with other fibers and resin. Failure due to wear was more common in automobile and failure of small parts leaded to the shut down in the industry. In this present investigation emphasis was placed on the wear behavior of the cotton fiber reinforced polyester composite (CFPC).

Many researchers have worked on different types of NFRPCs and have analyzed the effect of operating parameters (like load, speed, sliding distance, and temperature) and material parameters (like fiber length, fiber volume fraction, fiber orientation, and fiber treatment) on the wear behavior of NFRPCs. The work done of a few researchers is shown in the Table 1.

Table 1 reveals that most of the researchers have analyzed the wear rate of NFRPCs by varying different material parameters and different operating parameters. Very few have added fillers with the natural fiber and see the effect of fillers on the wear behavior of materials. Few studies show that use of proper wt.% of fillers with synthetic fiber helps to increase the wear resistance of the materials [16, 17].

---

* Corresponding author: Hiral H. PARIKH, E-mail: hiralp@nuv.ac.in

Table 1 Wear study by different researchers.

Research	Polymer	Fiber	Fillers	Variables	Observed wear rate
Chittaranjan Acharya [2]	Epoxy	Lantana camara	—	SD	Decrease
Chin Yousif [3]	Epoxy	Kenaf	—	*L*, FO, *S*	Decrease
Ganguluri et al. [4]	Epoxy	Pin wood dust	—	FVF	Decrease
Yousif et al. [5]	Polyester	Betelnut fruit	—	*L*	Decrease
Mishra and Acharya [6]	Epoxy	Sugar cane	—	FO, *L*	Decrease
Sayed et al. [7]	Polyester	Linen & Jute	—	FO	Decrease
Yousif et al. [8]	Polyester	Coir	—	FT	Decrease
Boopathi et al. [9]	Epoxy	Borassus fruit	—	*L*, *S*, SV, FT	Decrease
Yousif and El-Tayeb [10]	Polyester	Untreated & treated oil palm	—	FT, *L*	Decrease
Umar et al. [11]	Epoxy	Bamboo	—	FO	Decrease
Majhi et al. [12]	Epoxy	Rice husk	—	FT, *L*	Decrease
Dwivedi et al. [13]	Polyester	Bamboo powder	—	FVF, *L*	Decrease
Chandra et al. [14]	Epoxy	Coir	—	FVF, *L*	Decrease
Narish and Dirk [15]	Polyurethane (PE)	Kenaf	—	*L*, SD	Decrease

L: Load, *S*: Speed, SD: Sliding distance, FVF: Fiber volume fraction, FO: Fiber orientation, FT: Fiber treatment, SV: Sliding velocity

In the present investigation graphite fillers are used with the CFPC to analyze the effect of different wt.% of fillers on the wear behavior of CFPC.

The response behavior of material is implicit in the experiments. Usually, the behavior of materials is modeled analytically using mathematical expressions. However, it may not always be possible to have a simple expression. To create a complicated expression is difficult. The artificial feedforward neural network may be extremely helpful in terms of Refs. [18, 19]:

- The ability to implicitly detect complex nonlinear relationships between dependent and independent variables.
- The ability to detect all possible interactions between variables.
- The neural network is effective in terms of predicting the behavior of a new material before the material is produced. This may reduce the experiment cost and time.

An exhaustive literature review has been completed on the artificial neural network (ANN) to predict mechanical and tribological behavior of fiber reinforced polymer composites. Table 2 provides the summary of various studies for predicting the mechanical and tribological behavior of fiber reinforced polymer (FRP) composites with the ANN. In the present investigation

Table 2 Summary of various studies for predicting the properties of FRP composites with ANN.

Author	Study
Aymerich et al. [20]	Fatigue strength of composites
Velten et al. [21]	Wear volume prediction of polyamide 4.6 matrix composites reinforced with short carbon/glass fiber
Pleune et al. [22]	Fatigue life of carbon and low alloy steel
Haque et al. [23]	Corrosive fatigue behavior of steel
Allan et al. [24]	Predicting structural properties of polypropylene fiber
Hany and Yousif [25]	Fatigue life of glass fiber epoxy composite
Jia and Davalos [26]	Fatigue model for FRP wood composite
EI Kadi [27]	Mechanical modelling of FRP
Sha [28]	Machinability aspect of unreinforced and reinforced PEEK composites

predictions of wear behavior of the composite material comparisons are made between general regression statistical techniques with the ANN.

2 Experimental

2.1 Specimen preparation

Single wound 7 count cotton yarn procured from PBM Polytex Limited, Petlad, Gujarat was used as reinforcement. Unsaturated polyester resin, accelerator cobalt naphthenate and hardener were supplied by S K Enterprise, Surat, India. Matrix was prepared with a resin to hardener ratio 10:1. Graphite particles obtained from Heny Chemicals, Vadodara, India was used as filler with the average particle size 11.91 μm. Hand lay-up technique was used to prepare the composite plates of size 300 mm × 300 mm × 10 mm. The composition of fabricated composites with hand lay-up technique was listed in Table 3.

To determine graphite particle size distribution in the composites, the tensile test was carried out on the composites at Advance Metallurgical Services (AMS) Laboratory, Vadodara, Gujarat. The tensile test was performed according to the ASTM D 3039-M14 standard. A 10 kN load cell was used and three tests were repeated for each set of specimen and the average values were calculated and plotted in Fig. 1.

It was clear from the results that the addition of 3 wt.% graphite reduced the tensile strength of the cotton fiber polyester composites. The strength of the composite was even more deteriorated by increased graphite wt.%. This result was in agreement with Shalwan and Yousif [29] who concluded from their study that the addition of the graphite was highly recommended for the natural fiber composites which could enhance the wear characteristics of the polymer composites. However, the high content of the graphite deteriorated the mechanical properties. The micrograph of CFPC, 5 wt.% graphite filled cotton fiber reinforced polyester composite (5GCFPC), and 3wt.% graphite filled cotton fiber reinforced polyester composite (3GCFPC) were displayed in the Figs. 2–4, respectively.

Table 3 Formulation of fabricated graphite filled CFPC.

Material code	Resin content (wt%)	Cotton fiber (wt%)	Graphite (wt%)
CFPC	82	18	0
3GCFPC	79	18	3
5GCFPC	77	18	5

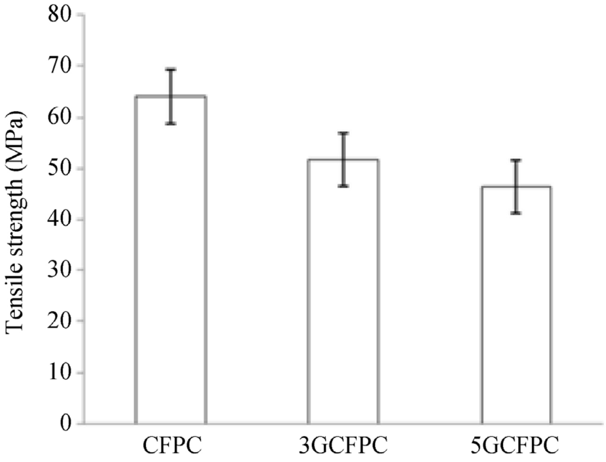

Fig. 1 Tensile strength of CFPCs.

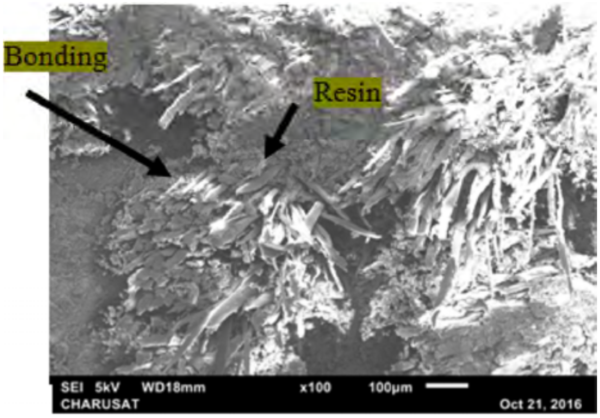

Fig. 2 Micrograph of CFPC after tensile test.

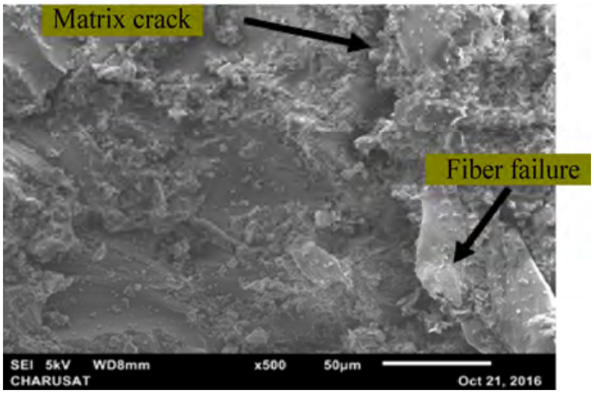

Fig. 3 Micrograph of 3GCFPC after tensile test.

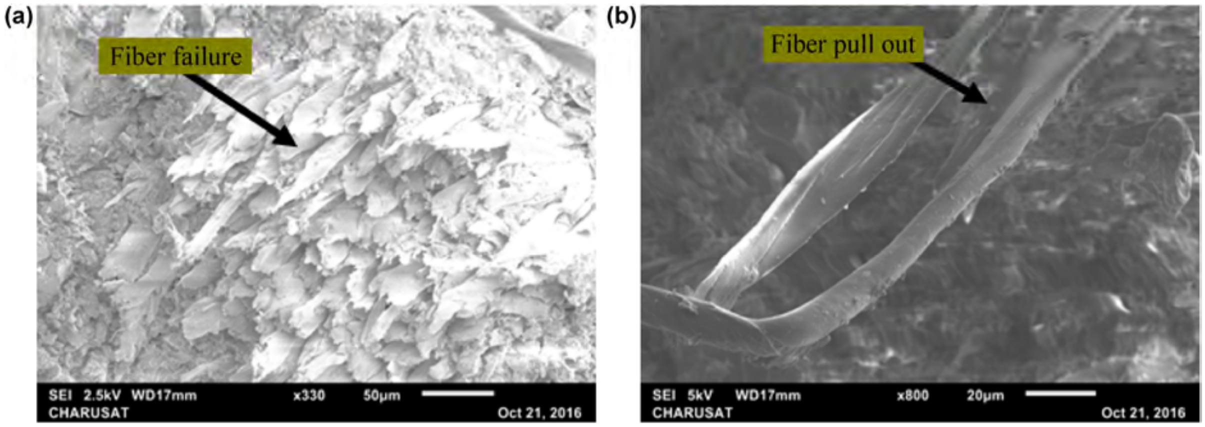

Fig. 4 Micrograph of 5GCFPC after tensile test: (a) low magnifacation and (b) high magnification.

From Fig. 2 good bonding between the resin and the fiber could be seen. This adhesion might be responsible for higher tensile strength. Figure 3 revealed that by adding 3% graphite in the CFPC, the first failure process was initiated from the matrix crack and then it was followed by the fiber failure in the direction of loading. Fiber pull out and fiber failure revealed from Figs. 4(b) and 4(a) for 5GCFPC that might be responsible for the low tensile strength of the material.

2.2 Test setup, test conditions, test parameters and design of experiments

To perform the wear test on the CFPCs, a pin-on-disc (POD) test setup (supplied by DUCOM, Bangalore) was used at CHARUSAT, Changa, Gujarat and it was shown in Fig. 5. The specimen was kept stationary against the disk and the counterface rotated. The load was functional through the lever mechanism.

The detailed experimental conditions were listed in Table 4. The specimen surfaces were prepared by rubbing them on different grade emery paper followed by acetone cleaning. The average surface roughness for the specimens before and after the test was measured with a Taylor Hobson Roughness tester and listed in Table 5.

Response surface methodology (Box Behnken method) was used to reduce the number of experiments in an organized way.

3 Results and discussion

3.1 Wear data from pin-on-disc machine

The operating parameters were set on the POD machine and experiments were performed. The wear response of composite materials was plotted from the POD machine and listed in Table 6.

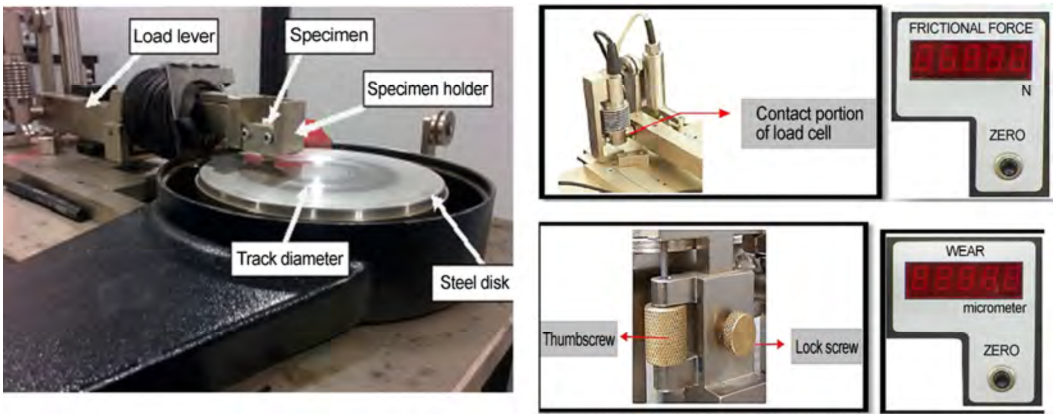

Fig. 5 Pin-on-disc wear test rig.

Table 4 Experimental conditions.

Parameters	Operating Conditions
Temperature	Ambient conditions (temperature: 29 °C)
Relative humidity	55(±5)%
Test disc	Hardened ground steel (EN-31, hardness 60 HRC)
Roughness of EN-31	1.6 m Ra
Duration of rubbing	600 s
Surface condition	Dry
Load	2 kg, 3 kg, 4 kg
Sliding speed	1.66 m/s, 2.49 m/s, 3.33 m/s
Sliding distance	1,000 m, 1,500 m, 2,000 m
Pin Material	Cotton fiber polyester composites (CFPC), 5 wt.% graphite cotton fiber polyester Composites (5GCFPC), 3 wt.% graphite cotton fiber polyester composites (3GCFPC)
Pin size (ASTM G99 Std.)	30 mm × 10 mm × 10 mm
The average contact pressure between the disc and specimen surface	0.3 MPa

Table 5 Surface roughness of test specimen.

Material	Average surface roughness Ra (μm)	
	Before test	After test
CFPC	1.45	1.7
3GCFPC	2.166	3.2
5GCFPC	1.7	2.2

Table 6 Observed data from POD.

	Operating parameters				CFPC	3GCFPC	5GCFPC
Exp. No.	Sliding speed (m/s)	Load (kg)	Contact pressure (MPa)	Sliding distance (m)	Wear (micron)	Wear (micron)	Wear (micron)
1	2.49	2	0.2	1,500	42	54	36
2	3.33	4	0.4	2,000	23	56	34
3	3.33	2	0.2	2,000	37	30	28
4	2.49	3	0.3	1,500	37	38	40
5	3.33	3	0.3	2,000	40	66	30
6	1.66	3	0.3	1,000	42	47	31
7	2.49	2	0.2	1,500	30	24	43
8	1.66	2	0.2	1,000	28	23	48
9	2.49	3	0.3	1,500	29	47	32
10	2.49	4	0.4	1,500	41.2	53	26
11	1.66	3	0.3	1,000	30	25	17
12	3.33	3	0.3	2,000	22	37	25
13	1.66	4	0.4	1,000	35	35	39
14	2.49	3	0.3	1,500	29	47	32
15	2.49	4	0.4	1,500	44	69	39

3.2 Mean effects of operating parameters on response

The results of the mean wear for CFPC and graphite filled composites for different operating parameters were shown in Fig. 6.

Figures 6(a), 6(b), and 6(c) showed the effect of a normal load, speed, and sliding distance on the wear behavior of composite materials. The figures revealed by adding 5 wt.% graphite fillers wear resistance of the CFPC increased irrespective of operating parameters. Conversely, 3 wt.% of graphite fillers increased the wear of the CFPC. This finding was in agreement with Shivamurthy et al., Basavarajappa et al., and Rajesh et al. [30–32], who concluded from their studies that proper weight percentage of filler could improve the wear resistance of the materials.

To analyze the wear mechanism for the composite materials SEM analysis was performed on the wear surfaces.

3.3 Surface morphology

Figure 7(a) showed the SEM image for CFPC. It was clearly visible that good bonding between the fibers and matrix occurred. The fibers were not debonded normally from the matrix due to proper bonding. They were worn out during the wear process. Some fibers were peeled off during the wear process. Figure 7(b) revealed that 3GCFPC had undergone severe damage under the dry sliding conditions. Large

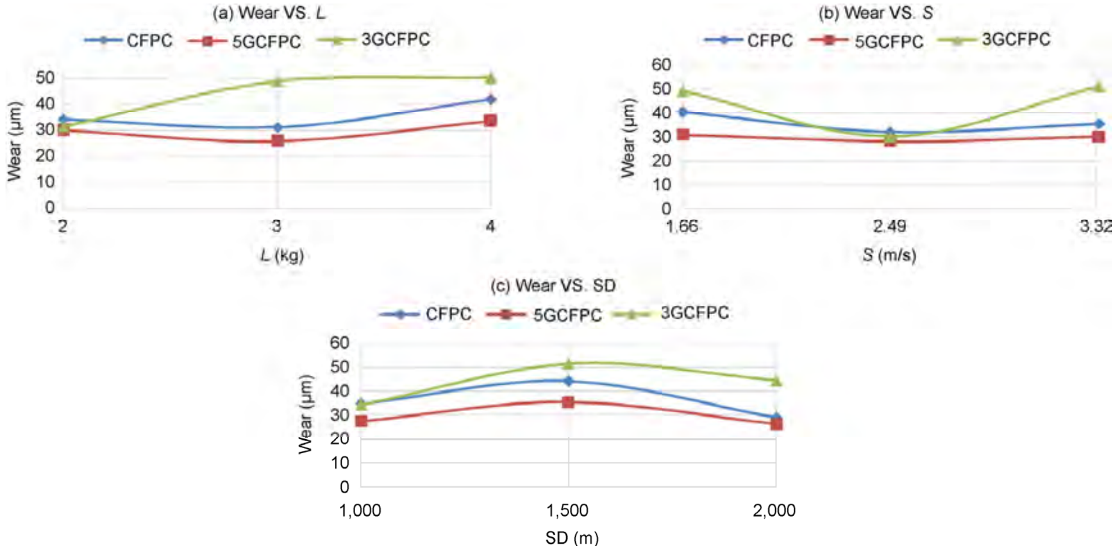

Fig. 6 Effect of operating parameters on wear.

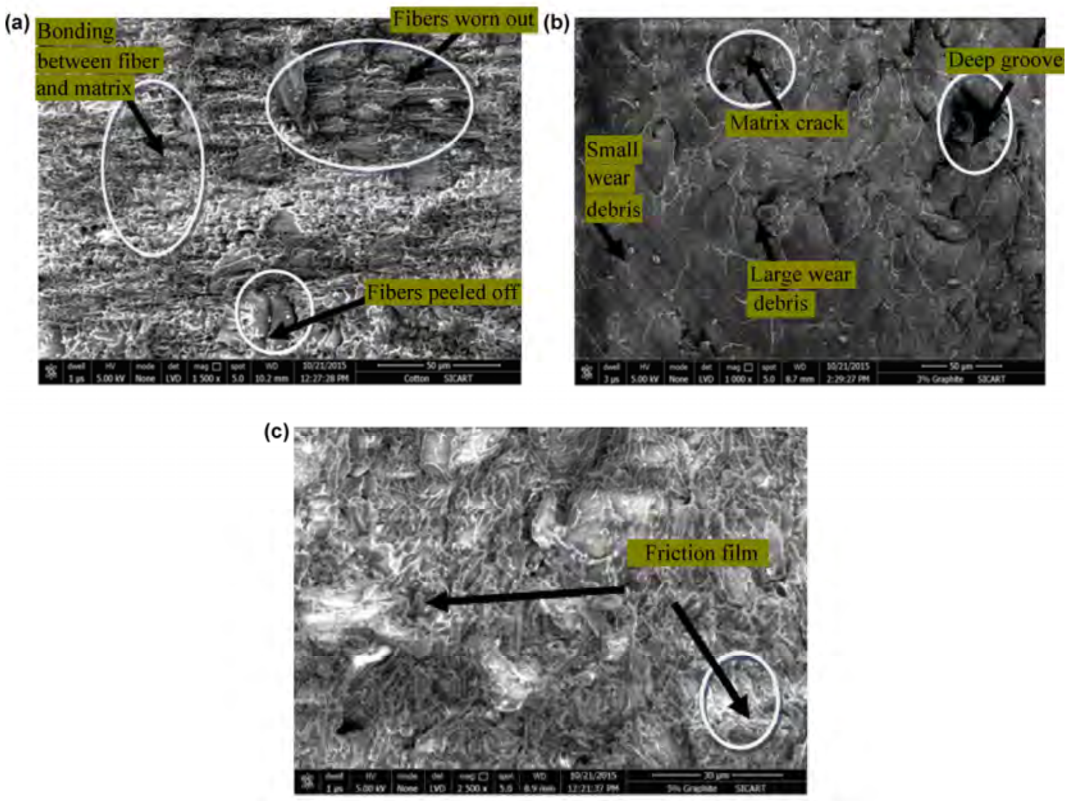

Fig. 7 Worn surface SEM analysis of (a) CFPC, (b) 3GCFPC, and (c) 5GCFPC.

and small wear debris was left over from the dry sliding condition on the worn surface of the specimen. The presence of this debris was mainly responsible for the large scale of wear. Matrix cracking was also found on the worn surface. These mechanisms were responsible for the high wear rate for 3GCFPC. Large scale disconnection of the matrix material and fibers produced several deep grooves on the specimen surface. Figure 7(c) indicated the formation of a friction film between two contact surfaces due to this less matrix cracks found and the tribological properties of a material improved in terms of less wear.

4 Regression mathematical models for wear

An ANOVA statistical tool was used with 95% confidence level with Minitab 17 software to quantify the influence of process parameters. Response surface methodology was used to create a mathematical model for wear of CFPCs. The second order general regression mathematical equations representing the relation between the wear and the input parameters (like load, speed, and sliding distance) for different materials were obtained and listed below.

CFPC

$$\text{Wear} = -22.883 - 0.108672 \times S - 19.25 \times L + 0.118664 \times \text{SD} - 0.012 \times S \times L - 0.013 \times L \times \text{SD} - 3.4 \times 10^{-5} \times \text{SD} + 0.000114 \times S^2 + 7.875 \times L^2 - 1.95 \times 10^{-5} \times \text{SD}^2 \tag{1}$$

3GCFPC

$$\text{Wear} = -243.0 + 61.13 \times L + 0.1095 \times S + 0.2080 \times \text{SD} - 0.05200 \times L \times S - 0.000090 \times S \times \text{SD} + 0.00650 \times L \times \text{SD} - 3.750 \times L^2 + 0.000132 \times S^2 - 0.000052 \times \text{SD}^2 \tag{2}$$

5GCFPC

$$\text{Wear} = -174.05 + 0.11238 \times S + 10.91 \times L + 0.11435 \times \text{SD} - 0.020800 \times S \times L - 0.000038 \times S \times \text{SD} + 0.000010 \times S^2 + 1.145 \times L^2 \times 0.000028 \times \text{SD}^2 \tag{3}$$

where L= load, S = Speed, and SD = Sliding distance.

The coefficient of determination (R^2) obtained for different models was listed in Table 7. It represented the ratio of variability explained by the model to the total variability in the actual data. Larger values of adjusted R^2 suggested models of greater predictive ability. Table 7 showed that all models satisfy this condition. All the response predicted R-sq values were in agreement with the adjusted R-sq values. This indicated the capability of the model was used effectively.

Table 7 Anova for the response surface.

	CFPC	3GCFPC	5GCFPC
R-sq	99.67%	99.82%	99.65%
R-sq (adjusted)	99.07%	99.57%	99.03%
R-sq (predicted)	94.69%	98.45%	94.44%

5 Configuration of artificial neural network (ANN)

The process of creating an artificial neural network (ANN) for the present research work was summarized in the following steps:

1. Collect the data and prepare the database: With the help of POD machine wear for the three different materials (CFPC, 3GCFPC, and 5GCFPC) was obtained. Box Behnken gave 15 design of experiments for the each material. Total 45 different wear values with one replica that is total 90 wear data were obtained for the three different materials.

2. Train the network: In this step network architecture, training functions and training algorithms for the network were required to select. The ANN model developed in the present research work was created using a MATLAB R13 software package. This package allowed the modification of the network architecture, such as generalized regression, Hopfield and feedforward backpropogation. Also the design parameters like number of neurons in each layer, number of hidden layers, neurons in the hidden layer, learning rate and momentum could be modified. Although this package offered a mixture of possible modification to the network design, not every modification was investigated. The work mainly focused on developing an ANN model for the wear instead of addressing an optimum network design. In the present work 72 data points (80%) were used for training/calibration and the remaining 18 data points (20%) were used for testing. The calibration/training data set and testing data set were selected randomly from the entire population. The schematic configuration of ANN was shown in the Fig. 8. Table 8 showed the design parameters used to train the network. The network was trained with a

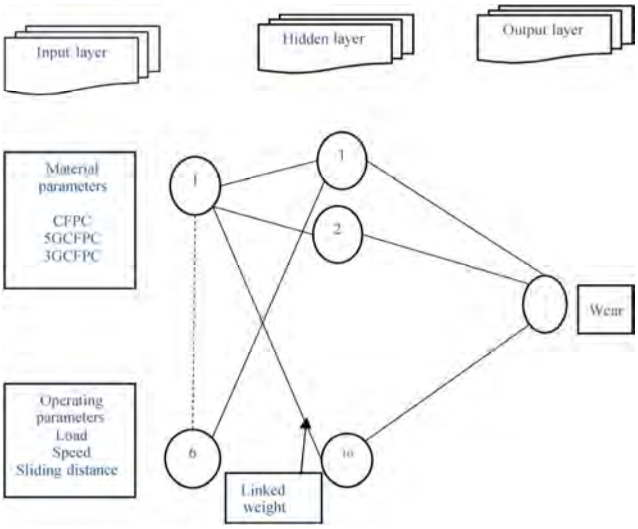

Fig. 8 Schematic configuration of ANN.

Table 8 Design parameters to train the network.

Design parameters	
Network type	Feed forward backpropogation algorithm
Training function	Train scaled conjugate gradient (TRANSCG)
Learning function	Gradient decent method (LEARNGDM)
Performance function	Mean square error (MSE)
No. of hidden layer	01
Neurons in the hidden layer	10

satisfactory coefficient of determination *R* = 0.99281 and was shown in the Fig. 9. For a better prediction the *R* value should be near 1. This network was used to simulate the test results.

3. Test the trained network: This was used to evaluate the network performance. After training the network, it was simulated for the test data in the same knowledge domain. For the testing total 18 data sets were used. Table 9 showed the simulated results with the ANN. A negative sign of the difference indicated underfitting the network while a positive sign indicated overfitting the network.

4. Use the trained ANN for simulating and predicting the wear behavior for new domain data set: To simulate the network conformation experiments were performed. Table 10 showed the selected input parameters and wear test results obtained from POD, ANN and regression equations. The test results were evaluated in terms of mean fitting error and mean average percentage deviation. The mean fitting error showed the overfitting for the ANN model and underfitting for the regression model. From the mean percentage deviation the ANN was an effective tool to predict the wear behavior of the material compare to the regression model.

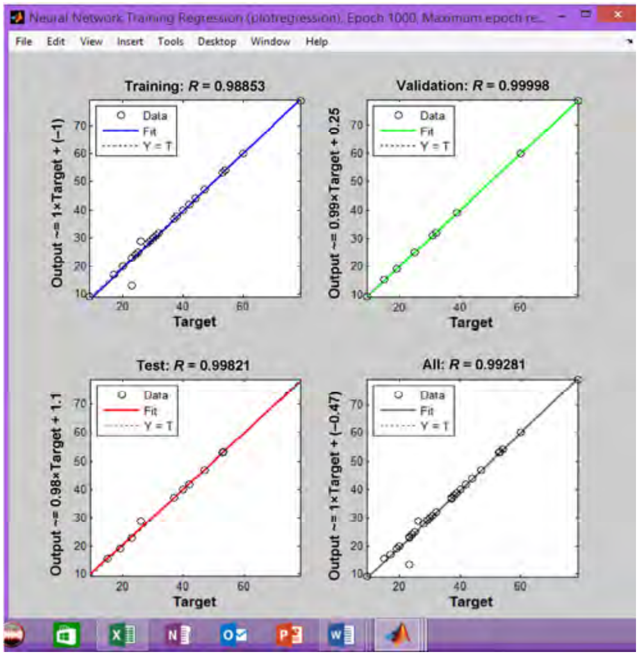

Fig. 9 Cofficient of Determination obtained by training a network.

Table 9 Simulated results with ANN.

Exp. No.	Experimental wear	Predicted wear with ANN	Difference
1	39	32.594	6.406
2	29	28.9987	0.0013
3	52	43.9037	8.0963
4	39	42.6385	–3.6385
5	32	31.9995	0.0005
6	39	45.5757	–6.5757
7	35	44.6696	–9.6696
8	47	46.9988	0.0012
9	69	77.5934	–8.5934
10	39	32.594	6.406
11	29	28.9987	0.0013
12	52	43.9037	8.0963
13	39	42.6385	–3.6385
14	32	31.9995	0.0005
15	39	45.5757	–6.5757
16	35	44.6696	–9.6696
17	47	46.9988	0.0012
18	69	77.5934	–8.5934

6 Conclusion

Experimental investigation and prediction of wear behavior of CFPC were summarized in the following points:

- The experimental results indicated that proper wt.% fillers had a considerable effect on controlling the wear rate of the material. The objective of the study was to identify the effect of the filler weight percentage of wear response of materials. It was observed from the results that adding graphite

Table 10 Conformation test data set and test results.

Exp. No.	CFPC	3GCFPC	5GCFPC	*S* (m/s)	*L* (kg)	SD (m)	Actual wear from POD	Predicted wear from ANN	Predicted wear from regression
1	1	0	0	1.25	3	750	33	30	29
2	0	0	1	1.67	4	1,000	34	32	40
3	0	0	1	2.49	3	1,500	33	31	43
4	0	1	0	2.49	2	1,500	42	45	40
5	0	1	0	3.33	4	2,000	80	76	70
6	0	0	1	2.49	3	1,500	37	42	50
Mean absolute deviation $=\sum_{i=1}^{16}\left(\frac{\lvert M_i-P_i\rvert}{n}\right)$								3.166667	7.5
Mean fitting error $=\sum_{i=1}^{16}\left(\frac{\lvert M_i-P_i\rvert}{n}\right)$								0.6 (indicates over fitting model)	–2.16 (indicates under fitting model)
Mean average percentage deviation $=\left\{\frac{1}{n}\left(\sum_{i=1}^{16}\left(\frac{\lvert M_i-P_i\rvert}{M_i}\right)\times 100\right)\right\}$								9.336774	18.74
where M_i is measured wear and P_i is predicted wear.									

5 wt.% wear resistance of the CFPC could increase. On the other hand, 3 wt.% graphite increased the wear of the CFPC.

- A well trained ANN was created with a mean square error of 0.99281. The conformation test results revealed the ANN to be an effective tool that predicted the wear behavior of the material over a general regression model.
- Furthermore, the well trained neural network could be applied to predict the wear without performing long and costly experiments.

References

[1] Mohammad L, Ansari M N M, Grace P, Jawaid M, Islam M S. A review on natural fiber reinforced polymer composite and its applications. *International Journal of Polymer Science* **2015**: 243947 (2015)

[2] Chittaranjan D, Acharya S K. Effect of fiber content on abrasive wear of Lantana Camara fiber reinforced polymer matrix composite. *Indian Journal of Engineering and Materials Sciences* **17**: 219–223 (2010)

[3] Chin C W, Yousif B F. Potential of kenaf fibers as reinforcement for tribological applications. *Wear* **267**: 1550–1557 (2009)

[4] Kranthi G, Nayak R, Biswas S, Satapapathy A. Wear performance evaluation of pine wood dust filled epoxy composites. In *Proceeding of the International conference on advancements in Polymeric Materials APM*, 2010.

[5] Yousif B F, Lau S T W, McWilliam S. Polyester composite based on betelnut fiber for tribological application. *Tribology International* **43**: 503–511 (2010)

[6] Mishra P, Acharya S K. Anisotropy abrasive wear behavior of bagasse fiber reinforced polymer composite. *International Journal of Engineering Science and Technology* **2**(11): 104–112 (2010)

[7] Sayed E L, El-Sherbiny MG , Abo-El-Ezz A S, Aggag G A. Friction and wear properties of polymeric composite materials for bearing applications. *Wear* **184**: 45–53 (1995)

[8] Yousif Belal F, Leong O B, Ong L K, Jye W K. The effect of treatment on tribo performance of CFRP composites. *Recent Patents on Materials Science* **2**: 67–74 (2009)

[9] Bhoopathi L, Sampath P S, Mylsamy K. Influence of fiber length in the wear behaviour of borassus fruit fiber reinforced epoxy composites. *International Journal of Engineering Science and Technology* **4**(9): 4119–4129 (2009)

[10] Yousif B F, El-Tayeb N S M. Wet adhesive wear characteristics of untreated oil palm fiber reinforced polyester and treated oil palm fiber reinforced polyester composites using the pin on disc and block on ring techniques. *Journal of Engineering Tribology* **224**: 123–131 (2009)

[11] Umar N, Jamil H, Low K O. Adhesive wear and frictional performance of bamboo fibers reinforced epoxy. *International Journal of Tribology* **47**: 122–133 (2012)

[12] Majhi S, Samantarai S P, Acharya S K. Tribological behavior of modified rice husk filled epoxy composite. *International Journal of Science & Engineering Research* 3(6): 1–5 (2012)

[13] Dwivedi U K, Ghosh A, Navin C. Abrasive wear behavior of bamboo powder filled polyester composites. *Journal of Bio Resources* **2**(4): 693–698 (2007)

[14] Chandra C K R, Madhusudan S, Raghavendra G, Venkateswara R E. Investigation into wear behaviour of coir fiber reinforced epoxy composites with taguchi method. *Journal of Engineering Research and Applications* **2**(5): 371–374 (2012)

[15] Narish S B F Y, Dirk R. Tribological characteristics of sustainable fiber-reinforced thermoplastic composites under wet adhesive wear. *Tribology Transactions* **54**: 736–748 (2011)

[16] Bijwe J, Indumathi J, John Rajesh J, Fahim M. Friction and wear behavior of polyetherimide composites in various wear modes. *Wear* **249**: 715–726 (2001)

[17] Kolluri D K, Satapathy B K, Bijwe J, Ghosh A K. Analysis of load and temperature dependence of tribo-performance of graphite filled phenolic composites. *Materials Science and Engineering A* **456**: 162–169 (2007)

[18] Tu J V. Advantages and disadvantages of using artificial neural networks versus logistic regression for predicting medical outcomes. *Journal of Clinical Epidemiology* **49**(11): 1225–1231 (1996)

[19] He W, Bao G H, Ge T J, Luyt A S, Jian X G. Artificial neural networks in prediction of mechanical behavior of high performance plastic composites. *Polymer Processing* **501**: 27–31 (2012)

[20] Aymerich F, Serra M. Prediction of fatigue strength of composite laminates by means of neural networks. *Key Engineering Materials* **144**: 231–240 (1998)

[21] Velten K, Reinicke R, Friedrich K. Wear volume prediction with artificial neural networks. *Tribology International* **33**: 731–736 (2000)

[22] Pleune T T, Chopra O K. Using artificial neural networks to predictthe fatigue life of carbon and low-alloy steels. *Nuclear Engineering and Design* **197**: 1–12 (2000)

[23] Haque M, Sudhakar K V. Prediction of corrosion-fatigue behavior of DP steel through artificial neural network. *International Journal of Fatigue* **23**: 1–4 (2001)

[24] Allan G, Yang R, Fotheringham A, Mather R. Neural modeling of polypropylene fiber processing: predicting the structure and properties and identifying the control parameters for specified fibers. *Journal of Materials Science* **36**: 3113–3118 (2001)

[25] EI Kadi H, AI Asaaf Y. Prediction of the fatigue life of unidirectional glass fiber/epoxy composite laminate using different neural network paradigms. *Composite Structures* **55**(2): 239–246 (2002)

[26] Jia J, Davalos J F. An artificial neural network for the fatigue study of bonded FRP-wood interfaces. *Composite Structures* **74**(1): 106–114 (2006)

[27] EI Kadi H. Modeling the mechanical behavior of fiber-reinforced polymeric composite materials using artificial neural networks—A review. *Composite Structures* **73**(1): 1–23 (2006)

[28] Sha W. Some comments on ‘investigative study on machinability aspects of unreinforced and reinforced peek composite machining using ann model. *Journal of Reinforced Plastics and Composites* 30: 641–642 (2011)

[29] Shalwan A, Yousif B F. Influence of date palm fibre and graphite filler on mechanical and wear characteristics of epoxy composites. *Materials and Design* **59**: 264–273 (2014)

[30] Shivamurthy B S, Prabhuswamy M S. Influence of SiO_2 fillers on sliding Wear resistance and mechanical properties of compression molded glass epoxycomposites. *Journal of Minerals & Materials Characterization & Engineering* **8**(7): 513–530 (2009)

[31] Rajesh S, Rajakarunakaran S, Sudhakara P. Modelling and optimization of sliding specific wear and coefficient of friction of Al based red mud, metal matrix composite using Taguchi method and RSM. *Journal of Materials Physics and Mechanics* **15**: 150–166 (2012)

[32] Basavarajappa S, Arun K V, Davim J. P. Effect of filler material on dry sliding wear behavior of polymer matrix composites─A Taguchi approach. *Journal of Minerals & Materials Characterization & Engineering* **8**(5): 379–391 (2009)

Hiral PARIKH. She is currently serving as an assistance professor in the School of Engineering and Technology at the Navrachana University, Vadodara. She did her post-graduation in machine design from Birla Vishvakarma Mahavidyalaya (BVM) College of Engineering, V. V. Nagar in 2006. Since then she has been engaged in teaching and research. Currently she is pursuing her Ph.D degree from CHARUSAT, Changa University in the field of Tribological Characterization of Polymer Matrix Composites. She has authored various research papers in referred journals, national & international conferences. She has also published 2 book chapters with reputed publishers like SPRINGER, ACME, etc. She is also a member of Tribology Society of India and Indian Society of Technical Education.

Piyush P. GOHIL. He is working as associate professor in Mechanical Engineering Department at Faculty of Technology & Engineering, the MS University of Baroda, Vadodara (Gujarat). He did his Ph.D. degree in August 2010 from SVNIT-Surat (Gujarat) India. Dr. Gohil's area of research includes design, manufacturing and tribology of composites. He is a life member of ISTE, TSI, ISAMPE, FRP Institute and annual member of SAE. He has guided 2 PhD students and 4 pursuing, also guided 35 ME/M.Tech Dissertations. He has more than 70 research papers in referred journals, national & international conferences. He has also published 5 book chapters in reputed publishers like SPRINGER, ACME, etc., and also edited one conference proceeding and one thematic journal issue. He has delivered more than 30 expert lectures in various faculty development programmers and many expert lectures to student community. He is acting as reviewer in many national and international journals of SAGE, SPRINGER, ELSEVIER, INDERSCIECE publishers in his area of research. He has completed two MODROB projects of AICTE-New Delhi INDIA. He has also received research project grants from DST Delhi and GUJCOST Gandhingar. He was awarded travel grants as a Young Scientist from DST INDIA in March 2011 for Malaysia & under UGC Merged scheme in March 2015 for London. Dr. Gohil is also acting as External Expert BOS member at BVM, CHRUSAT.

Friction **5**(2): 194–206 (2017) ISSN 2223-7690
DOI 10.1007/s40544-017-0146-x CN 10-1237/TH

Research Article

Reduction of friction by normal oscillations. II. In-plane system dynamics

Xinyu MAO[1,2], **Valentin L. POPOV**[1,3,4,*], **Jasminka STARCEVIC**[1,4], **Mikhail POPOV**[1,3,4]

[1] *Technische Universität Berlin, Berlin 10623, Germany*

[2] *Tsinghua University, Beijing 100084, China*

[3] *Tomsk Polytechnic University, Tomsk 634050, Russia*

[4] *Tomsk State University, Tomsk 634050, Russia*

Received: 31 August 2016 / Revised: 24 December 2016 / Accepted: 11 January 2017

Abstract: The influence of out-of-plane oscillations on friction is a well-known phenomenon that has been studied extensively with various experimental methods, e.g., pin-on-disk tribometers. However, existing theoretical models have yet achieved only qualitative correspondence with experiment. Here we argue that this may be due to the system dynamics (mass and tangential stiffness) of the pin or other system components being neglected. This paper builds on the results of a previous study [19] by taking the stiffness and resulting dynamics of the system into account. The main governing parameters determining macroscopic friction, including a dimensionless oscillation amplitude, a dimensionless sliding velocity and the relation between three characteristic frequencies (that of externally excited oscillation and two natural oscillation frequencies associated with the contact stiffness and the system stiffness) are identified. In the limiting cases of a very soft system and a very stiff system, our results reproduce the results of previous studies. In between these two limiting cases there is also a resonant case, which is studied here for the first time. The resonant case is notable in that it lacks a critical sliding velocity, above which oscillations no longer reduce friction. Results obtained for the resonant case are qualitatively supported by experiments.

Keywords: sliding friction; out-of-plane oscillation; stiffness; system dynamics; macroscopic friction coefficient

---

1 Introduction

Vibrations can be applied to reduce and control friction, which is widely used in many industrial branches, such as metal forming, wire drawing and drilling [1, 2]. One of the earliest studies of friction reduction due to oscillations was carried out by Godfrey in 1967 [3]. He conducted experiments, in which a rider slid along a steel plate and was vibrated in the direction perpendicular to the plane. Afterwards numerous studies were carried out, which can be roughly classified by whether the static or sliding friction is considered and by the direction of the oscillations, see, e.g., Refs. [4–6]. The three possible directions of oscillation are: (1) in the sliding direction; (2) perpendicular to the sliding direction in the contact plane; (3) perpendicular to the contact plane (out-of-plane oscillations). Arbitrary combinations of these three modes are also possible, some of which can produce directed motion even in the absence of a directed mean force, thus producing a frictional drive. In this regard, active control of friction through oscillations is closely related to oscillation-based frictional drives [7, 8]. However, in the present paper we consider only sliding friction under the influence of out-of-plane oscillations.

Friction under the action of out-of-plane oscillations has been studied experimentally in the past in a number of works [9–12]. The first theoretical description

---

[*] Corresponding author: Valentin L. POPOV, E-mail: v.popov@tu-berlin.de

was proposed in Refs. [13, 14], where the movement of a rigid body under constant tangential force and oscillating normal force was considered. Unfortunately this model achieved only qualitative correspondence with experimental results. In Ref. [7], it was shown that the macroscopic behavior of a frictional contact is strongly influenced by the contact stiffness. Related studies of the dependence of friction on tangential oscillations [15, 16] and a study of frictional drives [17] came to the same conclusion. In a recent experimental study [18] the contact stiffness was also confirmed as one of the main parameters governing the response of a tribological contact to high frequency oscillations.

Based on these indications of the importance of contact stiffness, Popov et al. [19] carried out a theoretical study of friction under the action of out-of-plane oscillations with explicit account of finite contact stiffness. In this paper it was assumed that the stiffness of the system is much larger than that of the contact, which allowed avoiding consideration of system dynamics. In real systems, depending on their particular mechanical design, the stiffness of the system may be comparable with the contact stiffness, thus bringing the whole system dynamics into play. In the present paper, we extend the previous study [19] by considering the complete dynamics of a system with a tribological contact.

2 Simplified model of the experimental set-up

The model studied in the present paper is motivated by experimental studies of active control of friction by out-of-plane oscillations in a pin-on-disk tribometer (e.g., Refs. [7, 14–16]). The design of the pin is shown in Fig. 1(a). Assuming that the vertical stiffness of the set-up is much larger than the normal contact stiffness, the vertical macroscopic motion of the pin can be considered to be displacement controlled. The tangential stiffness of the pin assembly is much smaller than its vertical stiffness, so that it is no longer guaranteed that the tangential stiffness of the pin is larger than the tangential contact stiffness. Therefore, the tangential stiffness of the pin is explicitly taken into account in our model. Assuming that the transversal dynamics of the pin is controlled by only one bending normal mode of the pin, we arrive at the simplified model of the system, which is sketched in Fig. 1(b): a one-degree-of-freedom model taking into account the normal and tangential contact stiffness, the inertia of the pin and its tangential stiffness. Modal analysis of the pin could be used for estimation of a more accurate modal mass, but we do not do this here, as our aim is to present a high-level analysis without considering particular geometrical realizations. We will show that the frequency of free oscillations of the pin, $\omega_0 = \sqrt{k_x / m}$, is the most important system parameter; when describing a real experiment, it has to be adjusted to the ground frequency of the free oscillations of the pin. Naturally, our model abstracts away many (possibly important) aspects of real frictional systems, in particular the differential contact stiffness of curved bodies (we model the contact as a single spring with constant stiffness). However, in the first part of this series [19] we found that the detailed contact mechanics had surprisingly little influence on the results, relative to a one-spring model. In particular, abstracting the exact geometry of the contact does not change the relevant dimensionless variables. Due to this, and in view of the already large number of system parameters, we restrict ourselves to the simple model described above.

The model, as shown in Fig. 1(b), consists of a rigid body with mass m that is connected to an external actuator, which imposes the body's z-coordinate. The body is pulled by a spring with a tangential stiffness k_x and interacts with the substrate through a "contact spring" that has the normal stiffness $k_{z,\mathrm{c}}$ and tangential stiffness $k_{x,\mathrm{c}}$. The vertical movement of the mass is determined explicitly by the external oscillation:

$$u_z = u_{z,0} + \Delta u_z \cos \omega t \tag{1}$$

where $u_{z,0}$ is a constant initial indentation, Δu_z is the amplitude of normal oscillations, and ω is the angular frequency of the oscillation. The attached "system spring" is pulled tangentially with a constant velocity v_0. The motion of the body in the x-direction under the influence of the attached springs is described by Newton's Second Law for the tangential displacement u_x. The tangential displacement of the immediate contact point is denoted with $u_{x,\mathrm{c}}$. For simplicity, we assume Coulomb's law of friction with a constant

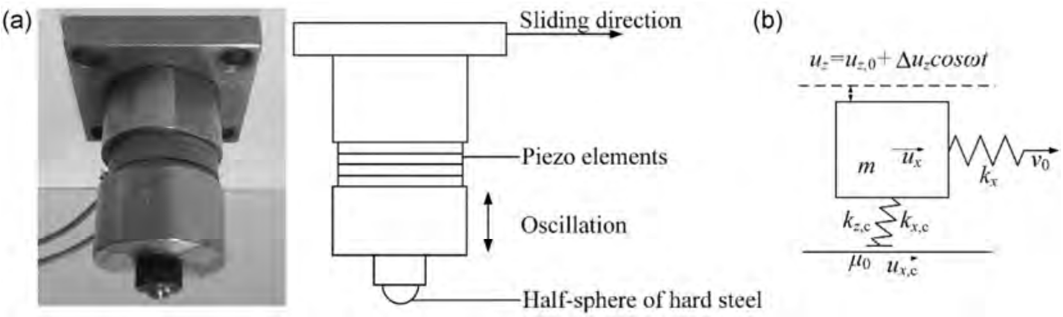

Fig. 1 (a) Photograph and diagram of the pin assembly of a pin-on-disk tribometer used in Refs. [7, 16] and in the experimental part of the present study; (b) a simplified model of the pin in contact with the disk, which is studied in the present paper.

coefficient of friction μ_0 in the immediate contact point between the substrate and the contact spring. Although this may be an unrealistic assumption in general, the aim of this study is to understand how changes in the *macroscopic* coefficient of friction can arise from pure system dynamics even with *constant microscopic* friction. Experimental results might be best approximated by a combined theory, including system dynamics, contact mechanics and changes of the local coefficient of friction, but this is left for later studies.

Note that the amplitude of oscillation can be either smaller than the mean indentation (non-jumping), in which case the body is always in contact with the substrate, or larger (jumping case), where contact with the substrate is intermittent. Initially we will focus on the permanent contact case. Jumping will be introduced later in the paper.

3 Qualitative analysis

All previous studies of the influence of normal oscillations on friction, including the first part of the present work [19], have shown qualitatively the same dependence of the macroscopic coefficient of friction (COF) on velocity: At zero velocity the friction force is at its static value, which is determined solely by the minimum value of normal force during one oscillation cycle:

$$\mu(v_0 = 0) = \begin{cases} \mu_0(1 - \Delta u_z / u_{z,0}), & \text{for } \Delta u_z < u_{z,0} \\ & \text{(non-jumping case)} \\ 0, & \text{for } \Delta u_z > u_{z,0} \\ & \text{(jumping case)} \end{cases} \quad (2)$$

At higher velocities the COF increases until it reaches μ_0 at some critical velocity v_0^* ("point of insensitivity"), and remains constant thereafter. The static COF and the critical velocity v_0^* are the two main reference points of the velocity dependence of the COF. While the first reference point is universal (Eq. (2)), the second one is determined by the dynamics of the tribological system.

We begin our analysis with the case of small oscillation amplitudes, $\Delta u_z < u_{z,0}$, so that the lower point of the indenter remains in contact with the substrate at all times. In this case, the normal component of the contact force F_N is non-vanishing and is determined by the product of the current indentation depth (Eq. (1)) with the normal contact stiffness $k_{z,c}$:

$$F_\text{N} = k_{z,c}(u_{z,0} + \Delta u_z \cos\omega t) \quad (3)$$

At sufficiently large pulling velocities v_0, the contact point will be sliding all the time (without stick) in one direction (except for the resonant case that will be described later). Under these conditions, the average tangential force is equal to the average normal force times μ_0, and the macroscopically observed COF, which we define as the ratio of the mean values of tangential and normal forces over one period of oscillation, will be constant and equal to μ_0. When the above conditions are satisfied the tangential force of the contact spring is in equilibrium with the friction force (normal force times μ_0), since the contact stiffness is not associated with any mass:

$$k_{x,c}(u_x - u_{x,c}) = \mu_0 k_{z,c}(u_{z,0} + \Delta u_z \cos\omega t) \quad (4)$$

The equation of motion of the body m along the

x-axis is

$$m\ddot{u}_x = k_x(v_0 t - u_x) - k_{x,\mathrm{c}}(u_x - u_{x,\mathrm{c}}) \tag{5}$$

Taking Eq. (4) into account, the equation of motion reads

$$m\ddot{u}_x + k_x u_x = k_x v_0 t - \mu_0 k_{z,\mathrm{c}} \Delta u_z \cos\omega t - \mu_0 k_{z,\mathrm{c}} u_{z,0} \tag{6}$$

The particular solution of this equation is

$$u_x = v_0 t - \mu_0 \frac{k_{z,\mathrm{c}}}{k_x} u_{z,0} + \frac{\mu_0 k_{z,\mathrm{c}} \Delta u_z}{m\omega^2 - k_x} \cos\omega t \tag{7}$$

Differentiating this solution with respect to time gives

$$\dot{u}_x = v_0 - \frac{\mu_0 k_{z,\mathrm{c}} \Delta u_z}{m\omega^2 - k_x} \omega \sin\omega t \tag{8}$$

Differentiating the equilibrium condition (Eq. (4)),

$$k_{x,\mathrm{c}}(\dot{u}_x - \dot{u}_{x,\mathrm{c}}) = -\mu_0 k_{z,\mathrm{c}} \Delta u_z \omega \sin\omega t \tag{9}$$

Substituting Eq. (8) into Eq. (9) and resolving the resulting equation with respect to $\dot{u}_{x,\mathrm{c}}$, we obtain the following expression for the sliding velocity of the immediate contact point (lower point of the contact spring)

$$\dot{u}_{x,\mathrm{c}} = v_0 - \frac{k_{z,\mathrm{c}}}{k_{x,\mathrm{c}}} \frac{k_{x,\mathrm{c}} + k_x - m\omega^2}{(m\omega^2 - k_x)} \mu_0 \omega \Delta u_z \sin\omega t \tag{10}$$

Due to our previous assumption of continuous sliding this velocity must remain positive at all times. This is the case if

$$v_0 > v_0^* \tag{11}$$

where

$$v_0^* = \mu_0 \omega \Delta u_z \frac{k_{z,\mathrm{c}}}{k_{x,\mathrm{c}}} \frac{\left|k_{x,\mathrm{c}} + k_x - m\omega^2\right|}{\left|k_x - m\omega^2\right|} \tag{12}$$

This relatively simple equation is one of the central results of the present paper and it is instructive to discuss it in some detail. First, let us consider limiting cases that have already been studied in the literature:

I. In the case of a very soft system ($k_x << m\omega^2$) with very large contact stiffness ($k_{x,\mathrm{c}} >> m\omega^2$) we effectively have a rigid body under the action of constant tangential force. In this case, which was considered in Ref. [14] (see esp. Fig. 20 and discussion) the critical velocity reduces to

$$v_{0,\mathrm{soft}}^* = \mu_0 \omega \frac{\Delta u_z k_{z,\mathrm{c}}}{\left|m\omega^2\right|} = \mu_0 \frac{\Delta F_\mathrm{N}}{m\omega} \tag{13}$$

II. The limiting case of a very stiff system ($k_{x,\mathrm{c}} << \left|k_x - m\omega^2\right|$) was considered in the first part of the present work [19]. In this case Eq. (12) simplifies to

$$v_{0,\mathrm{stiff}}^* = \mu_0 \omega \Delta u_z \frac{k_{z,\mathrm{c}}}{k_{x,\mathrm{c}}} \tag{14}$$

There are two other limiting cases which involve resonances and have not yet been considered in the literature:

III. If $k_{x,\mathrm{c}} + k_x - m\omega^2 \approx 0$, the critical velocity is very small: $v_0^* \approx 0$. The body is in permanent sliding state even at very low velocities and the COF is constant and equal to μ_0 at all sliding velocities.

IV. If $k_x - m\omega^2 \approx 0$, the critical velocity is infinitely large and the system never achieves the state of continuous sliding. It will be shown that in this case the macroscopic coefficient of friction reaches a plateau at large velocities, with a value lower than μ_0. This case is of a special interest and it will be considered below in detail and was also studied experimentally.

Let us now consider the movement of the body in the general case, when the contact point slides during some part of the oscillation cycle and sticks at other times. The movement of the slider is still governed by the Eq. (5), however, Eq. (4), which describes the tangential force in the contact spring, is only valid during the sliding part of the period, while during the sticking phase the following is true for the immediate contact point:

$$\dot{u}_{x,\mathrm{c}} = 0,\quad k_{x,\mathrm{c}}(u_x - u_{x,\mathrm{c}}) < \mu_0 k_{z,\mathrm{c}}(u_{z,0} + \Delta u_z \cos\omega t) \tag{15}$$

To study the dynamics of the system in detail, the equation of motion (Eq. (5)) was integrated numerically with account of Eqs. (4) and (15). The nontrivial behavior that can result when both stick and slip occur is illustrated in Fig. 2, which presents the time dependencies of the normal and tangential force (the

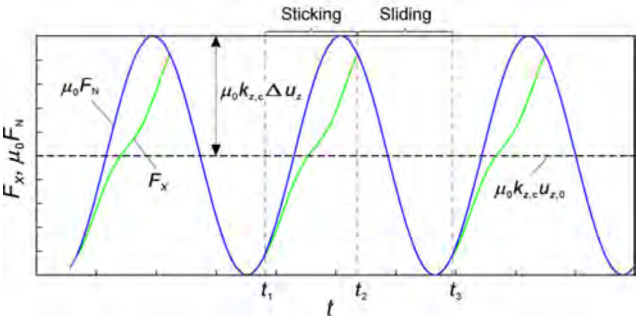

Fig. 2 An example of the dynamics of normal and tangential contact forces showing the phases of slip, where the tangential force (green line) coincides with the normal force multiplied with μ_0 (blue line), and the sticking phase, where the tangential force is smaller than the normal force multiplied with μ_0.

former multiplied with μ_0). During the sliding phase (e.g., before t_1 and between t_2 and t_3), these two quantities are equal, while during the sticking phase the tangential force (green line) is less than the normal force times μ_0 (blue line). The beginning of stick (t_1) is determined by the condition that the velocity of the immediate contact point (lower end of the contact spring) becomes zero, while the end of the sticking phase (t_2) is determined by the condition that the tangential force becomes equal to the normal force times μ_0.

4 Dimensionless formulation of the problem

Introducing the dimensionless variables

$$\bar{v} = \frac{v_0}{v_0^*} \tag{16}$$

$$\tau = \omega t \tag{17}$$

$$\xi = u_x \frac{\omega}{v_0^*} \tag{18}$$

$$\xi_c = u_{x,c} \frac{\omega}{v_0^*} \tag{19}$$

where v_0^* is defined by Eq. (12), with two additional dimensionless parameters

$$\alpha = \frac{k_x}{m\omega^2}, \quad \beta = \frac{k_x + k_{x,c}}{m\omega^2} \tag{20}$$

We can rewrite the Eqs. (4), (5) and (15) in the following form:

$$(\xi - \xi_c) = \left(\frac{u_{z,0}}{\Delta u_z} + \cos\tau\right)\frac{\alpha - 1}{\beta - 1} \tag{21}$$

$$\xi'' = \alpha(\bar{v}\tau - \xi) - (\beta - \alpha)(\xi - \xi_c) \tag{22}$$

$$\xi_c' = 0, \quad \xi - \xi_c < \left(\frac{u_{z,0}}{\Delta u_z} + \cos\tau\right)\frac{\alpha - 1}{\beta - 1} \tag{23}$$

where $\xi' = \mathrm{d}\xi/\mathrm{d}\tau$, $\xi'' = \mathrm{d}^2\xi/\mathrm{d}\tau^2$.

One can see that the behavior of the above system is unambiguously determined by the following set of variables:

$$\bar{v}, \ \Delta u_z / u_{z,0}, \ \alpha, \text{ and } \beta \tag{24}$$

After solving the Eqs. (21)–(23), one can go back to the initial dimensional variables and calculate the average normal force $\langle F_N \rangle$ and the average tangential force $\langle F_x \rangle = \langle k_x (v_0 t - u_x) \rangle$. The macroscopic coefficient of friction is then defined as

$$\mu_{\text{macro}} = \frac{\langle F_x \rangle}{\langle F_N \rangle} \tag{25}$$

It is easy to see that with the given dimensionless variables (24) the macroscopic coefficient of friction will be proportional to μ_0. Thus, it is more convenient to define the reduced coefficient of friction, $\mu_{\text{macro}} / \mu_0$, which is a function solely of the variables (24). In the following, we will explore the dependence of the reduced COF on the dimensionless velocity (16) on the parameter plane (α, β).

5 Numerical results and analysis

We begin with a general classification of the numerical results (Fig. 3). According to the definition (20), β is always larger than α, therefore we only consider the upper half of the parameter space above the line $\alpha = \beta$. In the figure, it is easy to identify the previously described special cases: the limiting case of a very soft system with a stiff contact (case I, according to the above classification) corresponds to small values of $\alpha << 1$ and large values of $\beta >> 1$, and is thus to be found in the upper left corner of the diagrams. The limiting case of very stiff system with low contact stiffness (case II), corresponds to $\alpha \approx \beta$ and is found along the diagonal of the diagram. The resonant

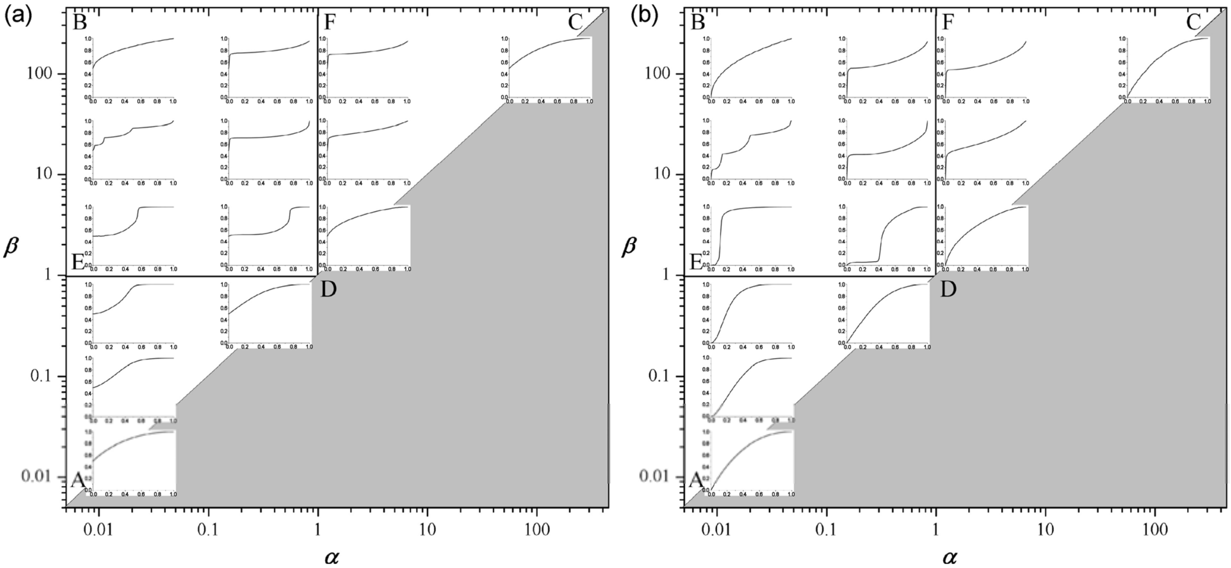

Fig. 3 Typical dependencies of $\mu_{\text{macro}} / \mu_0$ on $\overline{v}$ for the oscillation amplitude $\Delta u_z / u_{z,0} = 0.5$ (a) and for the maximal non-jumping oscillation amplitude $\Delta u_z / u_{z,0} = 1.0$ (b) arranged in a matrix of the dimensionless parameters α and β. The individual curves start at the static COF value at $\overline{v} = 0$, which only depends on the oscillation amplitude and is equal to $\mu_0 / 2$ in (a) and zero in the diagrams in (b). With increasing velocity, the reduced COF monotonically increases and reaches the value "1" at the velocity $\overline{v} = 1$. In between, however, the velocity-dependence of the COF is determined by the particular system dynamics.

case III corresponds to the line $\beta = 1$ and the resonant case IV to $\alpha = 1$.

Since case II occupies the diagonal of the diagram, there are infinitely many possible transitions from II to I. We will consider two such transitions: between A and B in Fig. 3, which passes over the resonant case III and from C to B, which passes over the resonant case IV.

5.1 Limiting cases of soft (case I) and stiff (case II) system and transition over resonant case III

Let us consider the transition from the stiff to the soft system over the resonant case III in more detail. We start with the separate consideration of the limiting cases of the very stiff and the very soft system. The diagram in Fig. 4(a) shows results of numerical simulation for the parameter set $(\alpha, \beta) = (0.01, 0.02)$, which corresponds to the limiting case I according to the classification of Section 3. This case was considered in detail in the publication [19]. In Fig. 4, results of numerical simulations are compared with the semi-empirical equation

$$\frac{\mu_{\text{macro}}}{\mu_0} \approx 1 - \frac{\Delta u_z}{u_{z,0}} \left[\frac{3}{4} (\overline{v} - 1)^2 + \frac{1}{4} (\overline{v} - 1)^4 \right] \tag{26}$$

derived in Ref. [19] with $\overline{v}$ given by Eq. (16) and v_0^* by Eq. (14). The numerical data practically ideally coincide with the result (Eq. (26)).

The right-hand-side diagram Fig. 4(b) presents a comparison for the opposite case of very soft system. Again, numerical data are compared with the analytical expression

$$\frac{\mu_{\text{macro}}}{\mu_0} = \left(1 - \frac{\Delta F_{\text{N}}}{F_{\text{N},0}}\right) + \frac{\Delta F_{\text{N}}}{F_{\text{N},0}} \left[\sqrt{\frac{4\pi}{9}}\, \overline{v} + \left(1 - \sqrt{\frac{4\pi}{9}}\right) \overline{v}^{1.2} \right] \tag{27}$$

obtained in Ref. [14], with v_0^* given by Eq. (13). In this case too we see a very good agreement. However, numerical data have a noticeable fine structure which the limiting-case curves do not have (a sort of small-amplitude oscillations).

With these two limiting cases, we establish the connection to previous studies and at the same time pose the more general problem of investigating the dependencies of the coefficient of friction on velocity in between these two poles.

As the character of the transformation of the law of friction is very similar for various oscillation amplitudes, in the following we illustrate this transformation only

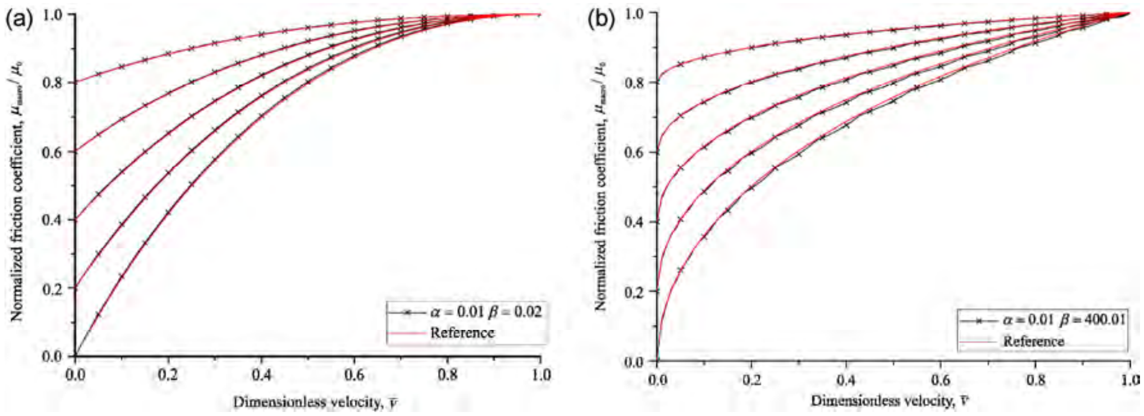

Fig. 4 The dependence of μ_{macro}/μ_0 on $\bar{v}$ for $(\alpha, \beta) = (0.01, 0.02)$ and $(\alpha, \beta) = (0.01, 400.01)$ for the oscillation amplitudes $\Delta u_z / u_{z,0} = 0.2,\ 0.4,\ 0.6,\ 0.8,\ 1.0$ (from top to bottom). The crosses and black lines represent results of numerical simulation and the red lines the analytical results (26) and (27).

for the case of the critical amplitude $\Delta u_z / u_{z,0} = 1$. The transition from the lower left corner of the diagram in Fig. 3 to the upper left corner means that the value of the parameter α remains small, while parameter β is changing from very small to very large values. The corresponding transformation of the dependencies of the reduced coefficient of friction on the dimensionless velocity is shown in Fig. 5(a) for the values of β in the lower left quarter of the parameter space and in Fig. 5(b) for the values of β in the upper left quarter of the diagram. In the lower quarter, the changes of the form are relatively slow until parameter β becomes very close to the value of "1". In the vicinity of this "resonant value" the upper point of the curve starts to slide to the left forming a plateau (as is clearly seen in Fig. 5(a) for $\beta = 0.91$). In the exact resonant case, the whole "dependence" consists only of this single plateau, that means that the coefficient of friction is constant and equal to μ_0. Much more dramatic changes occur after passing the resonant value $\beta = 1$. The resonant plateau then sharply decreases and a second plateau appears at the same time. This process repeats many times producing an oscillating curve whose "upper envelope" tends toward the limiting solution for the soft system, as already shown in Fig. 4(b).

5.2 Resonant case IV

We now turn our attention to the resonant case IV, where the frequency of oscillation is equal to the natural

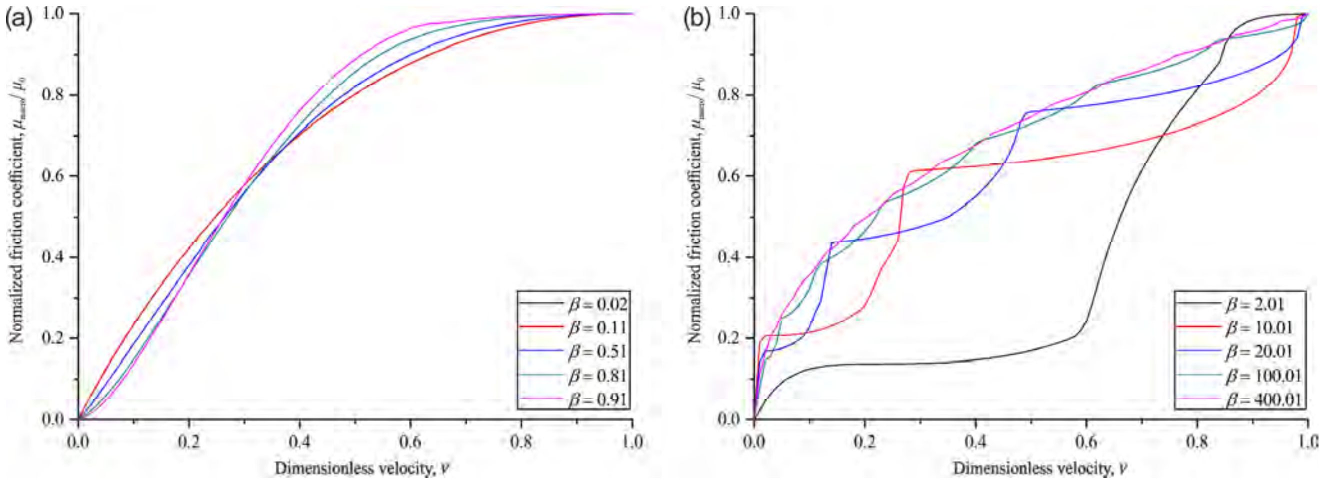

Fig. 5 The dependence of μ_{macro}/μ_0 on $\bar{v}$ for $\Delta u_z/u_{z,0}=1$, $\alpha=0.01$ and a series of β: (a) lower left quarter of the diagram in Fig. 3 (note that the curves for β = 0.02 and 0.11 practically coincide and cannot be resolved in the figure), (b) upper left quarter of the diagram.

frequency of the slider $\omega=\sqrt{k_x/m}$ and the system's behavior is qualitatively different from previously considered cases. For convenience we consider an equivalent system, where the right end of the system spring k_x in Fig. 1 is fixed and the substrate is instead moving with velocity v_0. Note also that the velocity dependence of the COF cannot be displayed as a function of $\bar{v}$ in the resonant case, because v_0^* tends to infinity and $\bar{v}$ becomes zero. We therefore return to the ordinary dimensional variables in this section. Since we are here concerned with very large values of β, we can consider the contact stiffness to be infinitely large for the purposes of this analysis. We chose the direction of the x-axis as the direction of movement of the substrate. The equation of motion then reads

$$m\ddot{x}+k_x x=\mu_0 F_{\mathrm{N}}\operatorname{sign}(v_0-\dot{x}) \tag{27}$$

In our model the normal force oscillates according to

$$F_{\mathrm{N}}=F_{\mathrm{N},0}+\Delta F\cdot\cos\omega t \tag{28}$$

Thus, the complete equation of motion is

$$m\ddot{x}+k_x x=\mu_0(F_{\mathrm{N},0}+\Delta F\cdot\cos\omega t)\operatorname{sign}(v_0-\dot{x}) \tag{29}$$

For an approximate analysis, let us assume that the body begins with a small-amplitude oscillation

$$\dot{x}=\Delta v\cos\omega t \tag{30}$$

Then the amplitude will be increasing over time until Δv becomes larger than v_0. Indeed, multiplying Eq. (29) with Eq. (30) and noting that the left-hand side of the resulting equation is the time derivative of the energy of the system, we arrive at the energy equation

$$\frac{\mathrm{d}}{\mathrm{d}t}\left(\frac{m\dot{x}^2}{2}+\frac{k_x x^2}{2}\right)=\mu_0(F_{\mathrm{N},0}+\Delta F\cdot\cos\omega t)\Delta v\cos\omega t\cdot\operatorname{sign}(v_0-\Delta v\cos\omega t) \tag{31}$$

If $\Delta v<v_0$, then the average value of the right-hand side is positive, and the energy of the system is monotonously increasing from one period to the next. However, if $\Delta v>v_0$ then the amplitude of oscillation stabilizes at the value for which the average change in energy during one period vanishes

$$\langle(F_{\mathrm{N},0}+\Delta F\cdot\cos\omega t)\Delta v\cos\omega t\cdot\operatorname{sign}(v_0-\Delta v\cos\omega t)\rangle=0 \tag{32}$$

where $\langle\ldots\rangle$ means averaging over one period of oscillation. During one oscillation period, there is a time interval $\tau_1<\tau<\tau_2$ where $v_0-\Delta v\cos\tau<0$:

$$\tau_{1,2}=\pm\tau^*=\pm\arccos(v_0/\Delta v) \tag{33}$$

Assuming that the oscillation amplitude Δv exceeds the mean sliding velocity v_0 only slightly, τ^* can be approximated by

$$\tau^*\approx\sqrt{2(1-v_0/\Delta v)} \tag{34}$$

In this approximation, the condition (32) can be written, after some simple transformations, as $-4(F_{\mathrm{N},0}+\Delta F)\sqrt{2(1-v_0/\Delta v)}+\pi\Delta F=0$. For the ratio of sliding velocity and oscillation velocity amplitude we finally find

$$\frac{v_0}{\Delta v}=1-\frac{1}{2}\left(\frac{\pi\Delta F}{4\left(F_{\mathrm{N},0}+\Delta F\right)}\right)^2 \tag{35}$$

Let us now calculate the macroscopic coefficient of friction. It is given by the equation

$$\begin{aligned}\mu&=\mu_0\frac{\langle(F_{\mathrm{N},0}+\Delta F\cdot\cos\tau)\operatorname{sign}(v_0-\dot{x})\rangle}{F_{\mathrm{N},0}}\\&=\frac{\mu_0}{2\pi}\left[-4\int_0^{\tau^*}\left(1+\frac{\Delta F}{F_{\mathrm{N},0}}\cdot\cos\tau\right)\mathrm{d}\tau+2\pi\right]\end{aligned} \tag{36}$$

which, assuming sufficiently small τ^* and considering Eqs. (34) and (35), leads to the equation

$$\frac{\mu_{\text{macro}}}{\mu_0}\approx1-\frac{\Delta F}{2F_{\mathrm{N},0}} \tag{37}$$

Comparing this with numerical results (Fig. 6) shows that the obtained approximation describes the plateau value of the COF in the resonant case very well.

6 Large oscillation amplitudes ("jumping")

If the amplitude of normal oscillation Δu_z exceeds the average indentation depth $u_{z,0}$, the body starts to "jump": For part of the oscillation period, it will be in contact with the substrate and out of contact the rest of the time. In previous studies this case has not usually been studied in detail. In the first part of this

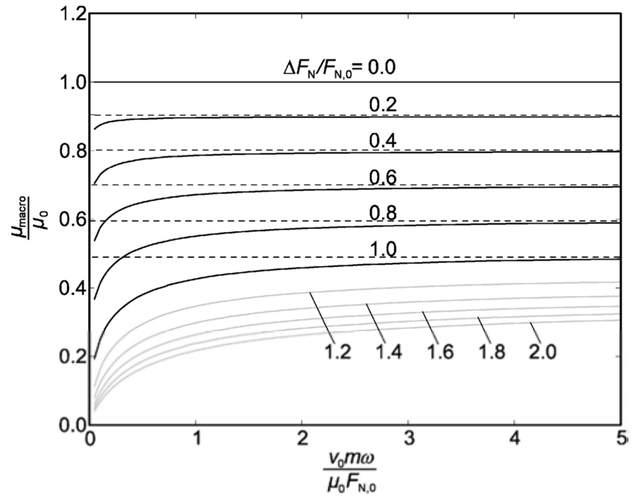

Fig. 6 The dependence of μ_{macro}/μ_0 on the dimensionless velocity $v_0 m\omega/(\mu_0 F_{\text{N},0})$ for the resonant case. The curves start at zero velocity at the static value $\mu/\mu_0 = 1-\Delta F_{\text{N}}/F_{\text{N},0}$ and tend to the limiting value $\mu/\mu_0 = 1-\Delta F_{\text{N}}/(2F_{\text{N},0})$ given by Eq. (37) at large velocities. The black curves correspond to the non-jumping case $\Delta F_{\text{N}}/F_{\text{N},0} \leqslant 1$, and the gray curves to jumping conditions ($\Delta F_{\text{N}}/F_{\text{N},0} > 1$).

publication [19] the jumping case was also considered (in the context of a stiff system) and it was found that the general character of the dependence of the coefficient of friction on dimensionless sliding velocity is very similar between the jumping and non-jumping cases: In both cases there is a critical velocity above which the COF no longer depends on velocity. Also, the shape of the velocity-dependences changes little after exceeding the critical oscillation amplitude ($\Delta u_z = u_{z,0}$). In analogy to Fig. 3 we present the different dependences for the jumping case in Fig. 7. Comparison with the corresponding graph at the critical amplitude $\Delta u_z = u_{z,0}$ presented in Fig. 3(b) shows that the general character of the dependences remains roughly the same. In particular, in the resonant case IV considered above (corresponding to $\alpha = 1$) there is still a plateau. However, the level of the plateau decreases with increasing oscillation amplitude.

7 Comparison with experiment in the resonant case

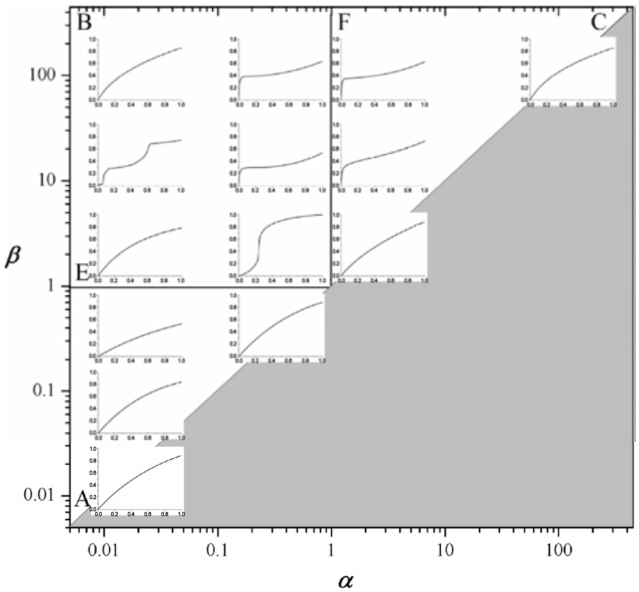

Fig. 7 Typical dependencies of the reduced coefficient of friction μ_{macro}/μ_0 on the dimensionless velocity $\bar{v}$ for the relative oscillation amplitude $\Delta u_z/u_{z,0} = 1.5$ (jumping case).

Of the various cases considered in the above discussion, several were studied experimentally in the past. The case I of a stiff system (or high-frequency oscillation) was studied experimentally, e.g., in Ref. [16]. On the other hand, we are not aware of previous experiments for the resonant case IV. We therefore conducted experiments using a pin-on-disc tribometer (Fig. 8(a)). The natural frequency of the pin was determined by impacting the pin and measuring its damped oscillation with a laser vibrometer (Fig. 8(b)).

As the determined natural frequency was around 800 Hz, the usual method of exciting oscillations with built-in piezo-elements could not be used, and the tribometer was extended with an electromagnetic shaker as shown in Fig. 8(a). The frequency of the shaker was tuned to the natural frequency of the pin, thus creating the conditions of the resonant case IV. The results are presented in Fig. 9. In contrast with non-resonant cases, where the COF increases monotonically with increasing velocity, in the resonant case it was approximately constant (within the relatively large stochastic error).

8 Summary

We presented a general theoretical analysis of the influence of out-of-plane oscillations on the macroscopically observed coefficient of friction. Unlike previous works, we explicitly took into account both the contact stiffness and the stiffness of the measuring system.

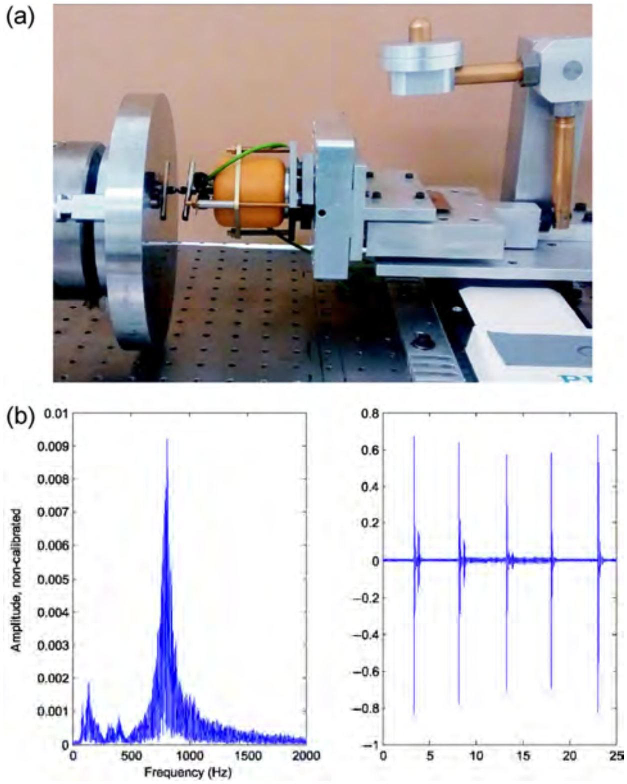

Fig. 8 (a) A photograph of the experimental set-up: a pin-on-disc tribometer is equiped with an electromagnetic shaker producing out-of-plane oscillations at the resonant frequancy of the pin. (b) The resonant frequency was determined by impacting the pin in the tangential direction and determining the Fourier spectrum of the response. The measured natural frequency of the pin was about 800 Hz.

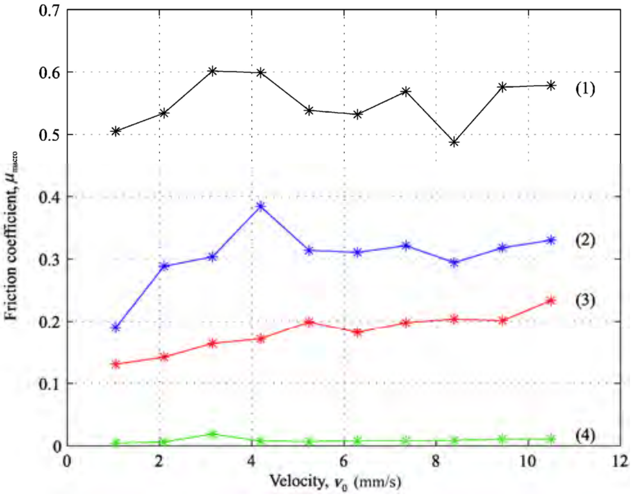

Fig. 9 Dependence of the coefficient of friction on velocity for the resonant case. The oscillation amplitudes were: (1) 1.3 μm; (2) 5.4 μm; (3) 8.2 μm; (4) 60 μm.

The main governing parameters of the resulting system appear to be the ratios of two natural frequencies of the system (one related to the contact stiffness of the system and the other to combined stiffness of the system and contact) to the frequency of the normal oscillation. As observed in previous works, the velocity-dependence of the COF was found to have two main reference points:

(1) The value at vanishing sliding velocity (static coefficient of friction), which naturally does not depend on the dynamic properties and is solely determined by the smallest normal force during the oscillation cycle.

(2) The characteristic velocity above which the COF no longer depends on the sliding velocity and is equal to its microscopic value μ_0.

The only exceptions from this rule are the two resonant cases: One where the COF is constant and equal to μ_0 at all velocities (III) and a second case where the oscillation frequency is equal to the natural frequency of the pin. In this latter case the COF tends to a plateau value below μ_0 and does not have a maximum velocity above which the reduction of the COF disappears. To the best of our knowledge, this resonance case was not studied yet and is described here for the first time.

Figure 10 summarizes schematically the main findings of the present paper. Contrary to the previous figures, we use the non-normalized coefficient of friction and the non-normalized sliding velocity v_0,

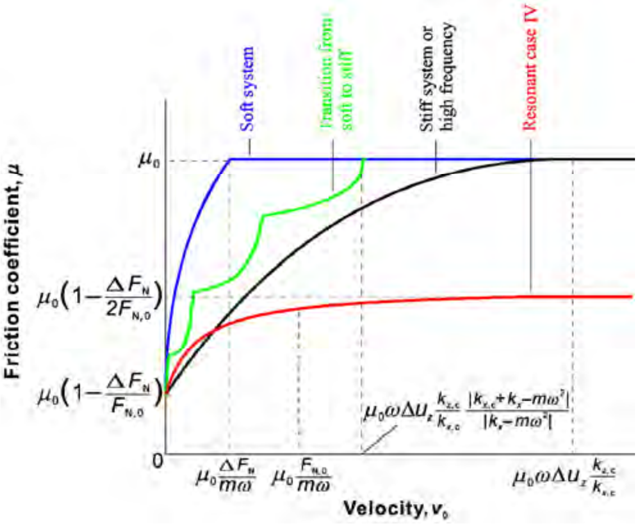

Fig. 10 Schemetic representation of the law of frition (dependence of the friction coefficient on the macroscopic sliding velocity) for different relations between the contact and system stiffness as well as eigenfrequencies and the oscillation frequency.

as this better highlights the main tendencies and is easier to compare with experiment.

All dependencies of the macroscopically observed coefficient of friction start at the same static value $\mu_0(1-\Delta F_{\mathrm{N}}/F_{\mathrm{N},0})$, which is determined by the smallest normal force during the oscillating cycle. The further shape of the law of friction depends strongly on the dynamical properties of the system.

The case of the very soft system (and stiff contact), which was studied theoretically in Refs. [7] and [14], is shown in Fig. 10 with a blue line. In this case, the coefficient of friction first increases very rapidly from the static value, reaches the macroscopic value μ_0 at the critical velocity $\mu_0\Delta F_{\mathrm{N}}/m\omega$ and does not further change with increasing velocity. The critical velocity, in this case, depends solely on the inertial properties of the system, but not on its stiffness. However, in this approximation the theoretical predictions showed poor fit with experimental data [7]. According to Ref. [7] a much better fit to experimental data is achieved if the contact stiffness is taken into account.

The case of finite contact stiffness and very rigid measuring system was considered in detail in the first part of this series [19] and is represented in Fig. 10 with a black curve. The curve starts at the same static value $\mu_0(1-\Delta F_{\mathrm{N}}/F_{\mathrm{N},0})$ of the COF and increases with increasing velocity, however not as rapidly as in the case of the soft system. After reaching the value μ_0 at the critical velocity $\mu_0\omega\Delta u_z k_{z,\mathrm{c}}/k_{x,\mathrm{c}}$, it remains constant. In this case the critical velocity does not depend on inertial properties of the system. However, the contact stiffness also does not enter explicitly into the critical velocity; only the ratio of the normal and tangential stiffness (the Mindlin ratio) appears in the equation. This ratio only depends on the Poisson ratio of the contacting partners and is equal to 1.25 for the typical case of $\nu = 1/3$. As shown in this paper, this case is also applicable at very high oscillation frequencies independently of contact and system stiffness.

The law of friction in the transition region between soft and stiff system is schematically represented by the green curve in Fig. 10. In the transition region the dependencies of the coefficient of friction on the sliding velocities can have a complicated shape and are sensitive to the parameters of the system and the frequency of oscillations (see Figs. 5 and 6). Regardless of this complexity, all curves start at the same static friction value $\mu_0(1-\Delta F_{\mathrm{N}}/F_{\mathrm{N},0})$ and reach μ_0 at the critical velocity given by Eq. (12). Depending on parameters, this velocity can range from zero to infinity.

When approaching the resonant case IV where the frequency of the external oscillation is equal to the natural frequency of the system, the critical velocity tends to infinity and the COF reaches a plateau value less than μ_0. For the exactly resonant case, the COF does not exceed the value $\mu_0(1-\Delta F_{\mathrm{N}}/(2F_{\mathrm{N},0}))$, which is larger than the static value $\mu_0(1-\Delta F_{\mathrm{N}}/F_{\mathrm{N},0})$, but smaller than μ_0 even at very high sliding velocities.

In conclusion, we would like to stress once again that the entire analysis of this paper is based on the assumption that Coulomb's law of friction with a constant coefficient of friction is valid locally, in the immediate contact point. We have shown that the macroscopic behavior can be very non-trivial despite the simplicity of the underlying local law of friction. However, a more general analysis taking into account system dynamics, contact stiffness and changes of local friction may eventually achieve the best fit with experimental data. Nonetheless, we believe that changes in the local COF will not impact the overall classification of the discussed dynamic cases. One of the most robust predictions of the present analysis is the existence of the characteristic velocity above which the coefficient of friction does not depend any more on the presence of oscillations. The existence of such velocity was already confirmed for a more general case of a contact with a viscoelastic material [20].

Acknowledgements

The authors would like to thank Juliane Wallendorf and Qiang Li for their help with preparing figures for the paper. This work was supported in part by Tomsk State University Academic D.I. Mendeleev Fund Program (No. 8.2.19.2015).

References

[1] Siegert K, Ulmer J. Superimposing ultrasonic waves on tube and wire drawing. *J Eng Mater Technol* **123**(724): 517–523 (2000)

[2] Egashira K, Mizutani K, Nagao T. Ultrasonic vibration drilling of microholes in glass. *CIRP Ann Technol* **51**(1): 339–342 (2002)

[3] Godfrey D. Vibration reduces metal to metal contact and causes an apparent reduction in friction. *ASLE Trans* **10**(2): 183–192 (1967)

[4] Fridman H D, Levesque P. Reduction of static friction by sonic vibrations. *J Appl Phys* **30**(10): 1572–1575 (1959)

[5] Broniec Z, Lenkiewicz W. Static friction processes under dynamic loads and vibration. *Wear* **80**(3): 261–271 (1982)

[6] Littmann W, Storck H, Wallaschek J. Sliding friction in the presence of ultrasonic oscillations: superposition of longitudinal oscillations. *Arch Appl Mech* **71**(8): 549–554 (2001)

[7] Teidelt E. Oscillating contacts: Friction induced motion and control of friction. Ph.D. Thesis. Berlin (Germany): Technische Universität Berlin, 2015.

[8] Popov V L, Wetter R. Symmetry breaking as a general design principle of oscillation-based methods for fixation and manipulation of nano-objects. *Advanced Biomaterials and Devices in Medicine* **3**(1): 10–18 (2016)

[9] Weishaupt W. Reibungsverminderung durch mechanische Schwingungen. *Tech Mess* **11**: 345–348 (1976)

[10] Goto H, Ashida M, Terauchi Y. Effects of ultrasonic vibration on the wear characteristics of a carbon steel: Analysis of the wear mechanism. *Wear* **94**(1): 13–27 (1984)

[11] Chowdhury M A, Helali M M. The effect of frequency of vibration and humidity on the coefficient of friction. *Tribol Int* **39**(9): 958–962 (2006)

[12] Chowdhury M A, Helali M M. The effect of amplitude of vibration on the coefficient of friction for different materials. *Tribol Int* **41**(4): 307–314 (2008)

[13] Popov V L, Starcevic J, Filippov A E. Influence of ultrasonic in-plane oscillations on static and sliding friction and intrinsic length scale of dry friction processes. *Tribol Lett*: **39**(1): 25–30 (2010)

[14] Teidelt E, Starcevic J, Popov V L. Influence of ultrasonic oscillation on static and sliding friction. *Tribol Lett* **48**(1): 51–62 (2012)

[15] Milahin N, Li Q, Starcevic J. Influence of the normal force on the sliding friction under ultrasonic oscillations. *Facta Univ Ser Mech Eng* **13**(1): 27–32 (2015)

[16] Milahin N. Robuste Einflussparameter für Reibung und Oberflä-chenmodifizierung unter Einfluss von Ultraschall. Ph.D. Thesis. Berlin (Germany): Technische Universität Berlin, 2016.

[17] Nguyen H X, Teidelt E, Popov V L, Fatikow S. Dynamical tangential contact of rough surfaces in stick-slip microdrives: modeling and validation using the method of dimensionality reduction. *Physical Mesomechanics* **17**(4): 304–310 (2014)

[18] Cabboi A, Putelat T, Woodhouse J. The frequency response of dynamic friction: enhanced rate-and-state models. *Journal of the Mechanics and Physics of Solids* **92**: 210–236 (2016)

[19] Popov M, Popov V L, Popov N V. Reduction of friction by normal oscillations. I. Influence of contact stiffness. *Friction* **5**(1): 45–55 (2017)

[20] Popov M. Critical velocity of controllability of sliding friction by normal oscillations in viscoelastic contacts. *Facta Universitatis, Series: Mechanical Engineering* **14**(3): 335–341 (2016)

Xinyu MAO. Double master degree candidate in the majors of Mechanical Engineering at the Tsinghua University and Engineering Science at the Berlin University of Technology. He obtained his bachelor degree in mechanical engineering at Tsinghua University in 2014. His research interests include tribological simulations, especially friction and wear (fretting) under the action of vibration.

Valentin L. POPOV. Full professor at the Berlin University of Technology, studied physics (1976–1982) and obtained his doctorate in 1985 from the Moscow State Lomonosov University. He worked at the Institute of Strength Physics of the Russian Academy of Sciences. After a guest professorship in the field of theoretical physics at the University of Paderborn (Germany) from 1999 to 2002, he has headed the Department of System Dynamics and the Physics of Friction of the Institute of Mechanics at the Berlin University of Technology. His areas of interest include tribology, nanotribology, tribology at low temperatures, biotribology, the influence of friction through ultrasound, numerical simulation of frictional processes, research regarding earthquakes, as well as topics related to materials science such as the mechanics of elastoplastic media with microstructures, strength of metals and alloys, and shape memory alloys. He has published over 100 papers in leading international journals during the past 5 years. He is the author of the book "*Contact Mechanics and Friction: Physical Principles and Applications*" which appeared in three German, two English, Chinese, and Russian editions and co-author of the book on "*Method of Dimensionality Reduction in Contact Mechanics and Friction*" which appeared in German, English and Chinese editions. He is the joint editor of international journals and regularly organizes international conferences and workshops on diverse tribological themes. He is a member of the Scientific Council of the German Tribological Society. He has intensively collaborated with many industrial corporations and possesses experience in implementing the results of scientific research in industrial applications.

Jasminka STARCEVIC. She is the head of experimental laboratories at the Institute of Mechanics at the Berlin University of Technology. She studied mechanical engineering at the Berlin University of Technology and obtained the degree of Diplom-Ingeneiur in 1997 and the doctorate in 2008. She is a co-author of 25 papers in international journals. Her research interests include physics of friction, active control of friction by ultrasonic oscillations, tribospectroscopy, as well as development of methods for earthquake prediction. She has intensively collaborated with many industrial corporations and possesses experience in implementing the results of scientific research in industrial applications.

Mikhail POPOV. He obtained the bachelor degree in computer science from the Freie Universität Berlin in 2011 and the master degree in engineering science from the Tomsk Polytechnic University and Berlin Technical University in 2016. Currently he is a research assistant at the Tomsk Polytechnic University and Berlin University of Technology. His research interests include efficient numerical methods in tribology, rubber friction, as well as friction and damping under the influence of oscillations.

Friction **5**(2): 207–218 (2017)
DOI 10.1007/s40544-017-0147-9

ISSN 2223-7690
CN 10-1237/TH

RESEARCH ARTICLE

Finger pad friction and tactile perception of laser treated, stamped and cold rolled micro-structured stainless steel sheet surfaces

S. ZHANG[1,2,*], X. ZENG[3], D. T. A MATTHEWS[2,4], A. IGARTUA[5], E. RODRIGUEZ–VIDAL[5], J. CONTRERAS FORTES[6], E. VAN DER HEIDE[2,7]

[1] *State Key Laboratory of Tribology, Tsinghua University, Beijing 100084, China*

[2] *Laboratory for Surface Technology and Tribology, Faculty of Engineering Technology, University of Twente, Drienerlolaan 5, Enschede 7522 NB, the Netherlands*

[3] *Shanghai Advanced Research Institute, Chinese Academy of Sciences, China*

[4] *Tata Steel, Research & Development, PO Box 10000, IJmuiden 1970CA, the Netherlands*

[5] *IK4-Tekniker, C/Ignacio Goenaga 5, Eibar 20600, Spain*

[6] *Acerinox Europa SAU, Los Barrios, Spain*

[7] *TU Delft, Faculty of Civil Engineering and Geosciences, Stevinweg 1, Delft 2628 CN, the Netherlands*

Received: 23 September 2016 / Revised: 30 November 2016 / Accepted: 11 January 2017

Abstract: Tactile perception is a complex system, which depends on frictional interactions between skin and counter-body. The contact mechanics of tactile friction is governed by many factors such as the state and properties of skin and counter-body. In order to discover the connection between perception and tactile friction on textured stainless steel sheets, both perception experiments (subjective) and tactile friction measurements (objective) were performed in this research. The perception experiments were carried out by using a panel test method to identify the perceived roughness, perceived stickiness and comfort level from the participants. For the friction experiments, tactile friction was measured by a multi-axis force/torque transducer *in vivo*. The perceived stickiness was illustrated as an effective subjective stimulus, which has a negative correlation to the comfort perception. No significant evidence was revealed to the connection between the perceived roughness and comfort perception, and this relationship may be influenced by the participants' individual experience, gender and moisture level of skin. Furthermore, the kinetic tactile friction was concluded as an objective stimulus to the comfort perception with a negative correlation.

Keywords: tactile friction; perception; pleasant touch; biotribology

1 Introduction

Tactile comfort, a concept with a mechanical, physiological and a psychological perspective, is of particular concern to industry and academia. The hedonic attributes of tactile comfort are influential to our daily life like wearing clothes, using personal care products, holding tool handles or in domestic appliances [1–3]. In the case of designing hand tools, the relationships of comfort descriptors and comfort factors with users' experiences have been investigated, and the relation with skin friction to enhance the comfort level of products is described in detail [4–6]. In a more prosaic case, the degree of comfort in tactile contact between the skin and stainless steel surface for domestic appliances greatly affects the quality of

---

* Corresponding author: S. ZHANG, E-mail: s.zhang@utwente.nl

our daily life. Stainless steel is one of the most common materials used in automobile, architecture, kitchenware, medical applications, etc. However, the study of perception and friction on stainless steel material is limited. The enhancement of tactile comfort in daily interaction with stainless steel products can directly increase the customers' satisfaction by the stimulation of the somatosensory system in a positive way. A higher added value could be created by understanding the stimulus parameters and pleasantness factors [7] validated by an experimental approach for stainless steel sheet material.

A basic understanding of the skin anatomy is important to tactility-related research. The skin has a complicated structure composed of three main layers: epidermis, dermis and hypodermis [8]. Each layer has a different composition, thickness, hydration degree and mechanical properties [9]. In addition, the state and properties are a function of the body region, age, degree of hydration or nutritional condition as well [10–15]. Overall, the skin behaves in a viscoelastic, non-homogeneous, nonlinear and anisotropic manner under load.

The tactile friction can be influenced by the surface texture during the measurements. According to the work of Tomlinson et al., additional effects including interlocking and hysteresis can be added to adhesion [16, 17]. From the psychological perspective, humans are able to distinguish multidimensional textural stimuli including sensations of roughness versus smoothness, hardness versus softness, stickiness versus slipperiness, and warmth versus coolness [18]. In this paper, the perception experiment was focused on the following three surface properties: hardness, roughness and stickiness. Stainless steel sheet samples were used with the same thermal properties and within the same hardness range, therefore, only roughness and stickiness were variables in this research.

In total, five surface textures are analyzed: four deterministic surface textures with specific geometric shapes, designed for this research, and one conventionally finished sample (2G finish) as reference. Three different surface fabrication methods, i.e., laser surface texturing, stamping (or pressing) and cold rolling were used to produce the experimental surface textures on stainless steel samples. This combination of production technologies is unique and not reported before in surface haptic related research. The objective of this research is to investigate the relationship between tactile comfort and friction, specifically for stainless steel sheet surfaces.

2 Methods

2.1 Subjects and conditions

The finger friction measurements and perception experiments were performed in a controlled laboratory having an ambient temperature of 20 ± 1 °C and relative humidity of 50% ± 10%. The total number of subjects were sixteen (eight female and eight male volunteers) aged from 20 to 30 years with no known skin disease. All tests were conducted on the middle finger of the non-dominant hand to avoid any bias, because the dominant finger (index finger) of the dominant hand can have more wear of the finger ridges due to frequent daily use. No external skin care products were used prior to the experiments. The fingertips were cleaned with alcohol and air-dried for ten minutes before testing. A Corneometer CM 825 (Courage+Khazaka GmbH, Germany) was used to measure the hydration level of the skin (up to 120 AU) before the experiments. The range of hydration level of all subjects was 62~120 AU. The evaluation of hydration related skin types can be categorized by arbitrary units (AU) into: very dry skin (<30 AU), dry skin (30~40 AU), normal skin (40~100 AU), wet skin (100~120 AU), very wet skin (>120 AU) [19].

2.2 Testing objects

Five stainless steel EN-1.4301 tiles, four textured and one conventionally finished surface 2G, were used in the tests (see Table 1 and Figs. 1 & 2). The test areas of samples in contact with fingers during sliding were approximately 30 mm × 30 mm. The 1 mm × 1 mm area of each sample was measured by a three-dimensional (3D) areal confocal microscope (μSURF-mobile, NanoFocus AG, Germany) with a 20× objective (height resolution = 63 nm) and a 4 μm filter. According to the literature, 3D roughness parameters give more complete assessment of the roughness over the surface compared to two-dimensional (2D) roughness parameters on the flat surface structures [20]. The 3D surface

Table 1 The surface parameters of the samples with depth (*D*), spacing (λ), width (*W*), 3D surface roughness (Sa) were measured using a 3D areal confocal microscope (μSURF-mobile, NanoFocus AG, Germany).

Sample name	Fabrication method	Surface texture	Sample size (mm)	Depth, *D* (μm)	Width, *W* (μm)	Spacing, λ (μm)	Sa (μm)
1HV90	Stamping	Crater	35 × 65 ×1	20	50	50	0.49
1HV90-1%	Cold rolling	Grid	35 × 65 ×1	20	50	60	1.34
HDG-1	LST	Grid	35 × 35 ×1	30	75	90	4.02
LDG-3	LST	Grid	35 × 35 ×1	30	100	115	6.56
2G	Cold Rolling	—	35 × 65 ×1	—	—	—	0.13

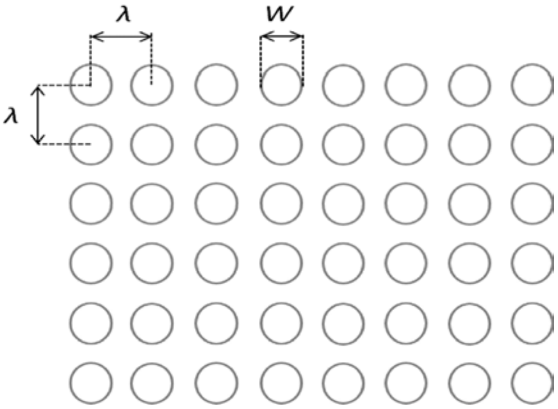

Fig. 1 Texture parameters for crater and grid structures.

roughness Sa of the texture denotes the average vertical deviation at the location of the measured surface area, and is greatly influenced by the height of pattern. Compared to the line roughness Ra, the 3D surface roughness Sa is conducted in an areal measurement which is more accurate to describe the surface characteristic in roughness. Therefore, surfaces of the samples were measured in 3D surface roughness Sa in this work.

All samples were using the same stainless steel sheet material EN-1.4301 with different surface texture produced by various fabrication methods and taken from a large set of microstructured samples based on the topographical quality of the texture produced in an EU project [21]. Sample 1HV90 was fabricated by a stamping method with tools that contain the negative of a crater pattern which is hemispherical (see Fig. 2(a)). The grid pattern on sample 1HV90 with 1% elongation was produced by cold rolling with rolls that contain the negative of the pattern (see Fig. 2(b)). The low density grid pattern on sample

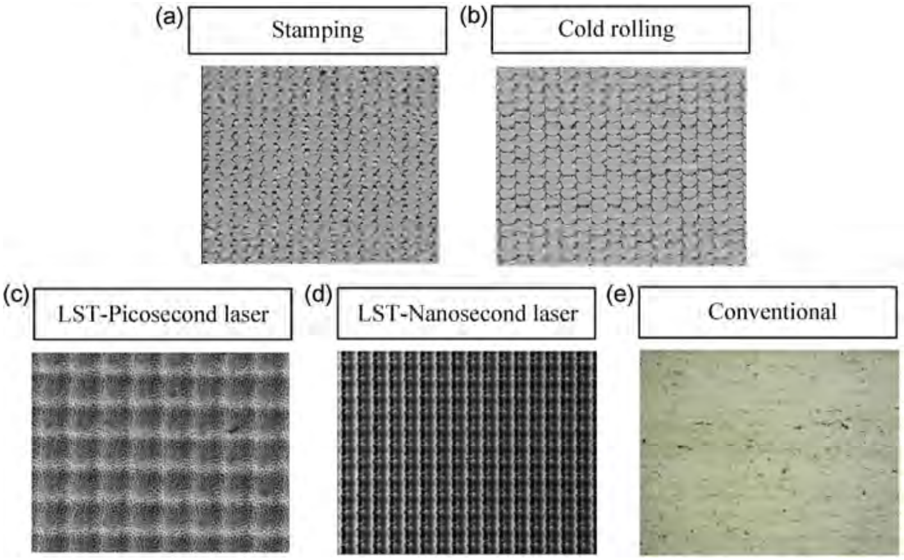

Fig. 2 SEM images of sample (a) 1HV90 (stamping), (b) 1HV90-1% (cold rolling), (c) HDG-1 (LST–Picosecond), (d) LDG-3 (LST–Nanosecond) and (e) 2G (reference).

LDG-3 (see Fig. 2(d)) was produced by direct laser surface texturing with a nano-second laser, and the high density grid pattern on sample HDG-1 (see Fig. 2(c)) was fabricated by direct laser surface texturing (LST, pico-second laser). The sample 2G, produced by cold rolling and subsequent skin pass rolling, was used as received condition and served as a reference specimen for comparison (see Fig. 2(e)). The samples 1HV90, LDG-3 and HDG-1 are specifically designed for touch perception, and produced for the first time.

2.3 Testing methods

The experiments were conducted in two parts: perception experiments (subjective rating) and tactile friction measurements (objective measurement). First, the perception experiments were carried out by using a panel test method to identify the perceived roughness, perceived stickiness and comfort level from the subjects (see Fig. 3(a)). The work of Whitaker shows both vision and touch is able to contribute information to the perception of texture in an independent but complementary manner. The exposure of the object to a visual stimulus can increase or decrease the preference during the touch perception [22]. Therefore, all the participants were blindfolded to avoid vision interference on perception and focus on touch perception only. Before the perception experiments, the participants (all master students from an English-based course) were explained by the author in English, and any rising questions were answered to clear the doubts. The four samples having designed textures and one reference stainless steel samples were presented to the subjects in random order. The subjects were requested to use the middle finger of their non-dominant hand to touch and slide along the sample surface toward the body. The same sliding direction was performed in the friction measurements. According to the previous study, the sliding direction to the texture can alter the kinetic tactile friction between the fingertip and the counter-surface [23]. During the perception tests, the subject had unlimited time to explore the sample before reporting a judgment. The ratings from 0 to 10 were graded by each subject to describe the level of perceived roughness, perceived stickiness and comfort. The higher number represented a greater perception of roughness. The same ten-point scale was used for the perception of surface stickiness and comfort level. The participants may have confusion about the perception of stickiness between stick-slip friction and stickiness-adhesion. Since the assessment was given during the sliding motion, it is more likely the panelists graded the perception of stickiness based on how smooth the motion is. In addition, the subjects may touch and slide the samples more than one time before the grades were given.

For the friction experiments, a multi-axis force/torque transducer (ATI Industrial Automation, Apex, NC, USA) was used to measure kinetic skin friction *in vivo* (see Fig. 3(b)). This apparatus, described in full detail in Ref. [23], is able to measure the outputting forces

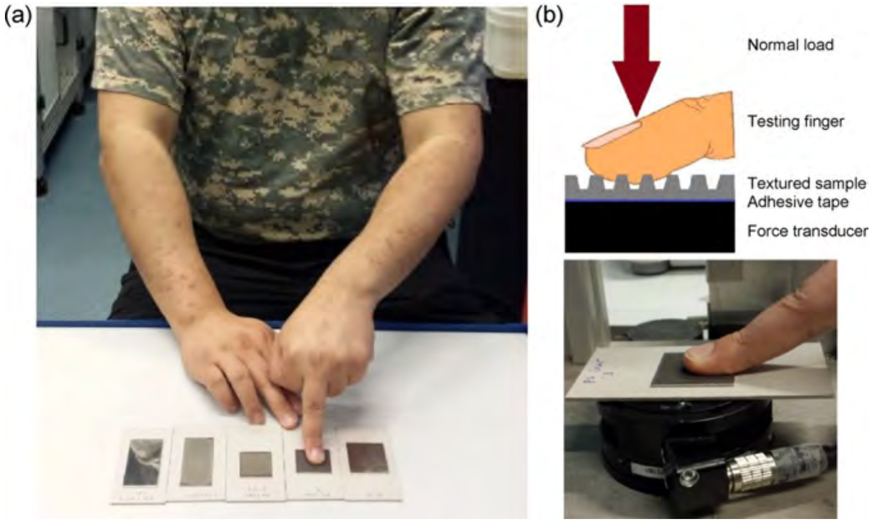

Fig. 3 (a) Perception experiment (blindfolded); (b) friction measurement set-up.

and torques from all three Cartesian coordination (x, y, and z) with the resolution of 25 mN in normal direction and 12.5 mN in tangential direction. Double sided tape was used to firmly fix the testing samples to the top of the force transducer. The same fingers used during the perception tests were used to perform sliding motion on the samples towards the body. Each friction measurement consisted of five repetitions of sliding motion. All participants were instructed to slide in a stable and natural way with no external load. The range of the resulting average normal force was from 0.12 to 0.63 N which can be regarded as light touch conditions (<1 N) (see Fig. 4) [24]. The stroke length was 30 mm for all samples. During the tests, the sliding velocity was kept as constant as possible. The sliding velocity of each friction measurement was recorded by the force transducer. In this manner, the data of friction force and normal load were acquired with a sampling rate of 100 Hz. The values of friction coefficient (COF) were calculated as the ratio of friction force F_f and normal load F_N $\left(\mathrm{COF}=\dfrac{F_f}{F_N}\right)$.

3 Results and discussion

3.1 Friction measurements

The kinetic friction measurements of all sixteen participants on the stainless steel samples are plotted in Fig. 5, and the average values of COF for the five samples were sorted in decreasing order in Fig. 6. From Fig. 5 it shows that certain participants slide their finger pad with higher values of the friction force than other participants, although the counter surface has the same topography. This phenomenon is related to the system dependence of friction, which could be caused by many factors including the resulting contact area, hydration level of skin, and applied load. These factors can be understood from the well-described two-term friction model, for skin friction, which consists of both an adhesive and a deformation component of friction [25, 26].

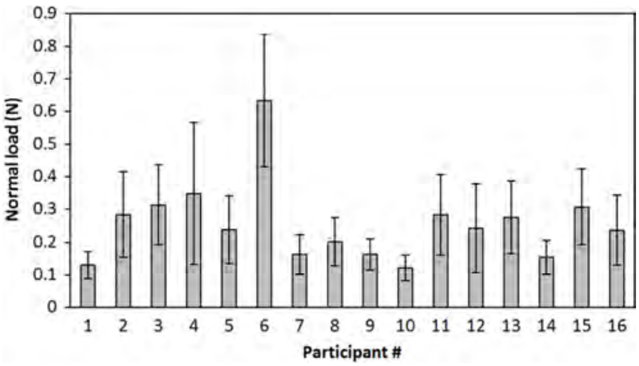

Fig. 4 The average applied normal load (with standard deviation) of each participant during friction measurements.

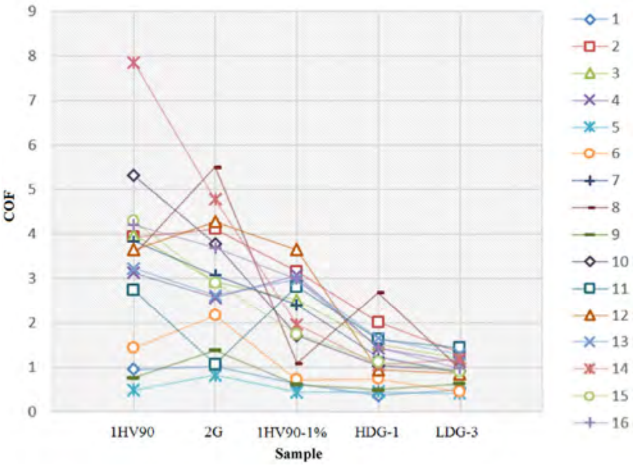

Fig. 5 Finger friction measurements of the participants on the stainless steel samples.

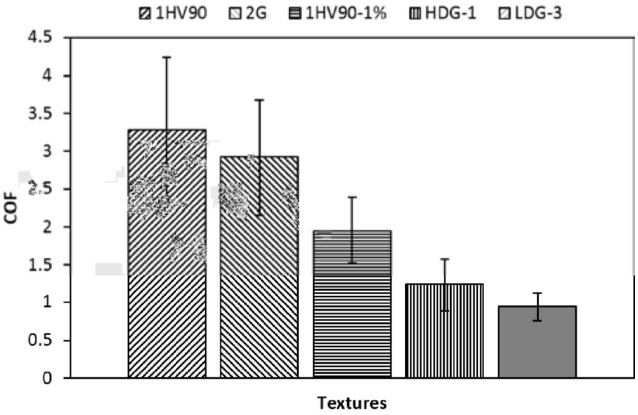

Fig. 6 The average values of COF of the kinetic friction measurements (five sliding cycles) for the 5 samples, sorted in decreasing order.

$$F_{f,tot}=F_{f,adh}+F_{f,def} \tag{1}$$

$$F_{f,adh}=\tau\cdot A_{real} \tag{2}$$

$$F_{f,def}=\frac{3}{16}\beta\frac{\delta}{a}F \tag{3}$$

where F is the normal load; A_{real} is the real contact area; τ is the shear strength of the interface; a is the contact radius of the fingertip; β is the viscoelastic loss fraction and δ is the indentation of the skin. Related studies show that adhesive component of friction plays the dominant role in skin friction and greatly depends on the real contact area [27, 28].

The hydration level is another important element of skin friction. Related studies suggest that the increased hydration level of skin can increase the values of COF [29–31], and it is an influential factor in the tactile friction measurement. According to the literature, with the same real contact area, the moist skin has a lower elastic modulus, which leads to the increase of the adhesive component of friction [32]. In our case, the hydration level of all participants ranged from 62 AU to 120 AU with an average value of 90.9 ± 17.8 AU. Except for participant #5 (119.7 AU) and participant #14 (111.2 AU), the skin type of most participants can be categorized as normal skin (40~100 AU). These two outliers are close to the average value. In this case, the influence of hydration level is limited compared to other factors.

Furthermore, the relationship between the normal load and COF needs to be discussed. In the literature, a linear relationship was found over the load range of 1 N [33, 34]. In our case, the overall normal load ranged from 0.13 N to 0.63 N with an average normal load of 0.25 ± 0.12 N, and the lower normal loads were slightly employed with the higher values of COF (see Fig. 7). Moreover, the sliding velocity can affect the frictional response as well. The force transducer recorded the sliding velocity of each friction measurement, and the sliding velocity of all participants ranged from 25 mm/s to 124 mm/s. According to the research conducted by Tang et al., as the sliding velocity increases, the kinetic tactile friction increases accordingly due to the hysteretic friction with more energy lost in elastic hysteresis [35]. Tang et al. found that values of COF were larger when sliding velocity increased from 0.5 mm/s to 4 mm/s and the “stick-slip” phenomenon became severer. Therefore, the variations of kinetic skin friction from Fig. 5 can be explained by contact area, hydration level and sliding velocity of each subject. From Fig. 6, it shows that even with the influence described above, certain texture shows higher average value of COF, for example, the texture 1HV90 (crater) has the highest COF compared to others.

More importantly, the surface roughness of the counter-surface was investigated. The measured values of the 3D surface roughness Sa are listed in Table 1 which shows that the laser surface textured samples in general are rougher than both the stamped samples and the reference sample. In this research, the reference stainless steel sample (2G) had the lowest 3D surface roughness Sa. As shown in Fig. 8, a significant reduction in COF is observed with the sample of higher surface roughness, and illustrating that higher 3D surface roughness Sa result in lower tactile friction with a determination coefficient of 0.8313. A similar phenomenon was found in the study of Derler [32], that the adhesive component of skin friction is reduced when sliding against a rough glass surface. In our case, the normal load is less than 1 N which is considered in the light touch regime, therefore, the possible indentation of the skin is relatively smaller than the surface texture under partial contact condition. When in contact with the rougher surface, the skin has a smaller contact area, and lower friction force is generated. Under a constant normal force, the coefficient of friction is reduced significantly, in the current case

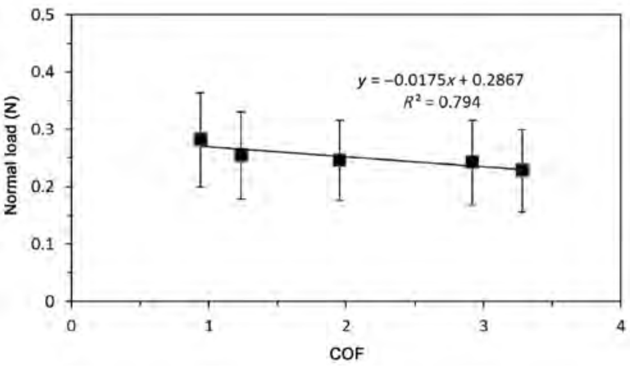

Fig. 7 The average normal load versus COF.

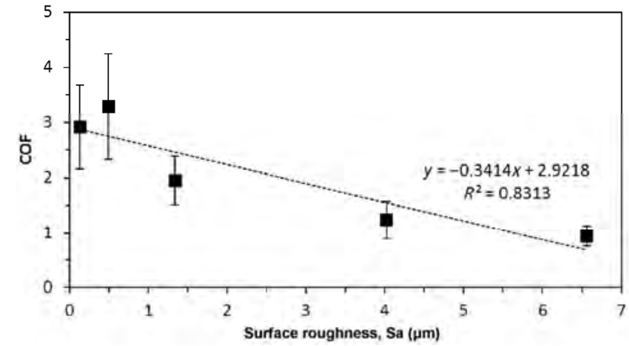

Fig. 8 COF versus measured 3D surface roughness Sa.

with 250% reduction compared between the lowest COF with the reference sample.

3.2 Perceived roughness & stickiness

The magnitude estimation method is considered as one of the most common psychophysical methods for the perception experiments. In our case, the perceived roughness and perceived stickiness were ratio scaled by the participants from 0 to 10 based on the intensity of impression towards the stimulus. Compared to the smaller ratio scale like from 1 to 5, the larger numeric range (from 0 to 10) gave wider perceptual intensity to the individual participants to better describe their natural perception towards the stimulus. In addition, the estimations were then normalized and calculated into the geometric mean.

The perceptual properties of roughness and stickiness are two important elements that contribute to the perception of texture. In this research, the goals of perceived roughness and perceived stickiness were conducted in two parts: (a) perceptual discrimination; and (b) the influence of kinetic tactile friction. As the part (a), we first need to determine whether the participants were able to distinguish the perceptual stimuli like the perceived roughness and perceived stickiness. In our case, the subjects were able to discriminate the perceived stickiness of the samples, and the relationship between the perceived stickiness and 3D surface roughness Sa is in a negative correlation (R^2 = 0.8001) (see Fig. 9(b)). Moreover, the perceived roughness is consistent with measured 3D surface roughness Sa, and a positive correlation was found (R^2 = 0.7434) (see Fig. 9(a)). The results show that the participants can distinguish a set of stainless steel samples in terms of stickiness and roughness. Early research found that subjects were able to discriminate pattern height with difference of 1 μm to discriminate the perceived roughness of sandpaper and ridged stainless steel samples with different surface roughness [36]. According to the recent research conducted by Skedung et al., the tactual perception of human finger is able to perceive features of surface textures as small as submicron in both wavelength and amplitude [37]. In our case, the 3D surface roughness Sa was ranged from 0.49 μm to 6.56 μm.

The influences of kinetic tactile friction were also concerned in this study. Figure 9(c) reveals the negative correlation of perceived roughness with the values of COF from the friction measurements (R^2 = 0.7312). According to the research conducted by Smith et al.,

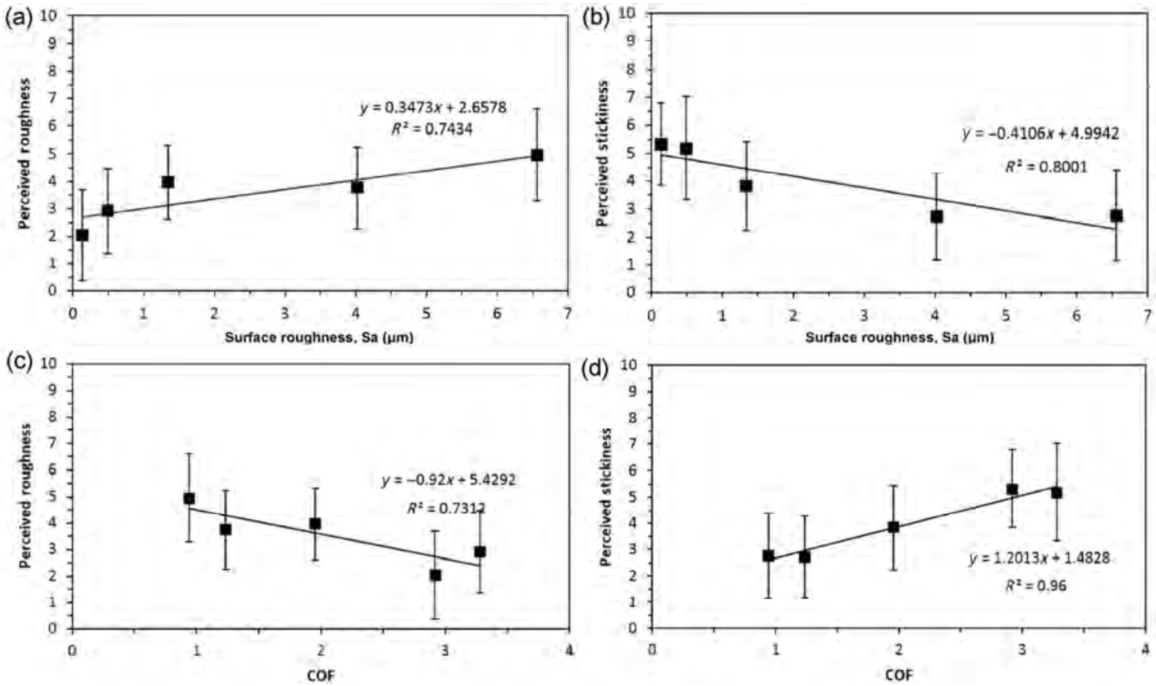

Fig. 9 Geometric mean of perceived roughness versus (a) 3D surface roughness Sa, and (c) COF; and geometric mean of perceived stickiness versus (b) surface roughness Sa, and (d) COF.

the sensation of roughness (perceived roughness) is a reflection of variation in tangential force [38]. The changes of spacing and height would contribute to the variations in kinetic tactile friction, which ultimately affect the perception of roughness. In Fig. 9(d), the perceived stickiness was found to have a positive correlation with COF ($R^2 = 0.96$). The results revealed that the perceived stickiness was significantly influenced by the variation of friction, and similar phenomenon was found in the study of Hollins et al. [39].

3.3 Comfort Level

The impression and emotional feeling of an object by touch becomes apparent through sensation, perception and cognition [40]. Moreover, the perception of pleasantness (comfort) is individual, subjective and closely related to the properties of counter-body. From research on multidimensional subjective experience of surface texture, perceptual stimuli of cold-warm, hard-soft, smooth-rough and slippery-sticky can be extracted as four principal subjective dimensions [41–43]. Stainless steel EN-1.4301 was used as the material for all samples, therefore, the perceptual dimension of hard-soft did not apply to this study. Same for the perceptual stimuli of cold–warm, which is same for the same material. In addition, one important physical dimension of kinetic tactile friction was concerned. As such, it becomes possible to explore the relation between the physical stimulus of finger pad friction, and the perceptual stimuli of roughness and stickiness to comfort (or pleasant) touch.

Based on the perception experiments, the relationship between the comfort level and perceived roughness shows no correlation with determination coefficient of 0.2473 (see Fig. 10(a)). This indicates that the perceived roughness is an insignificant stimulus for pleasant touch. According to the literature, the relationship between comfort level and perceived roughness can be biased upon subjects' experiences in tactile sensation [44]. In another study of Barnes et al. [45] on surface and touch, the influence of perception with measured roughness was investigated and no clear relationship was found between roughness and feeling. However, the perceived stickiness shows a negative influence on comfort perception with a rather high coefficient of determination ($R^2 = 0.7214$) (see Fig. 10(b)). Based on the results, the sample HDG-1 and sample LDG-3 showed the highest comfort level when the perceived stickiness decreased (See Table 2). It appears that the perceived stickiness is a dominant

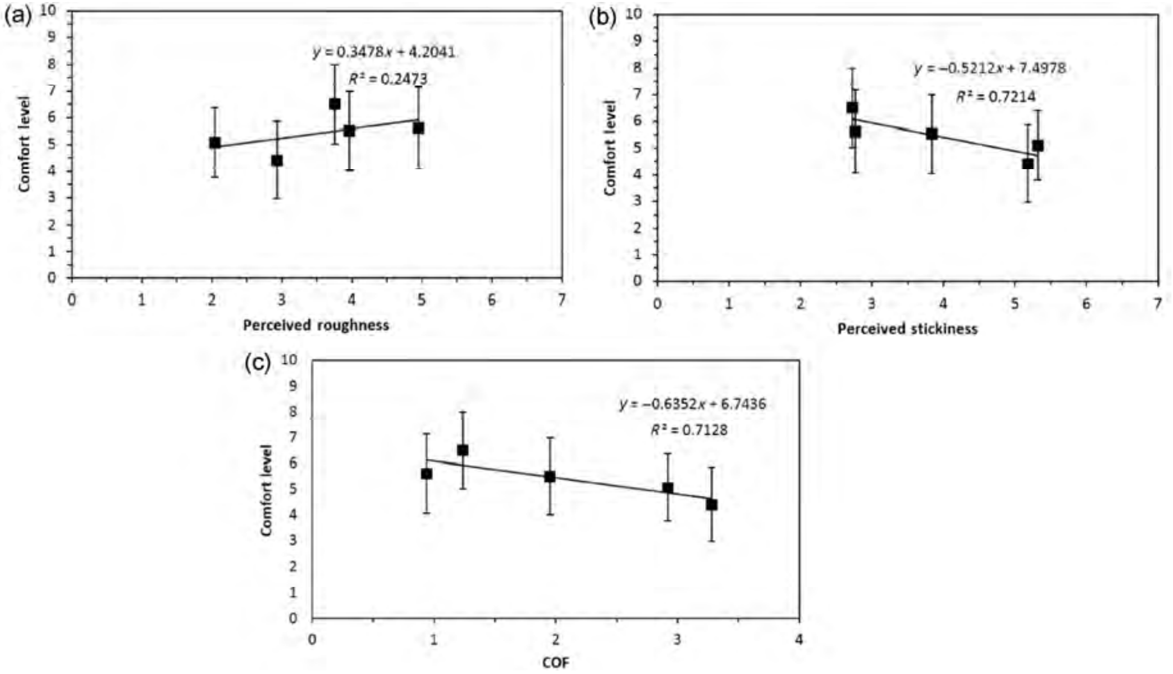

Fig. 10 Geometric mean of (a) comfort level versus perceived roughness; (b) comfort level versus perceived stickiness; (c) comfort level versus COF.

Table 2 The geometric mean of perceived stickiness, perceived roughness, comfort level of sixteen participants from perception experiments; the average values of COF with standard deviations (STD) from friction measurements.

Sample name	Comfort level	STD	Perceived stickiness	STD	Perceived roughness	STD	COF	STD
HDG-1	6.5	1.5	2.7	1.5	3.8	1.5	1.24	0.34
LDG-3	5.6	1.5	2.8	1.6	5.0	1.7	0.94	0.18
1HV90-1%	5.5	1.5	3.8	1.6	4.0	1.3	2.03	0.49
2G	5.1	1.3	5.3	1.5	2.0	1.7	2.92	0.76
1HV90	4.4	1.4	5.2	1.9	2.9	1.5	3.28	0.96

perceptual stimulus to affect the level of comfort on the same type of material (same hardness). However, the perceived roughness did not align a meaningful dimension in the comfort level of perception.

In the study on the physical factors influencing pleasant touch, Ref. [7] shows that participants rated comfort level based on the comparison of the friction forces during the perception experiments. In the current case, friction was used as a physical stimulus to the comfort level, based on a crater and grid texture design. From the results, the geometry of grid can change the surface roughness greatly and had a better effect in reducing the kinetic skin friction compared to the crater structure and reference sample. A clear negative correlation was found between the level of comfort and the COF with the determination coefficient of 0.7128 (see Fig. 10(c)). The comfort level increases when the tactile friction between the skin and counter-surface decreases which is consistent with the experimental results of Klöcker et al. [7]. Therefore, the kinetic tactile friction can be concluded as a physical stimulus to predict the comfort feeling based on the experimental data. And grid structure is one unique and desired texture to create high comfort touch conditions.

4 Conclusions

In this research, subjective and objective measurements were performed by sixteen participants on five different stainless steel samples with designed microstructured surfaces. Based on the results of perception tests (subjective measurements) and friction measurements (objective measurements), the conclusions can be summarized as follows:

(1) The participants had the ability to distinguish the perceived roughness and stickiness of the counter-surface by touching the objects in sliding motion. The perceived roughness was consistent with 3D surface roughness Sa in a positive correlation. And the perceived stickiness was found to correlate in a negative relationship with 3D surface roughness Sa. In addition, both perception of stickiness and roughness can be influenced by the variation of kinetic tactile friction.

(2) From the subjective perspective, the perceived stickiness was illustrated as a perceptual stimulus which was able to influence the comfort level of perception in a negative correlation. However, the effect of the perceived roughness was insignificant in the connection to the perception of comfort.

(3) From the objective perspective, the kinetic tactile friction was proved to be an effective physical stimulus which has a negative correlation to the comfort perception.

The results of this study can be beneficial to understand the relationship between the tactile friction and perceptual attributes including perceived roughness, perceived stickiness and comfort level. In the future research, the effect of temperature on tactile friction and perception will be investigated.

Acknowledgments

This work was supported by the Research Programme of the Research Fund for Coal and Steel, under Contract No. RFSR-CT-2011-00022.

References

[1] Schreiner S, Rechberger M, Bertling J. Haptic perception of friction─Correlation friction measurements of skin against polymer surfaces with subjective evaluations of the surfaces' grip. *Tribology International* **63**: 21–28 (2011)

[2] Tang W, Bhushan B. Adhesion, friction and wear characterization of skin and skin cream using atomic force microscope. *Colloids and Surfaces B: Biointerfaces* **76**: 1–15 (2010)

[3] Harih G, Dolsak B. Tool-handle design based on a digital human hand model. *International Journal of Industrial Ergonomics* **43**(4): 288–295 (2013)

[4] Kuijt-Evers L F M, Groenesteijn L, de Looze M P, Vink P. Identifying factors of comfort in using hand tools. *Applied Ergonomics* **35**: 453–458 (2004)

[5] Kuijt-Evers L F M, Vink P, de Looze M P. Comfort predictors for different kinds of hand tools: Differences and similarities. *International Journal of Industrial Ergonomics* **37**: 73–84 (2006)

[6] Ramalho A, Szekeres P, Fernandes E. Friction and tactile perception of textile fabrics. *Tribology International* **63**: 29–33 (2013)

[7] Klöcker A, Oddo CM, Camboni D, Penta M, Thonnard J L. Physical factors influencing pleasant touch during passive fingertip stimulation. *PLOSONE* **9**(7): e101361 (2014)

[8] Haggard P. Sensory neuroscience: from skin to object in the somatosensory cortex. *Current Biology* **20**: 884–886 (2006)

[9] Nakanishi Y. *Hydrated Materials: Applications in Biomedicine and the Environment*. Singapore: Pan Stanford Publishing Pte. Ltd, 2015.

[10] Lapière C M. The ageing dermis: The main cause for the appearance of "old" skin. *British Journal of Dermatology* **122**: 5–11 (1990)

[11] Hendriks C P, Franklin S E. Influence of surface roughness, material and climate conditions on the friction of human skin. *Tribology Letters* **37**: 361–373 (2010)

[12] Derler, S, Huber R, Feuz H P, Hadad M. Influence of surface microstructure on the sliding friction of plantar skin against hard substrates. *Wear* **267**: 1281–1288 (2009)

[13] Diridollou S, Vabre V, Berson M, Vaillant L, Black D, Lagarde J M, Grégoire J M, Gall Y, Patat F. Skin ageing: changes of physical properties of human skin *in vivo*. *International Journal of Cosmetic Science* **23**: 353–362 (2001)

[14] Cua A B, Wilhelm K P, Maibach H I. Frictional properties of human skin: relation to age, sex and anatomical region, stratum corneum hydration and trans epidermal water loss. *British Journal of Dermatology* **123**: 473–479 (1990)

[15] Veijgen N K, Masen M A, van der Heide E. Relating friction on the human skin to the hydration and temperature of the skin. *Tribology Letters* **49**: 251–261 (2013)

[16] Tomlinson S E, Carré M J, Lewis R, Franklin S E. Human finger contact with small, triangular ridged surfaces. *Wear* **271**(9–10): 2346–2353 (2011)

[17] Tomlinson S E, Lewis R, Carré M J, Franklin S E. Human finger friction in contacts with ridged surfaces. *Wear* **301**(1–2): 330–337 (2013)

[18] Bensmaia S, Manfredi L. The sense of touch. *Encyclopedia of Human Behavior* **2**: 379–386 (2012)

[19] Heinrich U, Koop U, Leneveu-Duchemin M C, Osterrieder K, Bielfeldt S, Chkarnat C, Degwert J, Hantschel D, Jaspers S, Nissen H P, Rohr M, Schneider G, Tronnier H. Multicentre comparison of skin hydration in terms of physical-, physiological- and product-dependent parameters by the capacitive method. *International Journal of Cosmetic Science* **25**: 45–53 (2003)

[20] Durakbasa M N, Osanna P H, Demircioglu P. The factors affecting surface roughness measurements of the machined flat and spherical surface structures─The geometry and the precision of the surface. *Measurement* **44**(10): 1986–1999 (2011)

[21] van der Heide E, Saenz de Viteri V, Rodringuez-Vidal E, Pagano F, Wadman B, Wiklund D, Matthews D T A, Contreras Fortes J, Zhang S. *Steel Sheet Surfaces with Enhanced Tactile Feel*. Luxembourg: RFCS Publications, 2016.

[22] Whitaker T, Simoes-Franklin C, Newell N F. Vision and touch: independent or integrated systmens for the perception of Texture. *Brain Research* **1242**: 59–72 (2008)

[23] Zhang S, Rodriguez Urribarri A, Morales Hurtado M, Zeng X, van der Heide E. The role of the sliding direction against a grooved channel texture on tool steel: An experimental study on tactile friction. *International Journal of Solids and Structures* **56**–**57**: 53–61 (2015)

[24] Lackner J R, Dizio P, Jeka J, Horak F, Krebs D, Rabin E. Precision contact of the fingertip reduces postural sway on individuals with bilateral vestibular loss. *Experimental Brain Research* **126**: 459–466 (1999)

[25] Adams M J, Briscoe B J, Johnson S A. Friction and Lubrication of Human Skin. *Tribology Letters* **26**(3): 239–253 (2007)

[26] Duvefelt K, Olofsson U, Johannesson C M, Skedung L. Model for contact between finger and sinusoidal plane to evaluate adhesion and deformation component of friction. *Tribology International* **96**: 389–394 (2016)

[27] Greenwood J A, Tabor D. The friction of hard sliders on lubricated rubber: The importance of deformation losses. *Proceedings of the Physical Society* **71**(6): 989–1001 (1958)

[28] Johnson S A, Gorman D M, Adams M J, Briscoe M J. The friction and lubrication of human stratum corneum. In *Proceedings 19th Leeds-Lyon Symposium on Tribology*, Leeds, UK, 1993: 663–672.

[29] El-Shimi A F. In vivo skin friction measurements. *Journal of the Society of Cosmetic Chemists* **28**: 37–51 (1977)

[30] Comaish S, Bottoms E. The skin and friction: deviations from Amonton's laws, and the effects if hydration and lubrication. *British Journal of Dermatology* **84**: 37–43 (1971)

[31] Nacht S, Close J, Yeung D, Gans E H. Skin friction coefficient: Changes induced by skin hydration and emollient application and correlation with perceived skin feel. *Journal of the Society of Cosmetic Chemists* **32**: 55–65 (1981)

[32] Derler S, Gerhardt L C, Lenz A, Bertaux E, Hadad M. Friction of human skin against smooth and rough glass as a function of the contact pressure. *Tribology International* **42**: 1565–1574 (2009)

[33] Childs T H C, Henson B. Human tactile perception of screen-printed surfaces: Self-report and contact mechanics experiments. *Proc IMechE, Part J: J Engineering Tribology* **221**: 427–441 (2007)

[34] Skedung L, Danerlov K, Olofsson U, Aikala M, Niemi K, Kettle J. Finger-friction measurements on coated and uncoated printing papers. *Tribology Letters* **37**: 389–399 (2010)

[35] Tang W, Ge S, Zhu H, Cao X, Li N. The influence of normal load and sliding speed on frictional properties of skin. *Journal of Bionic Engineering* **5**: 33–38 (2008)

[36] Miyaoka T, Mano T, Ohka M. Mechanisms of fine-surface-texture discrimination in human tactile sensation. *Journal of the Acoustical Society of America* **105**: 2485–2492 (1999)

[37] Skedung L, Arvidsson M, Chung J Y, Stafford C M, Berglund B, Rutland M W. Feeling small: exploring the tactile perception limits. *Scientific Reports* **3**: 1–6 (2013)

[38] Smith A M, Chapman C E, Deslandes M, Langlais J S, Thibodeau M P. Role of friction and tangential force variation in the subjective scaling of tactile roughness. *Experimental Brain Research* **144**: 211–223 (2002)

[39] Hollins M, Lorenz F, Seeger A, Taylor R. Factors contributing to the integration of textural qualities: Evidence from virtual surfaces. *Somatosensory and Motor Research* **22**(3): 193–206 (2005)

[40] Lui X, Yue Z, Cai Z, Chetwynd D G, Smith S T. Quantifying touch-feel perception: tribological aspects. *Measurement Science and Technology* **19**(8):817–822 (2008)

[41] Skedung L, Danerlov K, Olofsson U, Johannesson C M, Aikala M, Kettle J, Arvidsson M, Berglund B, Rutland M W. Tactile perception: Finger friction, surface roughness and perceived coarseness. *Tribology International* **44**: 505–512 (2011)

[42] Hollins M, Faldowski R, Rao S, Young F. Perceptual dimensions of tactile surface texture: a multidimensional scaling analysis. *Perception & Psychophysics* **54**: 697–705 (1993)

[43] Picard D, Dacremont C, Valentin D, Giboreau A. Perceptual dimensions of tactile textures. *Acta Psychologica*ol **114**: 165–184 (2003)

[44] Annett J. Subjective rating scales: science or art. *Ergonomics* **45**: 966–987 (2002)

[45] Barnes C J, Childs T H C, Henson B, Southee C H. Surface finish and touch–a case study in a new human factors tribology. *Wear* **257**: 740–750 (2004)

Sheng ZHANG. He received his bachelor degree in mechanical engineering in 2008 from California State University (USA), and obtained his Ph.D degree in mechanical engineering at University of Twente (the Netherlands) in 2016. His current position is a post-doctoral researcher in the State Key Laboratory of Tribology at Tsinghua University. His research interests include bio-tribology and surface texture design.

Emile VAN DER HEIDE. He obtained his M.Sc. and Ph.D degrees in mechanical engineering from University of Twente in 1995 and 2002. His current position is a professor, chair of Skin Tribology, Laboratory for Surface Technology and Tribology, Faculty of Engineering Technology, University of Twente. He has received President's International Fellowship 2016/17 from Chinese Academy of Sciences. His research areas cover the surface engineering, bio-tribology and contact mechanics.

Friction **5**(2): 219–230 (2017) ISSN 2223-7690
DOI 10.1007/s40544-017-0152-z CN 10-1237/TH

RESEARCH ARTICLE

Nano-montmorillonite-doped lubricating grease exhibiting excellent insulating and tribological properties

Zhengfeng CAO, Yanqiu XIA[*], Xiang XI

School of Energy Power and Mechanical Engineering, North China Electric Power University, Beijing 102206, China

Received: 28 October 2016 / Revised: 13 January 2017 / Accepted: 10 February 2017

Abstract: Three types of nano-montmorillonite were doped as additives to afford lubricating greases. The physicochemical, insulating, and tribological performances of the obtained lubricating greases were investigated in detail. Furthermore, the tribological action mechanisms were analyzed by high magnification optical microscope, Raman spectroscopy, and energy dispersive X-ray spectroscope (EDS). The results show that the inorganic modification montmorillonite (IOMMT) can significantly increase the number of electron traps in the base grease, leading to excellent insulating performances. Moreover, IOMMT as a novel lubricant additive (1.5 wt% in grease) significantly enhances the friction reducing and anti-wear abilities for steel/steel contact that comprises a unique layered structure to prevent friction between the contact pairs and the protective tribofilm generated by physical adsorption and chemical reaction.

Keywords: nano-montmorillonite; insulation; friction and wear

---

1 Introduction

The primary function of lubricating agents as engineering materials is to enhance equipment efficiency, reduce frictional loss, and extend the service life of machines [1–3]. However, since mechanical equipments are used in various fields, they present some special demands apart from excellent friction reducing and anti-wear properties. For instance, the lubricating greases applied in some electrical equipment should possess good conductive capacity [4–6], whereas the space lubricating greases should maintain long-term reliability under high-energy irradiation, high vacuum, and high/low temperature [7–10]. Lubricating grease applied in some electrical devices, such as a cable connector, a battery terminal, or a plug connection, should exhibit high levels of insulation to eliminate discharge and excellent tribological properties to reduce frictional loss generated by frequent operations [11–13]. We have proved in our previous study that the greases synthesized with nanometer SiO_2 and TiO_2 have an outstanding insulation and tribological performance [11].

Montmorillonite (MMT) is a type of natural nanometer silicate mineral with a layered structure. It has drawn intensive attention across the industry and academia because of its unique performance, including high strength, large special surface area (SSA), superior insulating property, outstanding adsorption capacity, and novel tribological performances. Furthermore, MMT has a sandwich structure, wherein the upper and lower layers are silicon–oxygen tetrahedrons and the middle layer is aluminum–oxygen octahedron. Moreover, exchangeable cations, such as Na^+, Mg^+, and Al^+, exist between the layers [14–18]. Due to its unique characteristics of having a nano-scale layered structure and exchangeable cations, MMT can be easily modified and used for various applications. There are two methods to modify MMT: organic modification (OMMT) and inorganic modification (IOMMT). The modified MMT possesses higher SSA, adsorption capacity, and dispersive capacity, and it is widely

---

[*] Corresponding author: Yanqiu XIA, E-mail: xiayq@ncepu.edu.cn

applied in the composite, electrical engineering, and medical fields [19–21]. Pojanavaraphan et al. found that MMT significantly improved the material properties, including the mechanical, rheological, and swelling behavior in aerogel/pre-vulcanized natural rubber composites produced by freezing-drying [22]. Rashmi et al. reported that the epoxy nanocomposite with 5 wt% OMMT exhibited outstanding wear resistance [23]. Yuan et al. prepared a novel cellulose insulating paper with modified MMT and the breakdown voltage was increased from 50.3 kV to 56.9 kV [24]. Fan et al. investigated the tribological properties of a self-lubricating liner based on MMT reinforced phenolic nanocomposites and found that the addition of 2 wt% OMMT induced the required friction and wear properties [25].

In this study, new types of lubricating greases exhibiting excellent insulating and tribological performances were synthesized with nano-montmorillonite and SiO_2. The insulating and tribological performances of the lubricating greases were investigated using an automatic electrical breakdown tester, volume resistivity tester, and a MFT-R4000 reciprocation friction and wear tester. High magnification optical microscopy, Raman spectroscopy, and energy dispersive X-ray spectroscopy (EDS) were also employed to explore the lubricating mechanisms.

2 Experimental details

2.1 Materials

Based on the Lv's work and our previous article [11, 26, 27], naphthenic oil (25# Karamay transformer oil) was selected as the base oil, and Table 1 shows its typical characteristics. Polytetrafluoroethylene (PTFE, Dyneon^{TM} TF9207,) with a density of 2.2 g/cm^3 and 4-μm grain size was used as a thickener and analytically pure acetone (Sinopharm Chemical Reagent Co., Ltd.) was used as a polar dispersant. Three types of nano-montmorillonite and nano-SiO_2 were purchased from Haichengxingye Technology Co., Ltd (Shenzhen, China) and DK Nano-technology (Beijing, China), respectively. Table 2 lists the typical characteristics and Fig. 1 shows the Fourier transform infrared spectrum of nano-montmorillonite.

Table 1 Typical characteristics of the naphthenic oil.

Item	25# Karamay	Standard
Kinematic viscosity (40 ˚C) (mm^2/s)	9.936	ASTM D445
Density (20 ˚C) (kg/m^3)	883	ASTM D4052
AC breakdown voltage (2.5 mm gap) (kV)	60	ASTM D149
Pour point (˚C)	−35	ASTM D97
Flash point (˚C)	145	ASTM D92
Acid value (mgKOH/kg)	0.02	ASTM D664
Moisture (mg/kg)	<30	ADTM D6304

Table 2 Main characteristics of the nano-montmorillonite and nano-SiO_2.

Item	MMT	OMMT	IOMMT	SiO_2
Grain size (nm)	70−80	70−80	70−80	30−40
Density (g/m^3)	2.5−3	2.5−3	2.5−3	2.2
Purity (wt%)	98%	98%	98%	98%
SSA (m^2/g)	80	320	200	300

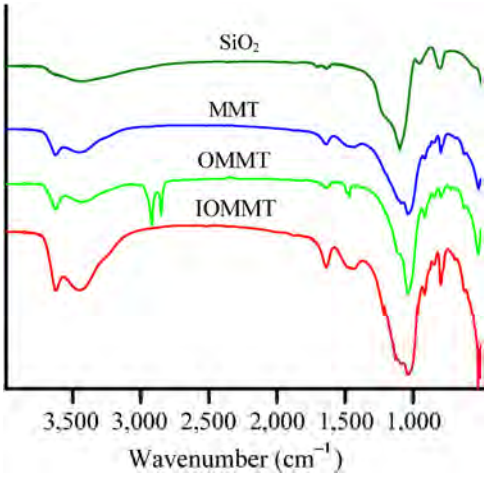

Fig. 1 Fourier transform infrared analysis spectra of the MMT, OMMT, IOMMT and SiO_2.

In the curves of the three types of MMT, the peaks from 3,450 cm^{-1} to 3,650 cm^{-1} and 1,480 cm^{-1} to 1,630 cm^{-1} are assigned to the stretching vibration and bending vibration, respectively, of H–O–H. These peaks prove that absorbed water exists between the MMT layers, and crystal water is present as the lattice. The peak at 1,030 cm^{-1} is attributed to the stretching vibration of Si–O–Si, whereas the peak at about 700 cm^{-1} is assigned to flexural vibration of Si–O tetrahedron and Al–O octahedron. There are also some typical peaks (520 cm^{-1}

and 860 cm^{-1}) in the infrared spectra of silicate. These are assigned to the stretching vibrations and flexural vibration of Si–O–Al. In the infrared spectra of the OMMT, the obvious peaks at 2,850–2,920 cm^{-1} are attributed to the stretching vibration bands of –CH_3 and –CH_2, respectively [25, 28, 29]. It indicates that organic chains exist between the MMT layers.

2.2 Preparation of the insulating greases

The insulating greases were synthesized by the following procedures. First, the base oil (70%, mass fraction, the same hereafter) was infused into the reaction vessel and agitated at once. Second, the PTFE powder (30%) and lubricating additives were gently poured into the vessel and fiecely agitated. As the base oil was blended homogenously with the PTFE powder, acetone, whose mass was approximately half of the PTFE, was injected dropwise and agitated for about 30 min to confirm that the PTFE powder was entirely homo-dispersed within the base oil. Third, the compound was warmed to 80 °C for another 30 min to remove acetone. Last, the mixture was cooled to room temperature, and the insulating grease was obtained after three steps of fine grinding/homogenization with a three-roller mill.

2.3 Characterization of the insulating greases

The HJC-50 kV automatic 50-Hz electrical breakdown tester (Huayang equipment CO., LTD) was employed to determine the alternating current (AC) breakdown voltage of the insulating greases according to GB/T 1408. The electrical breakdown tester consists of plate electrodes, and the distance between the plate electrodes was 1.5 mm (Fig. 2). The voltage rate was set to 0.2 kV/s. All the tests were conducted at room temperature and each experiment was repeated two times to ensure the reliability of the data, with a third test if the relative error was greater than 5%. The surface volume resistivity of the prepared grease was acquired using GEST-121 surface volume resistivity. The penetration, dropping point, and copper strip tests were conducted according to the national standards, including GB/T 269, GB/T 3498, and GB/T 7326, respectively.

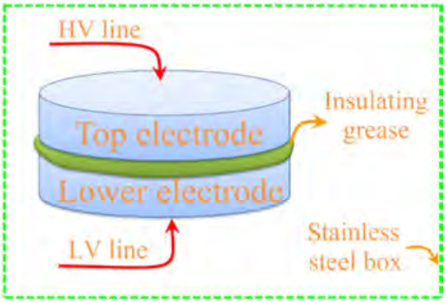

Fig. 2 Diagram of plate electrode structure.

2.4 Friction and wear tests

The tribological properties of the insulating greases were investigated using a MFT-R4000 reciprocation friction and wear tester with a ball-on-disk configuration (Fig. 3) at room temperature. The upper ball (commercially available AISI 52100 steel ball, diameter: 5 mm, hardness: 710 HV) was driven to reciprocally slide against the lower fixed disk (Φ 24 mm × 7.9 mm, AISI 52100 steel, hardness: 590–610 HV) at a stroke of 5 mm. The upper ball and lower disks were cleaned using an ultrasonic cleaner comprising petroleum ether for 10 min before and after the friction test. About 1 g of grease was introduced into the reciprocating sliding region. The tribological test parameters, including applied loads and frequencies, range from 50 N to 200 N (corresponding to the Hertzian pressure in the range of 1.7–2.7 GPa) and 2 Hz to 5 Hz, respectively. The computer connected with the MFT-R4000 tribometer can record the coefficient of friction (COF) automatically. Each tribological test lasts for 30 min and was repeated three times to guarantee the reliability of the experimental data. After the tribological test, the upper ball and lower blocks were cleansed in petroleum ether for 10 min utilizing an ultrasonic cleaner. Then, an optical microscope (Olympus, Japan) was employed to acquire the wear width and morphology of the worn

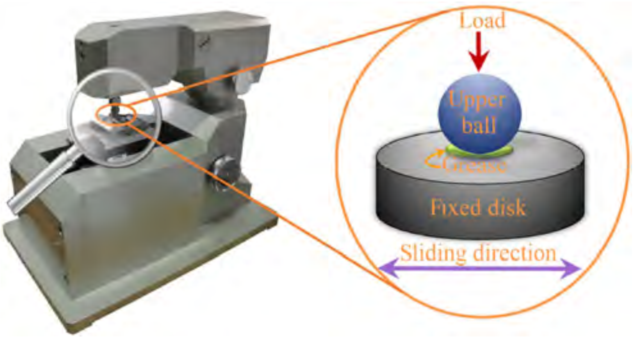

Fig. 3 The MFT-R4000 reciprocation tribometer and contact configuration of the friction pairs.

surface on the lower disk. A Raman spectroscope with 514 nm laser excitation (Renishaw, UK) and an energy dispersive X-ray spectroscope (Bruker, Germany) were utilized to evaluate the lubricating mechanisms.

3 Results

3.1 Properties of the insulating greases

3.1.1 Physicochemical characteristics of the insulating greases

The physicochemical parameters of grease can affect the fundamental characteristics. According to the tribological tests shown in the following section, we provided the typical properties of the lubricating greases, containing 1.0% OMMT, 1.5% IOMMT, 1.5% MMT, and 1.0% SiO_2, in Table 3. Compared with the base grease, it was observed that all the additives improved the dropping point and penetration and all the greases possessed good corrosion resistivity. The lubricating grease with 1.0% OMMT exhibited the lowest penetration among all the greases. The main reason leading to low penetration is that the OMMT has a relatively high SSA and pore volume, which result in a high adsorption capacity. OMMT can restrict the movement of the liquid molecules due to the surface force (which is similar to the intermolecular force). Therefore, the OMMT grease possesses a relatively lower penetration [30].

3.1.2 Insulating capacity of the prepared greases

A dielectric conductor loses its dielectric properties under the action of a strong electric field to become an electric conductor. This phenomenon is called dielectric breakdown, and the corresponding voltage is called the breakdown voltage [31, 32]. Volume resistivity is the current impedance of the material per unit volume and is used to characterize the material's electrical properties [33, 34]. Therefore, we measured these parameters to characterize the material's insulating performance. Figure 4(a) shows the AC breakdown voltage of the insulating greases with different additive contents. It is clearly observed that the AC breakdown voltage increases with increasing additive content except for 1.5% OMMT. Compared with the base grease, the AC breakdown voltage of 1.5% IOMMT grease (6.54 kV) increased by 21%. Figure 4(b) describes the volume resistivity evolution of insulating greases with different additive contents. As the content of the additive increases, the volume resistivity increases; the IOMMT greases possess the highest volume resistivity among all the insulating greases. The volume resistivity of 2.0% IOMMT grease is about 65% higher than that of base grease. The AC breakdown voltage and volume resistivity indicate that the IOMMT grease possesses excellent insulating property.

Table 3 Typical properties of the several kinds of insulating greases.

Sample	Dropping point (˚C)	1/4 Penetration (0.1 mm)	Copper corrosion (T2 copper, 100 ˚C, 24 h)
Base grease	332	122	1a
OMMT (1.0 wt%) grease	>350	81	1a
IOMMT (1.5 wt%) grease	>350	94	1a
OMMT (1.5 wt%) grease	>350	92	1a
SiO_2 (1.0 wt%) grease	>350	89	1a

The electron capture theory is used to explain the insulating mechanism [35, 36]. Existing studies have proved that under the effect of the local electric field, the electron can polarize the surrounding molecules to develop charged particles and form a directional movement. After the charged particles move some distance, the electron will detach and reform into new charged particles and continue to move, thereby generating the current. Nevertheless, in the process of movement and developing new charged particles, the energy of the electron gradually decreases. These charged particles can be named as the electron trap [37, 38]. The addition of nano-montmorillonite can significantly increase the number of electron traps in the base grease, which can reduce the electron transfer rate and energy, leading to a conductive path that is difficult to form [24, 39]. Thus, the AC breakdown voltage and volume resistivity of the insulating greases are improved. A high trap density is generated by IOMMT in the grease, which makes a positive contribution for high AC breakdown voltage and volume resistivity.

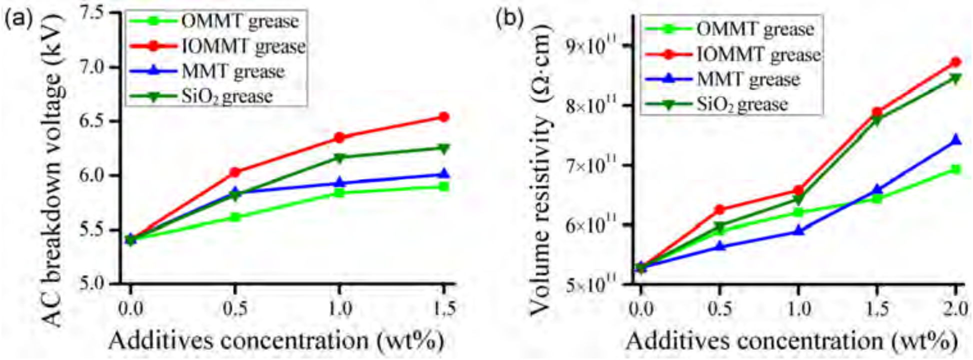

Fig. 4 The AC breakdown voltage (a) and volume resistivity (b) of the prepared insulating greases at different additives concentrations.

3.2 Tribological test results

To evaluate the tribological performances of the additives, this article investigated three predominant factors (additive concentration, load, and frequency).

3.2.1 *Effect of additive concentration*

A MFT-R4000 tribometer was employed to investigate the tribological properties of the insulating greases. Figure 5 compares the evolution in the COFs and wear widths for the insulating greases at 50 N, 5 Hz, and room temperature (RT). As shown in Fig. 5(a), it is clearly observed that with the increasing concentration of additives, the COFs of all the insulating greases decrease first and then increase. When the concentration of the additives is 1.0%, 1.5%, 1.5%, and 1.0%, the grease exhibits the best friction reducing property. As shown in Fig. 5(b), the wear width has a similar variation tendency. Compared with the base greases (about 0.19 mm), the lubricating grease with 1.0% OMMT, 1.5% IOMMT, 1.5% MMT, and 1.0% SiO_2 exhibited the lowest wear width (about 0.146–0.174 mm). For friction reducing and anti-wear performances, the 1.5% IOMMT grease shows the best tribological performances among all the insulating greases.

Similarly, it can be clearly observed that the best concentration of OMMT in the grease is not the same as that of IOMMT and MMT. This is because the nano-montmorillonite modified by the organics possesses a high SSA and pore volume, due to which OMMT is not uniformly dispersed in the base grease and goes against the formation of the lubrication film during the friction process. Therefore, in the following experiments, the concentration of OMMT, IOMMT, MMT, and SiO_2 in the greases was 1.0%, 1.5%, 1.5%, and 1.0%, respectively.

3.2.2 *Effect of load*

Figure 6 lists the evolution of the COFs and wear widths for the lubricating greases at different loads, 5 Hz, and RT. It is obviously seen that the COFs of the greases increase gradually with the increasing loads, but the IOMMT grease always shows smaller COFs among all the insulating greases under different

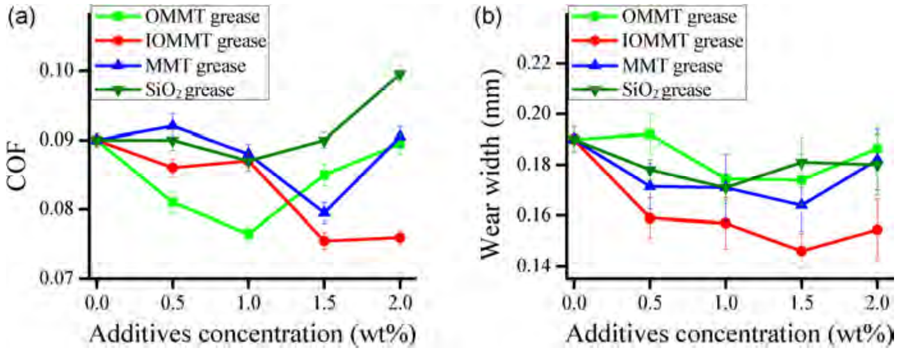

Fig. 5 The average COFs (a) and wear widths change (b) under the lubrication with insulating greases at different additives concentrations at 50 N, 5 Hz, and RT.

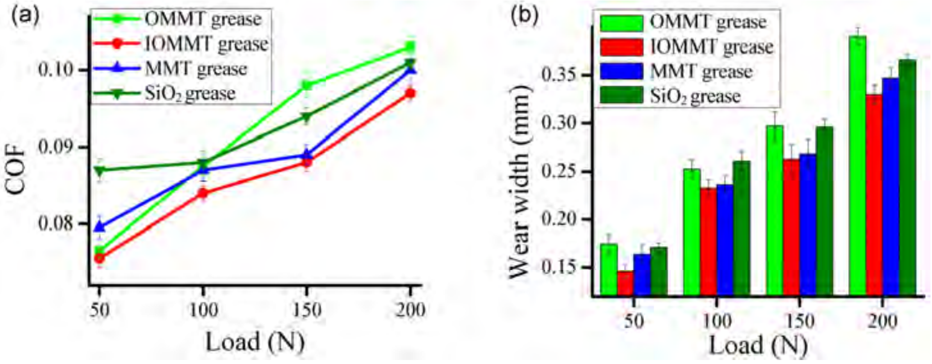

Fig. 6 The average COFs (a) and wear widths change (b) under the lubrication with insulating greases at different loads, 5 Hz, and RT.

loads. As shown in Fig. 6(b), the IOMMT greases show an obviously lower wear width under 50 N and 200 N. When the loads are 100 N and 150 N, the wear widths of IOMMT greases (about 0.23 mm and 0.26 mm) are close to that of the MMT greases (about 0.24 mm and 0.27 mm). The results indicate that the IOMMT grease has better tribological properties than other greases.

3.2.3 *Effect of frequency*

Figure 7 displays the COFs and wear widths of insulating greases at different frequencies, 200 N, and RT. As shown in Figs. 7(a) and 7(b), the COFs and wear widths decrease first and then increase with the frequency ranging from 2 Hz to 5 Hz. At the same time, compared with the other greases, the IOMMT grease exhibited lower COFs and wear widths. The results demonstrate that the IOMMT grease possesses better friction reducing and wear resistance performances than the other lubricating greases.

3.2.4 *Analysis of the worn surfaces*

The surface morphologies of the worn surfaces lubricated with insulating greases are provided in Fig. 8. All the surface morphologies are obtained under the same conditions. The wear width (Fig. 8(b)) and the high magnification morphology (Fig. 8(b)) of the worn surface lubricated with IOMMT grease are the narrowest and smoothest. There are just a few shallow furrows. In contrast, the worn surfaces lubricated with OMMT, MMT, and SiO_2 exhibited more dense furrows and larger pits, which are dominated by abrasive and adhesion wear. The images of worn surfaces clearly demonstrate that the IOMMT grease has a better anti-wear performance than that of the other greases.

EDS is an excellent experimental tool to characterize the typical elements on the worn surfaces. To further explore the friction reducing and anti-wear mechanism of the insulating greases, the EDS spectra of the wear scratches lubricated with insulating greases at 200 N and 5 Hz are provided in Fig. 9. It can be obviously seen that there are some emblematic elements of nano-montmorillonite, such as Al and Si, existing on the wear scratches in Figs. 9(a), 9(b), and 9(c). Compared

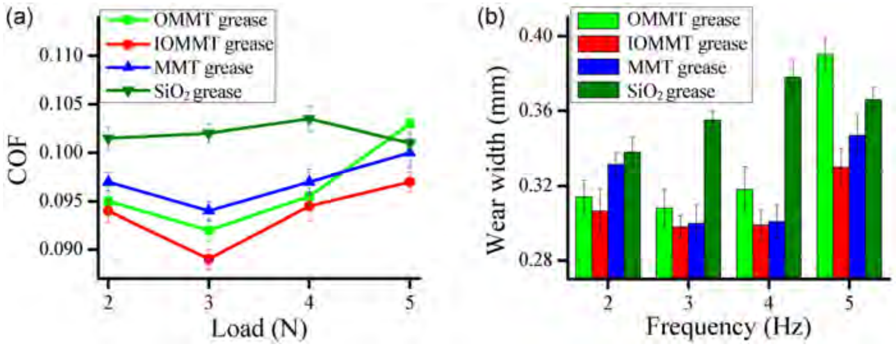

Fig. 7 The average COFs (a) and wear widths change (b) under the lubrication with insulating greases at different frequencies, 200 N, and RT.

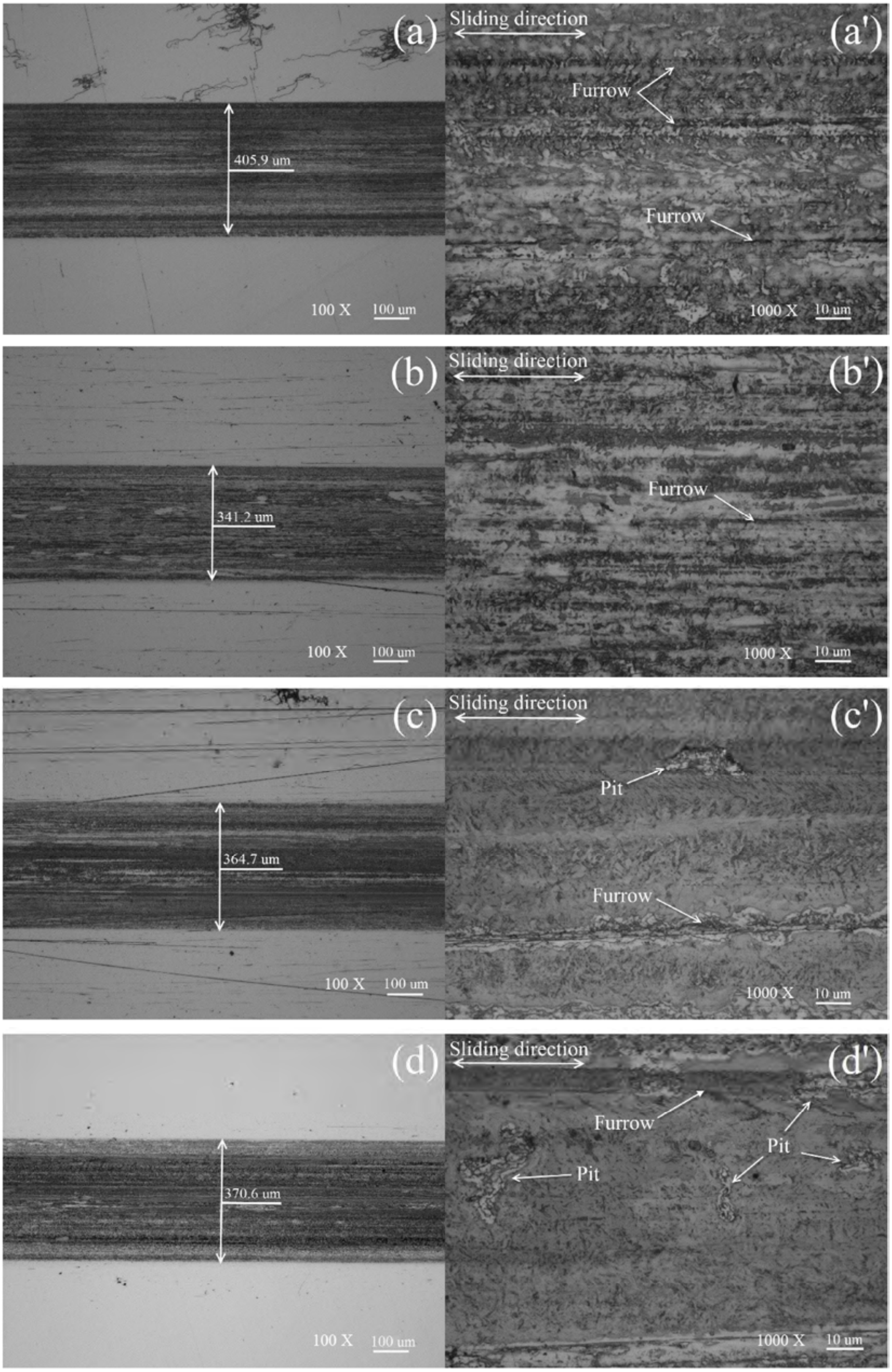

Fig. 8 Morphologies of the worn surfaces lubricated with insulating greases at 200 N, 5 Hz, and RT. (a) and (a') OMMT grease, (b) and (b') IOMMT grease, (c) and (c') MMT grease, (d) and (d') SiO_2 grease.

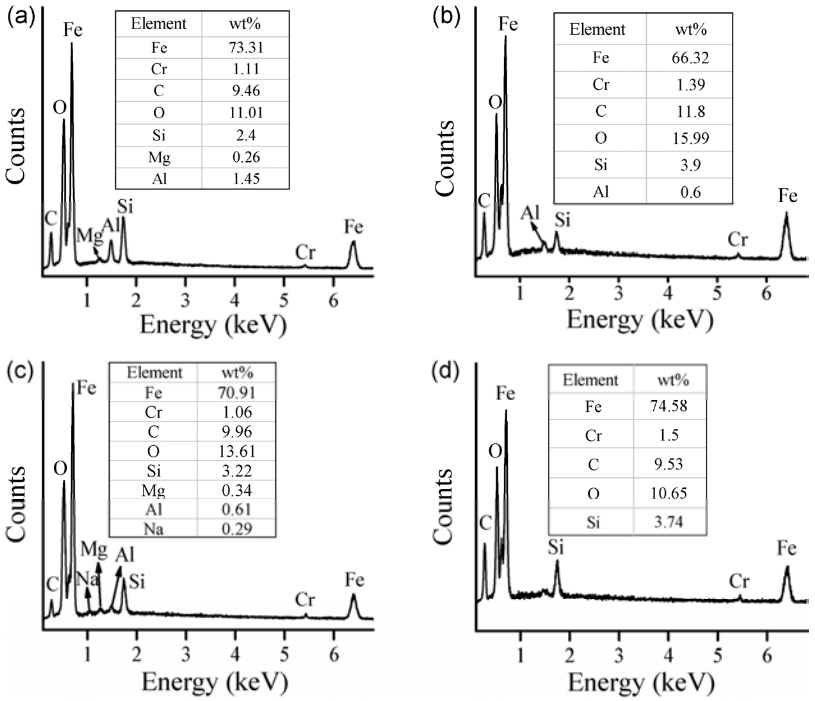

Fig. 9 EDS of the worn surfaces lubricated with insulating greases at 200 N, 5 Hz, and RT. (a) OMMT grease, (b) IOMMT grease, (c) MMT grease, and (d) SiO_2 grease.

with the wear scratch lubricated with MMT grease (Fig. 9(c)), the sodium and magnesium elements are not observed on the wear scratches lubricated with OMMT and IOMMT greases (Figs. 9(a) and 9(b)), respectively. There is also plenty of Si (3.7%) on the wear scratch lubricated with SiO_2 grease (Fig. 9(d)), but the contents of C (9.53%) and O (10.65%) are much lower compared to that of the IOMMT grease. From the EDS spectra, we obtain that the contents of C (11.8%), O (15.9%), and Si (3.9%) on the wear scratch lubricated with IOMMT grease are higher than those of the other greases. It is presumed that a sufficiently protective tribofilm is generated on the worn surface in the sliding process. Consequently, the IOMMT grease performs outstanding friction reducing and anti-wear performances.

Figure 10 corresponds to the Raman spectra of IOMMT and the worn surface lubricated with 1.5% IOMMT grease at 200 N, 5 Hz, and RT. The IOMMT is characterized by bands located at 200 cm^{-1}, 270 cm^{-1}, 450 cm^{-1}, 710 cm^{-1}, and 1,090 cm^{-1} [40, 41]. After the tribological test, the disk is cleaned ultrasonically in petroleum ether for 10 min. Then, the worn surface is examined using a Raman microscope. It is obviously seen that these typical peaks of IOMMT exist on the worn surface. At the same time, we also acquire some other bands (224 cm^{-1}, 328 cm^{-1}, 425 cm^{-1}, and 609 cm^{-1}), which are assigned to various iron oxides [42, 43]. The Raman test results prove that IOMMT is adsorbed on the worn surface to form an adsorption film and iron oxides are generated on the worn surfaces to form a chemical reaction film.

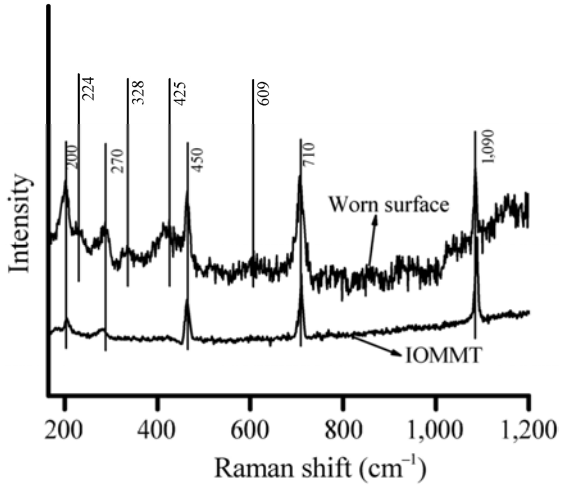

Fig. 10 Raman spectra of the nanometer IOMMT and worn surface lubricated with IOMMT grease at 200 N, 5 Hz, and RT.

3.2.5 *Tribological tests discussion*

Herein, the intricate lubrication behavior of the prepared insulating greases was studied for steel/steel friction pair with addition of 1.5% IOMMT, which exhibited better tribological performances than that of the other greases. Figure 11 is a schematic of the nano-additive dispersed in the insulating greases during the sliding process, which can explain the friction and wear mechanisms. The friction reducing and anti-wear properties can be illustrated by the following factors. First, the crystal cell of nano-montmorillonite is similar to a sandwich structure; the upper and lower layers are silicon–oxygen tetrahedrons and the middle layer is an aluminum–oxygen octahedron [14–18]. The primary connection forces between the two layers are molecular and hydrogen bonds [44]. Under the friction heat, the connection forces are easily broken, leading nano-montmorillonite to release numerous small secondary particles and active oxygen. These secondary particles can act as spacers, preventing the close contact between the contact pairs [23, 25]. Second, there is a large number of unsaturated and dangling bonds, such as Si–O–Si, O–Si–O, and Mg–O, existing on the nano-montmorillonite powder surface. It makes the particles possess strong polarity and adsorb tightly on the friction surface. Thus, the adsorption film possessing friction reducing and anti-wear properties is formed on the friction surface [45, 46]. Third, the local high temperature and pressure caused by the asperity collision during the sliding process are beneficial for active atoms to be deposited and react, promoting the formation of an oxidation protecting film on the worn surface. At the same time, it can also induce decomposition and fracture of the lubrication oil chains to be deposited on the worn surface. These factors work together to generate the friction reducing and anti-wear properties [45, 47–49].

4 Conclusions

We summarize the abovementioned experimental works of insulating greases as follows: the inorganic modified nano-montmorillonite (IOMMT) as an insulating additive in the grease can significantly increase the number of electron traps to improve the AC breakdown voltage and volume resistivity. The insulating grease synthesized with IOMMT also exhibits better friction reducing and anti-wear performances for the steel/steel contact pairs, and the optimal concentration for IOMMT is recommended as 1.5 wt%. The friction reducing and anti-wear performances are mainly attributed to the unique layered structure that prevents the close contact between the touching pairs and the protective tribofilm generated by the physical adsorption and chemical reaction. This indicates that IOMMT as a solid additive is highly effective to improve the insulation and tribological performances of lubricating greases for extensive applications.

Acknowledgements

This work is supported by the National Natural Science Foundation of China (No. 51575181) and Beijing Natural Science Foundation of China (No. 51575181).

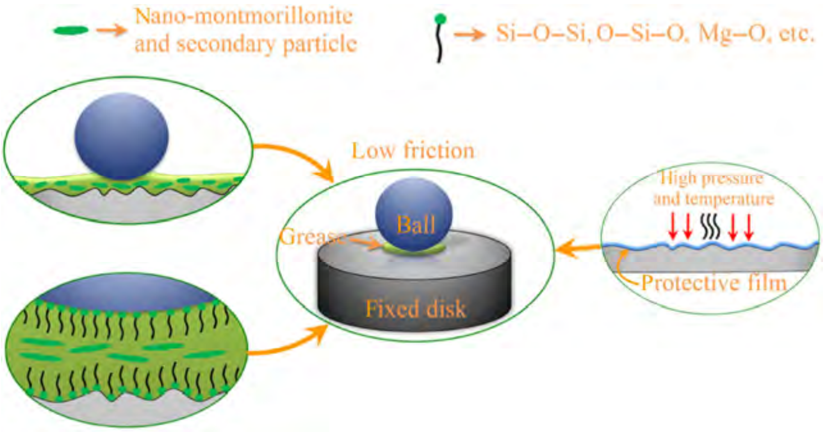

Fig. 11 Schematic of friction mechanism of the insulating greases.

References

[1] Waara P, Hannu J, Norrby T, Ake B. Additive influence on wear and friction performance of environmentally adapted lubricants. *Tribol Int* **34**(34): 547–556 (2001)

[2] Qu J, Bansal D G, Yu B, Howe J Y, Luo H, Dai S, Li H, Blau P J, Bunting B G, Mordukhovich G, Smolenski D J. Antiwear performance and mechanism of an oil-miscible ionic liquid as a lubricant additive. *Acs Appl Mater Interfaces* **4**(2): 997–1002 (2012)

[3] Piet M, Lugt. A review on grease lubrication in rolling bearings. *Tribol Trans* **52**(4): 470–480 (2009)

[4] Ge X Y, Xia Y Q, Shu Z Y, Zhao X P. Conductive grease synthesized using nanometer ATO as an additive. *Friction* **3**(1): 56–64 (2015)

[5] Ge X Y, Xia Y Q, Feng X. Influence of carbon nanotubes on conductive capacity and tribological characteristics of poly(ethylene glycol-ran-propylene glycol) monobutyl ether as base oil of grease. *Trans ASME J Tribol* **138**: 0742–4787 (2015)

[6] Fan X Q, Xia Y Q, Wang L P. Tribological properties of conductive lubricating greases. *Friction* **2**(4): 343–353 (2014)

[7] Fan X Q, Wang L P, Wen L, Wan S. Improving tribological properties of multialkylated cyclopentanes under eimulated epace environment: two feasible approaches. *Acs Appl Mater Interfaces* **7**(26): 14259–14368 (2015)

[8] Fan X Q, Wang L P. Highly conductive ionic liquids toward high-performance space-lubricating greases. *Acs Appl Mater Interfaces* **6**(16): 14660–14671 (2014)

[9] Voevodin A A, Zabinski J S. Nanocomposite and nano-structured tribological materials for space applications. *Compos Sci Technol* **65**(5): 741–748 (2005)

[10] Marchetti M, Jones W R, Street K W, Wheeler D, Dixon D, Jansen M J, Kimura H. Tribological performance of some pennzane-based greases for vacuum applications. *Tribol Lett* **12**(4): 209–216 (2002)

[11] Ge X Y, Xia Y Q, Cao Z F. Tribological properties and insulation effect of nanometer TiO_2 and nanometer SiO_2 as additives in grease. *Tribol Int* **92**: 454–461 (2015)

[12] Hassan A M, Shahba R M A, Youssif M A, Youssif M A, Mazrouaa A M, Youssif M A E. Preparation of some dielectric greases from different types of polymers. *J Appl Polym Sci* **119**(2): 1026–1033 (2011)

[13] Ferrito S J, Makal J M. Accelerated aging characteristics of lubricating greases used for separable insulated connector applications. In *Transmission and Distribution Conference—IEEE*, 1999: 89–93.

[14] Zahed S, SharifiSanjani N. The role of clay-montmorillonite on thermal characteristics and morphology of electrospun PAN nanofibrous mats. *E-Polym* **11**(18): 898–905 (2013)

[15] Yang T, Knutsson S. Swelling properties and permeability of expandable clays of potential use for nuclear waste disposal. *J Earth Sci Geotech Eng* **6:** 49–61 (2016)

[16] Calvet R. Cation migration into empty octahedral sites and surface properties of clays. *Clays Clay Miner* **19**(3): 175–186 (1971)

[17] Cheng M M, Song W J, Ma W H, Chen C C, Zhao J C, Lin J, Zhu H Y. Catalytic activity of iron species in layered clays for photodegradation of organic dyes under visible irradiation. *Appl Catal B* **77**(3–4): 355–363 (2008)

[18] Lin F H, Chen C W, Kuo T F. Modified montmorillonite as vector for gene delivery. *Biomaterials* **27**(17): 3333–3338 (2006)

[19] Usuki A, Kawasumi M, Kojima Y, Okada A, Kurauch T, Kamigaito O. Swelling behavior of montmorillonite cation exchanged for ω-amino acids by–caprolactam. *J Mater Res* **8**(5): 1174–1178 (1993)

[20] Biswas M, Ray S S. Recent progress in synthesis and evaluation of polymer-montmorillonite nanocomposites. *Adv Polym Sci* **155:** 167–221 (1970)

[21] And K E S, Manias E. Structure and properties of poly (vinyl alcohol)/Na+ montmorillonite nanocomposites. *Chem Mater* **12**(10): 2943–2949 (2000)

[22] Pojanavaraphan T, Schiraldi D A, Magaraphan R. Mechanical, rheological, and swelling behavior of natural rubber/montmorillonite aerogels prepared by freeze-drying. *Appl Clay Sci* **50**(2): 271–279 (2010)

[23] Rashmi, Renukappa N M, Suresha B, Devarajaiah R M, Shivakumar K N. Dry sliding wear behaviour of organo-modified montmorillonite filled epoxy nanocomposites using Taguchi's techniques. *Mater Des* **32**(8–9): 4528–4536 (2011)

[24] Yuan Y, Liao R. A novel nanomodified cellulose insulation paper for power transformer. *J Nanomater* **2014**(17): 1–6 (2014)

[25] Fan B L, Yang Y L, Feng C, Ma J, Tang Y, Dong Y, Qi X W. Tribological properties of fabric self-lubricating liner based

on organic montmorillonite (OMMT) reinforced phenolic (PF) nanocomposites as hybrid matrices. *Tribol Lett* **57**(3): 1–12 (2015)

[26] Du Y F, Lv Y Z, Li C R, Chen M T, Zhou J Q, Li X X, Zhou Y, Tu Y P. Effect of electron shallow trap on breakdown performance of transformer oil-based nanofluids. *J Appl Phys* **110**(10): 1–4 (2011)

[27] Du Y F, Lv Y Z, Li C R, Zhong Y X, Chen M T, Zhang S N, Zhou Y, Chen Z Q. Effect of water adsorption at nanoparticle–oil interface on charge transport in high humidity transformer oil-based nanofluid. *Colloids Surf A* **415**(415): 153–158 (2012)

[28] Ravichandran J. Properties and catalytic activity of acid-modified montmorillonite and vermiculite. *Clays Clay Miner* **45**(6): 1–7 (2014)

[29] Chi X H, Gao J G, Zhang X H. Electrical tree propagating characteristics of polyethylene/nano-montmorillonite composites. *IEEE Trans Dielectr Electr Insul* **22**(3): 1530–1536 (2015)

[30] Wang H X, Wang H X, Xue L. Study of adsorption of industrial oil by expanded graphite. *Carbon Tech* **23:** 21–23 (2004)

[31] Taguchi Y, Matsumoto T, Tokura Y. Dielectric breakdown of one-dimensional mott insulators Sr_2CuO_3, and $SrCuO_2$. *Phys Rev B* **62**(11): 7015–7018 (2000)

[32] Oka T, Aoki H. Ground-state decay rate for the Zener breakdown in band and mott insulators. *Phys Rev Lett* **95**(13): 137601–137601 (2005)

[33] Liang Y, Chen Y X, Liu Y P. The development of the three-electrode testing system for the volume resistivity of composite insulation materials. *Sensors-Basel* **10**(3): 1–5 (2012)

[34] Rakowska A, Hajdrowski K. Influence of different test conditions on volume resistivity of polymeric insulated cables and polyethylene samples. In *Dielectric Materials, Measurements and Applications*, *English International Conference—IEEE*, 2000: 281–284.

[35] Huang J G, O'Sullivan F, Zahn M, Hjortstam O, Pettersson L A A, Liu R. Modeling of streamer propagation in transformer oil-based nanofluids. In *Electrical Insulation and Dielectric Phenomena—IEEE*, 2008: 361–366.

[36] Henry C H, Lang D V. Nonradiative capture and recombination by multiphonon emission in GaAs and GaP. *Phys Rev B* **15**(2): 989–1016 (1977)

[37] Zhou J Q, Du Y F, Chen M T, Li C R, Li X X, Lv Y Z. AC and lightning breakdown strength of transformer oil modified by semiconducting nanoparticles. In *Electrical Insulation and Dielectric Phenomena—IEEE*, 2011: 652–654.

[38] Du Y F, Lv Y Z, Li C R, Chen M T, Zhou J Q, Li X X, Liu Tong. Insulating property and mechanism of semiconducting nanoparticles modified transformer oils. *Proc Csee* **32**(10): 177–182 (2012)

[39] Zhang W, Xu M, Zhang X, Xie D R. Study of montmorillonite concentration on dielectric property and dispersion of cross-linked polyethylene/montmorillonite nano-composites. In *Electrical Insulation and Dielectric Phenomena—IEEE*, 2013: 531–534.

[40] Frost R L, Rintoul L. Lattice vibrations of montmorillonite: an FT Raman and X-ray diffraction study. *App Clay Sci* **11**(2-4): 171–183 (1996)

[41] Xu K, Wang J, Xiang S, Chen Q, Zhang W D, Wang P X. Study on the synthesis and performance of hydrogels with ionic monomers and montmorillonite. *App Clay Sci* **38**(s1–2): 139–145 (2007)

[42] Lübbe M, Gigler A M, Stark R W, Moritz W. Identification of iron oxide phases in thin films grown on Al_2O_3(0001) by Raman spectroscopy and X-ray diffraction. *Sur Sci* **604**(7–8): 679–685 (2010)

[43] Shim, Duffy SH/, Thomas S. Raman spectroscopy of Fe_2O_3 to 62 GPa. *Am Mineral* **87**(2-3): 318–326 (2015)

[44] Hensen E J M, Tambach T J, Bliek A, Smit B. Adsorption isotherms of water in Li–, Na–, and K–montmorillonite by molecular simulation. *J Chem Phys* **115**(7): 3322–3329 (2001)

[45] Yu H L, Xu Y, Shi P J, Wang H M, Zhao Y, Xu B S, Bai Z M. Tribological behaviors of surface-coated serpentine ultrafine powders as lubricant additive. *Tribol Int* **43**(3): 667–675 (2010)

[46] Frost R L, Cash G A, Kloprogge J T. Rocky Mountain leather, sepiolite and attapulgite–an infrared emission spectroscopic study. *Vib Spectrosc* **16**(2), 173–184 (1998)

[47] Zhang B S, Xu Y, Xu B S, Gao F, Shi P J, Zhang B. The self-reconditioning effect of the phyllosilicate lubricating material on Fe-based tribopairs. *J Funct Mater* **42**(7): 1301–1304 (2011)

[48] Yang Y, Gu J, Kang F, Kong X, Wei M. Surface restoration induced by lubricant additive of natural minerals. *Appl Surf Sci* **253**(18): 7549–7553 (2007)

[49] Wang F. Research on microstructure of the auto-restoration layer of worn surface of metals. *Mater Sci Eng A* **399**(1–2): 271–275 (2005)

Zhengfeng CAO. He received his bachelor and master degrees from North China Electric Power University in 2013 and 2016, respectively. After that, he is currently a PhD student at the same university. His research interests are focused on preparation and tribological property investigation of lubricating greases.

Yanqiu XIA. He received his PhD degree from Northeastern University in 1999, and was selected as Hundreds Talent Program of Chinese Academy of Science Professor in 2007. He joined the School of Energy Power and Mechanical Engineer, North China Electric Power University in 2010. His current position is a professor. His research areas cover tribology of mechanical and electrical equipment, focusing on lubricants, greases, additives, and tribochemistry.